Dissertation

submitted to the
Combined Faculties for the Natural Sciences and for Mathematics of
the Ruperto-Carola University of Heidelberg, Germany
for the degree of
Doctor of Natural Sciences

Put forward by
Dipl. Phys. Florian Freundt
born in Lemgo

Oral examination: 12.07.2017

Application of Helium Isotopes in Shallow Groundwaters for Geothermal Energy Exploration in the Upper Rhine Graben

Referees:

Prof. Dr. Werner Aeschbach
Prof. Dr. Mario Trieloff

Abstract

The helium isotope system is an established tool in hydrology for identifying mantle fluids in deep aquifers. This study applies the helium tracer system for the first time in shallow, unconfined aquifers of the Upper Rhine Graben. The Graben is a part of the Cenozoic Rift system of Western and Central Europe, a continental rift zone with unusually high geothermal gradients, making it an ideal region of Germany for geothermal energy development. The aim of this study is to develop a suite of natural groundwater tracers able to achieve a cost and effort reduction in geothermal prospection. The $^{3}He/^{4}He$-ratio is therefore applied, as part of a multi-tracer approach including ^{3}H, $\delta^{18}O$, $\delta^{2}H$, $\delta^{13}C$, ^{14}C and ^{222}Rn, to identify and locate fault zones with suitable permeabilities for power plant operation. Three target areas along the graben were studied, each located on one of the main fault lines.
A mantle-derived helium signature could be identified and separated from tritiogenic helium in a shallow aquifer in the north-west of the Graben. The mixing component of mantle-derived fluid in the shallow groundwater is calculated to reach up to 5 %, based on the analysis of the $^{3}He/^{4}He$ isotope system. The employed method proves that the local permeability of the fault zone is high. The origin of the locally occurring upwelling of salinated water can be redetermined by the data.

Zusammenfassung

Die Helium-Isotopie ist ein etabliertes Werkzeug in der Hydrologie zur Identifizierung von Manteleinflüssen in Tiefenwässern. Diese Arbeit wendet die $^{3}He/^{4}He$-Helium-Isotopie zum ersten Mal auf flache, ungespannte Aquifere im Oberrheingraben an. Als Teil des Westeuropäischen Grabensystems, einer kontinentalen Riftzone, die sich durch ungewöhnlich hohe Wärmeanomalien auszeichnet, ist der Oberrheingraben eine ideale Region Deutschlands für die Entwicklung von geothermischer Energiegewinnung. Das Ziel der Arbeit ist, eine Multi-Tracer-Methodik zu entwickeln, die es anhand natürlicher hydrologischer Tracer ermöglicht, die Kosten und das Fündigkeitsrisiko bei der Exploration für Geothermiekraftwerke zu verringern. Die Helium-Isotopie wird daher, zusammen mit ^{3}H, $\delta^{18}O$, $\delta^{2}H$, $\delta^{13}C$, ^{14}C und ^{222}Rn, dazu verwendet, Störungszonen zu lokalisieren und identifizieren, die eine geeignete Permeabilität für den Betrieb Geothermischer Kraftwerke aufweisen. Dazu wurden drei Gebiete längs des Oberrheingrabens untersucht, jedes ist auf einer der Hauptgrabenrandstörungen lokalisiert.
In einer der drei Regionen im Nordwesten des Grabens konnte eine permeable Störungzone identifiziert werden. Die Herkunft der dort vorgefundenen Helium-Isotopie kann eindeutig dem Mantelreservoir zugeordnet und von einer tritiogenen Überprägung abgegrenzt werden. Die nachgewiesene Beimischung von mantelbeeinflusstem Fluid wird auf bis zu 5 % bestimmt. Eine dort auftretende Grundwasserversalzung kann dadurch in ihrer Herkunft neu zugeordnet werden. Die angewande Methodik weist damit nach, dass die lokale Permeabilität der Störungszone den Aufstieg eines Tiefenfluides ermöglicht.

Contents

Chapter 1

Introduction

1.1 Geothermal Energy Production

Exploiting geothermal energy has remarkable benefits, compared to energy production from fossil fuels as well as renewable energy sources, as it is both low on CO_2 emissions and independent from weather influences, thereby being able to provide stable base load. However, the resource is geographically restricted and hard to explore – in Germany, only three regions are reasonable candidates for geothermal exploration based on current technology: the North German Basin, the Bavarian Molasse Basin and the Upper Rhine Graben.

A good example for this kind of geothermal energy production is Iceland, where volcanic activity is high, and associated heat anomalies can be found close to the surface. As of 2011, only four active geothermal power plants with a total plant capacity of 6.75 MW existed in Germany [DiPippo, 2012]. By 2014, those numbers rose to 9, with a plant capacity of 36.9 MW and 32 further projects in various development stages [GtV, 2017]. Several of the existing and prospected plants are located in the Upper Rhine Graben, in Landau, Insheim, Soultz-sous-Forets (France), Bruchsal, Ketsch, and Groß-Gerau, of which some are facing diverse geological and political challenges in the planning phase as well as during operation.

The prospecting phase of drilling into a geothermal reservoir and actually finding the required parameters – temperature, hydraulic permeability and sufficient amounts of geothermal fluid – is by far the main risk associated with geothermal power plant projects [Bauer, 2014; ÜWG, 2016]. However, even in a successfully established plant, problems stemming from the geology of the target region can lead to massive risks during operation and even entire project shutdowns [ITG, 2014].

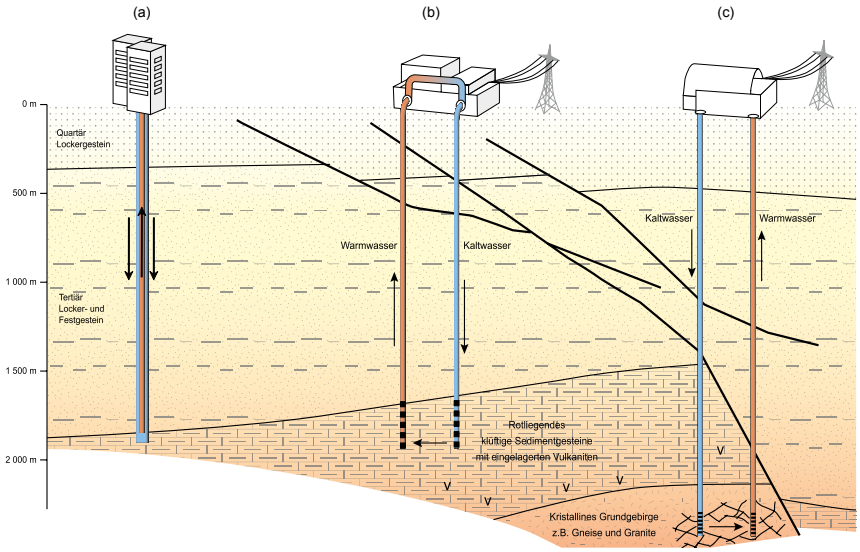

Figure 1.1: Schematic illustration of different geothermal energy applications: (a) simple deep hole heat exchanger (b) hydrothermal aquifer doublet system for heat and energy production (c) hot-dry-rock (HDR) or EGS system [HLUG, 2010].

1.1.1 Principle and Potential

The generation of electricity on an industrial scale is usually associated with high enthalpy reservoirs at relatively shallow depths, providing high water temperatures above 200℃ [Bauer, 2014]. The low enthalpy reservoirs available in the local geology of Germany can, however, be exploited for power production by using binary fluid systems like the *Organic Rankine Cycle* and *Kalina Cycle* technology, where the hydrothermal water is not used directly to drive turbines but used to heat a working medium with lower boiling temperatures [DiPippo, 2012], see Fig. A.4 for possible power plant outputs.

Natural hydrothermal systems offer existing thermal water that has to be pumped to the surface by a production well, the thermal energy is then being exploited in the power plant generators and the cooled liquid is re-injected into the hydrothermal aquifer by a second well (doublet system, see Fig. 1.1). Alternatively, enhanced geothermal systems (EGS) can be established (as the plant at Soultz-sous-Forets is [Baria et al., 1999]) – making use of hot but dry bedrock, which is injected with large amounts of high pressured fluid. This hydraulic stimulation (often combined with chemical stimulation) is necessary to increase the hydraulic permeability of the crystalline bedrock, allowing suitable flow rates for power plant operation. Stimulating such reservoirs usually works by reactivating previous crevices resealed by mineral deposits, or even by creating new rifts on the scale of hundreds of meters length [Bauer, 2014].

Hydraulic permeability of the target region is a key factor in operating geothermal power plants. The higher the permeability, the less pressure is required to operate the plant efficiently, while also lowering

the probability of induced seismicity. The minimum permeability for cost effective plant operation is given in Bauer [2014] as $2 \times 10^{-4}\,\mathrm{m}^3/\mathrm{s}$, otherwise the required power to run the pumps makes energy production inefficient. The energy required for active production can exceed 50 % of a geothermal power plant's output, depending on the given permeability [STMWIVT, 2004].

The construction and operation of geothermal power plants, both in hydrothermal as well as EGS systems comes with the risk of induced seismicity. This seismicity ranges from micro-events to magnitudes of up to, in rare cases, $5\,\mathrm{M_L}$ on the Richter scale [Majer et al., 2007]. In most recent projects, the magnitude of induced seismicity was in the range of $3\,\mathrm{M_L}$ though, with little to moderate risk of endangering property or health of local residents in the plant's vicinity. As low enthalpy plants (with reservoir temperatures below 200°C are usually also used for district heating, positioning the plants and the wells close to settlements is required to maximize efficiency, to allow for effective heat transfer.

The mechanisms of induced seismicity are fourfold, as Majer et al. [2007] explicates:

- An increase of pore pressure by increasing fluid pressure in the pore matrix due to fluid injection can relieve the external stress of the surrounding environment, leading existing fractures to slip.
- The introduction of thermoelastic strain, by cooler liquids coming into contact with warmer rocks, causing volume contraction in fault areas, and thereby reducing the overall pressure of the system, leading to slippage.
- Volume changes related to the introduction and abstraction of fluid during the power plant operation.
- Geochemical alterations of fracture surfaces by introduction of non native fluids with different chemical properties.

As all these processes release energy from the pre-existing stress field of the exploited fault system, the larger that system is, the higher the risk for high magnitude events – which likely contributed to the termination of the Basel Deep Heat Mining project, as it was located in a high-stress region [Majer et al., 2007].

Therefore, acquiring a better knowledge about key factors of the hydrothermal target systems, by developing cost-effective exploration methods, is paramount for mitigating the prospection risks.

1.1.2 Current State of Exploration Methods

The licensed fields in geothermal energy development are usually in the order of 100 to $300\,\mathrm{km}^2$. This area is extensively investigated from the surface, via field mapping as well as aerial and satellite mapping, whenever possible resorting to already available data. The aim is to get as much relevant information

about the geologic subsurface structure as is possible from the surface, before resorting to more expensive subsurface investigations. However, analysing and extrapolating outcrops of rock layers of the target formations is prone to uncertainties and errors. Since the regions of interest in geothermal energy production have a rather large overlap with those of petroleum and natural gas resources in Germany [BGR, 2009; Bauer, 2014], data from exploration boreholes can often be acquired to allow for more direct, though punctual information. Further data on the location, the direction, and angle the fault strikes, requires more extensive and expensive geophysical research like gravimetrical, geomagnetical and geoelectrical analysis – but most prominently the application of 3D reflection seismics. This method uses the characteristic velocities of artificially induced seismic waves in different types of rock, to gain information on the subsurface structure and its physical properties as permeability, porosity, and density. Shooting a 3D seismic survey in an area as big as the initial fields of interest in geothermal prospection comes with very high costs though, and not merely financially: The required field campaign for shooting a 3D seismic, including the placement of geophones and heavy machinery for seismic induction on or close to private property, can cause or amplify political opposition to geothermal plant projects, as was witnessed by our team during the sampling campaign at Groß-Gerau.

More extensive and detailed information on the current state of technology and science in geothermal exploration can be found in Bauer [2014].

1.2 The TRACE Project

The project *TRACE* (*TiefenReservoir-Analyse und Charakterisierung von der Erdoberfläche*) was proposed in 2011 by the departments of Geology and Physics of *Heidelberg University* (namely by the research group *Hydrogeochemistry and Hydrogeology, Department of Geosciences* of Prof. Dr. Margot Isenbeck-Schröter and the research group *Groundwater and Paleoclimate, Department of Environmental Physics (IUP)* of Prof. Dr. Werner Aeschbach) and the engineering bureau *GeoThermal Engineering GmbH*.

The aim of the project is to develop a cost effective exploration method, based on hydrogeochemistry and natural isotopic tracer data, to lower the exploration risks associated with geothermal power plant placement and construction. Fielding a tracer analysis of shallow groundwater at relatively low costs, while not meant to replace existing exploration methods, should allow for a narrowing of the field of interest for further, more expensive geophysical methods of investigation, and thereby for a significant reduction of the exploration costs.

The project is mainly targeted on identifying a suite of hydrological and isotope system tracers, able to point to highly permeable reservoirs in great depths, using the readily accessible shallow aquifers located well above the target aquifers. In highly permeable formations, upwelling of fluids from the target aquifer along fault zones should imprint the shallow aquifers with characteristic signals. The aim of this study,

and its part in the TRACE project, is to investigate whether the stable noble gases, especially the $^{3}He/^{4}He$, and other hydrological tracers like tritium, ^{14}C and radon, can offer valuable information to identify those imprints.

While the focus of this study is on tracer and isotope systems used in environmental physics, the interdisciplinary TRACE projects includes more tracers: the hydrogeochemical properties of the sampled waters, main and trace elements as well as rare earth elements were analysed by Dr. Sami Al Najem, the results can be found in his dissertation [Al Najem, 2016]. The $^{87}Sr/^{86}Sr$ isotopic ratios were analysed by Dr. Gerhard Schmidt and can be found in several publications [Schmidt et al., 2017a,b,c].

Chapter 2

Environmental Tracers in Hydrology

This chapter gives a short intro into the basics of hydrology and the environmental tracers used in this study – for a complete and a lot more detailed insight into each topic, see the references cited in the respective sections, on which this overview is based on.

2.1 Hydrogeologic Basics

Groundwater is an important reservoir of the hydrological cycle, containing about 30 % of earth's fresh water reserves [Hölting and Coldewey, 2009], and groundwater hydrology deals with all its aspects: recharge, residence time, movement. During recharge, precipitating meteoric water infiltrates into the ground, entering the subsurface. The unsaturated (or vadose) zone is the uppermost part of the earth's immediate subsurface, where the pore space is still aerated and filled mostly by air. Its thickness can range between a few centimeters (close to surface water masses, e. g. lakes and rivers) and up to several hundred meters in arid regions. The percolating meteoric water is imprinted with the atmospheric noble gas signal within the vadose zone, modulated by soil temperature, as well as biological processes potentially affecting the soil air composition [Mayer, 2017; Freundt et al., 2013]. Once the water enters the saturated zone, entering the *aquifer*, contact with the atmosphere is severely limited. The most shallow aquifer is typically called *unconfined*, meaning the unsaturated zone begins right above the groundwater table. A confined aquifer is characterized by an *aquitard* layer above the aquifer, a soil structure impermeable to water, restricting upwards movement of the groundwater as well as isolating it from exchange with the soil air of the unsaturated zone. The water pressure at the upper aquifer boundary of a confined aquifer is above the atmospheric pressure, causing the water to rise when the aquitard is fractured. If the hydraulic head reaches above the relief surface, the groundwater can discharge through such fractures and pathways, the

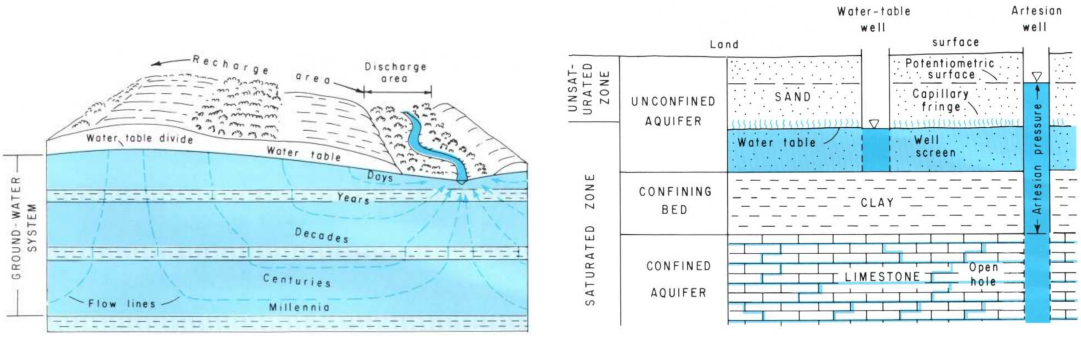

Figure 2.1: A schematic depiction of the basic subsurface regime, concerning groundwater flow and nomenclature, from Heath [1983].

resulting springs are called *artesian*. The groundwater's movement is driven by gravitation and pressure gradients, the resulting flow rates and residence times within aquifers therefore vary depending on the soil's hydraulic properties an recharge rates. Water in confined aquifers can reach ages of up to several 10^5 yr [Sturchio et al., 2004].

2.1.1 Groundwater Flow

Groundwater flow is driven by gravitational forcing, pressure gradients and affected by the properties of the aquifer matrix. A more detailed description than given in the following can be found in Hölting and Coldewey [2009].

For groundwater to move through the soil matrix, reasonably connected flow paths must exist. The *porosity* ϕ, defined by the fraction of pore space volume and total volume

$$\phi = \frac{V_{\text{pore}}}{V_{\text{tot}}} \tag{2.1}$$

is a measure of the space available for water within the soil matrix – for transport processes it represents an upper limit, as some of the volume is not interconnected. The porosity is highly dependent on the soil type, for typical sedimented soils it ranges between 0.3 to 0.65 [Blume et al., 2009].

To describe the dependency of the volumetric flow $\dot{V}$ [$\mathrm{m^3\,s^{-1}}$] of a fluid through a porous medium (laminar flow from the height difference h, through an area A and along the flow path length l), Henry Darcy

formulated *Darcy's Law* in 1856 from experimental observation [Darcy, 1856]:

$$\dot{V} = k_f \cdot A \cdot \frac{h}{l} \tag{2.2}$$

where k_f is the *conductivity coefficient*. The resulting filtration velocity v_f (which is not representing a physically occurring velocity, as the area A is not the actual area available to fluid transport) is then

$$v_f = \frac{\dot{V}}{A} \tag{2.3}$$

and the actual velocity v_{gw} of the moving groundwater is, dependent on the *effective porosity* ϕ_{eff}:

$$v_{\mathrm{gw}} = \frac{v_f}{\phi_{\mathrm{eff}}} = \frac{k_f}{\phi_{\mathrm{eff}}} \cdot \frac{h}{l}\,. \tag{2.4}$$

Permeability

The *permeability* K [Darcy] of a target region for geothermal exploration is of high importance, as the required energy to achieve fluid transfer from the injection well towards the production well affects the plants effectivity and plays a role in induced seismicity. The definition of the permeability parameter originates from the petrochemical industry and is given in Hölting and Coldewey [2009] as

$$K = \eta \cdot \frac{\dot{V}}{A} \cdot \frac{l}{\Delta p} \tag{2.5}$$

where η [Pa s] is the *dynamic viscosity* and Δp [Pa] the pressure difference. It is constant specific to the rock type, characterising the pore medium's conductive properties without regard to the fluid's characteristics.

Darcy's law is valid for laminar flow in porous media, but the flow paths in jointed rocks are usually along the faults, allowing for turbulent flow conditions. On a large scale, in heavily jointed rocks, Darcy's law can still be used for quantitative descriptions of the system. The various tectonic processes acting on consolidated rock, fracturing it by compression, shearing and extension, lead to the formation of anisotropic permeabilities. Quantification of permeabilities is therefore usually only possible for larger scales [Hölting and Coldewey, 2009].

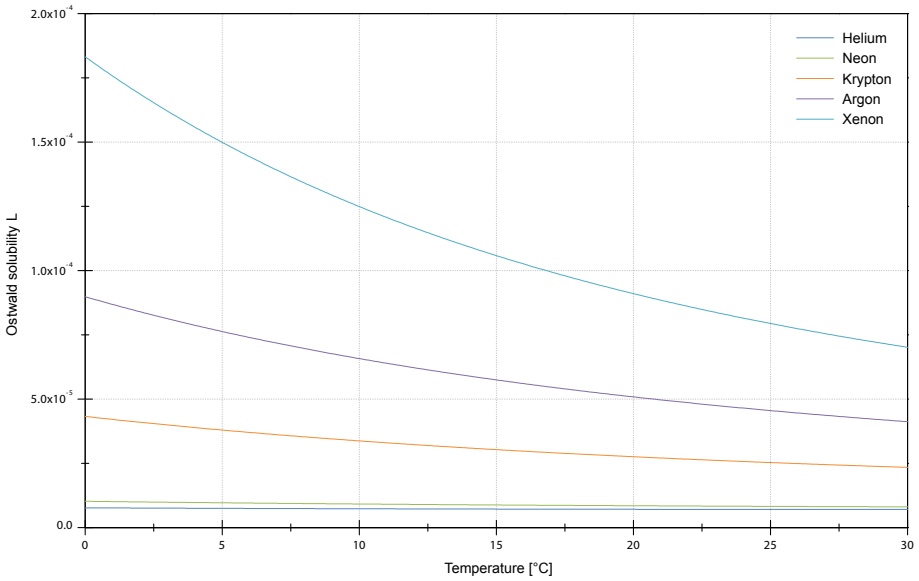

Figure 2.2: Temperature dependency of the Ostwald solubility $L(T, S = 0)$ for the noble gases He, Ne, Ar, Kr and Xe, at atmospheric pressure. The heavier gases show a higher solubility in general as well as a stronger temperature dependency of the solubility. Plot data is calculated using the fit equation and parameters provided by Benson [1976].

2.2 Gas Solubility in Water

The dissolved gas content of water in contact with a gas phase stems from an equlibration between gas phase and water, described in 1803 by William Henry as *Henry's Law* [Henry, 1803]:

$$C_{\mathrm{i}}^{\mathrm{g}}(T, P_a) = H_{\mathrm{i}}(T, S) \cdot C_{\mathrm{i}}^{\mathrm{w}}(T, S, P_a) \tag{2.6}$$

where $C_{\mathrm{i}}^{\mathrm{g}}$ and $C_{\mathrm{i}}^{\mathrm{w}}$ are the concentrations of gas i in the gas and the water phase respectively. H_{i} is the gas specific *Henry constant*, a dimensionless constant that is a function of temperature T and salinity S of the water, and P_a is the atmospheric pressure.

Influences on H_{i} by chemical interactions of solutes found in water can be neglected for groundwater [Kipfer et al., 2002]. Since the Henry constant is dimensionless, its numerical value is defined by the units chosen for the gas concentrations C. The reciprocal of the Henry constant, called *Ostwald solubility* L

[Battino, 1984], is a measure of solubility:

$$L_{\mathrm{i}}(T,S) = \frac{1}{H_{\mathrm{i}}(T,S)} = \frac{C_{\mathrm{i}}^{\mathrm{w}}(T,S,P_a)}{C_{\mathrm{i}}^{\mathrm{g}}(T,P_a)} \tag{2.7}$$

The dependency on temperature of specific gas species is determined experimentally by fitting experimental data to an equation of the form

$$\ln\big(L_{\mathrm{i}}(T,S=0)\big) = a_0 + a_1\frac{1}{T} + a_2\frac{1}{T^2} \tag{2.8}$$

where T is the temperature in Kelvin, resulting in the parameters a_{i} as given in table C.1 [Benson, 1976]. The resulting functions for individual noble gases are shown in Figure 2.2 where the Ostwald solubility $L_{\mathrm{i}}(T,S=0)$ is plotted versus temperature.

Using the partial pressure p_{i} of a gas species i can be more convenient, using the equilibrium concentration C_i^{eq} as described in Kipfer et al. [2002], Henry's Law is formulated as

$$p_{\mathrm{i}} = H_{\mathrm{i}}(T,S)\cdot C_{\mathrm{i}}^{\mathrm{eq}} \tag{2.9}$$

The partial pressure of noble gases in atmospheric air can be calculated from the volume fraction z_{i} of the gas i in dry air, given in table C.3 [Porcelli et al., 2002] and from ambient atmospheric pressure p_{tot}:

$$p_{\mathrm{i}} = z_{\mathrm{i}}\cdot\left(p_{\mathrm{tot}} - e_{\mathrm{W}}(T)\right) \tag{2.10}$$

where $e_{\mathrm{W}}(T)$ is the water vapor content. Local specifics of the recharge area (e. g. elevation) require the correction of the total pressure due to the atmosphere's barometric pressure profile:

$$p_{\mathrm{tot}}(h) = p_0\cdot\exp\left(-\frac{h}{h_0}\right) \tag{2.11}$$

with h and p_0 being the local elevation and pressure above sea level and h_0 the scale height, typically at around 8000 to 8300 m [Kipfer et al., 2002]. The equilibrium concentration in groundwater can then be expressed as

$$C_{\mathrm{i}}^{\mathrm{eq}}(T,S,p_{\mathrm{tot}}(h)) = \frac{z_{\mathrm{i}}\cdot\left(p_{\mathrm{tot}}(h) - e_{\mathrm{W}}(T)\right)}{H_{\mathrm{i}}(T,S)}\,. \tag{2.12}$$

2.2.1 Excess Air

The observed amount of noble gases in groundwater, schematically shown in Fig. 2.3(a), is usually higher than the sheer equilibration with atmospheric air would lead to expect. This excess amount of noble gases additional to the *equilibrium component* has atmospheric isotopic composition and has therefore been named *excess air* [Andrews and Lee, 1979; Heaton and Vogel, 1981]. Its origin has been established

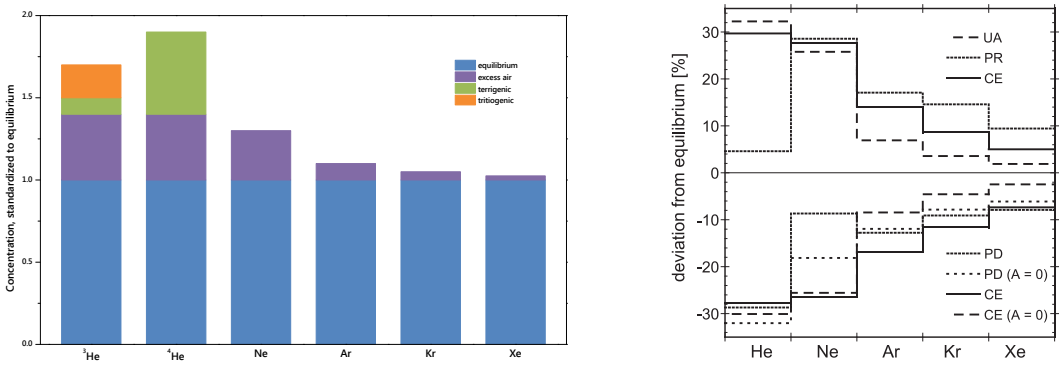

(a) **(b)**

Figure 2.3: (a) The components of dissolved noble gases in groundwater, normalised to equilibrium concentrations, adapted from Wieser [2011]. (b) Excess air patterns of noble gases predicted by the different models, from Aeschbach-Hertig et al. [2008].

as the inclusion of air bubbles during groundwater table fluctuations [Holocher et al., 2002; Klump et al., 2007, 2008]. These air bubbles are dissolved partially or in their entirety, when the hydrostatic pressure in the groundwater increases. However, the resulting increase in noble gas concentrations is not purely of atmospheric isotopic compositions. To account for this observation, several modeling approaches were proposed, which are partially illustrated in Fig. A.7 and further described in the following subsections.

As water table fluctuations are connected to recharge and precipitation, the amount of excess air can be used as an indicator on precipitation patterns [Aeschbach-Hertig et al., 2002]. To that end, the relative excess air component of neon,

$$\Delta\mathrm{Ne}\,[\%] = \frac{C_{\mathrm{Ne}}^{\mathrm{exc}}}{C_{\mathrm{Ne}}^{\mathrm{eq}}} \cdot 100\,\% \tag{2.13}$$

can be used as climate proxy [Zhu and Kipfer, 2010], as the neon concentrations in water are dominated only by equilibrium and excess air [Lehmann et al., 1993].

The following description of some of the different approaches to model the observed excess air content in groundwater samples is largely based on Aeschbach-Hertig and Solomon [2013], where a more detailed description and complete overview can be found. The actual application of these models on the dataset is done using *PANGA* [Jung and Aeschbach, submitted], a specialized software described in further detail in section 5.1.2.

The UA Model

The first approach to account for excess air in groundwater was proposed by Heaton and Vogel [1981] with the *unfractionated air (UA) model*, which assumes total dissolution of the enclosed air bubbles:

$$C_{\mathrm{i}}^{\mathrm{UA}} = C_{\mathrm{i}}^{\mathrm{eq}} \cdot (1 + A \cdot H_{\mathrm{i}}) \tag{2.14}$$

where A is the volume ratio of trapped air to water. However, this approach can not account for many existing data sets showing an enrichment of the heavier noble gases [Aeschbach-Hertig et al., 2002].

The PR Model

The *partial re-equilibration (PR) model* introduced by Stute et al. [1995b,a], like the PR model assumes total dissolution, but accounts for the possibility of diffusive loss following the dissolution – effectively resulting in an enrichment of the heavier noble gases due to their lower diffusivity:

$$C_{\mathrm{i}}^{\mathrm{PR}} = C_{\mathrm{i}}^{\mathrm{eq}} \cdot \left[1 + A \cdot H_{\mathrm{i}} \cdot e^{-F_{\mathrm{PR}} \left(\frac{D_{\mathrm{i}}}{D_{\mathrm{Ne}}}\right)^{\beta}}\right] \tag{2.15}$$

where D_{i} are the diffusion coefficients of the noble gases in water and F_{PR} is a parameter for the loss of excess air due to re-equilibration. The parameter β was initially not included, it originates from the theory of gas transfer and can range from 0.5 to 1 [Aeschbach-Hertig et al., 2008]. A variation of this model is the *multi-step partial re-equilibration (MR) model* [Kipfer et al., 2002], allowing for more than one degassing step.

The PD Model

In principle similar to the PR model, the *partial degassing (PD) model* allows for the degassing of both the equilibrium as well as the excess air component of the dissolved noble gases:

$$C_{\mathrm{i}}^{\mathrm{PD}} = C_{\mathrm{i}}^{\mathrm{eq}} \cdot [1 + A \cdot H_{\mathrm{i}}] \cdot e^{-F_{\mathrm{PR}} \left(\frac{D_{\mathrm{i}}}{D_{\mathrm{Ne}}}\right)^{\beta}} . \tag{2.16}$$

The CE Model

A different model was introduced with the *closed system equilibration (CE) model* by Aeschbach-Hertig et al. [2000, 2008], which approaches the problem not by the concept of diffusive loss, but by solubility. The idea is that the enclosed air bubbles are not dissolved entirely, leading to a fractionation governed

by the respective solubilities:

$$C_{\mathrm{i}}^{\mathrm{CE}} = C_{\mathrm{i}}^{\mathrm{eq}} \cdot \left[\frac{1 + A \cdot H_{\mathrm{i}}}{1 + B \cdot H_{\mathrm{i}}}\right] = C_{\mathrm{i}}^{\mathrm{eq}} \cdot \left[1 + \frac{(1 - F_{\mathrm{CE}}) \cdot A \cdot H_{\mathrm{i}}}{1 + F_{\mathrm{CE}} \cdot A \cdot H_{\mathrm{i}}}\right] \tag{2.17}$$

The parameter A describes in this case only the initial ratio of trapped air to water, not the one that is actually dissolved, which is given by $A - B$ in this case, with B denoting the remaining entrapped gas volume. The occurring fractionation factor is $F_{\mathrm{CE}} = A/B$ and the model can describe both excess air ($F_{\mathrm{CE}} < 1$) as well as degassing ($F_{\mathrm{CE}} > 1$).

The OD Model

One mechanism possibly affecting noble gas concentrations in groundwater is ignored by the previous models: when the balance of O_2 and CO_2 in the soil air is changed by microbial activity, the resulting partial pressure differences can alter the composition of the soil air, at times significantly deviating from the atmospheric composition [Freundt et al., 2013; Mayer, 2017]. The *oxygen depletion (OD) model* introduced by Hall et al. [2005] accounts for that, modifying the equilibrium component by a constant factor P_{OD}:

$$C_{\mathrm{i}}^{\mathrm{OD}} = C_{\mathrm{i}}^{\mathrm{eq}} \cdot (P_{\mathrm{OD}} + A \cdot H_{\mathrm{i}}) \tag{2.18}$$

which describes the increase of noble gas partial pressures due to the change in O_2 partial pressures, which is limited to $1 < P_{\mathrm{OD}} < 1.26$ by the maximum amount of oxygen depletion (21 %).

2.3 The Stable Noble Gases

Noble gases have been an established tracer tool in hydrology for many years [Aeschbach-Hertig and Solomon, 2013]. Their low abundance (see Table C.3) and their chemical inertness, as well as a good understanding of sinks and sources make them a powerful tool in geosciences and environmental sciences. While there are also many applications for the radioactive isotopes of noble gases, mainly as dating tools for various age ranges [Lu et al., 2014; Suckow et al., 2013], this section focuses on the stable isotopes employed in this study, their origins, reservoirs and uses. The isotopic system of ^{3}He and ^{4}He, expressed by the ^{3}He/^{4}He ratio R, is of particular interest for this study's aims, as is explained in the following sections.

The stable noble gases consist of helium, neon, argon, krypton and xenon, in order of their mass. The most abundant of them, by far, is argon, constituting 0.934 % of the atmospheric air, while all others occur only in trace amounts (compare table C.3) [Porcelli et al., 2002]. The noble gas concentrations found in groundwater draw mainly from the atmospheric reservoir (see section 2.2). This component constitutes

a noble gas baseline in groundwater. Kipfer et al. [2002] describes groundwater as a binary mixture of two distinct noble gas components, the atmospheric one, and a residual radiogenic and/or terrigenic one. Deviations in concentration or fractionation from the atmospheric baseline can offer valuable information and insights, as they are either caused by modulations of the atmospheric component (e. g. by water table fluctuations (see section 2.2.1) or temperature changes), or changes in the radiogenic or terrigenic input. The latter are limited to few processes, as the subsurface production of neon, krypton and xenon is small enough to be negligible relative to the atmospheric component [Lehmann et al., 1993; Yatsevich and Honda, 1997]. Only ^{3}He, ^{4}He, ^{40}Ar and, very rarely, ^{21}Ne have production rates that make them distinguishable from the atmospheric baseline in groundwaters [Kipfer et al., 2002].

This makes the noble gas composition of groundwater a tool for identifying climatic conditions, quantifying residence times and renewal rates as well as pinpointing geological points of origin of non atmospheric mixing components.

Concentrations of dissolved noble gases in groundwater are expressed in units cm^{3}STP/g: gas volume at standard conditions ($T_0 = 273.15\,K$, $p_0 = 101.325\,kPa$) per gram of water. Using the ideal gas law, $1\,cm^3STP$ equals 4.46×10^{-5} mol, or 2.6868×10^{19} atoms.

2.3.1 Helium

Helium, the second most abundant element in the universe, is only a trace gas in earth's atmosphere, with a volume mixing ratio of $(5.24 \pm 0.05) \times 10^{-6}$ in dry atmospheric air [Porcelli et al., 2002]. The atmospheric helium concentration is mostly determined by helium outgassing through the lithosphere and thermal diffusive loss of helium to space [Morrison and Pine, 1955; Kockarts, 1973]. The main source of ^{4}He in the atmosphere is the flux through the continental crust. Mid ocean ridge volcanism and fluxes through the oceanic crust also contribute significantly to the atmosphere's ^{4}He concentration. The dominant terrestrial ^{3}He sources are subduction zones and mid ocean ridge volcanic activity [Torgersen, 1989], while non-terrestrial input of ^{3}He into the atmosphere (e. g. solar wind, cosmogenic production) play a lesser role [Lupton, 1983]. The resulting ^{3}He/^{4}He ratio of the atmosphere used in this study is $R_a = (1.384 \pm 0.006) \times 10^{-6}$, based on data from Clarke et al. [1976]. The ^{3}He/^{4}He ratios determined in this study are usually given relative to this atmospheric ratio, as it is assumed to be constant over geological timescales [Torgersen, 1989].

The production of ^{4}He in the earth's crust and mantle stems from radiogenic and nucleogenic reactions. The α decays of the U/Th decay chains generate the bulk of the ^{4}He [Graham, 2002], the yearly production rate in the crust (4.15×10^{-13} cm^{3}STP/g) far outweighs the production in the mantle (4.15×10^{-15} cm^{3}STP/g)[1] [Yatsevich and Honda, 1997]. The crustal environment also has a small source

[1] Note that these values in cm^{3}STP/g are given for grams of rock material, not water, as everywhere else in this study.

of ^{3}He in form of a second order decay process of lithium, starting with a neutron capture and subsequent decay: $^6\mathrm{Li}\,(\mathrm{n},\alpha)\,^3\mathrm{H}\,(\beta^-)\,^3\mathrm{He}$. The required neutrons originate from spontaneous fission processes, mostly of ^{238}U [Morrison and Pine, 1955]. Since the abundance of lithium in most occurring rock types is very low [James and Palmer, 2000], this production of ^{3}He in crustal environments can usually be neglected[2]. The resulting ^{3}He/^{4}He ratio in typical continental crust is $0.02\,\mathrm{R_a}$ [Mamyrin and Tolstikhin, 1984; Hooker et al., 1985].

In the mantle, ^{3}He is occurring in much larger abundances relative to ^{4}He, the origin of this ^{3}He is entirely primordial – helium that was incorporated into the earth during its planetary formation [Graham, 2002], while the mantle's ^{4}He is largely radiogenic [Mamyrin and Tolstikhin, 1984]. This primordial ^{3}He is most apparent in mid ocean ridge basalts (MORB) and in ocean island basalts (OIB): volcanic hotspots like Iceland and Hawaii, likely located above mantle plumes[3]. Anderson [1993] alternatively suggests the origin of the high ^{3}He/^{4}He ratios might be not or not entirely primordial, but extraterrestrial – introduced by interplanetary dust particles and moved towards the mantle by subduction of deep sea sediments. The global mean of ^{3}He/^{4}He ratios found in MORB is given by Graham [2002] as $(8.75 \pm 2.14)\,\mathrm{R_a}$, ranging from 1 to $18\,\mathrm{R_a}$. OIB on the other hand are much more variable in ^{3}He/^{4}He ratios, going up to 35 to $43\,\mathrm{R_a}$ in Iceland and $35\,\mathrm{R_a}$ in Hawaii. While these high ^{3}He/^{4}He ratios are found mostly in volcanic glasses, Hilton et al. [2002] compiles data for geothermal fluids in arc-related volcanism and calculates a global mean of $(5.4 \pm 1.9)\,\mathrm{R_a}$, with a maximum of $8.9\,\mathrm{R_a}$. An exact value for the Upper Rhine Graben continental rift zone is hard to pinpoint, the typical ^{3}He/^{4}He signal of MORB of $8\,\mathrm{R_a}$ is assumed in this study, as an upper limit. Clauser et al. [2002] use $8.6\,\mathrm{R_a}$ for the region, while Griesshaber et al. [1992] also use $8\,\mathrm{R_a}$.

The ^{3}He/^{4}He Ratio as a Tracer System

Since the three different reservoirs of helium in the environment (atmosphere, crust and mantle) differ significantly in their ^{3}He/^{4}He ratio, identifying their respective components in groundwater mixtures is relatively straightforward, given that means for an accurate ^{3}He measurement are available. However, as this is a three component mixing with the additional influence of tritiogenic ^{3}He (see section 2.4), separating the source signals requires using an additional parameter. To this end, the concentration of ^{20}Ne is used in this study. As neon underlies no significant sources or sinks in the observed systems (compare section 2.3.2), it allows for separating atmospheric ^{3}He/^{4}He ratios from crustal, mantle and tritiogenic influenced ones. Therefore a three-isotope plot of ^{3}He/^{4}He over the ^{20}Ne/^{4}He ratio, as shown schematically in Fig. 2.4, is used [Pyle, 1993].

[2] Additionally, release of the resulting radiogenic ^{3}He from the lithium rich minerals requires somewhat high temperatures above 400°C [Mamyrin and Tolstikhin, 1984]

[3] Though Castro et al. [2009] suggest that the occurrence of primordial noble gas signatures is not a compulsory argument for the presence of a mantle plume.

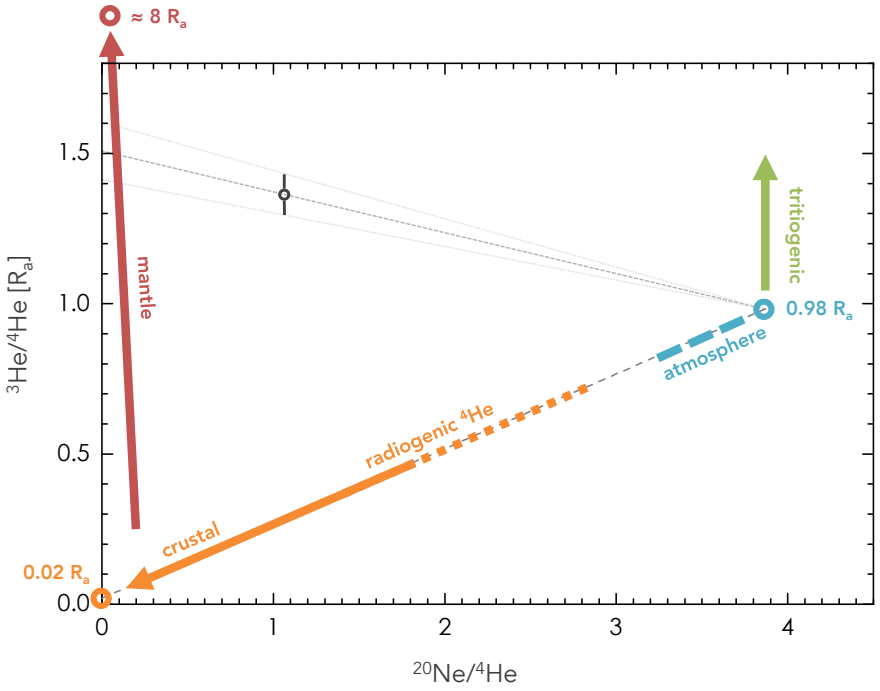

Figure 2.4: Separation of the different $^3He/^4He$ reservoirs by using the three-isotope-plot introduced by Pyle [1993], plotting $^3He/^4He$ over $^{20}Ne/^4He$. The original radiogenic $^3He/^4He$ of a sample can be graphically reconstructed as indicated, or calculated by separating the ^3He components as shown in section 2.4.1. Both methods are however susceptible to tritiogenic ^3He, shifting the ratios upwards.

In meteoric groundwater, the helium concentration is initially set by equilibration with the atmosphere during recharge. The atmospheric helium ratio in water R_{eq} is slightly different from the atmospheric ratio $R_a \approx R_{eq}/0.983$, due to isotope fractionation during equilibration [Benson and Krause, 1980]. The initial $^{20}Ne/^4He$ ratio from air equilibration is 3.871, the origin of neon is and remains usually purely atmospheric, therefore acting as a reference system for the ^4He concentration. Recently formed groundwater is found at the atmospheric endmember on the right hand side of the plot (Fig. 2.4). With increasing residence time in the aquifer, and dependent on the aquifer's rock composition, the helium composition of the groundwater is changing, the amount of ^4He increasing with time as α decays in the aquifer matrix produce ^4He. Since the crustal production of ^3He is negligible, the $^3He/^4He$ ratio is dropping with age, and the sample is moving along the indicated atmospheric-crustal mixing line towards the left. Groundwater with an entirely crustal signature is found to have a $^{20}Ne/^4He$ ratio of nearly zero and a $^3He/^4He$ ratio of $0.02\,R_a$ which marks the crustal endmember [Mamyrin and Tolstikhin, 1984; Hooker et al., 1985]. The $^3He/^4He$ ratio of the mantle endmember is difficult to pinpoint exactly and dependent on regional geology – this study assumes an upper limit of $8\,R_a$ for the Upper Rhine

Graben. The $^{20}Ne/^{4}He$ ratio of mantle fluids is similar to crustal ones extremely small. Samples with an intermixing of mantle influenced fluids can be found on a mixing line between the crustal and the mantle endmember. The additional influence of tritiogenic ^{3}He can easily be identified in this type of plot, as it shifts samples vertically along the y-axis and only affects young samples with relatively low ^{4}He amounts significantly, since the amount of tritiogenically produced ^{3}He is limited by the initially available ^{3}H activity. Graphically differentiating samples with high $^{3}He/^{4}He$ ratios in tritiogenic and mantle influence is therefore relatively simple, using the three-isotope plot.

For a numerical estimation of the mantle fraction of the helium composition, one separates the sample's $^{3}He/^{4}He$ ratio R_s into its components

$$R_s = \frac{^{3}He_s}{^{4}He_s} = \frac{^{3}He_m + {}^{3}He_{cr} + {}^{3}He_{atm}}{^{4}He_m + {}^{4}He_{cr} + {}^{4}He_{atm}} \tag{2.19}$$

where (atm) is the atmospheric component, the sum of the equilibration (eq) and the excess air (ea) component, and (m) and (cr) denote the mantle and crustal ratio, respectively.

Note that this separation ignores the tritiogenic (tri) component of ^{3}He, as this calculation is usually only applied to old waters from large depths, where a three component mixing is most likely and $^{3}He_{tri}$ can be neglected. For many groundwaters even the atmospheric component can be dismissed, Aeschbach-Hertig [2005] gives a formula for a two-component mixing system.

Based on the component separation, Mamyrin and Tolstikhin [1984] give an equation for groundwaters with gas contents composed from all three helium reservoirs. They do, however, ignore excess air components, using only the equilibration component $^{4}He_{eq}$ which they estimate by assuming $^{4}He_{eq}/^{20}Ne_s = 0.285$ at 10℃. Especially in shallow groundwaters, this assumption will not hold up, as degassing as well as excess air can significantly influence the noble gas composition. Therefore, as shown and applied by Kaudse [2014] and already indicated in equation 2.19, the atmospheric component formed from the sum of the equilibration (eq) and the excess air (ea) component is being used. $^{4}He_{atm}$ is acquired from the data evaluation using the CE model. Using each reservoir's helium ratio R_m, R_{cr} and R_{atm}, one can rewrite equation 2.19 to

$$\begin{aligned} R_s &= \frac{^{4}He_m R_m + {}^{4}He_{cr} R_{cr} + {}^{4}He_{atm} R_{atm}}{^{4}He_s} \\ &= {}^{4}X_m R_m + {}^{4}X_{cr} R_{cr} + {}^{4}X_{atm} R_{atm} \end{aligned} \tag{2.20}$$

with the relative components $^{4}X_i = {}^{4}He_i/{}^{4}He_s$, meaning that the sum of all $^{4}X_i$ equals 1 and by expressing the crustal fraction through $^{4}X_{cr} = 1 - {}^{4}X_m - {}^{4}X_{atm}$ one can eliminate it from the equation

and solve for the mantle fraction:

$$ {}^4X_\mathrm{m} = \frac{\mathrm{R_s} - \mathrm{R_{cr}} - {}^4X_\mathrm{atm}(\mathrm{R_{atm}} - \mathrm{R_{cr}})}{\mathrm{R_m} - \mathrm{R_{cr}}} \tag{2.21} $$

The ^{3}He mantle contribution ${}^3X_\mathrm{m}$ is, as Aeschbach-Hertig [2005] notes, given by

$$ {}^3X_\mathrm{m} = {}^4X_\mathrm{m} \cdot \frac{\mathrm{R_m}}{\mathrm{R_s}} \tag{2.22} $$

This approach is used successfully by Kaudse [2014] on data from thermal springs in the Jordan Rift Valley, however, the samples in question mostly had ^{3}H activities below the detection limit, meaning that the tritiogenic influence on the helium ratio could be neglected. This is not the case for many of the groundwater samples analysed in this study, whose composition essentially constitutes from a four component mixing system regarding ^{3}He, while ^{4}He remains unaffected. Therefore, no fraction ${}^4X_\mathrm{tri}$ exists, impeding the simple expansion of equation 2.24 by a tritiogenic component, by which its contribution could be reasonably accounted for. A correction of the calculated mantle contribution for tritiogenic influence is therefore not possible without using assumptions about the very value that is supposed to be calculated, as a correction in the form of

$$ \mathrm{R_s^{corr}} = \mathrm{R_s} - \mathrm{R_{tri}} = \frac{{}^3\mathrm{He_s} - {}^3\mathrm{He_{tri}}}{{}^4\mathrm{He_s}} \tag{2.23} $$

leading to

$$ {}^4X_\mathrm{m} = \frac{\mathrm{R_s^{corr}} - \mathrm{R_{cr}} - {}^4X_\mathrm{atm}(\mathrm{R_{atm}} - \mathrm{R_{cr}})}{\mathrm{R_m} - \mathrm{R_{cr}}} \tag{2.24} $$

would require the amount of tritiogenic $^3\mathrm{He_{tri}}$, which, given the available information from noble gas and tritium measurements, can only be estimated by making an assumption about the radiogenic endmember ratio (see section 2.4.1), the parameter that is supposed to be calculated.

The geographical plots of helium data in this study show only the absolute ^{3}He concentrations in cm^{3}STP/g, interpolated using a minimum curvature algorithm, as discerning mantle and atmospheric ratios is impractical in such a plot. Given the small mixing fractions of mantle helium to be expected in surface groundwater, and therefore the overlap of atmospheric, crustal and mantle ^{3}He/^{4}He ratios, no information can be transported plotting the ^{3}He/^{4}He without the additional information provided by the ^{20}Ne. The absolute ^{3}He amount, while possibly affected by tritiogenic ^{3}He, allows for a reasonable representation of mantle helium since even small admixtures of mantle helium cause the absolute amounts of ^{3}He in the groundwater to increase by orders of magnitude. In cases where high tritiogenic contributions are present, this is identified by the three-isotope-plot.

Transport of Helium Through Mantle and Crust

The transport of gases towards the atmosphere is governed by two distinct processes: diffusion and advection. Diffusion is driven by concentration gradients and is in general the slower of the two processes. On the other hand, advection requires pathways of certain sizes to be available within the rock matrix, allowing for fluid transfer driven mostly by pressure gradients. Within the ascending fluid flow, gas phase advective transport is another way for noble gases to ascend towards the atmosphere [Etiope and Martinelli, 2002]. The main idea behind this study – detecting a mantle helium signature in shallow, unconfined, easily accessible aquifers atop of the geothermal target aquifers at great depth – relies on the assumption that networks of highly permeable faults and fractures within the target aquifer allow for an increased transport of mantle tracers.

The coincidence of high $^3He/^4He$ ratios and increased heat flow in rift zones has been shown [Mamyrin and Tolstikhin, 1984; Clauser et al., 2002], the value of $^3He/^4He$ is additionally related to the age of the tectonic process: it decreases as the continental crust is aging. Furthermore, as helium is transported via diffusion and advection while heat is conducted[4], the helium signal associated with a heat anomaly can precede its occurrence at shallow depths [Ballentine and Burnard, 2002; Clauser et al., 2002]. As Griesshaber et al. [1992] showed for the Upper Rhine Graben, the $^3He/^4He$ signal is not necessarily corelated with heat flow.

Mamyrin and Tolstikhin [1984] argue that the transport of primordial ^3He can not be attributed solely to diffusive flow. The input of mantle volatiles into the crust requires the intrusion of molten mantle material into the crust [Ballentine and Burnard, 2002], which is supported by the correlation of strontium isotopic ratios of $^{87}Sr/^{86}Sr$ within silicate mantle material [Faure and Powell, 1972].

Kurz and Jenkins [1981] give experimental diffusion coefficients for helium in basaltic glass at temperatures ranging from 150 to 270°C in the order of 10^{-12} to $10^{-10}\,cm^2/s$. Even in less dense materials, direct diffusive transport of gaseous helium is simply too slow to account for mantle helium related to heat anomalies reaching shallow aquifers, even though helium is highly diffusive. For the diffusion through crustal sediments Stute et al. [1992] calculates, based on a diffusivity coefficient for helium in the upper crust of $2 \times 10^{-5}\,cm^2/s$, a transport distance of 2 km in 2×10^7 yr, while [Torgersen and Clarke, 1985] estimate $10^{-5}\,cm^2/s$ to be unreasonably high and suggest even coefficients in the range of 10^{-6} to $10^{-5}\,cm^2/s$ to be high. This supports that diffusive flux can not be an effective way of helium transport to the surface [Ballentine and Burnard, 2002]. None the less, the impact of diffusive processes in noble gas transport can be observed. The thermal dependence of diffusion coefficients can, for example, be seen in high $^4He/^{40}Ar$ ratios in certain geologic settings, where $^4He/^{40}Ar$ can serve as a tracer for depth and temperature of the point of origin of gases [Mamyrin and Tolstikhin, 1984; Elliot et al., 1993; Ballentine and Burnard, 2002].

[4] An extensive discussion of geothermal heat transfer processes can be found in Saar [2011].

Within the crustal regime, helium is migrating mainly by advection within transport media: dissolved in fluids and as a trace gas in carrier gases (e. g. CO_2 or CH_4) [Etiope and Martinelli, 2002; Aeschbach-Hertig, 1994]. The accumulation of sufficient amounts of helium to form an advective gas phase by itself is not possible, as production rates are too low [Ballentine and Burnard, 2002]. As Etiope and Martinelli [2002] details, high velocity gas migration can also be explained by a set of transport mechanisms covered by the so called *geogas theory*. Transport velocities of the resulting flow are highly dependent on the available pathway apertures, which in turn are specific to the geologic setting: ranging from 10 to 100 µm in clayey rocks and 400 to 500 µm in granite towards the occurrence of 10^{-2} to 10 mm and larger fissures[5] in geothermal systems and fractured crystalline bedrock, according to the overview compiled by Etiope and Martinelli [2002]. They estimate advective gas transport velocities to range from 1 to 10^3 m/d, and in highly permeable fractured rocks up to 10^4 m/d. While the occurrence of aquifers in the ascension path of the gas can even lead to higher transport velocities due to increased buoyancy [Etiope and Martinelli, 2002], the ascending helium can also be dissolved and trapped in deep circulating groundwaters [Kipfer et al., 2002].

Radiogenic Helium as a Dating Tracer

The production of ^{4}He within an aquifer rock matrix is a function of its uranium and thorium composition. As ^{4}He is not well retained in most mineral structures, the accumulation of radiogenic ^{4}He is a measure of groundwater travel times [Solomon, 2000]. In principle this method is suitable for dating over longer timescales $> 30\,000$ yr. The helium release rate, based on the aquifer mineral composition must be reasonably well known, and the influence of external sources must be negligible. Even though an aquifer is not a closed system for helium – which is the reason why helium is the main tracer of interest in this study – quantitative dating using ^{4}He has been done, e. g. by Stute et al. [1992]; Marty et al. [1993]; Andrews and Lee [1979]; Bottomley et al. [1984].

2.3.2 Neon

Neon has three stable isotopes in nature: ^{20}Ne, ^{21}Ne and ^{22}Ne, of which the most rare, ^{21}Ne, is not accounted for in this study. The atmospheric ^{20}Ne/^{22}Ne ratio is 9.80 ± 0.08 [Porcelli et al., 2002], while the primordial mantle ratio is reported to surpass 12.5 [Sarda et al., 1988; Graham, 2002].

Nucleogenic production of neon was first recognised by Wetherill [1954], related to the U/Th decay chain, as the production is induced by the reaction of α particles with O, F, Mg and Na. The production rates per year of neon in the mantle have been calculated by Yatsevich and Honda [1997] to be in the order of 1.74×10^{-23} cm^{3}STP/g for ^{22}Ne and 3.98×10^{-24} cm^{3}STP/g for ^{21}Ne, production in the crust is slightly

[5] A visual example of such fractures, and the precipitative growth sealing these over time, can be found in form of a core sample from the triassic Buntsandstein sandstone from Soultz-sous-Forêts, shown and described in Griffiths et al. [2016].

higher with 1.86×10^{-21} cm^{3}STP/g and 5.23×10^{-21} cm^{3}STP/g for ^{22}Ne and ^{21}Ne, respectively. These rates are negligible compared to the ^{4}He production rates, also given by Yatsevich and Honda [1997], which are orders of magnitudes higher. The production of neon's main isotope ^{20}Ne from the reaction $^{17}\mathrm{O}\,(\alpha, \mathrm{n})\,^{20}\mathrm{Ne}$ is also extremely low [Leya and Wieler, 1999].

In the typical aquifer environment, neon can therefore be assumed to be sourced only from the atmosphere during recharge and used accordingly as an atmospheric reference.

2.3.3 Argon

Argon is the most abundant noble gas in the atmosphere, with a volume mixing ratio of $(9.34 \pm 0.01) \times 10^{-3}$ [Porcelli et al., 2002]. Relevant for this study are the stable isotopes ^{36}Ar and ^{40}Ar, the third stable isotope ^{38}Ar is not being used. As a dating tracer, ^{39}Ar with its half-life of 269 yr is increasingly useful in groundwater analysis [Ritterbusch et al., 2014; Lu et al., 2014]. The atmospheric ratio of $^{40}\mathrm{Ar}/^{36}\mathrm{Ar}$ was determined to be 295.5 ± 0.5 [Nier, 1950; Steiger and Jäger, 1977], a value that is consistently being used in the analysis and data evaluation process of this study. However, a redetermination of the atmospheric ratio was done by Lee et al. [2006], resulting in a slightly higher ratio of 298.56 ± 0.31.

A relevant radiogenic source in the crust for ^{40}Ar is the electron capture decay of potassium. The reaction is $^{40}\mathrm{K}\,(\mathrm{e}^-, \beta^+)\,^{40}\mathrm{Ar}$, with a half-life of 1.25×10^9 years. In contrast to neon, this source of ^{40}Ar relative to ^{4}He is not negligible, Ballentine and Burnard [2002] calculates $^4\mathrm{He}/^{40}\mathrm{Ar}$ production ratios for the lower, middle and upper crust to be 3.09, 5.79 and 6.0 respectively. Due to the large atmospheric argon background, ^{40}Ar production is only noticeable in waters with very long residence times in the range of millions of years [Lippmann et al., 2003]. Production of ^{36}Ar in the crust by β decay of ^{36}Cl can be neglected, compared to the atmospheric equilibrium component in groundwater [Ballentine and Burnard, 2002].

2.3.4 Krypton and Xenon

The heavy stable noble gases krypton and xenon can be assumed to be, for all regular groundwater applications, free of sinks and sources. Production rates of fission of ^{238}U [Ballentine and Burnard, 2002] are so low that they are only a relevant source on timescales of several millions of years [Lippmann et al., 2003]. In the context of this study, the respective most abundant stable isotopes of krypton and xenon are analysed, ^{84}Kr and ^{132}Xe (compare table C.3).

2.4 Tritium

Tritium, ^{3}H, is a radioactive isotope of hydrogen with a half-life of (4500 ± 8) d [Lucas and Unterweger, 2000], or 12.32 yr, enabling it to be a dating tracer in the range of 0 to 50 yr. The β^- decay of tritium produces ^{3}He:

$$^3\mathrm{H} \longrightarrow {}^3\mathrm{He} + \mathrm{e}^- + \bar{\nu}_e \tag{2.25}$$

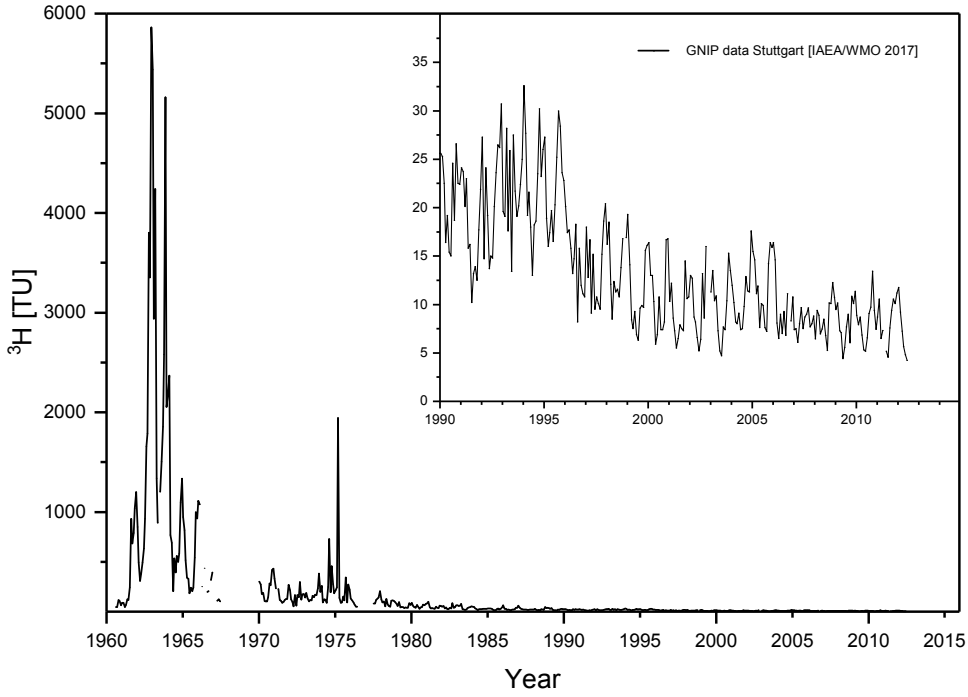

Figure 2.5: Tritium input curve at Stuttgart, plotted from GNIP data, illustrating the *bomb peak* and the decay of tritium activity in precipitation since then. Present day ^{3}H input varies seasonally around 10 TU [IAEA/WMO, 2017].

Tritium has both natural and anthropogenic sources. The natural production mainly stems from spallation of nitrogen (and to a lesser extent, oxygen) nuclei in the upper atmosphere, by impacting cosmogenic neutrons [Libby, 1946]:

$$^{14}\mathrm{N} + \mathrm{n} \longrightarrow {}^{12}\mathrm{C} + {}^3\mathrm{H} + -4.3\,\mathrm{MeV} \tag{2.26}$$

$$^{14}\mathrm{N} + \mathrm{n} \longrightarrow 3\,{}^4\mathrm{He} + {}^3\mathrm{H} + -11.5\,\mathrm{MeV} \tag{2.27}$$

from where the ^{3}H enters the global water cycle by oxidation to ^{1}H^{3}HO. Subsurface generation of tritium

is also occurring in the following ways:

$$^{2}\mathrm{H} + \mathrm{n} \longrightarrow {}^{3}\mathrm{H} + -6.26\,\mathrm{MeV} \tag{2.28}$$

$$^{3}\mathrm{He} + \mathrm{n} \longrightarrow {}^{3}\mathrm{H} + {}^{1}\mathrm{H} + -0.76\,\mathrm{MeV} \tag{2.29}$$

$$^{6}\mathrm{Li} + \mathrm{n} \longrightarrow {}^{3}\mathrm{H} + {}^{4}\mathrm{He} + -4.78\,\mathrm{MeV} \tag{2.30}$$

$$^{10}\mathrm{Be} + \mathrm{n} \longrightarrow {}^{3}\mathrm{H} + {}^{8}\mathrm{Be} + -0.23\,\mathrm{MeV} \longrightarrow {}^{3}\mathrm{H} + 2\,{}^{4}\mathrm{He} + -0.33\,\mathrm{MeV} \tag{2.31}$$

The origin of the neutrons driving these reactions can be either cosmogenic or radiogenic – depending on depth and rock density [Lal, 1987]. Most important in the context of tritium (and ^{3}He) in groundwater is the production from ^{6}Li (equation 2.30) though, in lithium-rich crustal environments [Aeschbach-Hertig, 1994].

Anthropogenic overprinting of the naturally occurring ^{3}H signal – estimated by Roether [1968] to be 5 TU[6] – took place with the onset of atmospheric nuclear weapons testing, peaking in the mid 1960s. These tests tainted natural ^{3}H as a tracer, increasing the tritium concentration in precipitation by a factor of up to 1000, which has been declining since then, as atmospheric testing has stopped [Mook and DeVries, 2000]. However, the anthropogenic 'bomb peak' itself can be utilized as an age tracer. As most of the anthropogenic ^{3}H has been introduced directly into the stratosphere, the tropospheric input curve shows an distinct seasonality due to atmospheric transport processes [Gat et al., 2001], making dating by comparison with the varying input curve difficult (see Fig. 2.5 for an input curve from the study region). Additionally to the global effect of the nuclear weapons testing, other anthropogenic ^{3}H sources of lesser and mostly regional effect exist: Industrial tritium production for consumer products containing tritium as an illuminant can be a local source [Santschi et al., 1987]. Tritium is also being produced for and used in medical applications. The second largest anthropogenic source is most likely the military and civil nuclear industry though, releasing tritium into the environment from nuclear power plants and reprocessing facilities, both in gaseous as well as liquid form, as tritiated water [IAEA, 2004]. This can have a strong effect on local aquifer tritium budget. River infiltration into the aquifers downstream from nuclear power plants, discarding tritiated water, both legally and by accident [König et al., 1976; Le Guen, 2009], can significantly alter the groundwater's ^{3}H concentration.

2.4.1 ^{3}H-^{3}He-Dating

Dating groundwater by measuring only ^{3}H requires a well known local input curve, and usually allows for identifying the bomb peak in vertical groundwater profiles [Robertson and Cherry, 1989]. The resolution does not allow for dating young groundwater however, as the input curve has flattened in magnitude since the end of atmospheric nuclear bomb tests, as visible in Fig. 2.5. Seasonal variation in the ^{3}H

[6] A commonly used unit in tritium analysis: 1 TU equals one ^{3}H atom per 10^{18} hydrogen atoms, or an activity of 0.118 Bq/l.

concentration in precipitation combined with the seasonality of groundwater recharge itself make the task even more complex. Acquiring an infiltration date of a water sample by relating it to a local, unambiguous ^{3}H input curve can therefore be quite difficult and unreliable [Sültenfuß and Massmann, 2004]. It can however provide a minimum age for the sampled water, and allow for a qualitative separation of very young and very old groundwater.

A more constrained dating tool can be obtained by including the daughter isotope of ^{3}H decay in the analysis, ^{3}He, which was proposed by Tolstikhin and Kamenskij [1969]. The relationship between mother and daughter nuclides of the β^- decay leads to an expression for the ^{3}H-^{3}He-age of the water, which is independent from any input functions and therefore removes all the ambiguities stemming from it[7]:

$$\tau = \frac{1}{\lambda} \cdot \ln\left(1 + \frac{^3\mathrm{He}_{\mathrm{tri}}}{^3\mathrm{H}}\right) \quad , \quad \lambda = 1.78 \times 10^{-9}\,\mathrm{s}^{-1} \tag{2.32}$$

However, this is not a groundwater infiltration age, but the time passed since the aquifer became confined, as contact with the atmosphere leads to loss of ^{3}He. As ^{3}H is incorporated in the water molecules and ^{3}He is dissolved, chemically inert, the information generally remains in place in piston-flow aquifers. Diffusion can cause slight dispersion of the information along the aquifer, as both the gradients of ^{3}H and ^{3}He, as well as their diffusion coefficients, differ [Cook and Solomon, 1997]. This affects the ^{3}He concentrations in unconfined aquifers most. There, diffusion of ^{3}He close to the groundwater table can lead to a loss of helium to the atmosphere, and thereby to an underestimation of age. Schlosser et al. [1988] estimated the order of magnitude of this type of ^{3}He-loss in an unconfined aquifer to about 10 to 20 %. However, the magnitude of this loss is correlated to the ^{3}He gradient between the air and water – while a large ^{3}H spike (like the bomb peak) will suffer most from ^{3}He loss, the effect should be smaller for young groundwater with low initial ^{3}H concentrations [Cook and Solomon, 1997]. Additionally, the confinement of ^{3}He to the groundwater is dependent on the downward directed vertical advection velocity of the groundwater and helium's diffusivity ($5.74 \times 10^{-5}\,\mathrm{cm}^2/\mathrm{s}$ at 10°C in water [Jähne et al., 1987]). Using the characteristic diffusion length $l = \sqrt{2Dt}$, diffusion can account for up to 3 cm per day, which can be, depending on the hydraulic conductivity of the soil material, small compared to vertical infiltration rates.

As pointed out in section 2.3.1, helium has several sources in the aquifer environment, other than ^{3}H, complicating matters. To allow for reliable dating, these other sources must be reasonably well quantified or estimated. A separation of the sample's He components

$$^3\mathrm{He}_{\mathrm{sample}} = {}^3\mathrm{He}_{\mathrm{tri}} + {}^3\mathrm{He}_{\mathrm{eq}} + {}^3\mathrm{He}_{\mathrm{exc}} + {}^3\mathrm{He}_{\mathrm{rad}} \tag{2.33}$$

must be possible. Easily quantifiable is the equilibrium component $^3\mathrm{He}_{\mathrm{eq}}$, which can directly be calculated according to Henry's law (equation 2.6) from the salinity, temperature and pressure at the given recharge

[7] The amounts of $^3\mathrm{He}_{\mathrm{tri}}$ and ^{3}H must be given in the same units for this calculation, it is therefore necessary to convert $^3\mathrm{He}_{\mathrm{tri}}$ from cm^{3}STP/g to TU: $1\,\mathrm{TU} = 2.488 \times 10^{-15}\,\mathrm{cm}^3\mathrm{STP/g}$

area, if available, or from the modeled equilibration component of ^{4}He acquired from fitting the data using *PANGA* (see section 5.1.5) and the equilibration ratio $R_{eq} = 1.36 \times 10^{-6}$:

$$^3He_{eq} = {}^4He_{eq} \cdot R_{eq} \tag{2.34}$$

The excess air component $^3He_{exc}$ (see section 2.2.1) can be quantified by the neon concentration measured in the water sample, as neon in most aquifers originates only from the atmosphere: $Ne_{sample} = Ne_{eq} + Ne_{exc}$ where Ne_{eq} can be calculated using the same reasoning as for $^3He_{eq}$. The excess air component of ^{3}He can then be expressed as

$$^3He_{exc} = (Ne_{sample} - Ne_{eq}) \cdot L_{exc} \cdot R_{exc} = Ne_{exc} \cdot L_{exc} \cdot R_{exc} \tag{2.35}$$

where $R_{exc} \approx R_a = 1.384 \times 10^{-6}$ and $L_{exc} = (He/Ne)_{exc} = 0.288$ [Ozima and Podosek, 1983]. However, as Peeters et al. [2003] showed, this general ratio might be inaccurate in certain cases and should be replaced by an approach taking into account an excess air model fit:

$$L_{exc} = \frac{He_{mod} - He_{eq}}{Ne_{mod} - Ne_{eq}} \tag{2.36}$$

where He_{mod} and Ne_{mod} are the modeled elemental concentrations, acquired from fitting the data with *PANGA*. The radiogenic component $^3He_{rad}$ can be determined from the radiogenic component $^4He_{rad}$ of ^{4}He:

$$^3He_{rad} = {}^4He_{rad} \cdot R_{rad} = \left({}^4He_{sample} - {}^4He_{eq} - Ne_{exc} \cdot L_{exc}\right) \cdot R_{rad} \tag{2.37}$$

However, knowledge of the local radiogenic ^{3}He/^{4}He ratio is required, a problem that is shared with the primordial component. While the amount of terrigenic $^3He_{ter}$ can usually be neglected in most surface aquifers, the aquifers sampled for this study were specifically chosen for their probability to show influence of mantle derived ^{3}He/^{4}He signals, and are thereby possibly enriched in terrigenic ^{3}He, complicating dating for certain samples. A value of $R_{rad} = 2 \times 10^{-8}$ [Aeschbach-Hertig, 1994] is assumed in this study as a baseline, for certain samples different ratios are used, as is explained in chapter 6 in such cases. While this correction is negligible for samples with mainly meteoric composition, for crustal or mantle influenced samples showing high He/Ne ratios, it becomes significant and influences the dating massively.

As tritium with its half-life of 12.32 yr is an indicator of young groundwater, deep geothermal fluids should contain none from the atmosphere's reservoir. An intermixing of recent groundwater in the uppermost aquifer with upwelling fluid might thus lead to a dilution of ^{3}H concentrations. Whether this can be resolved – given that many samples were measured using an analysis method with relatively large uncertainties – is questionable. In principle, an estimate of mixing factors is feasible by comparing the sum of $^3He_{tri}$ and ^{3}H with the locally expected ^{3}H concentration in precipitation at the dated time

[Sültenfuß and Massmann, 2004].

2.5 Radon

Radon is the heaviest naturally occurring noble gas, with no stable isotopes. The longest lived, ^{222}Rn ($t_{1/2} = 3.8235\,\mathrm{d}$) is the only one with a sufficiently long lifetime to be of use in hydrological studies. All occurring radon isotopes are part of the uranium and thorium decay chains, thus the radon concentrations in groundwater are largely dependent on the aquifer matrix. The relevant ^{222}Rn is part of the ^{238}U decay chain, with ^{226}Ra as its immediate predecessor, which decays by α decay. The resulting radon enters the groundwater by radioactive recoil. ^{222}Rn can also be used in limnology [Kluge et al., 2007] and in the unsaturated soil zone [Mayer, 2017].

With continuous natural input, low mobility and short half-life, the source of origin of ^{222}Rn is spatially limited in aquifers – slow diffusive transport in combination with the short half life and high background concentrations mask ^{222}Rn signals quickly [Etiope and Martinelli, 2002]. However, when relatively fast advective transport processes occur, e. g. fluid upwelling in fault zones, the rise in ^{222}Rn concentrations should be noticeable [Voltattorni and Lombardi, 2010; Barragán Reyes et al., 2008]. This has been used in the past in fault detection and mapping in volcanic and hydrothermal environments [Mismanos and Vasquez, 2015; Lombardi and Voltattorni, 2010; Walia et al., 2010] as well as in earthquake monitoring [King, 1978; Fleischer and Mogro-Campero, 1985].

2.6 Stable Isotopes: ^{18}O and ^{2}H

The water molecule H_2O is mainly constituted by ^{1}H and ^{16}O isotopes of hydrogen and oxygen, respectively. Of both elements, heavier stable isotopes exist though, the most frequently occurring types of water molecules are $^{1}H^{1}H^{16}O$, $^{1}H^{1}H^{18}O$ and $^{1}H^{2}H^{16}O$ [Roedel and Wagner, 2011]. Their occurrence offers a hydrological tracer system: by the ratio of their abundance compared to the main isotopes, information about the origin, type and temperature of precipitation can be gained, as the physical processes acting on the water within the hydrological cycle lead to fractionation effects and a characteristic range of composition in ^{18}O and ^{2}H.

Since isotope ratios R are usually very small, the δ-notation is defined, relative to a standard [Mook and DeVries, 2000]:

$$\delta = \left(\frac{\mathrm{R_{sample}}}{\mathrm{R_{standard}}} - 1 \right) \cdot 1000\,‰ \tag{2.38}$$

In case of the stable isotopes of water, that standard is *Vienna standard mean ocean water* (VSMOW),

with the isotope ratios as given by Hagemann et al. [1970] and Baertschi [1976]:

$$\left(\frac{^2\mathrm{H}}{^1\mathrm{H}}\right)_{\mathrm{VSMOW}} = (155.75 \pm 0.05) \times 10^{-6} \tag{2.39}$$

$$\left(\frac{^{18}\mathrm{O}}{^{16}\mathrm{O}}\right)_{\mathrm{VSMOW}} = (2005.20 \pm 0.45) \times 10^{-6} \tag{2.40}$$

2.6.1 The Different Fractionation Principles

A closed system constituted from a water and a gas phase, where neither water nor water vapor is removed, will reach an equilibrium between both phases. However, the incorporation of heavier isotopes in the water molecules leads to a slightly lower vapor pressure of the heavier water molecules, and therefore an isotopic depletion ($\delta^2\mathrm{H} < 0\,‰$, $\delta^{18}\mathrm{O} < 0\,‰$) of the water vapor compared to the water phase. This effect is called the *equilibrium fractionation*. In an open system, the vapor phase is continuously removed, thereby reducing the vapor pressure of the gaseous phase below saturation pressure. This leads to a diffusive transport of water molecules to the gas phase, however, the slightly different diffusion coefficients of the different molecules cause *kinetic fractionation*. Evaporation over the oceans is a good example of both processes occurring at once, the resulting water vapor is isotopically lighter than the initial water mass. Due to the reservoir size, the ocean water's isotopic composition can be assumed as unchanged and constant over time. When water vapor condenses again, forming precipitation (*Rayleigh condensation*, removing the condensate immediately from the system), reservoir sizes are of similar order, leading to a change in isotopic composition in both phases. The water phase is enriched in heavier molecules due to their lower vapor pressure, while the vapor phase is getting isotopically lighter. With decreasing temperatures, the precipitation is therefore increasingly lighter in isotopic composition. All three processes are described in great detail in Roedel and Wagner [2011]

2.6.2 Fractionation Effects in Hydrology

Various effects can be observed in the isotopic composition of water in the hydrosphere (see Dansgaard [1964] and Coplen et al. [2000]), which mainly have changes in altitude and temperature as a driving force:

Continental Effect Water vapor moving inland from the ocean loses water to precipitation induced by moving according to the surface relief, causing the resulting precipitation to become lighter in isotopic composition with increasing distance from the ocean.

Latitude Effect The isotopic composition of air masses moving towards higher latitudes is becoming more depleted as rain-out along the way removes the heavier isotopes. The effect is not linear, in mid-latitudes it amounts to approximately $-0.5\,‰$ per degree of latitude.

Altitude Effect With increasing altitude (e. g. on windward mountainsides), the amount of heavy isotopes decreases, when the water vapor gains altitude and cools as a consequence of adiabatic expansion. Additionally, evaporation during movement of the formed rain drops can deplete the reservoir even further. Typical gradients for δ^{18}O are -0.15 to $-0.5\,‰$ per 100 m [Yurtsever and Gat, 1981].

Amount Effect Heavy rainfall events have lighter signature in isotopic composition than light rain, as the time for evaporation during drop movement through the atmosphere is shorter.

Seasonal Effects Seasonal variations in the flow and trajectory of water masses and the overall atmospheric water balance can cause changes in the isotopic composition. Usually, winter precipitation is more depleted than summer precipitation.

Temperature Effect While the effects described above all affect the isotopic signature in principle, the isotopic composition of the average precipitation of a region is dominated by temperature [Dansgaard, 1964; Roedel and Wagner, 2011]. The isotopic composition is correlated with temperature, formulating an absolute relationship is not possible though. For local data, regression lines can be calculated. For data from Heidelberg, the following relationship is given by Jacob and Sonntag [1991]:

$$\delta^{18}\mathrm{O} = -10.8 + 0.27 \cdot T\ [^{\circ}\mathrm{C}] \tag{2.41}$$

Geological Effects While the atmospheric effects on the isotopic composition are expected to be the dominant ones in the sampled surface aquifers of this study, potential upwelling water from deep hydrothermal sources could introduce a geologic signature, called *oxygen shift*. At temperatures above 150°C, water-rock interaction leads to an enrichment of ^{18}O in hydrothermal waters, which usually shows no corresponding increase in δ^{2}H [Kato, 2000]. The effect is most pronounced with young hydrothermal systems, and becomes increasingly weaker with age, as the oxygen of the interacting rocks reaches equilibrium with the fluid [Nicholson, 1993].

2.6.3 Meteoric Water Lines

Since ^{18}O and ^{2}H are affected similarly by the processes noted above – with the exeption of the geothermal alteration – a global mean relationship between δ^{2}H and δ^{18}O can be expressed, as first done by Craig [1961] and later refined by Rózański et al. [1993], based on GNIP data:

$$\delta^{2}\mathrm{H} = 8.13 \cdot \delta^{18}\mathrm{O} + 10.8\,‰ \tag{2.42}$$

The constant offset of $10.8\,‰$ in δ^{2}H is called the *deuterium excess*. It is determined by the share of kinetic fractionation in the evaporation process and thereby an indicator for the humidity of the precipitation's region of origin – the higher the humidity, the lower the deuterium excess (as illustrated in Fig. 2.6).

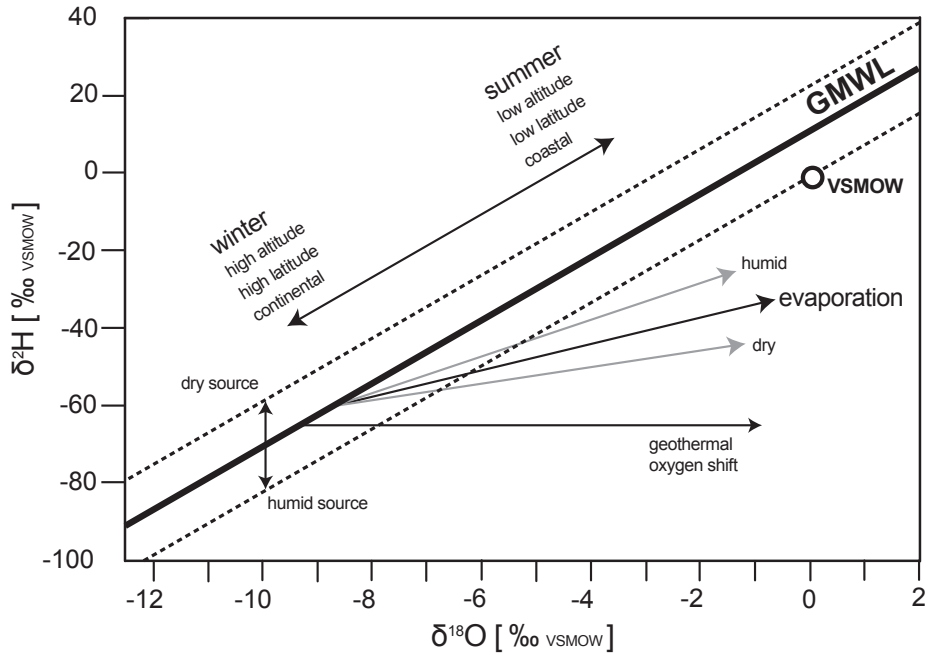

Figure 2.6: The global meteoric water line and the different effects acting on the isotopic composition, adapted from [Wieser, 2011].

Obviously, this infers that the GMWL is not necessarily valid on local scales. Interpreting regional stable isotope data therefore requires a local meteoric water line (LMWL), which can be calculated from direct precipitation measurements, if available. For the Odenwald, Friedrich [2007] calculated a LMWL from GNIP stable isotope data of precipitation from Karlsruhe, Stuttgart and Würzburg:

$$\delta^2\mathrm{H} = 7.91 \cdot \delta^{18}\mathrm{O} + 5.58\,‰ \tag{2.43}$$

However, given that the samples in this study originate from wells in the Upper Rhine Graben, I chose to omit the Würzburg data and replace it with data from Weil am Rhein, which is closer to the Freiburg sampling region. For the Groß-Gerau region, no data exists that is geographically closer, therefore the resulting LMWL

$$\delta^2\mathrm{H} = 7.82 \cdot \delta^{18}\mathrm{O} + 4.87\,‰ \tag{2.44}$$

from GNIP data [IAEA/WMO, 2017] from Karlsruhe (1977 to 2013), Stuttgart (1961 to 2013) and Weil am Rhein (1983 to 2013) is used for all samples in this study (see Fig. B.11). The precipitation weighted mean isotopic signal of the combined precipitation datasets, calculated as in Friedrich [2007], is $\overline{\delta^{18}\mathrm{O}} = -8.14\,‰$ and $\overline{\delta^2\mathrm{H}} = -58.61\,‰$.

2.7 Radiocarbon

Carbon, one of the most abundant elements found on earth, has three naturally occurring isotopes, two of which, ^{12}C and ^{13}C are stable. The third, ^{14}C (or radiocarbon), is radioactive via β^- decay

$$^{14}\mathrm{C} \longrightarrow {}^{14}\mathrm{N} + \mathrm{e}^- + \bar{\nu}_\mathrm{e} \tag{2.45}$$

with a half-life of $t_{1/2} = (5730 \pm 40)$ [Godwin, 1962]. The cosmogenic production of ^{14}C in the atmosphere

$$^{14}\mathrm{N} + \mathrm{n} \longrightarrow {}^{14}\mathrm{C} + \mathrm{p} \tag{2.46}$$

was discovered by Libby [1946] and developed into a dating tool [Libby, 1952], an application for which he received the Nobel prize in 1960. The ^{14}C produced in the upper atmosphere is oxidized and enters the atmospheric circulation and thereby the hydrological cycle as dissolved inorganic CO_2 (DIC). With a known initial activity A_0 of ^{14}C, a closed system where the amount of ^{14}C is only governed by radioactive decay, a sample's age t can be calculated from the measured activity $A(t)$:

$$t = -\lambda \cdot \ln\left(\frac{A(t)}{A_0}\right) = -\frac{t_{1/2}}{\ln 2} \cdot \ln\left(\frac{A(t)}{A_0}\right) \tag{2.47}$$

For the conventional ^{14}C age BP (before present, 1950), the wrong Libby half-life of 5567 yr is used in archaeology and geology, to ensure intercomparability with older data. In groundwater hydrology however, the true half-life is used [Mook and DeVries, 2000]. By convention, ^{14}C activities are expressed in *percent modern carbon* (pmC), where 100 pmC reflect the activity in the year 1950, or 13.56 decays per minute and gram carbon [Mook, 1980]. Over short periods of time (in the order of decades to few centuries), the atmospheric concentration of ^{14}C can be assumed to be constant, as cosmogenic production and radioactive decay build towards a secular equilibrium. In the long run, the ^{14}C activity has been found to fluctuate significantly though, complicating the dating: Since the ^{14}C production and therefore the initial activity A_0 is driven by cosmogenic neutron flux, the long term activity is modulated by changes in effective solar flux due to the variability of the sun's activity [Crowe, 1958; Stuiver and Quay, 1980; Hoyt et al., 1992] as well as that of the earth's shielding magnetic field [Damon et al., 1989]. These variations can be found in various natural archives, like tree rings [Becker and Kromer, 1993], foraminifera [Hughen et al., 2006] and corals [Fairbanks et al., 2005]. Based on such datasets of atmospheric ^{14}C activity over the past few ten thousands of years, a calibration curve for ^{14}C dating is compiled, the most recent is *IntCal13*, compiled and described by Reimer et al. [2013]. The real calendar age, in contrast to the simplified conventional ^{14}C age, is calculated using this curve and software tools like *OxCal* [Bronk Ramsey, 2009].

Additional to the natural variability, anthropogenic sources for ^{14}C exist: as with ^{3}H, nuclear bomb tests increased the amount of ^{14}C in the atmosphere [Münnich and Vogel, 1958], by a factor of two in ^{14}C/C

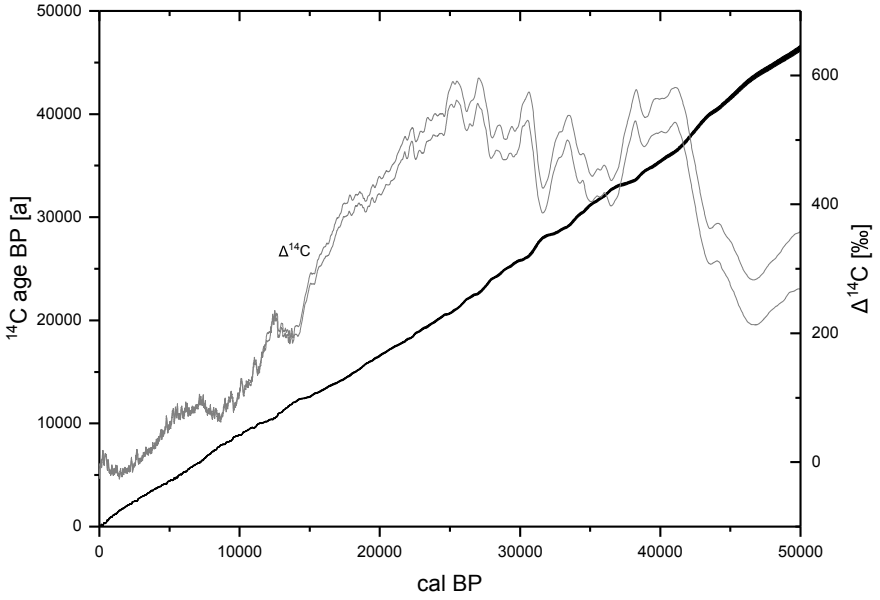

Figure 2.7: The IntCal13 calibration curve for ^{14}C, plotted from data provided by Reimer et al. [2013].

ratio in 1962/63 compared to 1950 [Levin et al., 2010]. Today, the dominant anthropogenic signal in ^{14}C is the *Suess effect* though, which describes the dilution of ^{14}C concentrations by the combustion of ^{14}C-dead (void of ^{14}C) fossil fuels [Suess, 1955].

While radiocarbon dating in solid samples (e. g. in archeological contexts) is usually possible up to a range of 50 000 years [Kromer, 2007], dating groundwater is somewhat limited by the complexity of the aquifer environment: since carbon is ubiquitous in the aquifer matrix, and ^{14}C-dead, dissolution of carbon into the water changes the isotopic composition of the DIC and thereby creates older apparent ^{14}C ages. This limits groundwater dating with ^{14}C to an effective range of about 30 000 years [Clark and Fritz, 1997] and requires modeling approaches to account for the dilution.

CO_2 enters the aquifers as dissolved inorganic carbon (DIC) by equilibration with the soil air, whose composition is initially atmospheric, but can be modulated strongly by biological activity [Freundt et al., 2013; Mayer, 2017], reaching up to several vol%. Plant respiration also affects the isotopic composition of carbon in the soil air, which is elaborated on in the following subsection.

During groundwater recharge, contact with the soil air leads to dissolution of CO_2 from the gaseous phase

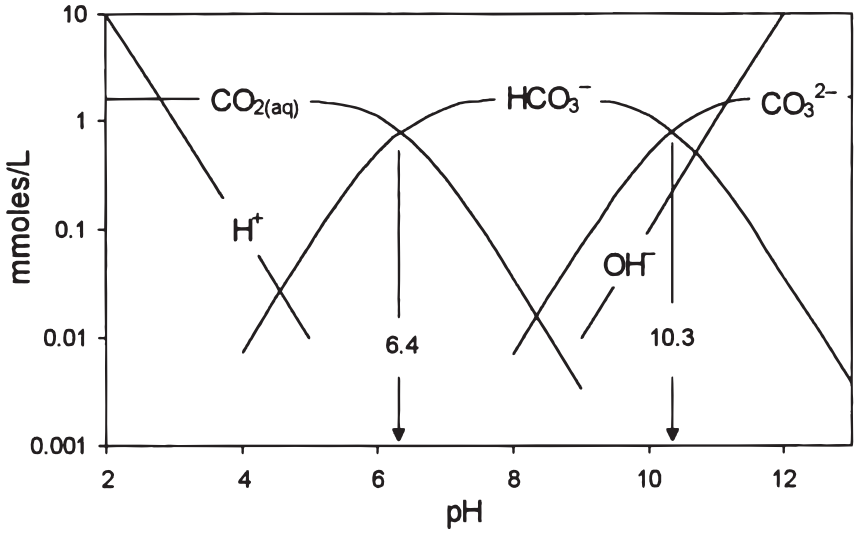

Figure 2.8: The different species of carbon as dissolved in groundwater, depending on pH. Calculated for a DIC content of 1.6 mmol L^{-1} at 25°C by [Clark and Fritz, 1997].

into water and is generally described by the following equilibrium reaction [Yamaguchi et al., 1977]:

$$\begin{aligned} CO_2(g) + H_2O &\rightleftharpoons H_2CO_3 \\ &\rightleftharpoons HCO_3^- + H^+ \\ &\rightleftharpoons CO_3^{2-} + 2\,H^+ \end{aligned} \tag{2.48}$$

In which dissolved state most of the carbon can be found is dependent on the water pH value, as shown in Fig. 2.8. As previously noted, ^{14}C-dead carbon can be dissolved from the aquifer matrix, especially from sedimented calcite ($CaCO_3$) layers. The lower the pH (and thus the more CO_2 is dissolved), the higher is dilution of the ^{14}C by the dissolution of the $CaCO_3$. Incorporation of non-atmospheric carbon is called the *reservoir effect*.

Several different model approaches to quantify this reservoir effect exist, a detailed overview can be found in Wieser [2011] while this study only approaches the topic and the dating broadly. The various models range from a statistical approach [Vogel, 1967, 1970] using a constant factor describing the contribution of aquifer calcite, to more complex modeling of each sample water's respective composition, by using the $\delta^{13}C$ [Pearson Jr., 1965], its geochemistry [Clark and Fritz, 1997] or both [Fontes and Garnier, 1979].

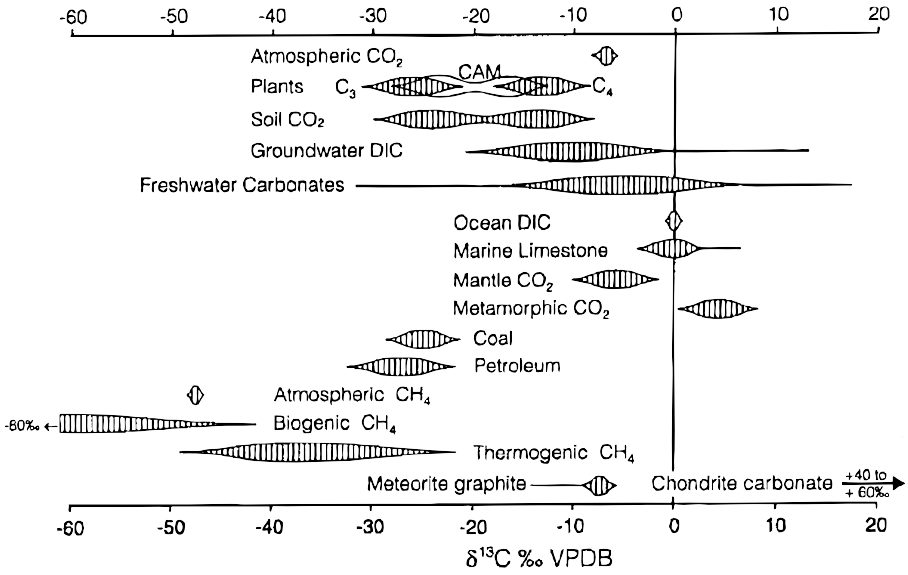

Figure 2.9: Variation of δ^{13}C in natural reservoirs [Clark and Fritz, 1997].

δ^{13}C Isotopic Information

The isotopic ^{13}C composition of carbon in the soil air, and in groundwater, is affected by various factors, as shown in Fig. 2.9 from Clark and Fritz [1997]. The ^{13}C to ^{12}C ratio is standardized to the *Vienna Peedee Belemnite* (VPDB, $^{13}C/^{12}C = 0.011\,237\,2$) [Craig, 1957; IAEA, 1993]. The ^{13}C data is expressed, similar to the stable isotopes, with the δ-notation (see section 2.6).

Atmospheric air is depleted in δ^{13}C at around $-7\,‰$. The soil air is then further depleted: Depending on the type of photosynthesis employed by the local vegetation, isotope fractionation occurs in different magnitudes as CO_2-fixiation usually favors the incorporation of the lighter $^{13}CO_2$ into the plant material. So called C3 plants[8], predominantly found in moderate and tropical climates, are characterised by a depletion of -22 to $-40\,‰$. C4 plants on the other hand, specialized on arid climates, lead to a smaller depletion of about -9 to $-19\,‰$ [Peisker, 1984]. Carbonates usually have δ^{13}C close to $0\,‰$ [Geyh, 2000], dissolution of $CaCO_3$ therefore enriches the groundwater in δ^{13}C. So can geogenic CO_2 originating from the mantle, with a δ^{13}C of $-6\,‰$ [Geyh, 2000], while Clark and Fritz [1997] even indicated positive δ-values for this case.

[8]Given the climate of central Europe and the Upper Rhine Graben, the dominance of C3 plants can be assumed. On short time scales, relative to the ^{14}C-clock, present day local agriculture might alter that, as for example much of the agricultural area in the Freiburg region was used for growing corn – a C4 plant. None of the few samples analysed for ^{14}C and δ^{13}C should be affected by that, however.

Chapter 3

The Geologic and Regional Setting

This chapter will give a short overview of the geologic setting of the studied region, the Upper Rhine Graben. It is based on the extensive and detailed description of the geology and hydrogeology given by Al Najem [2016], to which I refer to for deeper insight. A geologic map of the entire region is shown in Fig. 3.1, where the extent of this study's sampling regions is marked by red areas. Aside from a closer look at each sampling region, the chapter also includes a summary of the published helium data for the entire region.

3.1 The Upper Rhine Graben

This study is focused on the german part of the Upper Rhine Graben, which is part of the Cenozoic Rift system of Western and Central Europe, spanning across Europe from the North Sea to the Mediterranean Sea. Its extension along its NNE–SSW axis is about 300 km, spanning from the *Swiss Jura* at Basel towards the *Hunsrück* and *Taunus* of the *Rhenish Massif* at Frankfurt am Main. Its width ranges between 35 to 40 km.

The formational history of the structure is quite complex, Schumacher [2002] gives a detailed account of the changing basin geometry over time. Extension of the graben started about 50×10^6 yr ago, during the Eocene, beginning with a subsidence in the south, while the northern graben began to form in the early Miocene. During the Oligocene, several seawater floodings of the forming depression occurred, leading to marine sedimentation. From the middle of the Miocene on, sedimentation has been continental, mostly by fluvial deposition. Volcanism associated to the graben tectonics can be found in form of the *Kaiserstuhl* close to Freiburg and bordering the graben in the north-west, the *Eifel* in the Rhenish Massif [Griesshaber et al., 1992]. The uplifted and eroded graben shoulders expose the crystalline bedrock and

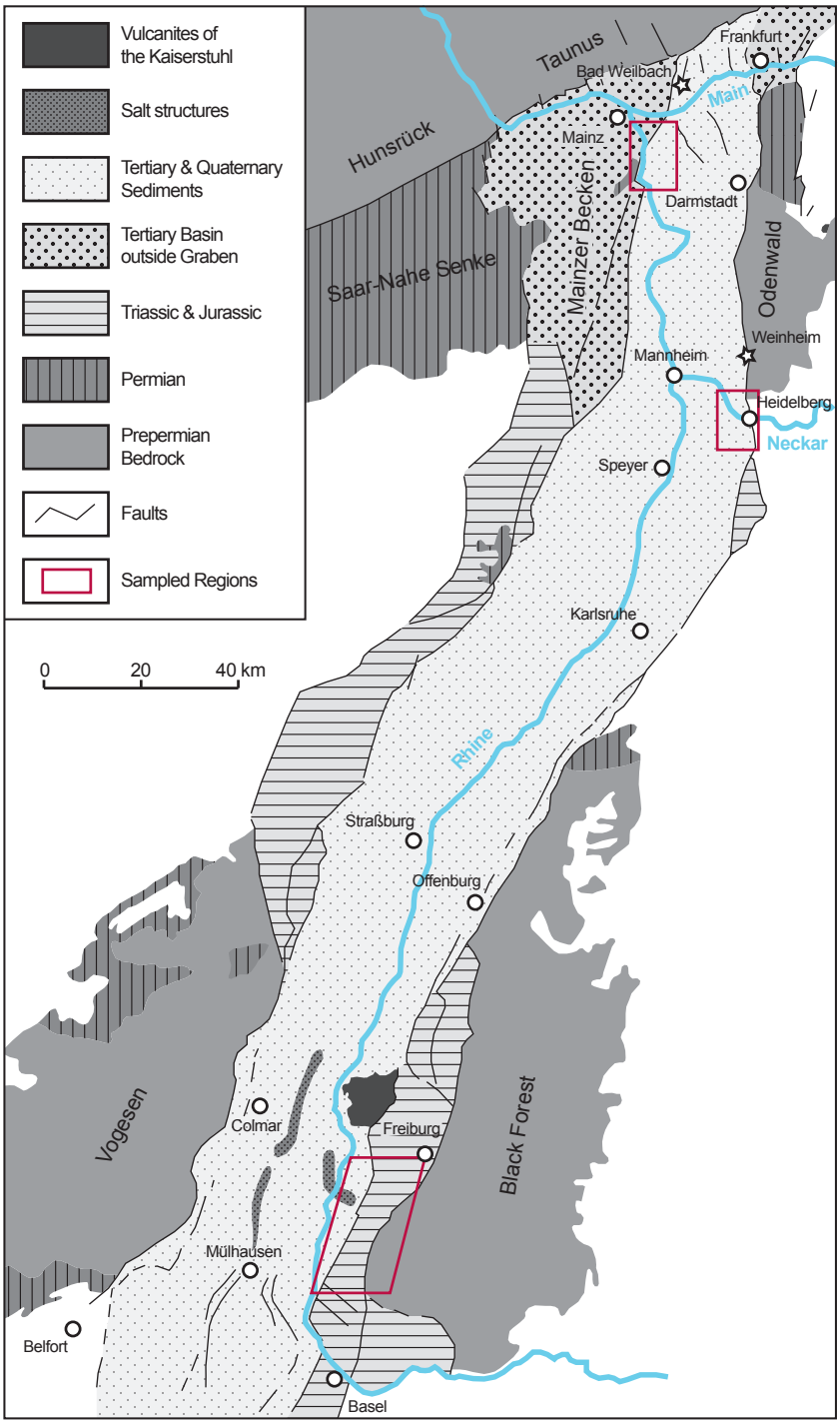

Figure 3.1: The geology of the Upper Rhine Graben, adapted and simplified from Walter [2007]. Regions sampled in this study are marked in red, stars note additionally sampled springs/wells.

mesozoic sediments, in form of the *Vosges* in the southwest, and northwards by the *Palatinate Forest, Haardt* and *Mainzer Becken*, while the eastern shoulders are formed by the *Black Forest* in the south, and the *Kraichgau*, *Odenwald* and the *Sprendlinger Horst* to the north. The eastern and western main fault show a lateral displacement of several kilometers, while the subsidence of the graben displaced the graben shoulders relative to the graben centre by an elevation of up to 3.5 km, a difference that was almost completely compensated by erosion of the shoulders and cenozoic sediments in the graben.

The general flow direction of shallow groundwater is from the graben shoulders towards the Rhine river, turning northwards with the elevation dip: The Rhine enters the graben in the south at Basel at 245 m asl and leaves it at Mainz, in the north, at 85 m asl. All three sampling regions are located east of the Rhine, all including one of the graben's main faults, while still mainly located on the sediment filled graben depression. Recharge of the upper aquifers sampled for the study mainly stems from direct precipitation and runoff/infiltration from the immediate eastern graben shoulders. The deep aquifers recharge from the graben shoulders, during the infiltration the waters undergo heavy water-rock interactions at high temperatures [Pauwels et al., 1993; Aquilina et al., 1997]. Some of the thermal waters also show signs of intermixing with fossil seawater [He et al., 1999].

The crustal extension of the graben structure decreases the thickness of the lithosphere, bringing the asthenospheric mantle closer to the surface. The geothermal gradient in the Upper Rhine Graben can therefore reach up to 10°C per 100 m [Pauwels et al., 1993; Pribnow and Schellschmidt, 2000], which makes the location highly suitable for geothermal energy production and thereby an area of interest [Agemar et al., 2013; Stober and Jodocy, 2009] for developing new methods in geothermal exploration. An exemplary heat profile of the subsurface can be found in Fig. A.6, plotted from measured data from the 5 km deep GPK-2 borehole at Soultz-sous-Forêt [Vidal et al., 2015].

3.2 Groß-Gerau Region

The geology of the area west of Groß-Gerau is shown in Fig. 3.2. East of the Rhine, sediments from the Holocene and Pleistocene form the upper graben filling. The western main fault strikes SSW to NNE, crossing the Rhine close to Nierstein, separating the Upper Rhine Graben on the east from the *Mainzer Becken* and the risen *Niersteiner Horst*, which is an upthrow block of the fault, outcropping the Permian *Rotliegend*, partially covered under thin holocene covers. The occurrence of the volcanic *Kisselwörth* maar diatreme [Lutz et al., 2013] indicates an early hydraulic activity in the Eocene of the northern part of the fault, long before subsidence started in the north.

Based on borehole analysis by Schmitt [1992] at the *Hof Schönau* pumping station, south of Rüsselsheim, several aquifers in the Quaternary and Tertiary graben filling are identified. The unconfined upper aquifer has a depth of around 100 m, followed by an aquitard and the second aquifer, which reaches to about 126 m

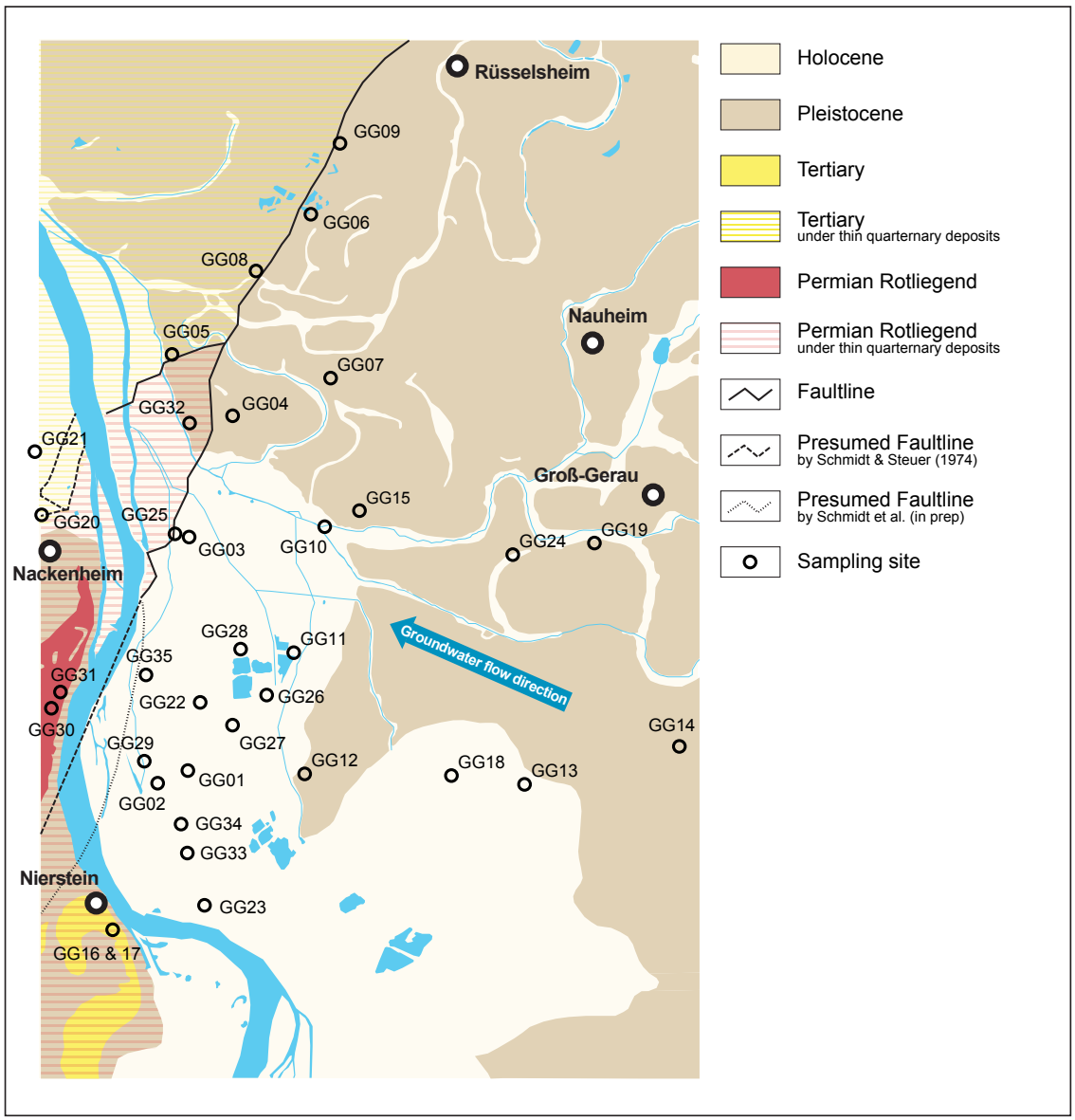

Figure 3.2: Geology of the region west of Groß-Gerau and the position of all sampled wells and springs. Based on maps by Steuer [1908] and Schmitt and Steuer [1974b,a].

depth into the Tertiary. A third aquifer follows at 133 m. A fourth, salinated aquifer is found by Schmitt [1992] at 190 m, the origin of the salinisation is usually seen in the dissolution of salts from Miocene sediments [Schmitt, 1992; Holting, 1969]. However, Al Najem [2016] concluded that the origin of the saline water is not from Miocene sediments, but from a fossil seawater component. Since the hydraulic head of the lower aquifer is above that of the unconfined [Schmitt, 1992], an upwelling of the deep, salinated water is possible given permeable passageways through the aquitards. Additionally, Schmitt and Steuer [1974a] argue that the crystalline bedrock of the Niersteiner Horst is limiting groundwater flow, increasing water pressure at the main fault. The result is an upwelling of salinated water, the rise in salinity of the unconfined aquifer is documented in an airborne electrical conductivity study executed by Siemon et al. [2001], shown in Fig. A.2. The data clearly shows two hotspots, one right on top of the main fault line, and one farther to the north-west. The fault line hotspot has a small, secondary minimum in resistivity, north of *Hessenaue*, where several quarry ponds are located.

The area is also characterised by a local heat anomaly, as shown in Fig. A.8 [HLNUG, 2017], which makes it a target region for geothermal energy production. The regional energy company *Überlandwerke Groß-Gerau* started a power plant project in 2007 [ÜWG, 2007], leading to an (unpublished) 3D reflection seismic survey and to the drilling of a first well[1] in 2016. Sufficient amounts of fluid were however not found and the project was canceled in 2016 [ÜWG, 2016].

3.3 Heidelberg Region

The region around Heidelberg forms the *Heidelberger Loch*, a part of the graben showing high subsidence rates, leading to a thick quaternary sediment filling of up to 350 m at Heidelberg [Haimberger et al., 2005; Hagedorn, 2004]. It is located on the eastern main fault of the Rhine Graben, where the *Neckar* river crosses the fault line, dividing the Odenwald in the north from the Kraichgau in the south. The shallow aquifers in the quaternary sediment filling are categorised into several sections, as shown in Fig. A.3: the upper, unconfined aquifer, which is partially separated by an aquitard into two subsections, and the confined middle and lower aquifers [Bender, 2003; LUBW, 1999]. The region was target of a 2D-seismic survey [Stadt Heidelberg, 2009] for geothermal exploration, however no further actions appear to have been undertaken at the time of this study's publication.

[1]The wellhead is located between GG15 and GG24, where the directional drilling headed in the subsurface was not published.

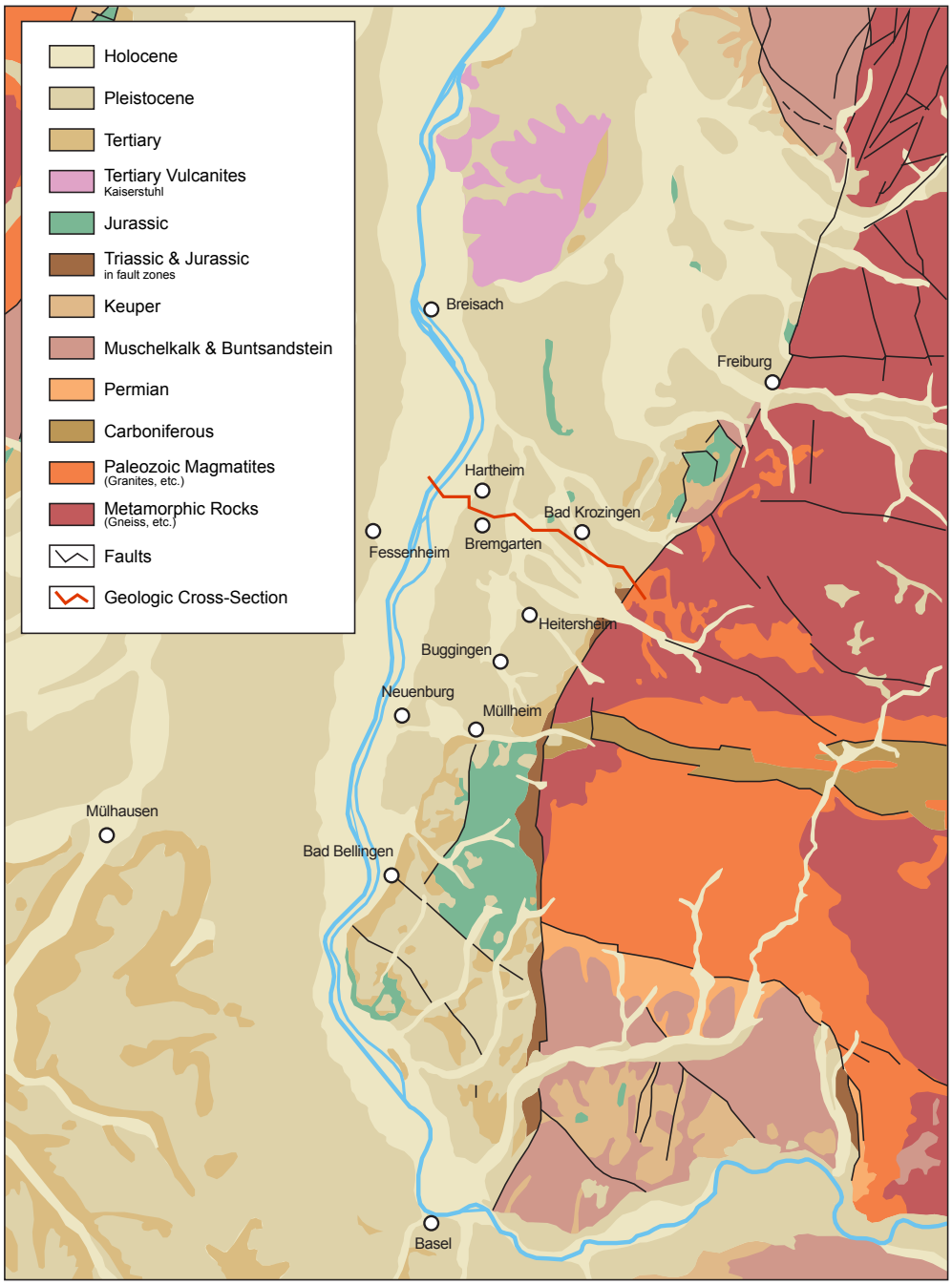

Figure 3.3: The geology of the extended Freiburg region, adapted from Huttner and Schreiner [1989] and simplified, the cross-section indicated in the map is displayed in Fig. 3.4.

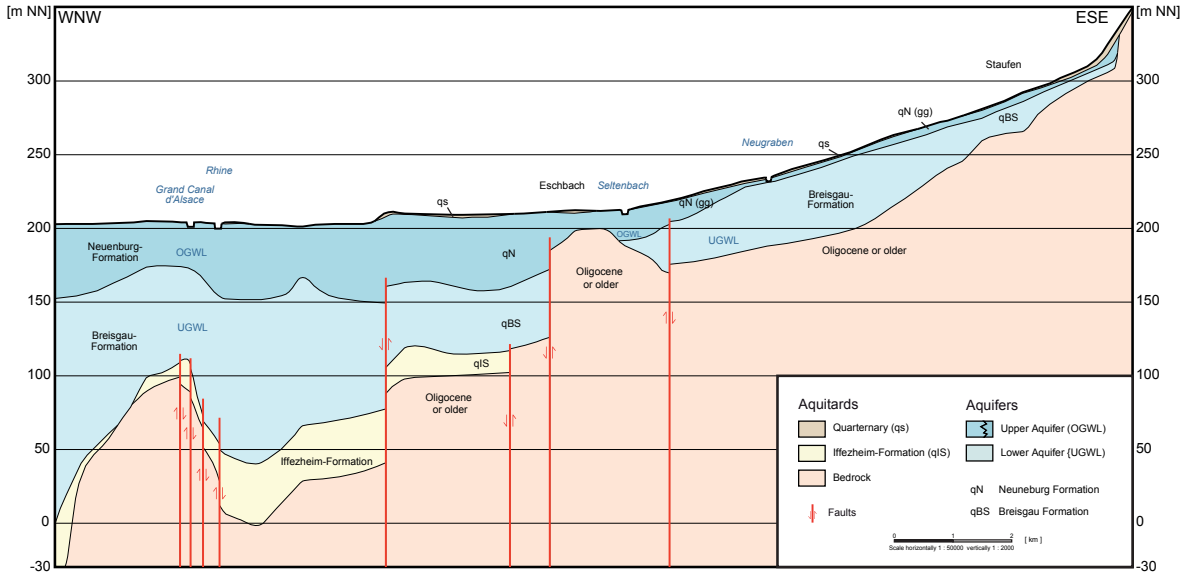

Figure 3.4: Hydrogeological ESE–WNW cross-section of the sampling area Freiburg, simplified from RPF/LGRB [2008]. The position of the cross-section is displayed in Fig. 3.3.

3.4 Freiburg Region

The area of interest is situated in the southern part of the Upper Rhine Graben (see Fig. 3.1), south of Freiburg and the Kaiserstuhl. To the east, its boundary is formed by the crystalline *Black Forest* and its mainly jurassic foot hills (*Vorbergzone*), which also constitute the main recharge area for deep aquifers of the region [He et al., 1999]. From Freiburg to Badenweiler, the Black Forest is characterised by metamorphic gneiss rocks, while granitic magmatic rocks dominate southward of Badenweiler. The outcropping palaeozoic bedrock of the Black Forest is submerged in the graben center at about 3.5 km depth, covered by tertiary and quaternary sediments, as detailed in Fig. 3.3. The upper aquifer systems of the region can be subdivided into two systems, as shown in the ESE–WNW cross-section shown in Fig. 3.4 [Huttner and Schreiner, 1989]. The hydrogeothermal aquifers of interest, from which many of the thermal springs of the region source, are the *Buntsandstein*, the *upper Muschelkalk* and the *Hauptrogenstein* [Stober and Jodocy, 2009]. An Oligocenic salt intrusion, the *Weinstetter Diapir*, exists in the north-west part of the area [Bauer et al., 2005]. Several mining dumps, also noted by Bauer et al. [2005] complicate the area regarding its geochemistry, but should not affect the tracers of this study. As Al Najem [2016] summarizes, the recharge of the shallow aquifer is formed from precipitation, recharge from small rivers originating in the Black Forest a varying source of river infiltration from the Rhine.

3.5 Existing Helium Data

The existing data on helium, especially mantle-derived $^3He/^4He$ ratios in shallow aquifers, is rather sparse for the Upper Rhine Graben. In particular, the focus of the existing studies is on waters discharging through thermal wells and springs. Other $^3He/^4He$ ratios reported from the Upper Rhine Graben are usually from deep aquifers, from petrochemical exploration wells and active geothermal power plants.

Hooker et al. [1985] report high mantle-derived $^3He/^4He$ ratios in groundwaters on the Alsacian western main fault of the graben, close to Colmar. While their main focus is on North Sea gas fields, they use Upper Rhine Graben data as a reference, citing a mantle-derived ^3He component for the Alsacian waters with $^3He/^4He$ ratios ranging from[2] 1.37 to 1.55 R_a (Soultzmatt, Soultzbach) – however they give no indication about the depth of the sampled aquifers, only note that some of the wells are used as mineral waters, suggesting them to be deep aquifers.

Griesshaber et al. [1992] compile data covering the Upper Rhine Graben region and beyond, including the volcanically active Eiffel, as well as the Black Forest forming the eastern boundary of the southern Upper Rhine Graben. The sampled groundwaters all stem from deep aquifers, mostly by sampling thermal and mineral wells and springs, summing up 128 water samples. They conclude that the spatial occurrence of mantle-derived ^3He is connected to surface volcanic activity (as Oxburgh and O'Nions [1987] suggest), but see no apparent correlation between tectonic and seismic activity or heat flow on a regional scale. They find the highest $^3He/^4He$ ratios just outside the Upper Rhine Graben area, in the volcanic Eifel, around the *Laacher See*, with ratios[2] as high as 5.94 R_a equaling to about 74 % mantle component. The ratios found in the graben area and on its main faults vary strongly, showing maxima on the southwestern fault line as already reported by Hooker et al. [1985] and around the Kaiserstuhl and close to Freiburg, while ratios sharply decrease to both the south and the north of that area, on the eastern fault, towards more likely crustal ratios close to Karlsruhe. Data of Griesshaber et al. [1992] from sampling sites also sampled by the campaigns of this study is compiled in table C.2, their data of the sampling sites in the Upper Rhine Graben is reproduced in Fig. A.1.

Aeschbach-Hertig et al. [1996] analysed the lake water of the *Laacher See* and find similarly high mantle-derived $^3He/^4He$ ratios as well as indications of increased $^{20}Ne/^{22}Ne$ and $^{40}Ar/^{36}Ar$ ratios, supporting the picture of a very localized surface mantle imprint connected to the complex local volcanism, consisting of several magmatic plumes [Bräuer et al., 2013].

Friedrich [2007] sampled monitoring and production wells, and springs, in the Odenwald 25 to 40 km north of Heidelberg, a few samples included wells from the *Hessisches Ried*, which is part of the Upper Rhine Graben valley. Those wells are located on the eastern main graben fault, and two of those samples showed terrigenic $^3He/^4He$ signatures indicating a mantle influence, from well depths ranging from 54 to

[2] Recalculated from the $R_a = 1.4 \times 10^{-6}$ used by the cited publication to $R_a = 1.384 \times 10^{-6}$ as used in this study [Clarke et al., 1976].

132 m, with ratios of $(0.537 \pm 0.004)\,R_a$ and $(0.357 \pm 0.002)\,R_a$. These two samples represent the only data, as far as I could find, of shallow aquifers containing mantle-derived $^3He/^4He$ ratios in the Upper Rhine Graben, outside of volcanically active areas.

Outside the geographical constrains of the Upper Rhine Graben, mantle helium signatures in the context of geothermal heat are mostly discussed in studies sampling deep monitoring or production wells, accessing already known geothermal reservoirs directly [Castro et al., 2009; Kennedy and van Soest, 2007, 2006; Oxburgh et al., 1986] or actively discharging hot springs [Umeda et al., 2007; Saar et al., 2005]. Kaudse [2014] sampled in a geologically similar setting to the Upper Rhine Graben: the Dead Sea Transform in Jordan and Israel, however, the sampled artesian and production springs source[3] from depths larger than 200 m, most larger than 900 m. The resulting $^3He/^4He$ ratios show a wide range of values, up to $4.882\,R_a$ (at 400 m well depth), almost all indicate the presence of mantle-derived helium. Kaudse et al. [2016] also used a mantle-derived $^3He/^4He$ ratio to identify groundwater flow patterns in a fault area in the Jordanian desert, unrelated to the larger Dead Sea Transform.

[3] As far as information on depths could be obtained, having been part of the sampling campaign in Jordan, I can attest that this was not an easy task.

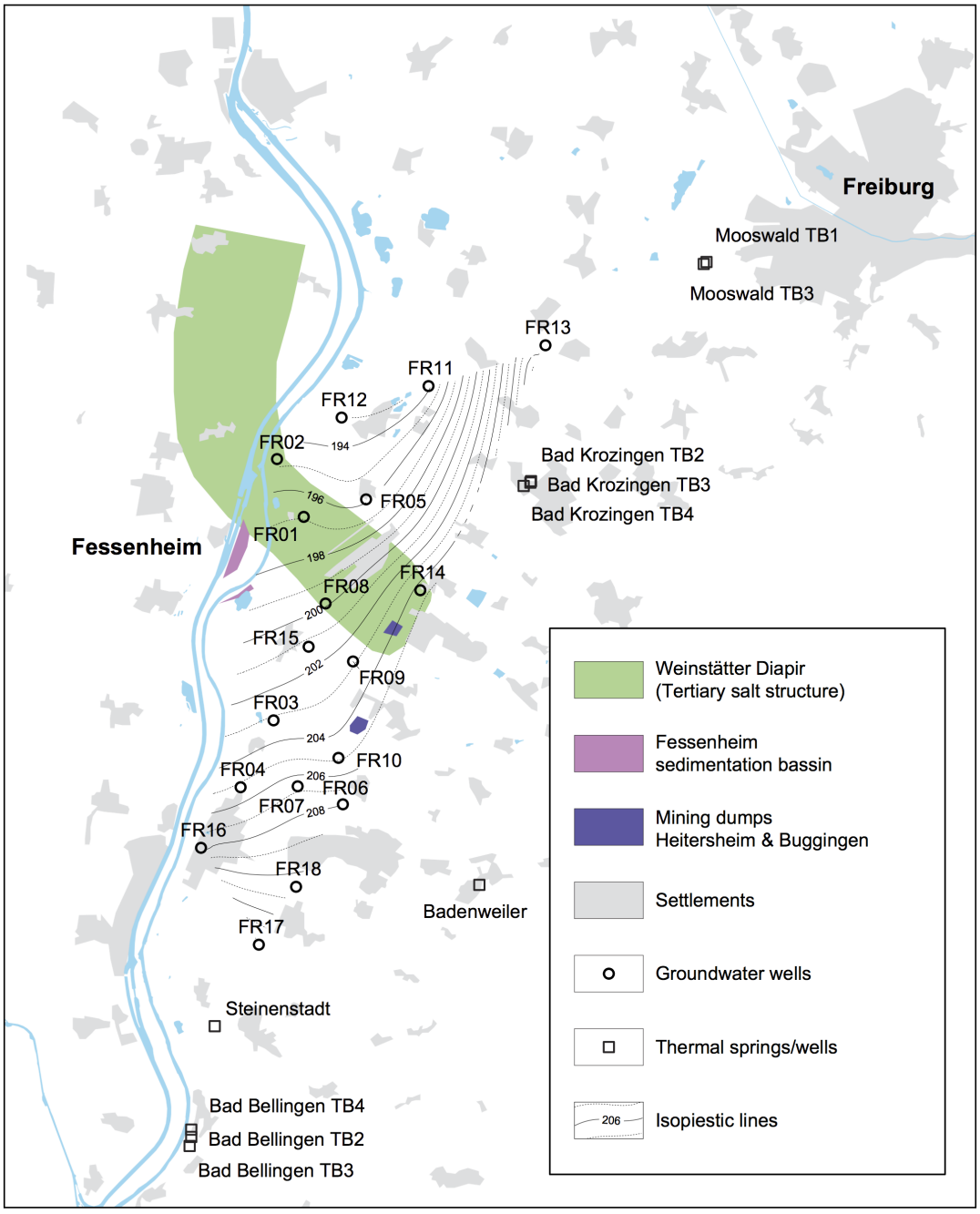

Figure 3.5: The sampling sites, both groundwater wells and thermal springs, of the Freiburg region. Both possible geogenic (Weinstetter Diapir) as well as anthropogenic (mining dumps and sedimentation basins) contamination sources are marked [Bauer et al., 2005]. The isopiestic lines of the groundwater are based on data collected during sampling. Map data based on OpenStreetMap contributors [2017].

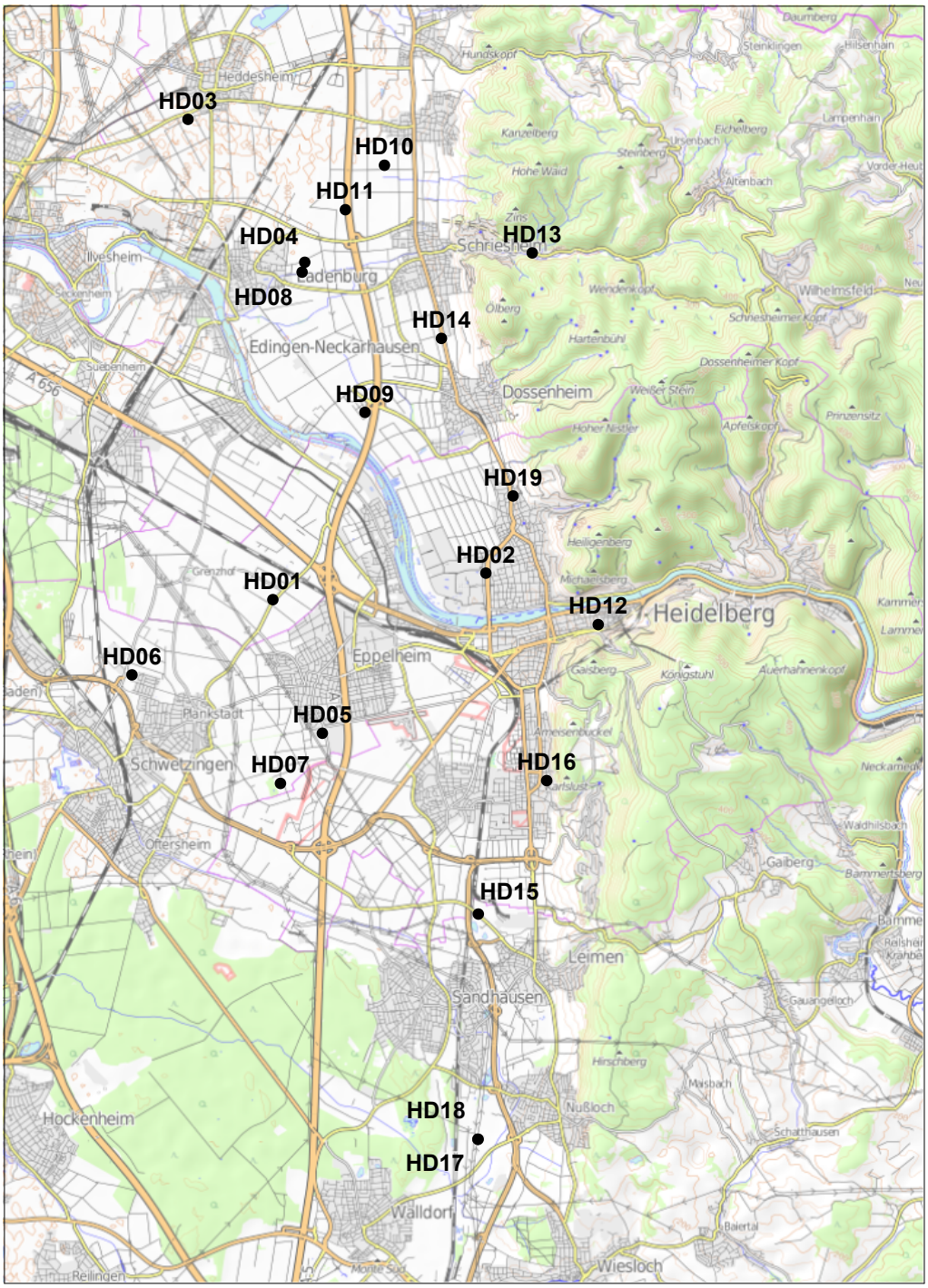

Figure 3.6: The sampling sites of the Heidelberg region. Map data based on OpenStreetMap contributors [2017].

Chapter 4

Methods in the Field

4.1 Sampling Campaigns

Three different regions[1] in the Upper Rhine Graben were in the focus of several sampling campaigns for this study, resulting in the collection of over 200 noble gas samples, as well as close to a hundred samples for tritium, ^{14}C, stable isotopes and ^{222}Rn each. The sampling campaigns were planned in cooperation with my colleague Dr. Sami Al Najem from the *Department of Geosciences* at *Heidelberg University* and Dr. Michael Kraml and Dr. René Grobe of *GeoThermal Engineering GmbH*. Access to the sampled wells and springs was coordinated and granted by the respective private owners or local administrative authorities *HLUG*, *LUBW* and *LGBRLP*. Since most local authorities use the GK3 coordinate system[2] in their databases, the same system is used for the data presented in this study (see table C.7 for locations of all sampling sites). The *Rechtswert* gives the distance to the reference median in meters, while the *Hochwert* signifies the distance to the equator in meters.

The field campaigns were executed in cooperation with Dr. Sami Al Najem, Dr. Gerhard Schmidt and various Masters and Bachelors students.

[1] Henceforth only referred to by their identifying city's names, Groß-Gerau, Heidelberg and Freiburg, even though those cities not necessarily lie within their borders.

[2] *Gauss–Krüger*, a cartesian coordinate system based on a universal transverse Mercator map projection, where the cypher 3 signifies its reference to the 9° East meridian. Conversion to the WSG84 system used in most modern GPS implementations is complicated, using the *Helmert Transformation*.

Figure 4.1: Groundwater sampling at the private irrigation well GG35 (in the foreground) in October 2013. Additionally, soil air samples are taken by B. Beck [2014] at a few meters distance from the well (left), J. Hartmann [2014] and F. Neuwirth work on CH_4 analysis (right) and G. Schmidt et al. [2017c] waits for his turn to collect a $^{87}Sr/^{86}Sr$ sample.

4.1.1 Groß-Gerau Region

The sampling region of Groß-Gerau, consisting of an area of about 140 km^2, was the first one to be approached for this study, as the available data on the region (see section 3.2) made it most suitable to test the suite of tracers employed by our team. The first of three sampling campaigns with focus on this region, consisting of 24 sampled wells and springs, was executed in autumn of 2012. The sites were chosen by their position relative to the main fault line as well as based on the conductivity data available by the study of Siemon et al. [2001]. Sampling sites as close as possible to the fault line as well as two transects crossing the fault were planned. However, access to the wells in terms of both physical accessibility with the available sampling tools, as well as available permits by local well and ground owners, limited the choice of sites[3]. The goal of the first sampling campaign was to produce a broad data overview of the target region, from which interesting hotspots could be identified and investigated further.

[3]Political opposition to a geothermal energy development project, ongoing at the time of sampling, made access to several, ideally positioned private irrigation wells, impossible. The opposition partially originated from the way the 3D-seismic survey was executed, resulting in small property damage [verbal accounts of locals].

This approach led to a second sampling campaign in spring of 2013, when, based on data from the first campaign, regions of heightened interest were sampled with a more narrow grid, decreasing the distance between sampling sites partially down to 500 m. Additionally, 6 previous wells were resampled[4] to be able to quantify seasonal changes of the, mainly meteorically dominated, upper aquifer. The third sampling campaign in November 2013 resampled another 6 wells, this time focusing on the isotopic composition of CH_4 [Hartmann, 2014], therefore only noble gas samples were gathered for this study. The position of all sampling sites is noted in Fig. 3.2.

Production and Monitoring Wells

Of the 31 wells sampled in the region, 10 are privately owned irrigation wells of mostly unknown filtration depth, while the remaining 21 are monitoring wells maintained by the *HLUG* and the *LGBRLP*. Two of the wells (GG20 and GG21) are located west of the Rhine, accessing an entirely different aquifer of the permian Rotliegend (see Fig. 3.2). East of the Rhine, only wells GG25 and GG32 may also be sourcing from the Rotliegend, as opposed to all other wells accessing the quaternary aquifer. None of the wells were in active production at the time and required purging previous to sampling. The maximum borehole depth[5] is 35 m, the mean depth of all sampled wells 11.6 m, therefore only the uppermost, unconfined aquifer is represented by the data. Monitoring wells accessing deeper aquifers are not available in the region.

Springs

The two springs GG16 and GG17, also known as the *Sirona* springs, are located in Nierstein, directly between the Rhine and the outcropping Rotliegend of the Niersteiner Horst. The spring catchment is an ancient, underground roman structure. The discharge of both springs is marginal, samples have to be taken from basins, see Fig. 4.2. Both basins contained suspended sediment load as well as small crustacean lifeforms. Sampling conditions are therefore less than ideal for both springs, with a likely atmospheric contamination/loss of information.

The two other sampled springs, GG30 and GG31, are located on the eastern flank of the Niersteiner Horst, and are very likely shallow, meteorically fed. Discharge was high enough to allow for contamination-free sampling directly from the metallic wellheads.

The artesian springs at Bad Weilbach, QWB1 (*Natron-Lithium-Quelle*) and QWB2 (*Schwefelquelle*), are located about 10 to 15 km north of the northernmost well of the sampling area, north of the river Main,

[4] Marked by the letter *b* in the sample ID.

[5] All depth measurements concerning wells, their filter screens and water tables used in this study are given relative to the upper edge of the well casing, called ROK (Rohroberkante), if not otherwise noted. ROK depths are usually about 0.5 to 1 m larger than below ground level (bgl) depths.

(a) (b)

Figure 4.2: (a) Sami Al Najem during the sampling of GG16 and GG17. Note the small basin on the right, which is the discharge basin of GG16 (b) Sampling the production wells HD04 and HD08.

following the main fault line. QWB1 is cased to a filter depth of 29 m, and used for mineral water production, while QWB2 is cased to about 6 m below the spring fountain (see Fig. A.11) [Thews, 1970]. Both springs were sampled in separate excursion in summer 2014.

4.1.2 Heidelberg Region

The region of Heidelberg, consisting of an area of about 150 km^2, was sampled last, in a single campaign in summer 2014. The same approach as in Groß-Gerau was planned: a sampling line along the eastern main fault line as well as two transects westward, following the groundwater flow direction. As results from the first campaign showed no immediately apparent area of interest, plans for a second, more focused campaign as done in Groß-Gerau, were scrapped. A total of 20 sites were sampled and analysed, their position can be found in Fig. 3.6.

Production and Monitoring Wells

The groundwater wells consisted of 10 monitoring wells, 3 privately owned irrigation wells and 6 active production wells. Of these, three wells (HD06, HD08 and HD18) are accessing the middle aquifer with depths larger than 60 m, HD08 likely even drawing from the third, lowest aquifer (compare Fig. A.3). HD09 could only be sampled behind a T-junction leading to a pressure vessel, possibly affecting the gas composition. HD13, a production well, was pumped irregularly, with uncontrolled breaks. Sampling was barely possible, access to the water was removed about 150 m from the wellhead. Located in a valley leading up into the Odenwald, HD13 is also one of only two wells possibly sourcing east of the main fault,

on the graben shoulder rather than in the quaternary graben filling. The other one is HD12, located directly within the old city of Heidelberg.

Thermal Well

The thermal well in Weinheim, located about 15 km north of the sampling region, began operation in 2007, producing water of 60.5℃ from a depth of 1050 m. Due to technical problems with the submersible pump of the installation, sampling the well failed several times, until in Spring 2015 samples could be acquired. The sampling conditions were imperfect though, as pump pressure did not remain constant and the bubble load of the water was extremely high. Resulting data on gas concentrations are therefor prone to large errors due to gas loss.

4.1.3 Freiburg Region

The sampling region close to Freiburg, spans an area of about 145 km^2, not including the surrounding thermal springs. The area of interest in the southern Upper Rhine Graben is located south of Freiburg, extending southward by about 21 km. Its western boundary is formed by the Rhine river, while on the east, the palaeozoic Black Forest and its jurassic foothills form its border. See Fig. 3.5 for the location of all springs and wells. The thermal wells were sampled in summer 2013, the groundwater wells in a separate campaign in autumn 2013.

Production and Monitoring Wells

Of the 18 wells sampled in the area, two are privately owned irrigation wells, only one of which (FR12) was in active production at the time of sampling. The remaining are monitoring wells. Except for FR02, the sampled wells access the upper aquifer[6] (Neuenburg Formation, compare Fig. 3.4), with well depths ranging from 14 to 64 m. FR02 is a monitoring well with a depth of 170 m, accessing the lower aquifer (Breisgau Formation). It is located within the extend of the Weinstetter Diapir, as well as only 2.5 km downstream the Rhine of the nuclear power plant at Fessenheim, France.

Thermal Springs

From five different locations, all east or south (upstream the groundwater flow, see Fig. 3.5) of the groundwater sampling area, on the eastern main fault, a total of 10 deep water samples were collected.

[6] Well FR14 might access both aquifers, though only filtered between 32 to 35 m [Al Najem, 2016]

The sampled thermal water wells are part of several thermal baths, sourcing from two different aquifers, the upper Muschelkalk and the Hauptrogenstein (see table C.5 for details).

The spring at Badenweiler (T09) is artesian, sourcing from the crystalline bedrock. It feeds into an open basin of about 1000 m^3, while the daily discharge is at about 800 m^3. Access to the spring head was not allowed without special sanitary precautions. The sample therefore has a high likelihood of being affected by degassing/contamination with atmospheric air.

4.2 Groundwater Sampling Methodology

The sampling of groundwater monitoring wells is being done using a submersible *Grundfos MP1* pump, to ensure that no under-pressure acts on the water samples, which would lead to degassing of dissolved gases and loss of information. The sampling procedure is based on the guidelines of the DVGW [2011]: monitoring and out of production wells are purged before sampling up until three times the volume of the water column in the well has been removed and the physical parameters, measured in-line during pumping, are stable, indicating access to the flowing aquifer water. The pump rate for purging and sampling with the *Grundfos MP1* is around 0.3 to 0.5 l/s. Active production wells are sampled using the available sampling ports. Most of the sampled thermal springs are in fact used for production and are actively pumped, offering good sampling conditions and pressure. The artesian springs however usually have very little discharge and offer suboptimal sampling conditions for gas samples, with high probability for atmospheric contamination. Sampling procedures had to be adapted to the given restrictions, samples possibly affected by this are marked as such in the results.

4.2.1 Physical Parameters

Temperature, electrical conductivity (κ_{25}), pH and dissolved O_2 content are monitored during pumping on site, using a bypass after which a multi-parameter probe (*WTW MultiLine*) is installed in the runoff as shown in Fig. 4.3, allowing for purging the wells at high pump rates through the main outlet while monitoring the parameters to see when stable conditions are achieved. Parameter data given in this thesis were recorded directly before sample collection was initiated.

4.2.2 Noble Gases

Noble gas samples are obtained using 10 mm × 1 mm copper tubes made from deoxidized copper (*Wieland cuprofrio® Cu-DHP*), installed in special aluminum racks with steel clamps at both ends. For each sampling site, a primary (A) and at least one backup sample (B) are collected. The sample length is

(a) (b)

Figure 4.3: (a) The sampling gear required for all of the TRACE study's participants, fitting into a small VW bus. (b) The *WTW MultiLine* probes during inline measurement at thermal well MM (the amount of bubble formation is the most extreme witnessed by the author in six years of groundwater sampling, an absolutely exceptional occurrence).

approximately 50 cm, providing an average sample size of 20 ml of water. A non-expanding hose connects the copper tube to either the pump or the sampling outlet of a production well, while the other side is connected to a transparent runoff hose, moving the point of pressure drop away from the sample container. This decreases bubble formation by degassing as well as offering means of a visual inspection of the bubble content of the sampled water. The groundwater is flushed through the tubing for a few minutes, while the tube itself is being hit with a blunt object to dispense of gas bubbles adhering to the copper surface. Once the water exiting the copper tube shows no (or at worst a minimal[7]) amount of gas bubbles, the exit clamp is tightened, then the inlet clamp. The resulting seals are helium-tight against atmospheric pressure and in timescales relevant to this project[8]. Analysis in the lab usually takes place within weeks or months for the A samples and up to several years after sample collection for the B samples.

As part of the project, samples of soil air were collected by Beck [2014]. Soil air sampling works by driving a lance into the ground to the intended sampling depth. The air is being pumped through the perforated lance tip and a 6 mm × 1 mm copper tube connected by gas tight plastic tubing between the lance and the pump, which is then cut off and contact-welded shut using pneumatic pliers. Details on the procedure and the site selection can be found in the resulting diploma thesis of Beck [2014].

[7] Depending on dissolved gas pressures, pump operation and at times circumstances beyond control during sampling, the occurrence of bubble formation can not be avoided at all times.

[8] Beyerle et al. [2000] notes that the leak rate for the copper tubes regarding helium is smaller than 10^{-9} cm^{3}STP/yr while the typical groundwater sample contains helium in the order of 10^{-6} cm^{3}STP/yr.

(a) (b)

Figure 4.4: On-site analysis at thermal well T01: (a) measurement of ^{222}Rn using the *Durridge RAD7*, the sample is being stored in the water bucket to buffer temperature changes. (b) Sami Al Najem performing hydrochemical analysis.

4.2.3 Tritium and Stable Isotopes

Samples are collected in 50 ml glass bottles each, sealed air tight, under water, without atmospheric contact and free of air inclusions. Stable isotope samples are filtered using a 0.45 µm filters in the lab, before analysis.

4.2.4 ^{14}C and δ^{13}C samples

Samples for ^{14}C dating are collected in 500 ml glass bottles. Directly after sampling the samples are sterilized with 0.1 g of silver nitrate ($AgNO_3$) to prevent all living organisms within the sample from altering the isotopic composition of the dissolved carbonate. Sample bottles are immediately stored in opaque containers until analysis to prevent the breakdown of the light sensitive $AgNO_3$.

4.2.5 Radon

Radon samples are collected in two 250 ml glass bottles, taken the same way as tritium and stable isotope samples, without atmospheric contact. As any gas bubbles included in the groundwater are discarded by the sampling method (in contrast to the noble gas samples, where a constant occurrence of gas bubbles in the water stream will be included in the sample), samples from degassing waters may underestimate the amount of ^{222}Rn carried in the sum of fluid and gas phase. Measurement of one of the samples usually occurred within a few hours in the field.

4.3 Radon Analysis

A *Durridge RAD7 Radon Detector* was used to analyse the ^{222}Rn activity in the field. Using a solid state detector, it can measure the α particles of characteristic energy, generated in the decay chain of ^{222}Rn and ^{220}Rn. The *RAD7* detects the 6.00 MeV α decay of ^{218}Po ($\tau_{1/2} = 3.05$ min), which itself is the product of ^{222}Rn decay, and the 6.78 MeV α decay of ^{216}Po ($\tau_{1/2} = 0.15$ s), belonging to the ^{220}Rn decay chain. Subsequent α decays within the respective chains with longer half-life times are not required for the calculation of ^{222}Rn and ^{220}Rn concentrations, allowing for short measurement times and fast recovery to background times.

Since the device is limited to dry air measurements, the samples have to be brought to equilibrium with a transport gas in the field. This is being done by recycling atmospheric air through the water sample using a glass frit, maximizing gas exchange. A single measurement consists of six steps of 20 min each: Purging the RAD7 with atmospheric air in an open system state. With an empty sample bottle installed, a background measurement is performed in a closed system. Afterwards, the sample is being installed in the closed system, and one equilibration run as well as three measurement runs are performed. The ^{218}Po decay counts of the three measurements are blank corrected, averaged and an initial activity in water, C_{W0} [Bq/m^3] is calculated from the data, taking into account the equilibration temperature as well as the time difference between sampling and measurement.

Chapter 5

Methods in the Laboratory

5.1 Noble Gas Analysis

While the measurement of ^{4}He and the heavier noble gases is possible using relatively small quadrupole mass spectrometers, the analysis of ^{3}He requires the use of a high resolution sector field mass spectrometer. Mass separation is achieved by using the dependence of the Lorentz force on the mass-to-charge ratio of the ionized sample gas being sent through an adjustable magnetic field. Analysing ^{3}He/^{4}He ratios remains difficult, as the naturally occurring ratios can be extremely low, down to 10^{-8} and lower. With ^{4}He easily approaching upper limits of gas pressures for the ion sources [Burnard and Farley, 2000], the actual amount of ^{3}He atoms available for measurement can be fairly small, as Mamyrin and Tolstikhin [1984] calculates.

Noble gas data (^{3}He, ^{4}He, ^{20}Ne, ^{22}Ne, ^{36}Ar, ^{40}Ar, ^{84}Kr and ^{132}Xe) for this study were acquired on a *GV Instruments 5400* sector field mass spectrometer set up with an ultra-high vacuum gas extraction, purification and separation system at the *IUP Heidelberg* by Friedrich [2007], and modified by Wieser [2011] and Kaudse [2014]. Including extraction and purification, the measuring time per sample is close to 5 h, and a total of over 125 have been analyzed for this study. While sample installation and extraction are manually executed, the gas separation and consequent measurement is largely automated using scripts, requiring constant operator oversight only in rare cases.

5.1.1 Sample Preparation

Analysing the different noble gas isotopes requires them to be extracted from the water and separated into their respective species, which is done in the ultra-high vacuum extraction line set up by Friedrich

[2007]. The copper tube sample is connected to the inlet part of the line, and the seal is broken. The water is caught in a glass bulb within the evacuated volume, leading to degassing of the dissolved gases as well as water vapor formation. The resulting gaseous phase is slowed down on its way to the cold traps by a capillary, to ensure a maximum removal of water vapor while moving through the water trap filled with zeolith (3 Å pore diameter). The remaining gases, including the noble gases down to argon are being trapped in a stainless steel trap (SST) at a temperature of 25 K, while the lighter noble gases helium and neon are being adsorbed in a second step onto an active charcoal trap (ACT) at 10 K. To prevent the trapping of the lighter noble gases under layers of heavier ones on the SST, Kaudse [2014] implemented a procedure described by Stanley et al. [2009]: closing the SST after 20 min of degassing the sample, reheating it to 60 K for a short period thereby allowing light noble gases caught under layers of heavier gases to escape. After cooling down the SST again, the ACT is then opened to adsorb the entirety of He and Ne (as well as hydrogen). Degassing of the sample takes up to 50 min. The separation of the different gas species is achieved by stepwise reheating of the traps, facilitating separate desorption: The desorption temperature for helium is at 42 K, the release of neon from the ACT starts at 90 K (see also Figure A.10) [Friedrich, 2007].

As both the electron multiplier as well as the faraday cup have limited measurement ranges, the gas amount for He and Ne is being checked against a limit, using a quadrupol mass spectrometer on the preparation line. If the amount is above the threshold, the sample size is reduced by expanding it into a known volume and discarding the rest, effectively splitting it by a known factor which is accounted for later on in the data evaluation.

In further purification steps, remaining reactive gases (H_2, N_2) are removed by exposing the sample splits to various getters, before they are processed into the mass spectrometer.

5.1.2 Mass Spectrometry

The principle parts of the *GV5400* sector field mass spectrometer are the ion source, the electromagnet and the two detectors, one faraday cup and one electron multiplier. The ion source is a Nier-type source as described in Burnard and Farley [2000], with a wolfram filament running at a current of 200 to 800 µA, depending on the gas species to be measured. The pressure dependency of the ion source's ionisation efficiency [Burnard and Farley, 2000] makes bulk measurements of multiple gas species impossible, as concentrations differ too greatly, requiring gas inlets for certain gases to be diluted by splitting. The parameters of the ion source are tuned to achieve single ionisation of the sample gas and ideal peak shape and height. Especially with ^{3}He, optimal tuning is crucial due to the low gas amounts, also relative to the neighboring HD ion peak, formed by residual hydrogen. Separation of the usually higher HD peak, at a mass difference of only 5.9×10^{-3} amu [Mamyrin and Tolstikhin, 1984] is essential for a reliable ^{3}He analysis (see Fig. A.9).

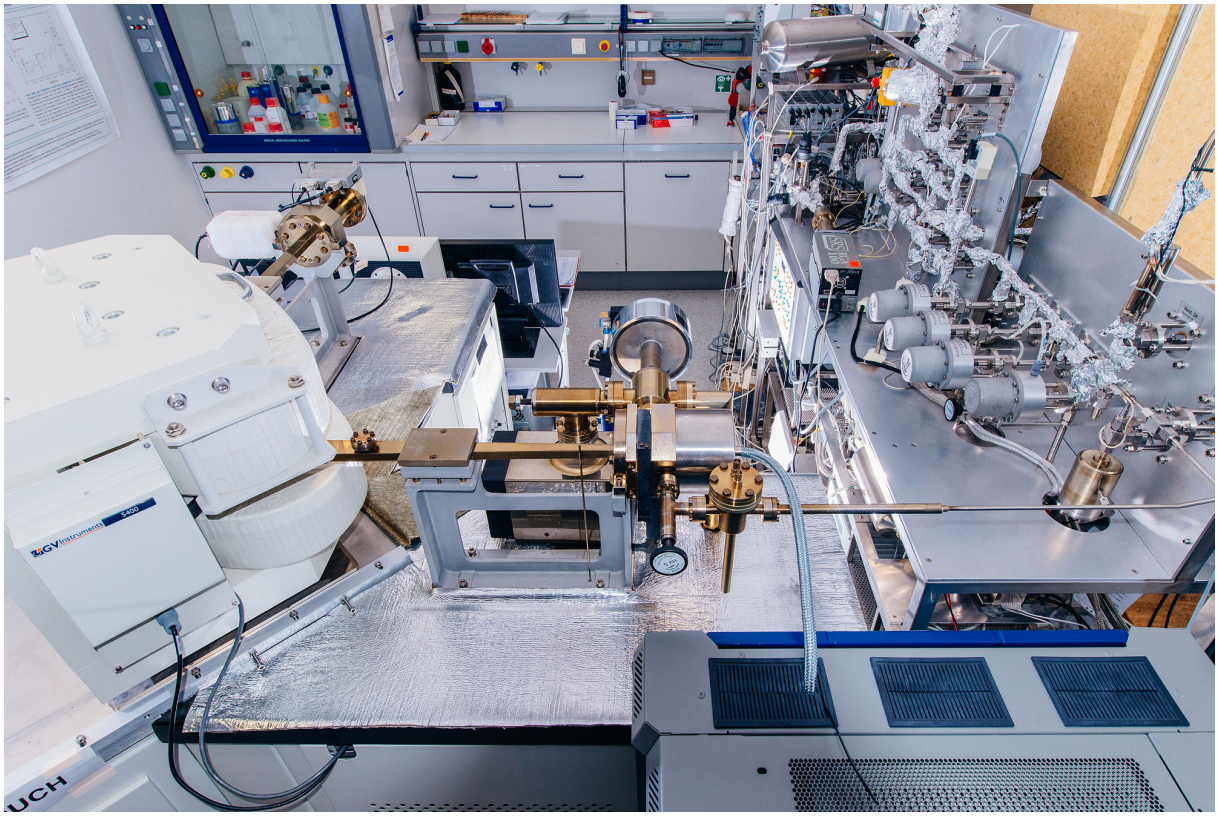

Figure 5.1: The mass spectrometry laboratory at the *Institute of Environmental Physics* at *Heidelberg University*. On the right is the extraction line built by Friedrich [2007], leading through a thin steel tube towards the ion source in the center of the image. On the left hand side, the flight tube and the magnet of the *GV5400* are visible.

The ions are being focused and accelerated into the flight tube, towards the electromagnet, where they pass through a homogenous magnetic field, acting on the ions according to the Lorentz-force. The resulting radius r of the ion path is

$$r = \frac{1}{B} \cdot \sqrt{\frac{q}{2m} \cdot U_{\text{acc}}} \tag{5.1}$$

where q is the ion's charge, m its mass, B the magnetic field strength and U_{acc} the accelerating voltage. By modulating the magnetic field, the sample gas ions can be targeted on either detector, depending on their mass. Since the radius is dependent on both mass and charge, singular ionisation is very important. Otherwise, part of the gas would remain undetected, as twice charged ions of the same mass would not hit the detector. This is also one of the reasons that a bulk measurement is not suitable, as twice ionized ^{40}Ar would overlap with single ionized ^{20}Ne, causing interference. Another factor is the hysteresis of the electromagnet: while switching between isotope masses causes only small delays, refocusing different

element masses on the detectors can not be achieved in a timely manner. Therefore, a separation of the sample gas into the different elements, as described in the previous section, is required.

The *GV5400* at the *Institute for Environmental Physics* at Heidelberg is equipped with two detectors: a faraday cup, which works detecting the ion current by measuring the voltage over a high resistivity, delivering a signal in V. The more abundant isotopes ^{4}He, ^{20}Ne, ^{22}Ne, ^{36}Ar and ^{40}Ar are analysed on the faraday. For the less abundant ^{3}He, ^{84}Kr and ^{132}Xe, a secondary electron multiplier is used, where a single charged particle starts an electron cascade over several dynodes. The resulting signal is processed into counts per second. The electron multiplier's efficiency is variable with the beam energy it is exposed to – exposing it to pronounced beam strength changes leads to non-linear signal integration [Wieser, 2011], which can cause a signal degradation during the first seconds of a measurement.

For the aim of this study, analysing He and Ne could have been sufficient, the full suite of heavy noble gases was analysed none the less, as they might offer additional insight by allowing for inverse modeling of recharge temperatures and excess air contents. The development of a shortened measurement routine, omitting all heavy noble gas measurements, was approached, but ultimately abandoned due to problems with achieving reproducible beam positioning: The extensive change in timing posed unexpected problems with the hysteresis of the electromagnet of the sector field spectrometer, which ultimately led to an unfavorable ratio of time saving versus information loss.

5.1.3 Data Evaluation

Each measurement starts with the inlet of a gas split, therefore at the time of injection, there is a certain absolute amount of gas present in the flight tube. Detection and integration of the gas ions starts a few seconds after injection, to account for non-linear tune-in behavior, both of the ion source as well as the electron multiplier. Per gas inlet, several integrations are performed, the amount and length depending on the commonly expected isotope abundance. By far the most (and longest) integrations are being done for ^{3}He, with 50 integrations over 30 s each, due to its usually very low abundance. The observed trend is usually decreasing, as the ions are being consumed during the measurement. The initial gas amount at the time of injection is being calculated by fitting the recorded data.

The resulting noble gas data (a voltage from the faraday cup, a count rate from the electron multiplier) is calibrated by measuring a spread of different aliquots of a calibration gas, containing noble gas concentrations in a similar range as the samples. As a calibration gas reservoir a dry atmospheric air standard is used, for which the noble gas composition is well known [Porcelli et al., 2002]. Calibration measurements of different gas amounts are executed fully automated each night. Blank measurements are done on a weekly basis. Additionally, to account for short term fluctuations in sensitivity, fast calibration (*fastcal*) measurements are being done right before each gas species is measured. While the standard calibration gas undergoes the exact same processing as the samples, to ensure a valid calibration of the data is

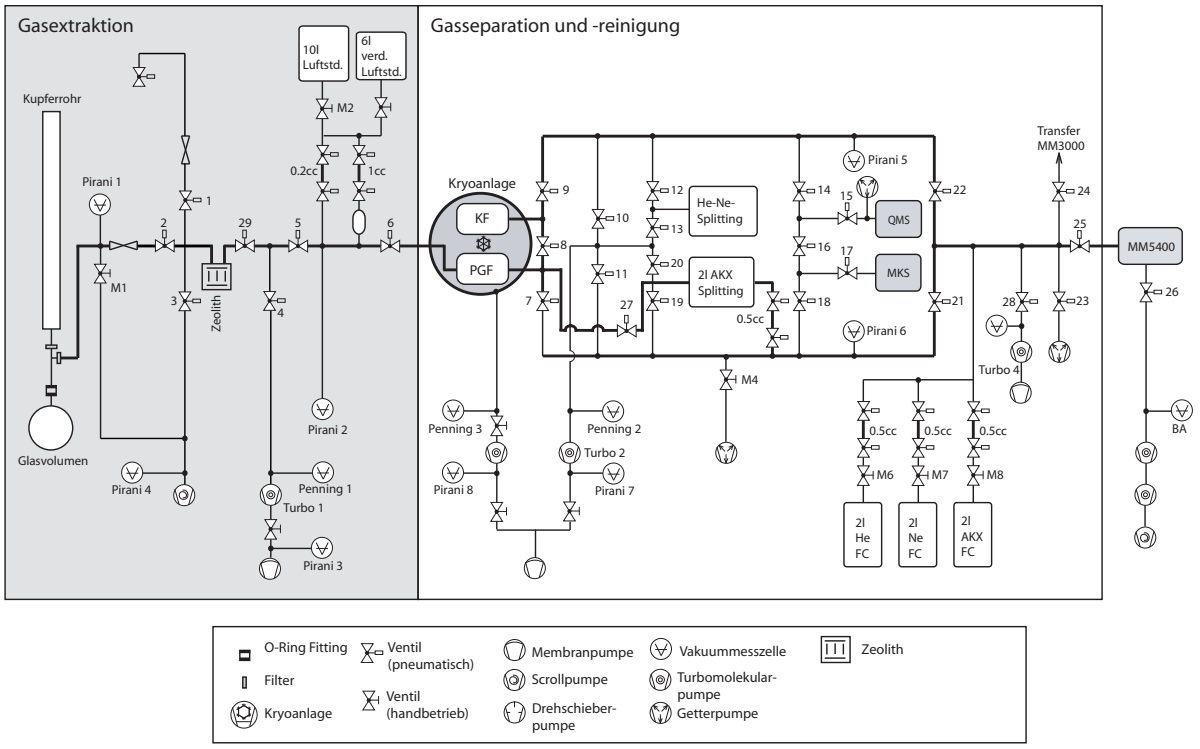

Figure 5.2: Schematic of the sample extraction, purification and measurement system used to analyse noble gas samples at the *IUP Heidelberg*, from Friedrich [2007].

possible, the fastcals use already separated reservoirs of He, Ne and a mixture of Kr and Xe[1].

Calculation of the final gas amounts in the water sample is done using the software *WUCEM*, developed specially for the IUP's noble gas line by Michael Jung. A detailed description of the data analysis process can be found in Wieser [2011]. Measurement outliers[2] are being removed by the operator, the remaining data, both of the sample measurements as well as the calibration measurements, including all the fastcals, are fitted to determine the initially injected amount and blank corrected with measurements for the respective isotope masses' background signal. The process delivers, in combination with the water sample's weight, the concentration of each noble gas isotope in units[3] cm^3STP/g.

The helium isotope ratio $^3He/^4He$ is being calculated from the measurement values acquired from *WUCEM*. In principle, a direct measurement of the ratio is possible by measuring both isotopes in parallel, from the same gas split. This is not being done on the *GV5400* though, which is set up and

[1] No fastcal for Ar exists, as the measurement of Ar on the faraday cup is very stable [Wieser, 2011]

[2] Mostly rare instabilities of the faraday cup measurements, as well as still visible non-linearity of the electron multiplier when the beam initially hits the detector.

[3] Gas at standard conditions for temperature and pressure, i. e. $T = 273.15\,K$, $p_0 = 101.325\,kPa$

tuned to measure the full range of noble gas isotopes. While a simultaneous measurement of ^{3}He and ^{4}He would likely have better accuracy, separating the helium measurement into two splits allows for a greater range of ratios to be measured: the amount of ^{4}He usually calls for a split to avoid exceeding the limits of inlet pressure as well as detection range on the faraday cup, causing the ^{3}He fraction to be diluted down too much. By separating the sample's helium component into two splits for two distinct measurements, measuring conditions for each isotope can be optimised, while sacrificing analytical precision on the ^{3}He/^{4}He ratio. Simultaneous ratio measurement is implemented for ^{20}Ne/^{22}Ne ratios, where the amounts of both isotopes are in a much more similar range.

5.1.4 Correction of ^{3}He Data for Tritiogenic Ingrowth

Sample analysis rarely is done within a short timespan after sampling, mostly due to scheduling of shared analysis time on the mass spectrometer between different projects. While the copper sampling tubes are gas – and especially helium – tight for long term storage, the tritium included in the samples decays. This results in an ingrowth of ^{3}He in the sample during storage, which can be described as following:

$$\left(\frac{^3\mathrm{He}}{^4\mathrm{He}}\right)_{\mathrm{corr}} = \left(\frac{^3\mathrm{He}}{^4\mathrm{He}}\right)_{\mathrm{meas}} - \left(1 - e^{-\lambda t}\right) \cdot \left(\frac{^3\mathrm{H}}{^4\mathrm{He}}\right)_{\mathrm{meas}} \tag{5.2}$$

where t is the time elapsed between sampling and analysis, and ^{3}H is the tritium activity given in cm^{3}STP/g. As Aeschbach-Hertig [1994] argues, the proportionality of the correction to the ^{3}H concentration potentially introduces a high error – which becomes irrelevant for samples measured using the helium ingrowth method (see section 5.2 and equation C.2), as the analytical error is far lower than for proportional counting. Given the present day tritium concentrations of most waters sampled in this study and sample storage times of less than a year, the correction is usually well below 1 % relative to the original measurement. Only for three samples is the correction larger than the initial analytical error of the ^{3}He/^{4}He measurement. Samples lacking a tritium analysis (27 in total) remain uncorrected. Of these, only one sample (MM) exceeds a storage time of 200 days, however, the deep well MM is expected not to contain tritium anyhow.

5.1.5 Further Noble Gas Evaluation

The resulting data from the evaluation represent the total noble gas concentrations per gram of sample water. See table 5.1 for a summary of how ratios and elemental concentrations are calculated for this study. A plot of the total xenon concentration over the neon concentration can give a first impression on whether the samples are affected by degassing or excess air: both noble gases source only from the atmospheric reservoir and should, if unaffected, plot on a line calculated from their temperature dependent solubility (see Fig. B.4).

Table 5.1: Calculation of isotope ratios and elemental gas amounts. Since measurement errors are of similar magnitude for neon, both isotopes are used for the calculation, while for argon, only ^{40}Ar is used, as its relative accuracy is about $^{2}/_{3}$ better than for ^{36}Ar.

Ratio	Calculated from
^{3}He/^{4}He	$\left(\frac{^{3}\mathrm{He}}{^{4}\mathrm{He}}\right)_{\mathrm{meas}} - \left(1 - e^{-\lambda t}\right) \cdot \left(\frac{^{3}\mathrm{H}}{^{4}\mathrm{He}}\right)_{\mathrm{meas}}$ [a]
^{20}Ne/^{22}Ne	measured
^{20}Ne/^{4}He	$\frac{^{20}\mathrm{Ne}_{\mathrm{meas}}}{^{4}\mathrm{He}_{\mathrm{meas}}}$
^{40}Ar/^{36}Ar	$\frac{^{40}\mathrm{Ar}_{\mathrm{meas}}}{^{36}\mathrm{Ar}_{\mathrm{meas}}}$
He	$^{3}\mathrm{He}_{\mathrm{meas}} + {}^{4}\mathrm{He}_{\mathrm{meas}}$
Ne	$\left(^{20}\mathrm{Ne}_{\mathrm{meas}} + {}^{22}\mathrm{Ne}_{\mathrm{meas}}\right) \cdot {}^{100}/_{99.73}$ [b]
Ar	$^{40}\mathrm{Ar}_{\mathrm{meas}} \cdot {}^{100}/_{99.60}$ [b]
Kr	$^{84}\mathrm{Kr}_{\mathrm{meas}} \cdot {}^{100}/_{57.00}$ [b]
Xe	$^{132}\mathrm{Xe}_{\mathrm{meas}} \cdot {}^{100}/_{26.89}$ [b]

[a] Aeschbach-Hertig [1994]
[b] Porcelli et al. [2002]
[c] for ^{40}Ar/^{36}Ar < 302, otherwise Ar is calculated from $^{36}\mathrm{Ar} \cdot {}^{100}/_{0.3364}$ [Porcelli et al., 2002]

The ^{3}He/^{4}He ratios require a correction for their atmospheric component. A basic calculation of this air correction is given by Griesshaber et al. [1992] as

$$\left(\frac{\mathrm{R}}{\mathrm{R_a}}\right)_{\mathrm{corr}} = \left[X \cdot \left(\frac{\mathrm{R}}{\mathrm{R_a}}\right) - 1\right](X-1)^{-1} \tag{5.3}$$

$$X = \frac{\beta_{\mathrm{Ne}}}{\beta_{\mathrm{He}}} \cdot \left(\frac{\mathrm{He}}{\mathrm{Ne}}\right)_{\mathrm{sample}} \Big/ \left(\frac{\mathrm{He}}{\mathrm{Ne}}\right)_{\mathrm{air}} \tag{5.4}$$

However, for samples showing crustal or mantle influence, this correction is usually negligible, as in such cases the He/Ne ratio is well above the atmospheric ratio, with radiogenic helium dominating the ratio.

For further quantitative analysis, i. e. calculating noble gas temperatures and ^{3}H-^{3}He dating, a separation of the different constituents of those concentrations is necessary – mainly, the calculation of the excess air component. This is done using the software *PANGA*, developed at the *Institute of Environmental Physics* at *Heidelberg University* by Michael Jung. The software's functionality and theoretical approach is described in detail in Jung [2014]; Jung and Aeschbach [submitted]. It implements all currently available

excess air models (see section 2.2.1 for a short summary, and Aeschbach-Hertig and Solomon [2013] for extensive detail) and allows for inverse modeling of the acquired noble gas data.

The software requires the elemental concentrations of the noble gases calculated from the single isotope concentrations that are measured by the *GV5400* as input data. Additionally, salinity S (usually negligible during recharge) and atmospheric pressure p (by estimating the recharge area's height) can be provided, for the entire dataset as well as on per sample basis. Helium is usually – and especially in this study – excluded from the modeling process, as its composition can be complicated by significant radiogenic and terrigenic components. This leads to an overdetermined system of four equations of the form $C_i^{\mathrm{tot}} = C_i^{\mathrm{eq}} + C_i^{\mathrm{exc}}$ and a set of at maximum three model parameters (A, F, T).

Additional to the straightforward fitting of the data to the model equations as presented in section 2.2.1, *PANGA* offers the option of scalable Monte Carlo simulations, in order to improve accuracy and to better cope with samples which lead to physically unreasonable results in the normal inverse modeling process. *PANGA* presents the results of the Monte Carlo simulation graphically, allowing for the application of manual corrections in cases where multiple clusters of probability occur, some of which are usually physically not reasonable.

In a first step, as advised by Jung and Aeschbach [submitted], the data is modeled using the UA model, to identify cases of degassing ($A < 0$) and unusual amounts of excess air. In a further step, the data is modeled (based on the recommendation of Jung and Aeschbach [submitted] and on the results of Mayer [2017]) using the CE model [Aeschbach-Hertig et al., 2000], handling degassed and excess air samples with different initial parameters[4]. The CE model is also a valid choice for the analysis of this study's data, as the preliminary xenon-neon plot (Fig. B.4) shows that samples are both affected by degassing as well as excess air.

5.2 Tritium Analysis

Two different methods of tritium analysis are employed in this study. Most of the samples were measured in-house at the *Institute of Environmental Physics* using low level counting. For the analysis, 18 ml of sample are mixed with magnesium chippings in order to be reduced to gaseous hydrogen by heating to 580°C. The resulting gas is being measured for 48 h in a proportional counting chamber, where 1 TU amounts to about 0.02 cpm signal, against a background of 0.4 cpm [Schneider, 2014]. The detection limit of the chamber measurement is 2 TU, with an accuracy of ±1 TU. The analysis setup and procedure is described further detail in Schneider [2014] and Grothe [1992].

The remaining samples were analysed using the tritium ingrowth method introduced by Clarke et al.

[4]Degassed shallow groundwater samples are approached with $A = 0.01$, $F = 3$ and $T = 10$, while for samples with excess air $F = 0.5$ is used.

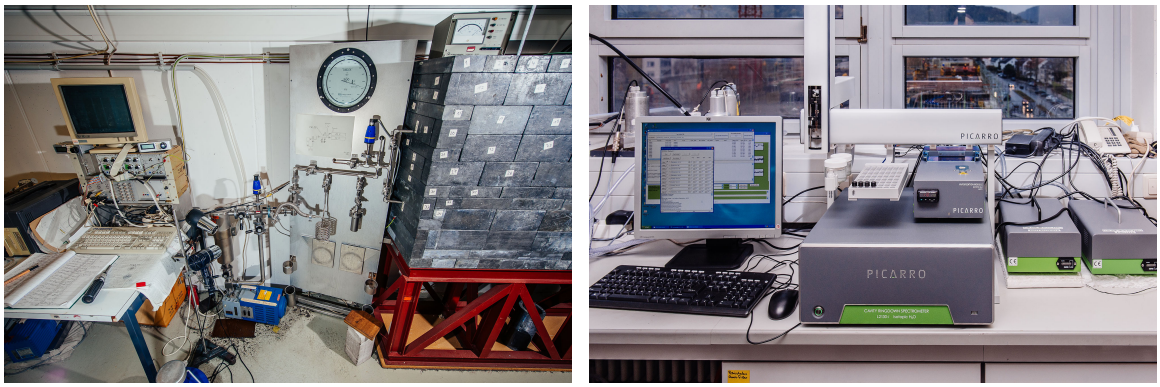

(a) (b)

Figure 5.3: The tritium proportional counting lab (a), with lead shielding for the counting tubes and the *Picarro L-2130i CRDS* used for stable isotope analysis (b) at the *Institute of Environmental Physics* at *Heidelberg University*.

[1976]. The measurements were done by the *Institute for Environmental Physics* at *University of Bremen* by Dr. Jürgen Sültenfuss, the laboratory facilities are described in detail in Sültenfuß et al. [2009]. Instead of measuring the β^- decay of ^{3}H directly, the water samples are degassed completely to remove all dissolved ^{3}He, both from previous ^{3}H decay as well as equilibration with other reservoirs. The remaining ^{3}H, incorporated in the water molecules, is then producing purely tritiogenic ^{3}He within the sample. Therefore, samples have to be stored up to six months after initial degassing to allow for sufficient ^{3}He to accumulate, depending on the expected tritium activity. The detection limit of this method, as employed in Bremen[5], is at 0.01 TU [Sültenfuß and Massmann, 2004].

Since the low level counting lab at the *Institute of Environmental Physics* encountered technical problems in 2016, some of the tritium samples remain unanalysed. Data is missing for all thermal wells from Freiburg, except T09, for the thermal well at Weinheim (MM) and for the Freiburg groundwater samples FR12 – FR15, FR17 and FR18. Some of the redundantly sampled wells from the Groß-Gerau region were also omitted from analysis, as tritium contents are not expected to change within short timespans.

5.3 Radiocarbon and δ^{13}C Analysis

Of the 500 ml samples collected for radiocarbon analysis, 76 ml were used to extract the DIC from. The extraction line at the *Institute of Environental Physics* at *Heidelberg University* was set up by Unkel [2006] and Kreuzer [2007]. The glass extraction line has been simplified since its initial construction, omitting the flow restricting capillary. Furthermore, as the samples for this study were treated with

[5] For 500 ml of sample water, stored for 6 months.

$AgNO_3$, no further addition of chemicals as described by Kreuzer [2007] is necessary. As used for this study, the line consists of an Erlenmeyer flask containing the sample, with a special finger attached to the flask where hydrochloric acid is being stored without contact to the sample. Following, there is a water trap filled with glass balls of a 2 mm diameter, which is cooled by a mixture of dry ice and isopropanol. A *Pirani* gauge is being used to monitor the systems pressure, and finally, there is removable trap for the CO_2, cooled with liquid nitrogen.

In a first step the sample and the acid used in the process are being thoroughly degassed. The DIC is then extracted from the water sample as CO_2 by adding hydrochloric acid (2 ml of 2 molar HCl), the resulting gaseous CO_2 is caught in the nitrogen cooled glass vial. The extraction takes between 10 to 20 repetitions, depending on the amount of DIC dissolved in the water, and takes up to 2 h per sample.

The resulting gaseous CO_2 is catalytically transformed (graphitised, using iron as a catalyst) to solid graphite to be a suitable target for accelerator mass spectrometry (AMS) [Unkel, 2006]:

$$CO_2 + 2\,H_2 \longrightarrow C + H_2O \tag{5.5}$$

Using AMS is required for ^{14}C analysis, as normal spectrometry can not resolve the molecules and isobars $^{12}CH_2^-$ or ^{14}N from ^{14}C and was first proposed by Muller [1977]. Several steps in the AMS setup act as a filter for those undesired molecules and isobars: not all of them form stable ions in the first place and a first mass selection is being done with a common spectrometer. After acceleration of the negatively charged ions towards a stripper, consisting of a thin foil or a gas, isobaric molecules are suppressed and the negative ions stripped of their electrons. The positively charged beam is then mass discriminated again, and detected.

The samples were measured at the *Klaus-Tschira-Laboratory* of the *Curt-Engelhorn-Centre for Archaeometry* in Mannheim, using a MICADAS-type spectrometer as described in Kromer et al. [2013]. While each well and spring was sampled for ^{14}C, due to cost restrictions and the unsuitable ^{14}C dating range for meteoric water, only a fraction of the samples for which analysis was deemed reasonable were measured.

5.3.1 Radiocarbon Dating

The carbon analysis delivers activities of ^{14}C in pmC (percent modern carbon, see section 2.7). Due to the complex carbonate chemistry of the groundwater environment, these data can not be used for dating without further corrections. The $\delta^{13}C$ however can directly be qualitatively interpreted according to Fig. 2.9.

5.4 Stable isotopes

All samples with an electric conductivity below 2 mSv/cm were analysed the at the *Institute of Environmental Physics* at Heidelberg by Michael Sabasch on a *Picarro Cavity Ring Down L-2130i Spectrometer* (CRDS). Samples with higher electric conductivity were analysed, on a *Picarro Cavity Ring Down L-2120i Spectrometer*, by Paul Königer at the *Federal Institute for Geosciences and Natural Resources (BGR)* at Hannover. The data measured both at the *IUP Heidelberg* as well at the *BGR Hannover* are measured relative to the VSMOW standard, with an uncertainty of 0.05 ‰. In contrast to the previously used isotope ratio mass spectrometry (IRMS), CRDS is based on the absorption of a laser by the sample atoms. The laser is coupled into an optical cavity consisting of high-reflecting mirrors. When shut off, the mean lifetime of the reflected light (ring-down time) decreases when the sample is introduced, compared to the evacuated cavity. With light paths of kilometers, the sensitivity of the system is very high, allowing for the detection of very small quantities of substances. A detailed description of the development and principle of CRDS systems can be found in Paldus and Kachanov [2005].

Chapter 6

Results

The basic sampling data concerning locations, dates, wells and physical parameters are summarized in table C.7. The complete dataset for noble gases is summarized in table C.9 and table C.10, while ^{3}H, δ^{18}O, δ^{2}H and ^{222}Rn data can be found in table C.8, the results of the calculation of ^{3}H-^{3}He-ages is shown in table C.14. ^{14}C and δ^{13}C data is shown in table C.15. Analytical errors are given in the tables for each measured and calculated value, some of the plots omit error bars in favour of a better overview when many data scatter closely, while in the logarithmic plots of ^{3}He the analytical errors are too small to show. Data from the hydrogeochemical analysis and the strontium isotopic composition are presented in Al Najem [2016] and in Schmidt et al. [2017a,b,c].

6.1 Noble Gas Fitting and Temperatures

As apparent from table C.4, noble gas data from A and B samples reproduce quite well, differing in ^{3}He concentrations by 5 % at most, and usually less. The following presentation of the data is based on single sample analysis. In cases where measurements of A samples failed, usually due to technical errors or leakage, B samples were substituted, but not marked as such. Note that a small 'b' in the ID of some samples from Groß-Gerau denotes a duplicated sample from the second campaign at Groß-Gerau, not a backup sample.

An exception in reproducibility is visible for GG16 where ^{3}He concentrations of A and B sample diverge by up to 17 %. GG16 is one of the Sirona springs, where sampling conditions were less than ideal (see section 4.1.1). Therefore, a contamination of one or both samples collected there is the most likely explanation. When compared with expected concentrations from purely atmospheric air equilibration at 10°C based on solubility data from Clever [1979a,b, 1980], the B sample shows a more atmospheric

signature in all noble gases than the A sample, indicating the greater amount of contamination. While GG16 A still has to be assumed to be atmospherically contaminated, it is most likely less affected than GG16 B and therefore used instead of the B sample in further analysis. Another exception is the sample from the thermal well at Weinheim, MM, where extreme bubble formation occurred. The choice in this case was made based on the accuracy of the ^{3}He measurement, as one of the samples had an uncertainty of 95 % caused by the gas splitting during analysis, which is required at high amounts of ^{4}He.

6.1.1 UA Model

The results of the preliminary fit of the entire dataset, using the UA model (see section 2.2.1) and 10^5 Monte Carlo simulations is shown in table C.11. Exemplary result plots from *PANGA* for varying χ^2 values and probabilities are shown in Figure B.23. Calculated values for A_{UA} indicate the occurrence of degassing for 22 of 94 fitted samples. Degassing only affects samples from the Groß-Gerau region and the thermal well at Weinheim. Resulting noble gas temperatures (NGTs) of most of the shallow groundwater samples scatter within 2 to 4°C of the present mean annual air temperature (MAAT, about 9°C for Baden-Württemberg [DWD, 2017], compare Fig. A.5, while the Upper Rhine Graben area is expected to be a little warmer, as the local MAAT from Mannheim of about 10°C indicates [DWD, 2011]), with a tendency to be warmer, even though Hall et al. [2005] found the UA model to underestimate rather than overestimate NGTs. Only a few samples, containing high amounts of ^{3}He, result in temperatures colder than the MAAT, at 7°C and less, together with most of the thermal spring waters (see Fig. B.5), which end up mostly below 5°C. The water from the Weinheim well, MM, appears to be difficult to fit, resulting in a large χ^2 value. As the fitting is sensitive on deviations of the gas composition from model expectations[1], this is taken as an indication that the gas composition is massively influenced by degassing due to the bubble formation witnessed during sampling.

6.1.2 CE Model

The CE model results shown in table C.12 for the shallow groundwater samples generally show low χ^2 values and χ^2 probabilities above 1 %, as well as relative uncertainties of the fitted temperatures below 2 %, indicated by Jung and Aeschbach [submitted] as criteria for reasonable results. A few rare exceptions exist for the Groß-Gerau data, which will be discussed in the following subsections, the Groß-Gerau Region is also the only sampling region where Monte Carlo simulations resulted in multiple clusters of probability, requiring further data analysis.

Many samples result in large, negative F_{CE} values of -1500 and lower, while showing very small values for the initial air to water volume fraction A_{CE}. This kind of behavior is discussed by Jung and Aeschbach

[1] Which is why the elemental argon amount for samples with high ^{40}Ar/^{36}Ar ratios has to be calculated from ^{36}Ar, as the fit models do not account for radiogenic ^{40}Ar, resulting in high χ^2 of the fits and large analytical uncertainties.

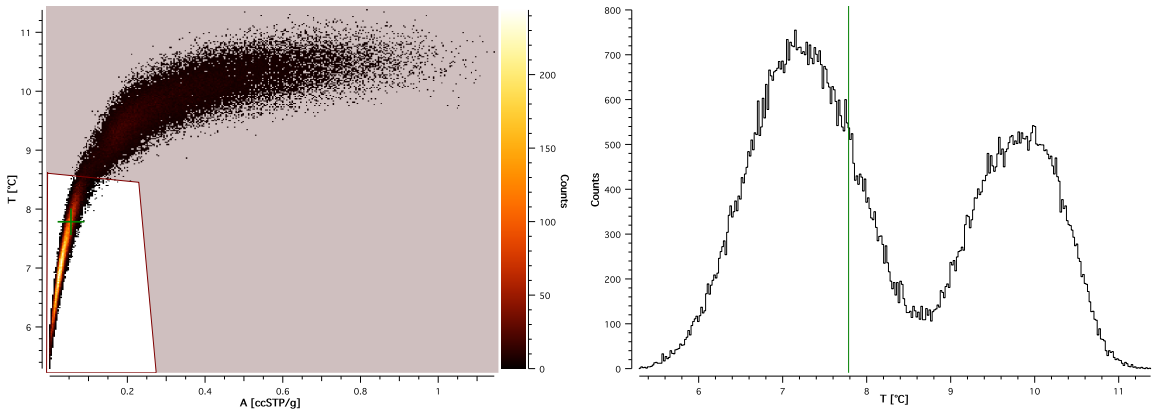

(a) (b)

Figure 6.1: (a) Monte Carlo results for sample GG26: Temperature over A_{CE} and the selected data masking (b) Temperature histogram, including the original fit for T, before masking was applied, clearly missing either of the most likely temperatures.

[submitted] in detail: they conclude the occurrence of extremely large $|F_{CE}|$ and extremely small A_{CE} to be a *limit case* of the UA model, where A_{UA} is replaced by $F_{CE} \cdot A_{CE}$, indicating a physically reasonable case of unfractionated excess air with complete bubble dissolution. Both groups were re-evaluated using *PANGA*'s *constrained mode*, which disallows large F_{CE} values. Such samples are marked accordingly in table C.12. As clearly visible in Fig. 6.2, the NGTs of these limit case samples calculated with the CE model are identical with the UA NGTs. Samples with low $^{20}Ne/^{4}He$ ratios on the other hand tend to result in warmer CE NGTs than the UA model calculates.

6.1.3 Groß-Gerau Region

As already indicated by the UA model fit, the CE model fitting results (see table C.12) reveal the occurrence of degassing for about half of the samples from the set: ΔNe values of the degassed samples range from −1 to −29 %, with an average of −11 %. At the same time, ΔNe values of excess air in the other half of the samples range from 1 to 27 %, averaging at 14 %. A seasonal occurrence of degassing, as found by Mayer [2017] in shallow groundwater, is not apparent in this case, as both degassing and excess air patterns show up during all sampling campaigns at Groß-Gerau. Seven of the excess air affected samples (GG11, GG11b, GG21b, GG26, GG33, GG34 and GG35) result in ambiguous Monte Carlo simulations, showing two possible recharge temperatures, as demonstrated for GG26 in Fig. 6.1. The chosen data masking (see Fig. B.26) leads to deviations from the initially fitted temperatures of up to 1.9°C. Samples GG04b and GG13 are fitted to reasonable recharge temperatures, (9.57 ± 3.53) °C and (9.17 ± 3.94) °C, respectively, but with very high uncertainties. Both samples show ΔNe below 1 % and

the NGTs of GG04 and GG04b are in good agreement. The occurrence of the high uncertainties is therefore expected to be an artifact of the fitting, as in both cases the Monte Carlo simulation creates few, but extremely unrealistic possible values for A_{CE}, as shown for both samples in Fig. B.24 (a) and (b).

The resulting noble gas temperatures for the entire sampling region average to 10.1℃, reasonably close to the present day MAAT of around 9℃ [DWD, 2017]. The maximum is at (14.8 ± 0.7) °C at site GG08, which also showed the highest water temperature of 15.9℃ during sampling (compare Fig. B.7). The minimum is found at GG25 with (4.2 ± 0.6) °C. As visible in Fig. B.6, samples with high amounts of ^{3}He tend towards lower NGTs. However, those samples were collected during the second campaign, in March 2013, after a cold winter (see Fig. A.11), while the first campaign was conducted in Autumn 2012, at the end of the summer – possibly reflecting a seasonal variation in recharge temperature[2] rather than a correlation of high amounts of ^{3}He and low NGTs.

6.1.4 Heidelberg Region

Fitting the noble gas samples of the Heidelberg area with the CE model results in the UA limit case (unfractionated excess air) for all samples except HD18 and HD19. The corresponding χ^2 values are very low, with high probabilities, as shown in table C.12. Samples from the upper Heidelberg aquifer show an average NGT of 11.4℃ the middle aquifer averages at 9.8℃. Since sampling of the region was completed in a single campaign within two weeks, no seasonal variation is found. None of the samples are affected by degassing, the observed ΔNe ranges for the entire set of samples from 0.2 to 25.5 %, averaging at 10.5 %.

The thermal well at Weinheim, sample MM, sourcing from 1050 m, behaves very differently and can, as with the UA model, not be reasonably described with the CE model either. The modeled NGT of the sample is, at (110.8 ± 0.3) °C, far off even from the production temperature of 60.5℃ of the well and hardy physically reasonable. The fit result is with a χ^2 of 5922 the least reliable of the entire data set. Additionally, the ΔNe of (-90.4 ± 0.6) % indicates strong degassing of the sample, which is not unexpected regarding the extreme amount of bubble formation during sampling (compare Fig. 4.3). This is also reflected in the extreme deviation of the A and B samples[3] analysed for the site, as shown in Table C.4. While ratios can be assumed to be somewhat unaffected by this, absolute gas concentrations are likely to be very unreliable, and the resulting NGT even more so (compare Fig. B.25).

[2] Mayer [2017] recorded variations in CE modeled NGTs of a single well (HD03 of this study) by about 2℃ spanning the different seasons.

[3] One of the samples had an extreme analytical error on the ^{3}He measurement, due to high overall helium gas amounts requiring splitting of the sample. This can lead to extremely small ^{3}He amounts left to be measured. The second sample, which was not affected as much by this as its absolute ^{4}He amount was below the splitting threshold, was chosen for further data analysis.

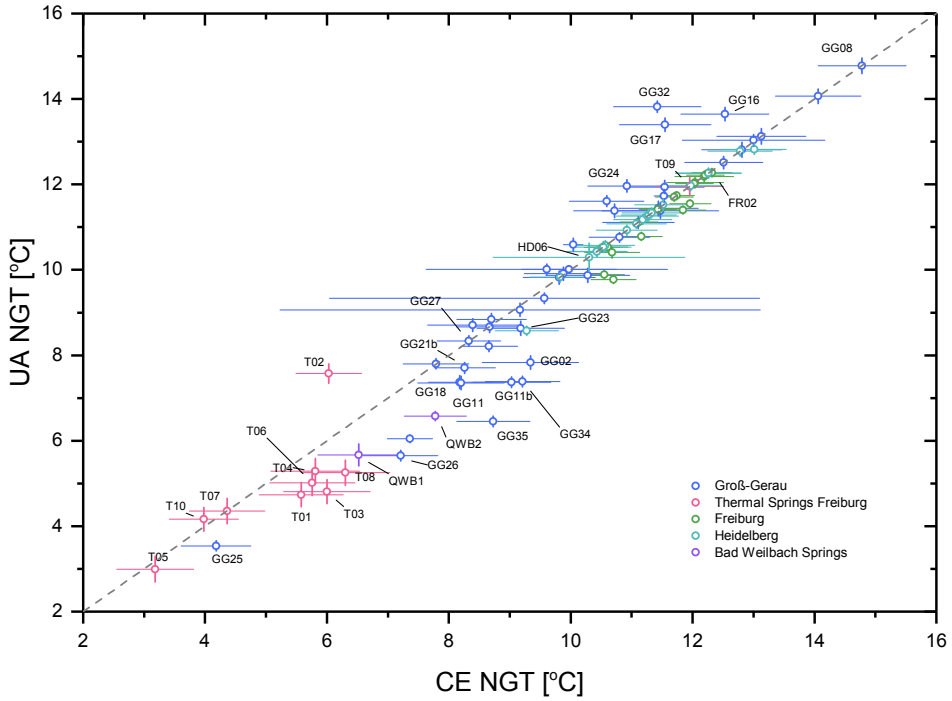

Figure 6.2: Noble gas temperatures calculated using the UA model, plotted over the NGTs modeled using the CE model, showing a deviation of CE NGTs for samples from the Groß-Gerau region and thermal wells, most of which have very low $^{20}Ne/^{4}He$ ratios.

6.1.5 Freiburg Region

The CE model delivers NGTs in the range of 10.5 to 12.3°C for the shallow groundwater samples from the Freiburg region, averaging at 11.5°C in good accordance with the present day MAAT. None of the samples exhibit any degassing, as ΔNe values range from 5.3 to 25.1 %.

When one accounts for the additional radiogenic ^{40}Ar most of the thermal wells exhibit, obvious from their high $^{40}Ar/^{36}Ar$ (see Fig. 6.7), by recalculating the elemental argon amount from the ^{36}Ar measurement, the thermal wells are fitted well by the CE model. The results have χ^2 values below 6.5 and high probabilities. The NGTs reflect very cold recharge temperatures, however, ranging between 3.2 to 6.3°C. Sample T09 is an exception, with a high NGT of (12.0 ± 0.6) °C. It is also the only sample with almost no excess air, while all other thermal wells show ΔNe values from 28.3 to 85.7 %.

6.2 Apparent Water Ages

6.2.1 ^{3}H-^{3}He-Dating

The ^{3}H concentrations found in the Groß-Gerau region (see table C.8) scatter between 1.87 to 11.55 TU, averaging at 5.9 TU. Compared with the closest precipitation input curve, based on GNIP data from Karlsruhe (1977 to 2012, see Fig. B.21) [IAEA/WMO, 2017], the range is in somewhat good agreement with recently formed water, however with some outliers towards very low values.

Samples from the upper aquifer in the Heidelberg region similarly range in between 3 to 10 TU, however, three outliers exist: wells HD01, HD02 and HD09 show much higher ^{3}H activities with 41 TU, 55 TU and 47 TU, respectively (see Fig. B.2). The Heidelberg region is the only area where several wells from different aquifers were accessible: HD06, HD08 and HD18 draw from the confined middle aquifer, with depths of 153 m, 205 m and 65 m, respectively. HD06 was measured to be ^{3}H-dead, while HD08 and HD18 have rather high concentrations of (11.79 ± 1.11) TU and (9.07 ± 1.07) TU, respectively.

Due to technical problems with of the proportional counters at the *IUP*, samples FR12 – FR15, FR17 and FR18 could so far not be analysed for tritium. The other analysed samples show ^{3}H activities consistent with recent precipitation, as shown for the region in the GNIP data from Weil am Rhein (Fig. B.22). Two exceptions exist: FR02 and FR16. Both sampling sites are located within less than 500 m of the Rhine river, and are analysed to have ^{3}H concentrations of (16.09 ± 1.10) TU and (18.03 ± 1.06) TU, respectively. Except for T09, none of the tritium samples of the thermal wells in the Freiburg region could be analysed so far. The expectation for such deep aquifers would be that they contain little to no tritium anyhow. Which is why the tritium value measured for T09, (6.36 ± 0.84) TU, is surprising and indicates contamination of some form, which will be discussed in chapter 7.

The ^{3}H-^{3}He dating is executed for all samples with existing ^{3}H analyses, as described in section 2.4.1, accounting for radiogenic helium by using the radiogenic endmember ratio of $R_c = 0.02\,R_a$. The resulting apparent ages are plotted in Fig. 6.3, against the inital ^{3}H activity in the sample, as calculated from measured ^{3}H concentration and $^3He_{tri}$, acquired from the separation of helium components given in section 2.4.1. This is set against the ^{3}H input curve for Stuttgart, based on GNIP data IAEA/WMO [2017], which is the longest running input curve available for the larger area. This plot allows for a validity check of the calculated ^{3}H-^{3}He ages, as the initial ^{3}H concentration must coincide with the measured input curve at the calculated age if the calculation was done correctly and based on valid assumptions about the ^{3}He composition.

While most samples from the Heidelberg and Freiburg regions produce a valid combination of ages and intitial ^{3}H, plotting well within the seasonal variation of the input curve, many of the samples from the Groß-Gerau region appear to have problematic ^{3}He compositions. Even though ^{3}H-^{3}He dating is limited to dates after the bomb peak (ca. 1960), as the initial natural ^{3}H background is too low [Roether, 1968],

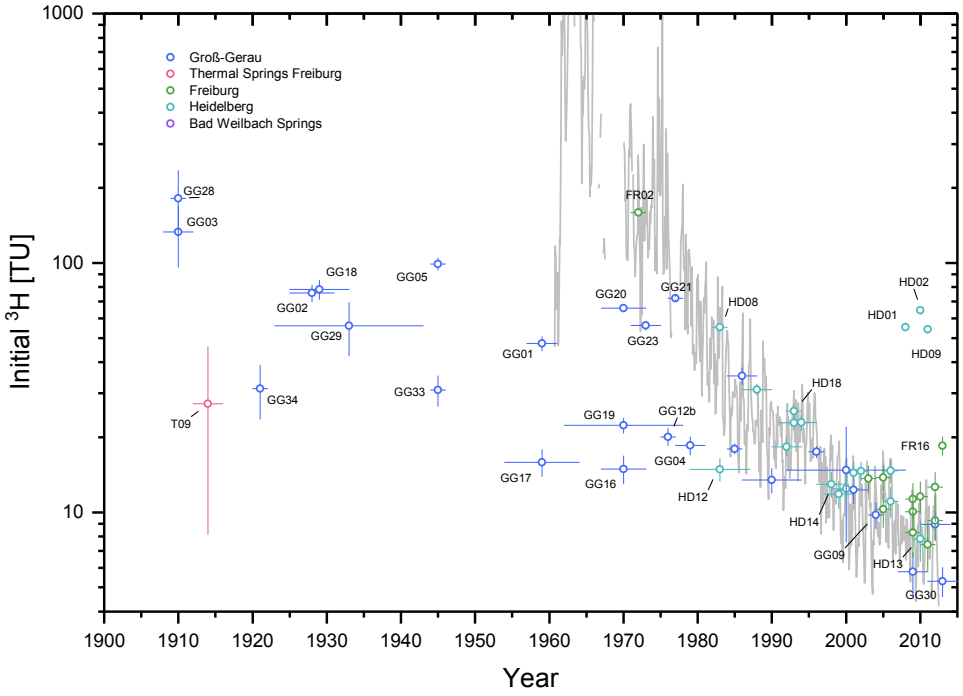

Figure 6.3: The sum of ^{3}H and calculated ^{3}He$_{tri}$ plotted logarithmically over the corrected ^{3}H-^{3}He dates, compared with the GNIP ^{3}H input function from Stuttgart [IAEA/WMO, 2017]. Note that samples older than 1960 exceed the reasonable age range of ^{3}H-^{3}He dating.

calculated recharge years up to 1900 are included in the plot, demonstrating how far off the resulting data for the Groß-Gerau samples is, while still omitting some samples that were calculated to even older dates or where the dating failed entirely, as the calculation of their tritiogenic helium component results in negative values (see table C.14). Most of those samples are clearly influenced by some form of mixing with old water, as visible in their high He/Ne ratios. The varying occurrence of degassing and excess air in the samples appears to be unrelated, as no clear correlation is found. For samples affected by complex helium compositions, a correction and recalculation has to be applied, which will be attempted in the following chapter.

6.2.2 Radiocarbon Analysis

A total of 15 samples were analysed for ^{14}C and δ^{13}C – the selection included the thermal wells (which are assumed to be ^{3}H-dead) and a few of the shallow groundwater wells, five from the Groß-Gerau region, one from the Heidelberg region, and the two Bad Weilbach springs. The modeling of the reservoir

effect was approached broadly using the models by Vogel [1967, 1970]; Pearson Jr. [1965]; Clark and Fritz [1997]; Fontes and Garnier [1979], the input data being used is summarized in table C.15 and the resulting corrections are used for dating with *OxCal* [Bronk Ramsey, 2009]. The calculated apparent ages (see table C.15) should only be taken as qualitative age information, not as definite residence times, as the modeling was done based on limited information. Additionally, independent of the reservoir effect correction, most samples appear to exceed the reasonable age range of ^{14}C groundwater dating, either by being too old, or too recent. Ages given in the following are the mean value of all resulting modeled ages, as there is no valid reason to prefer one model to another, given the limited information available. They are therefore rounded and the analytical error calculated by *OxCal* is omitted, as it is likely very much underestimated.

The shallow groundwater samples from the Groß-Gerau region (GG01, GG13, GG22, GG25 and GG26) represent a group of samples likely to be too young, as with most of the reservoir effect corrections, the resulting ^{14}C activities exceed the dating curve on the modern end – shallow groundwater is, as expected, dominated by recent precipitation, relative to the ^{14}C scale. Sample GG26 has with (55.30 ± 0.23) pmC the lowest ^{14}C activity, the apparent age is 4000 yr BP, while the other samples result in ages ranging from 200 to 2000 yr BP. The Heidelberg sample HD06, from the middle aquifer, is calculated to an age of 3300 yr BP. The samples QWB1 and QWB2 show very high ages, $> 30\,000$ yr BP and 21 000 yr BP, respectively, the former can be discarded as exceeding the reasonable limits of ^{14}C groundwater dating [Clark and Fritz, 1997]. Of the thermal wells from the Freiburg region, all but T09 exceed the dating range at calculated ages of $> 30\,000$ yr BP, while T02, dating at least with one reservoir effect correction below 30 000 yr BP may be somewhat younger than the other thermal well waters.

Both T02 and T09 deviate from the rest of the thermal wells in their δ^{13}C signature as well (see table C.15): while they are slightly lighter than the VPDB standard, the remaining thermal wells are isotopically enriched by 2 to 3 ‰, in extreme cases even more: T05 and T03 at 11.41 ‰ and 15.81 ‰, respectively. The Bad Weilbach springs also show a relatively strong enrichment of -2.77 and -0.80 In contrast the δ^{13}C signatures at Groß-Gerau are depleted at -10.61 to -15.12 ‰, while sample HD06 a little less so, at -8.41 ‰.

6.3 Noble Gas Isotopic Composition

6.3.1 ^{3}He/^{4}He Ratios

Measured helium concentrations deviate far from the equilibration concentrations, for both isotopes: Concentrations for ^{4}He go up to 10^{-4} cm^{3}STP/g and for ^{3}He up to 10^{-10} cm^{3}STP/g, spanning several orders of magnitude. As visible in Fig. 6.4, most samples deviating from atmospheric concentrations plot towards the crustal ratio line rather than the mantle ratio, but none is located close to the crustal

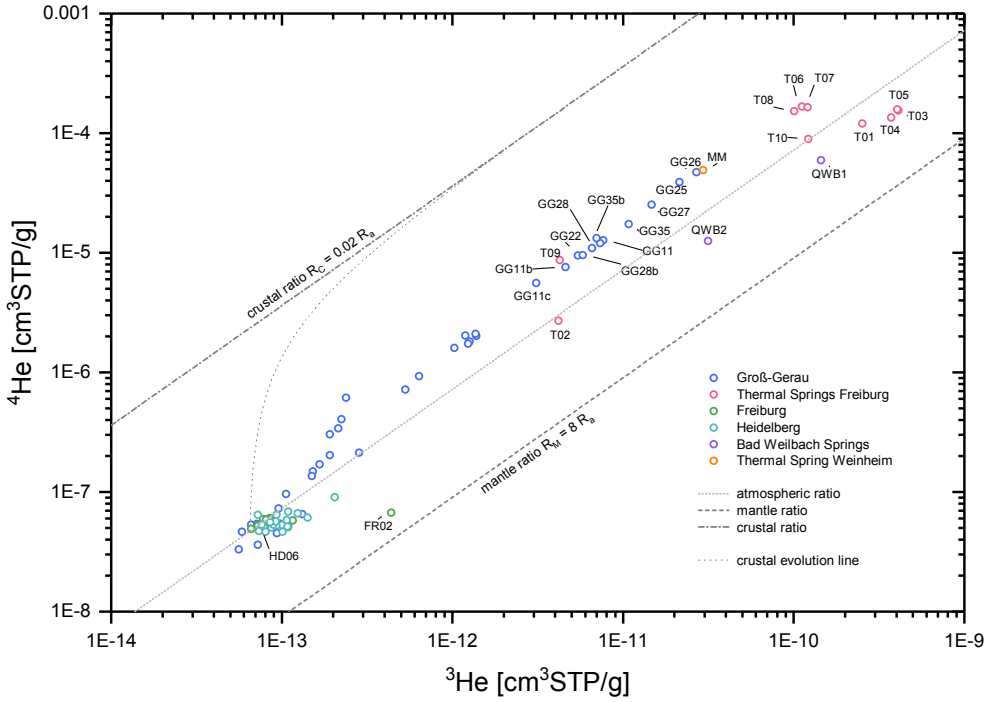

Figure 6.4: ^{3}He over ^{4}He for all analysed samples. The parallel lines indicate the ratios of the different reservoirs, atmosphere, crust and mantle. As it ages in a purely crustal dominated aquifer young groundwater will move along the indicated crustal evolution line.

evolution line, indicating three-component mixing rather than two-component mixing is affecting the gas composition. Helium ratios from all sampling regions are visualised, shown in in Fig. 6.5, using the three-isotope plot (see section 2.3.1), plotting the ^{3}He/^{4}He ratio[4] over the ^{20}Ne/^{4}He ratio. The following gives a short description of the data for each region and groups samples into clusters. The detailed discussion of which will follow in chapter 7.

The samples of the Groß-Gerau region form several clusters. A portion of the samples scatters close to atmospheric endmember of purely meteoric composition, showing a signature in ^{3}He/^{4}He and ^{20}Ne/^{4}He close to that of air equilibrated water, slightly offset towards higher ^{3}He/^{4}He ratios. This group (GG^{α}) consists of 11 samples[5]. Samples GG13 and GG19 scatter close-by, but at high ^{3}He/^{4}He ratios of nearly 1.5 R_a and ^{20}Ne/^{4}He ratios just below 3.0. The second group (GG^{β}) is formed by 6 samples[6], which scatter between ^{20}Ne/^{4}He ratios of 1.0 to 1.5 , with ^{3}He/^{4}He ratios of 0.28 to 0.68 R_a. A third cluster

[4]Corrected for tritiogenic ingrowth during sample storage, as described in section 5.1.4
[5]GG^{α}: GG06, GG07, GG08, GG09, GG10, GG14, GG15, GG15b, GG24, GG30 and GG31
[6]GG^{β}: GG04, GG04b, GG12, GG12b, GG23 and GG32

(GG^{γ}) is visible between $^{20}Ne/^{4}He$ ratios of 0.35 to 0.48 , made up from four samples[7] from the western side of the Rhine. Finally, there are 18 samples all with $^{20}Ne/^{4}He$ ratios below 0.21. As visible in the enlarged plot (Fig. 6.6), these also form distinct clusters: GG^{δ} consisting of seven samples[8] and the second GG^{ϵ}, with the lowest $^{20}Ne/^{4}He$ ratios of less than 0.03 containing ten samples[9]. For the discussion of the data, the groups are also marked in Fig. 7.1.

For most of the samples from the Heidelberg region, the noble gas composition is close to atmospheric air equilibrated water, with a shift toward higher $^{3}He/^{4}He$ ratios. Five samples with $^{20}Ne/^{4}He$ ratios below 3.5 are found: HD08, HD12, HD13, HD14 and HD18. Of these, only HD13 is close to the crustal mixing line, all others deviate towards higher than expected $^{3}He/^{4}He$ ratios.

The shallow groundwaters of the Freiburg area are, with the exception of FR02, entirely unremarkable concerning their isotopic helium composition. As seen in Fig. 6.5, all of the samples (excluding FR02 and FR09) have $^{20}Ne/^{4}He$ ratios of 3.6 and above, typical for recent meteoric waters. The $^{3}He/^{4}He$ ratios are accordingly scattering very close to $1\,R_a$, except for FR02, which has at $(4.73 \pm 0.17)\,R_a$ the highest $^{3}He/^{4}He$ ratio found in this study, at a $^{20}Ne/^{4}He$ ratio of 3.34 ± 0.04. Sample FR09 is with a $^{20}Ne/^{4}He$ ratio of $(3.37 \pm 0.04)\,R_a$ slightly moved to the left, along the mixing line between the atmospheric and crustal endmembers.

The springs of Bad Weilbach, located on the northwards continuation of the western main fault, about 15 km north of the Groß-Gerau region, show some of the highest $^{3}He/^{4}He$ ratios analysed in this study. QWB1 with $(1.772 \pm 0.028)\,R_a$ and QWB2 with $(1.828 \pm 0.028)\,R_a$ resemble helium signatures found in the thermal springs from the deep upper Muschelkalk aquifer in the southern Upper Rhine Graben.

All of the noble gas samples collected from the thermal wells and springs in the southern Upper Rhine Graben proved to be difficult to analyse, since the amount of CO_2 dissolved in the fluids is very high, up to 2950 mg/l in the Muschelkalk aquifer [He et al., 1999]. The high gas amounts possibly led to the loss of gas during sample preparation for mass spectrometry, since the surface of the SST cold trap for noble gas extraction and separation might not have been large enough – pressure above both the SST as well as the ACT trap remained higher than usual, even after manually prolonged freezing times. Reducing sample size by half did not improve the situation. The resulting data on absolute concentrations should therefore be interpreted as a lower limit rather than exact concentrations. However, a comparison of this study's data with those of Griesshaber et al. [1992] (see table C.2) shows that $^{3}He/^{4}He$ ratios found in this study agree quite well with their data, indicating that gas loss did not, if it occurred at all, lead to significant fractionation effects due to the differing freezing temperatures of the helium isotopes. While the absolute gas amounts might therefore be wrong, the ratio data can be expected to be trustworthy. However, the fact that the samples also could be fitted reasonably well applying the inverse modeling

[7] GG^{γ}: GG16, GG17, GG20 and GG21
[8] GG^{δ}: GG01, GG02, GG05, GG05b, GG18, GG29, GG34
[9] GG^{ϵ}: GG03, GG11, GG11b, GG22, GG25, GG26, GG27, GG28, GG35, GG35b

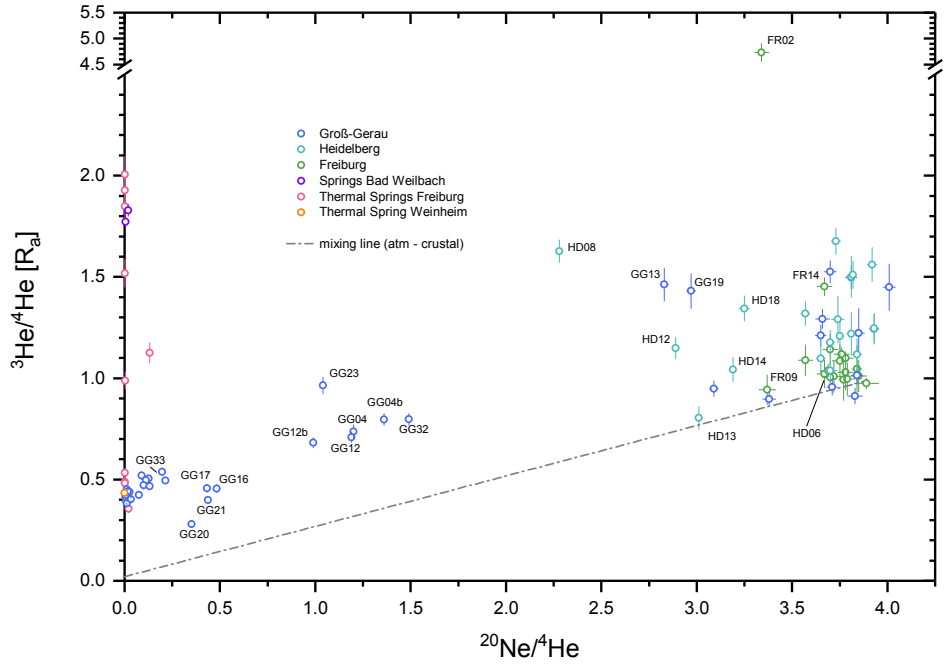

Figure 6.5: The $^3He/^4He$ ratio of all analysed samples, corrected only for tritiogenic ingrowth, plotted over the $^{20}Ne/^4He$ ratio.

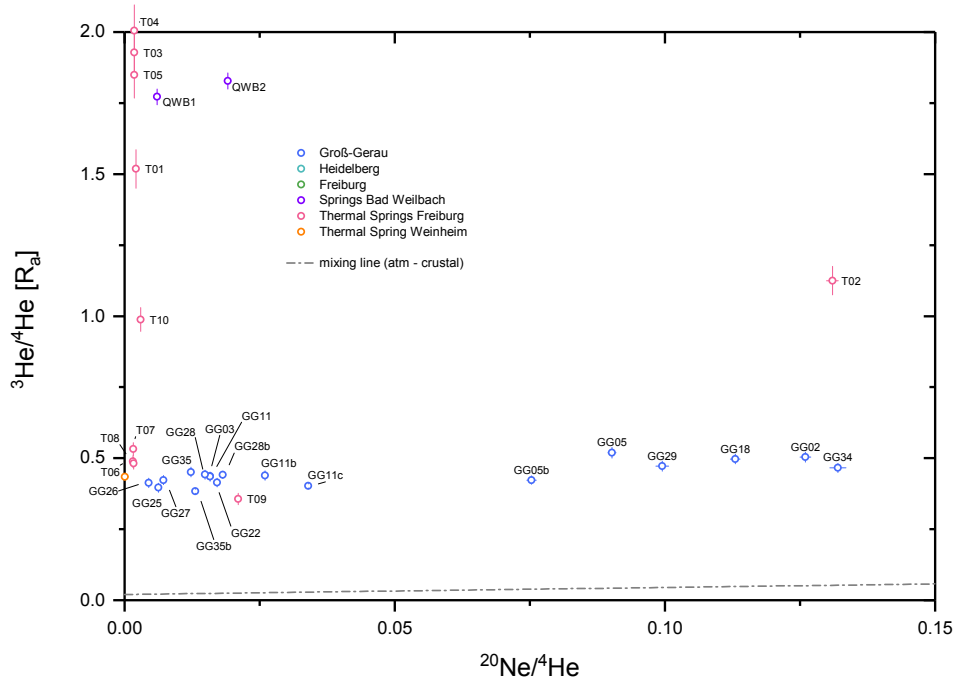

Figure 6.6: Enlargement of the above three isotope plot, focusing on the samples with $^{20}Ne/^4He$ ratios below 0.15.

in *PANGA* (low χ^2 values and analytical error on the modeled Temperature) supports that even the absolute amounts can not be far off, as gas loss would lead to an overestimation of NGTs, while the resulting NGTs are already very low.

The $^3He/^4He$ ratios of the thermal wells can be separated into distinct groups, matching their source aquifers. The highest ratios (1.52 to 2.00 R_a) are found in samples from the upper Muschelkalk (T01, T03, T04 and T05) while those from the Hauptrogenstein (T06, T07, T08) scatter much lower, around 0.5 R_a. T10, according to He et al. [1999] also sourcing in the Hauptrogenstein, is an outlier with $(0.99 \pm 0.04)\,R_a$. T02, another Hauptrogenstein water, has a similar $^3He/^4He$ signature, though is with a lot less ^4He characterised by much younger water. The Badenweiler spring, T09, sourcing the the crystalline bedrock, also shows much smaller amounts of ^4He and a $^3He/^4He$ ratio of only (0.36 ± 0.02)

The thermal well at Weinheim, only 15 km north of the Heidelberg, accessing water from a depth of 1050 m, proved to be similarly difficult to sample and analyse. While absolute concentrations may be far off for the sample, its noble gas ratios are found to be highly radiogenic, with a $^{20}Ne/^4He$ ratio of 5.8×10^{-5} and a $^3He/^4He$ ratio of $(0.43 \pm 0.01)\,R_a$.

6.3.2 Argon and Neon

Very few samples deviate from the atmospheric $^{40}Ar/^{36}Ar$ and $^{20}Ne/^{22}Ne$ ratios, as can be seen in Fig. 6.7. Mostly the deep sourcing waters are affected: The $^{40}Ar/^{36}Ar$ ratios of many of the thermal wells deviate significantly from the atmospheric ratio of 295.5 ± 0.5 [Nier, 1950; Steiger and Jäger, 1977]. Samples form distinct groups: the wells of Bad Krozingen from the upper Muschelkalk (T03, T04, T04) have the highest $^{40}Ar/^{36}Ar$ ratios, at about 342.5, while T01 from Mooswald has a ratio of 326.9 ± 4.1, close to the group formed just below by the remaining Hauptrogenstein samples (T06, T07, T08 and T07). Sample QWB1 shows a similar deviation, at a ratio of 317.3 ± 4.2. Samples T02 and T09 appear to have purely atmospheric $^{40}Ar/^{36}Ar$ ratios.

Of the shallow groundwaters, only HD14 with 312.6 ± 4.2 and GG31 with 279.4 ± 5.0 show significant deviation from the atmospheric value, all others scatter closely around it.

The deviation from the $^{20}Ne/^{22}Ne$ ratio is even less pronounced, given the uncertainty of the atmospheric ratio of 9.80 ± 0.08 [Porcelli et al., 2002], none of the samples deviate – however, as the data analysis is based on an air standard measurement, the observed trend represents a real deviation. Of the analysed samples, QWB1 plots at the highest $^{20}Ne/^{22}Ne$ ratio of 9.8762 ± 0.0083. The thermal wells with the highest $^{40}Ar/^{36}Ar$ ratios also tend to have somewhat increased $^{20}Ne/^{22}Ne$ ratios.

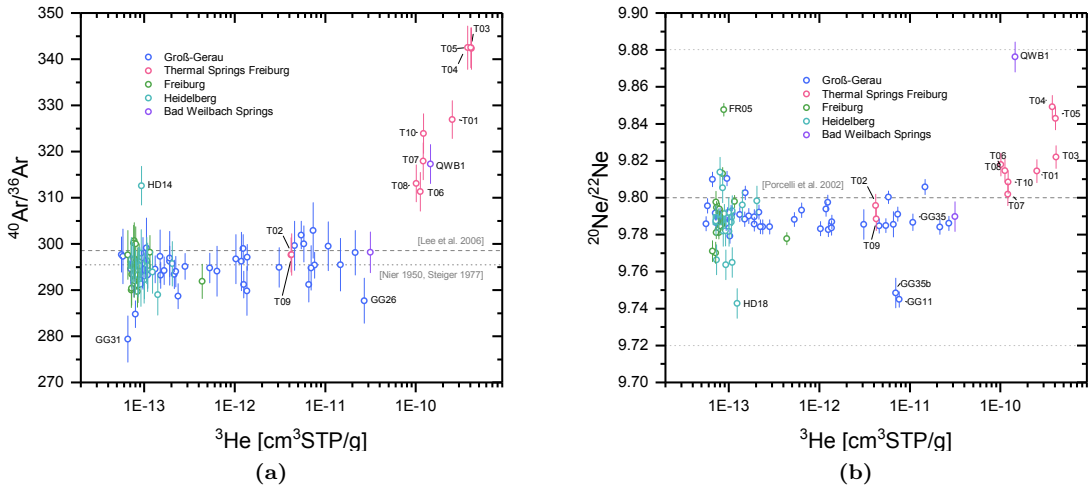

(a) (b)

Figure 6.7: (a) the $^{40}Ar/^{36}Ar$ ratio plotted over ^{3}He, with both atmospheric ratios, by Nier [1950]; Steiger and Jäger [1977] and by Lee et al. [2006] (b) $^{20}Ne/^{22}Ne$ ratio plotted over the ^{3}He, with the atmospheric ratio and its uncertainty (dotted lines) by Porcelli et al. [2002].

6.3.3 Radon

Radon activities (as shown in Fig. 6.8 and compiled in table C.8) in the Groß-Gerau region were measured during the first of three campaigns. The groundwater wells east of the Rhine river show very little variation and all range well below 4000 Bq/m³. Three outliers exist: the Sirona springs (GG16 and GG17) show radon activities beyond 20 000 Bq/m³, differing from one another by a few thousand Bq/m³ – a difference most likely caused by gas loss due to the sampling conditions rather than an actual signal, which allows for the possibility that not one but both springs' ^{222}Rn activities are underestimated. The southernmost groundwater well of the two sampled on the western side of the Rhine, GG20, is with (7721 ± 637) Bq/m³ somewhat different from the wells east of the Rhine, which do not exceed 4000 Bq/m³. The two springs QWB1 and QWB2 at Bad Weilbach show very different ^{222}Rn activities, at $(11\,145 \pm 741)$ Bq/m³ and (3355 ± 264) Bq/m³, respectively.

The ^{222}Rn activities of the Heidelberg wells are spread over a wider range than those of the Groß-Gerau region. But even though they source from two different aquifers, no systematic relationship is apparent, as wells from both the upper and lower aquifer scatter from 1000 to 5000 Bq/m³. A single well, HD12, is with $(11\,288 \pm 795)$ Bq/m³ above that range.

The groundwater of the Freiburg sampling area show a wide range of ^{222}Rn activities, from 5000 to 17 000 Bq/m³. The thermal springs of the region all have very low ^{222}Rn activities, with values as low as

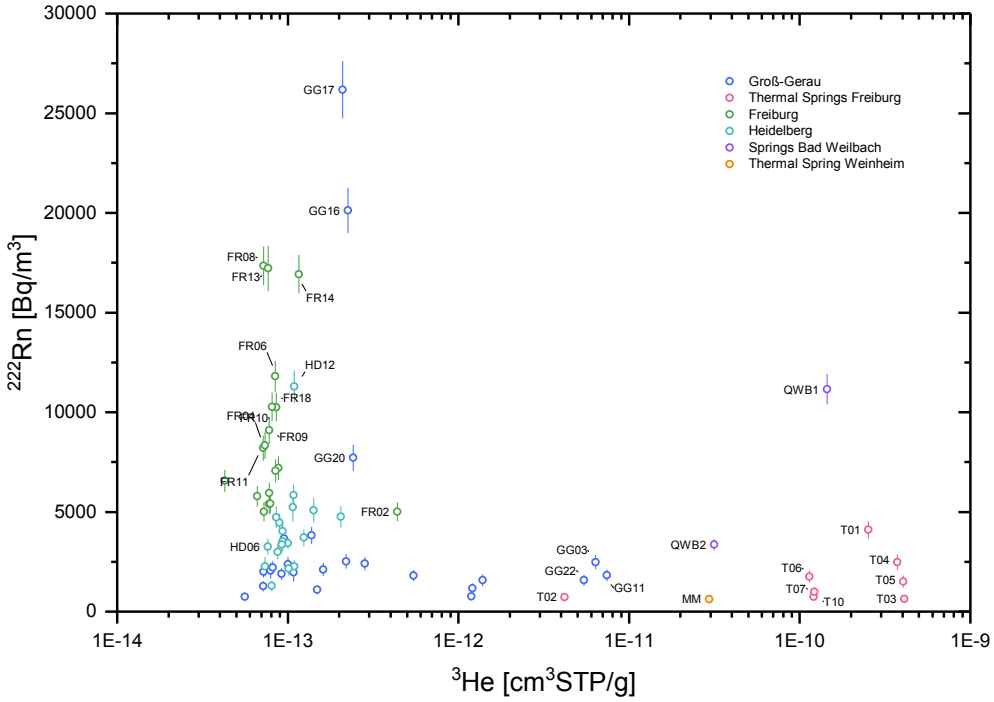

Figure 6.8: ^{222}Rn activities of all wells and springs sampled for radon, plotted against the corresponding ^{3}He concentrations.

(629 ± 190) Bq/m^3, some of the lowest found in the samples from this study. Data for T08 (measurement failure) and T09 (unsuitable sampling conditions) do not exist. Similarly, the sample from Weinheim's thermal spring shows, at (620 ± 158) Bq/m^3, very little ^{222}Rn activity. As all these wells and springs were affected by high dissolved gas amounts and bubble formation during sampling, these low ^{222}Rn readings are likely to be caused by loss of gas during sampling, as the ^{222}Rn sampling procedure is prone to gas loss in such cases. Since no gas phase measurement was done, a conclusion about the ^{222}Rn content of the well is not possible based on the data.

6.4 Stable Isotopes

Results of the stable isotope analysis are plotted in Fig. 6.9 and compiled in table C.8. Stable isotope data from the Groß-Gerau region scatter well within the combined local GNIP datasets [IAEA/WMO, 2017] as well as on the LMWL calculated as described in section 2.6.3. One obvious outlier exists: GG06 is with a δ^{18}O of -3.46 ± 0.04 and δ^{2}H of -34.78 ± 0.05 far distant from both the GMWL and the LMWL, heavier in δ^{18}O as all other samples from the region.

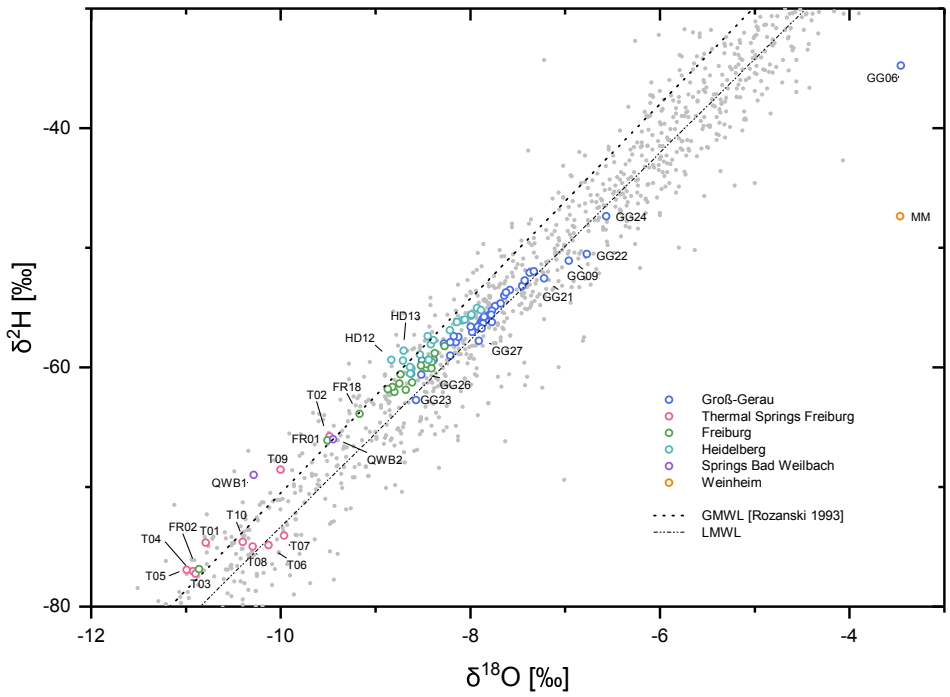

Figure 6.9: The δ^2H and δ^{18}O isotopic composition of all analysed water samples, plotted together with the GMWL [Rózański et al., 1993] and the LMWL calculated from local GNIP data [IAEA/WMO, 2017], which is also included as small grey dots.

Groundwater wells from the Freiburg region (see also Fig. B.13) show no deviation from the LMWL and scatter closely together, indicating no further influence beyond the normal hydrological cycle. Three outliers exist: FR02, the only sample from the second aquifer, a much lighter isotopic composition than all other Freiburg samples, while FR01 and FR18 only show a slight depletion. The thermal spring waters from the Freiburg area scatter at lighter isotopic compositions, below $\delta^2\mathrm{H} = -60\,‰$ and $\delta^{18}\mathrm{O} = -9\,‰$. Out of this group, samples T02 and T09 are the most enriched.

Stable isotope data from the groundwater wells in the Heidelberg region (see also Fig. B.12) show no deviation from the LMWL. A seasonal recharge signal is not apparent, as the data scatters around the precipitation weighted mean. The thermal well at Weinheim (MM) however has the second lightest δ^{18}O value observed in this study and plots far away from both the LMWL as well as the GMWL.

Chapter 7

Discussion

The following chapter interprets the datasets as presented in the previous chapter, with a focus on discerning possible indications of mantle-derived signatures. It will go into detail for each of the sampling regions separately and provide an improved ^{3}H-^{3}He dating based on the helium reservoir analysis discerned from the discussion of the data.

7.1 Groß-Gerau

The samples from the Groß-Gerau region very clearly indicate a mixing component with mantle-derived ^{3}He/^{4}He ratio, present in many of the shallow groundwater samples. For that reason, the results will be discussed mainly based on the grouping of the samples introduced in section 6.3.1, which is reproduced in Fig. 7.1 for better overview.

The first cluster, GG$^{\alpha}$, is interpreted as meteoric groundwater, affected in its helium composition only by atmospheric equilibration, excess air or degassing and tritiogenic ^{3}He, shifting the observed ^{3}He/^{4}He ratios from $1\,R_a$ upwards. While scattering at slightly lower ^{20}Ne/^{4}He ratios, the samples GG13 and GG19 are included into this group: while they do show relatively high ^{3}He/^{4}He ratios, their geographical position (see Fig. 3.2) makes it highly unlikely that they are affected by the upwelling of saline fluids [Siemon et al., 2001]. They are some of the most eastward situated sampling sites, far away from the main fault. Further, they are upstream the groundwater flow direction, relative to the fault. Based on their hydrogeochemistry, Al Najem [2016] also sees no connection of these samples to the saltwater upwelling occurring in the region.

On the other side of the plot, at extremely small ^{20}Ne/^{4}He ratios, scatter groups GG$^{\delta}$ and GG$^{\epsilon}$. This

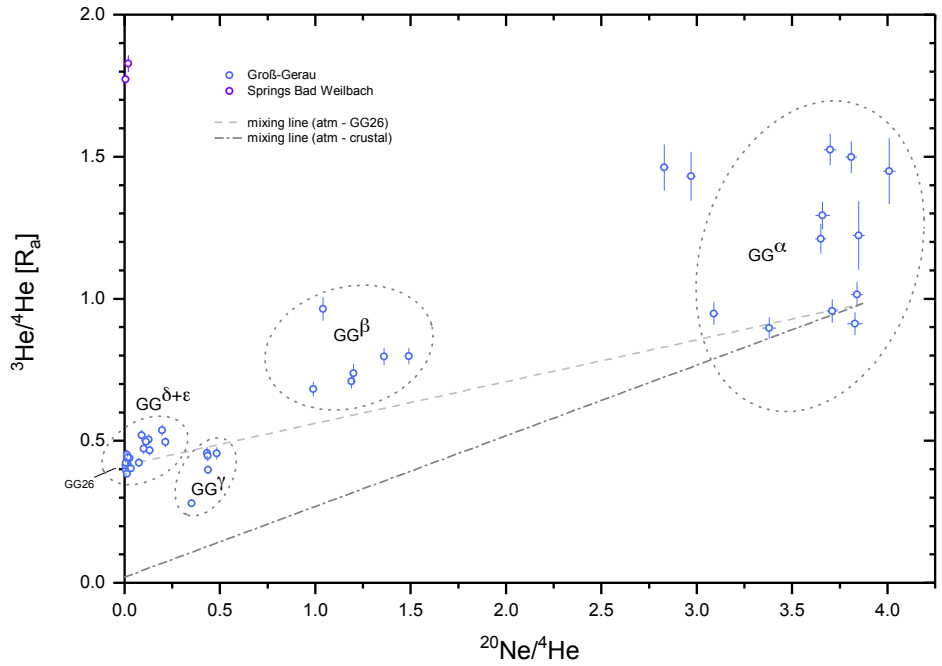

Figure 7.1: The ^{3}He/^{4}He ratio of all analysed samples, corrected only for tritiogenic ingrowth, plotted over the ^{20}Ne/^{4}He ratio, for the Groß-Gerau region, including the groups as defined in section 6.3.1 and a mixing line between the atmospheric endmember and sample GG26.

indicates a strong admixture of old water, unsurprisingly, as the occurrence of the saline water intrusion was the reason this region was chosen for this study. However, the ^{3}He/^{4}He ratios found for these samples clearly indicate a mantle-derived component rather than merely old crustal water containing radiogenic ^{4}He. The sample with the lowest ^{20}Ne/^{4}He ratio is GG26, at $(4.49 \pm 0.06) \times 10^{-3}$ and a ^{3}He/^{4}He ratio of $(0.41 \pm 0.02)\,\mathrm{R_a}$. This amounts to an absolute ^{3}He concentration in the sample of $(2.694 \pm 0.104) \times 10^{-11}$ cm^{3}STP/g, about three orders of magnitude higher than the equilibrium concentration and the highest ^{3}He concentration measured for all shallow groundwater samples in this study. At these concentrations, tritiogenic production of ^{3}He can not be a valid explanation, as it would require about double the initial activity of the bomb peak (compare Fig. 2.5) to produce these amounts of ^{3}He and a confined system to retain it. The origin beyond the Miocene sediments is also underlined by the strontium composition described by Schmidt et al. [2017c], who found the highest ^{87}Sr/^{86}Sr ratios in samples from group GG$^{\epsilon}$.

The water found at GG26 is a mixture of atmospheric and crustal water, which is likely diluted by a small mantle-derived fraction. Extrapolating the mixing line between the atmospheric endmember and GG26 to the y-axis (compare Fig. 2.4) determines the ^{3}He/^{4}He ratio of this mantle fraction to be

$(0.41 \pm 0.02)\,R_a$. This mixing line is plotted in Fig. 7.1, allowing for some interesting observations: all data from samples with $^{20}Ne/^{4}He$ ratios below 3.0 located east of the Rhine at Groß-Gerau (GG^{β}, $GG^{\delta}$and GG^{ϵ}) plot very close to or above this mixing line. The closer the sample is to the atmospheric endmember, i. e. the smaller the mantle-derived contribution to the water, the higher the samples tend to plot above the mixing line. This difference is attributed to the influence of ^{3}H decay, becoming more dominant in the $^{3}He/^{4}He$ as the mixing ratio of the water shifts towards being dominated by the atmospheric component.

The fact that most of the samples plot this well on and above the mixing line between air equilibrated water and sample GG26 supports the interpretation that all wells of the clusters GG^{β}, GG^{ϵ} and GG^{δ} are composed of varying dilutions of atmospheric water and the same mantle influenced endmember of the upwelling saline fluid. Therefore, this fluid needs to originate from greater depths than previously assumed based on the salinity alone [Schmitt, 1992; Holting, 1969].

Group GG^{γ} (GG16, GG17, GG20 and GG21) behaves differently, as all samples from the group scatter below the mixing line formed by GG26 and the atmospheric endmember. The samples of group GG^{γ} all originate from wells and spring located west of the Rhine (see Fig. 3.2), likely sourcing from the permian Rotliegend [Al Najem, 2016]. While definitely containing old water, as indicated by their $^{20}Ne/^{4}He$ ratios below 0.5, their $^{3}He/^{4}He$ ratios are relatively low. The Sirona spring samples GG16 and GG17 having a somewhat higher $^{3}He/^{4}He$ ratio of about $0.45\,R_a$, while the two groundwater monitoring wells, GG20 and GG21, show even lower ratios. Their calculated ^{3}H-^{3}He ages allow for further differentiation: both GG20 and GG21[1] plot reasonably close to the ^{3}H input curve in Fig. 6.3, GG20 (having the higher ^{3}He concentration despite a lower $^{3}He/^{4}He$ ratio than GG21) is slightly below it. In contrast, GG16 and GG17 end up at too little initial ^{3}H, falling far below the input curve. Sample GG17 is even being dated beyond the ^{3}H-^{3}He age range. While the origin of GG20 and GG21 pre-bomb water component remains unclear, it is very likely not carrying mantle-derived ^{3}He, or at least very small amounts, deviating from the endmember ratio found on the eastern side of the Rhine.

The Sirona springs GG16 and GG17 are indicated to have such a mixing component, even though they scatter slightly below the GG26 mixing line while showing some small amounts of tritium at the lower end of current precipitation concentrations [IAEA/WMO, 2017], GG16 at (5.36 ± 1.01) TU and GG17 at (3.13 ± 1.00) TU, suggesting that a tritiogenic helium component should have accumulated. Either the springs are affected by a mixing component with a slightly different radiogenic endmember, or the sampling conditions (see section 4.1.1) shifted the ratios, i. e. by diffusive fractionation during atmospheric contact[2]. Interestingly, the hydrochemical data for GG16 and GG17 by Al Najem [2016] does not support the hypothesis of a mixing component of a similar genesis as the saline fluid upwelling east of the Rhine.

[1] GG21 was not analysed for ^{3}H, while the helium measurement for GG21b failed. The ^{3}H-^{3}He age is calculated from the combination of both samplings, assuming the ^{3}H concentration remained relatively constant.

[2] To account for the possibility of a measurement error, the backup sample of GG17 was re-evaluated and found to scatter below the mixing line as well, at a $^{20}Ne/^{4}He$ ratio of 0.436 ± 0.004 and a $^{3}He/^{4}He$ ratio of $(0.45 \pm 0.02)\,R_a$, while the backup sample for GG16 is deemed atmospherically tainted, as argued in section 6.1.

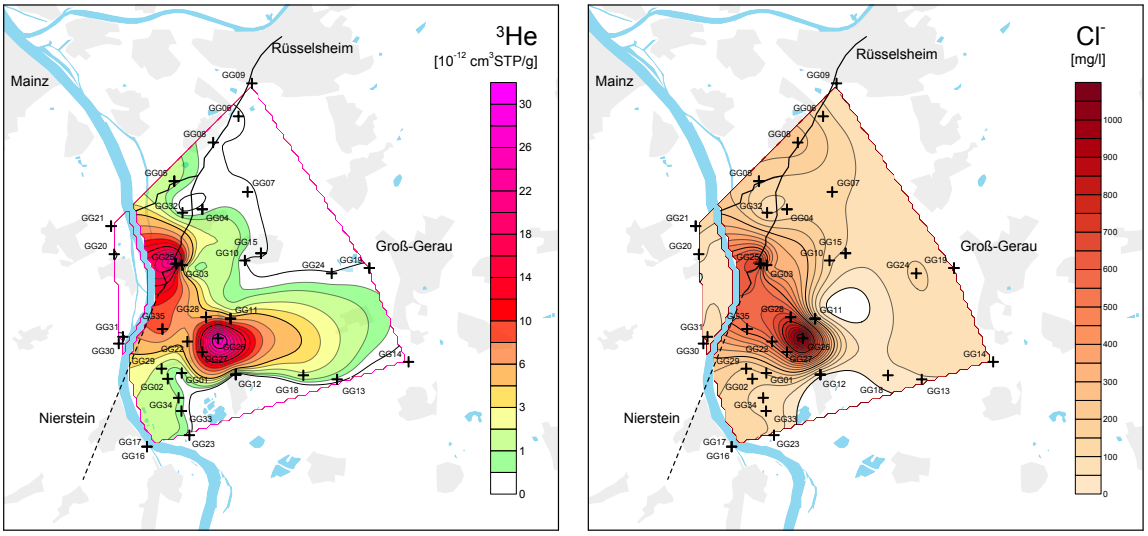

(a) **(b)**

Figure 7.2: Geographical plots of the ^{3}He concentrations in 10^{-12} cm^{3}STP/g (a) and concentrations of chloride ions, Cl^-, in mg/l as analysed by Al Najem [2016] (b) of the shallow groundwater in the Groß-Gerau region, compiled from all sampling campaigns. The data is interpolated, using a minimum curvature algorithm and the Rhine as a breakline, the striking of the western main fault is indicated by the dashed and solid line based on Schmitt and Steuer [1974b]. The color scale of the ^{3}He plot is chosen intentionally so that data in the range of purely atmospheric concentrations (around 6×10^{-14} cm^{3}STP/g) is plotted transparently. Compare Fig. A.2 for the resistivity data by Siemon et al. [2001].

While likely separated in their ^{3}He component origin, the samples GG16, GG17 and GG20 share a similarity in their ^{222}Rn activities. GG16 and GG17 show radon activities beyond 20 000 Bq/m^3, differing from one another by a few thousand Bq/m^3 – a difference very likely caused by gas loss due to the sampling conditions rather than an actual signal, which allows for the possibility that not one but both springs' ^{222}Rn activities are underestimated. The southernmost groundwater well on the western side of the Rhine, GG20, is with (7721 ± 637) Bq/m^3 slightly above the wells east of the Rhine. As visible in Fig. 3.2, these springs and wells are geologically located within the permian Rotliegend, which is likely the source for the high ^{222}Rn activities. The springs GG30 and GG31, located on the flanks of the Niersteiner Horst, are unaffected by radon as they source from meteoric runoff water (as also indicated by their very young apparent ^{3}H-^{3}He ages) with little contact to the underlying geology. For the well GG32, located east of the Rhine but also within the zone of the permian Rotliegend, no ^{222}Rn measurement exists. A connection of ^{222}Rn activities in the water and the fluid upwelling is unlikely, as none of the terrigenically imprinted waters east of the Rhine show any trend in their ^{222}Rn activity, compared to those unaffected by terrigenic helium.

In general, the samples from the region show no surprising behavior in their isotopic ^{2}H and ^{18}O composition, with the exception of GG06. It is with a δ^{18}O of -3.46 ± 0.04 and δ^{2}H of -34.78 ± 0.05 far distant from both the GMWL and the LMWL. Isotopically similar to deep fluid data from geothermal boreholes on the eastern and western main fault [Aquilina et al., 1997; Pauwels et al., 1993], as shown in Fig. 7.3, and geographically positioned right on top of the main fault line, this could suggest a imprint of geothermally altered fluid, enriched in δ^{18}O [Kato, 2000]. However, the well shows no other apparent indications supporting this, especially the ^{3}He/^{4}He and ^{20}Ne/^{4}He ratios are perfectly atmospheric for this sample. A closer look at the position of the GG06 well suggests a different, much simpler explanation: it is located about 150 m from a small lake, and with a depth of only 5.81 m might partially feed from lake water which is affected by evaporation. This can account for both the distance from the LMWL [Rózański et al., 1993] as well as the atmospheric ^{3}He/^{4}He ratio. A geothermal imprint is therefore highly unlikely. Direct confirmation via comparison with the lake water is not possible however, as surface waters were not sampled for this study. However, the ^{3}H-^{3}He analysis, dating to an apparent age of (0.6 ± 1.6) yr, supports the hypothesis of very recent meteoric surface water dominating the groundwater sample.

A linear fit of the stable isotope data from Groß-Gerau, excluding GG06 and the springs QWB1 and QWB2, results in

$$\delta^{2}\mathrm{H} = 6.34 \cdot \delta^{18}\mathrm{O} - 5.98\,‰ \tag{7.1}$$

with a negative deuterium excess (see Fig. B.14). This indicates that many of the samples show a slight increase of ^{18}O, not as obvious as GG06, but systematically enough to significantly shift the fit away from the LMWL. A small influence of hydrothermally altered water not noticeable in the isotopic composition of the individual samples might therefore be possible. A fit of data only from samples with ^{3}He concentrations higher than 10^{-12} cm^{3}STP/g results in a higher (yet still negative) deuterium excess ($-3.59\,‰$), while the occurrence of primordial ^{3}He as a mantle tracer would in theory suggest a decrease in deuterium excess by shifting the δ^{18}O [Kato, 2000]. As apparent from Fig. B.1, none of the Groß-Gerau samples with increased ^{3}He concentrations show a deviation from the LMWL by increased δ^{18}O values. An evaporation effect which affected the atmospheric component of the water mixture appears to be a more likely explanation for the shift from the LMWL, especially since the region is characterised by a multitude of small lakes and rivers (compare Fig. 3.2).

Following the first positive results of this study, as part of the TRACE project, Beck [2014] sampled and analysed the soil air at a few meters distance of several of this study's sampling sites. The aim of this sampling was to investigate wether the apparent mantle-signal in the groundwater can even be traced to the soil air of the unsaturated zone. However no deviation of the ^{3}He/^{4}He ratio was found. While the excess of helium found in the water should also affect the soil air by diffusion, it is very likely that aeration of the very thin unsaturated zone at the Groß-Gerau area (between 0.5 to 8 m, averaging at 2.6 m) dilutes the signal – if at all discernible against the high atmospheric background – too quickly, as Beck [2014] concludes.

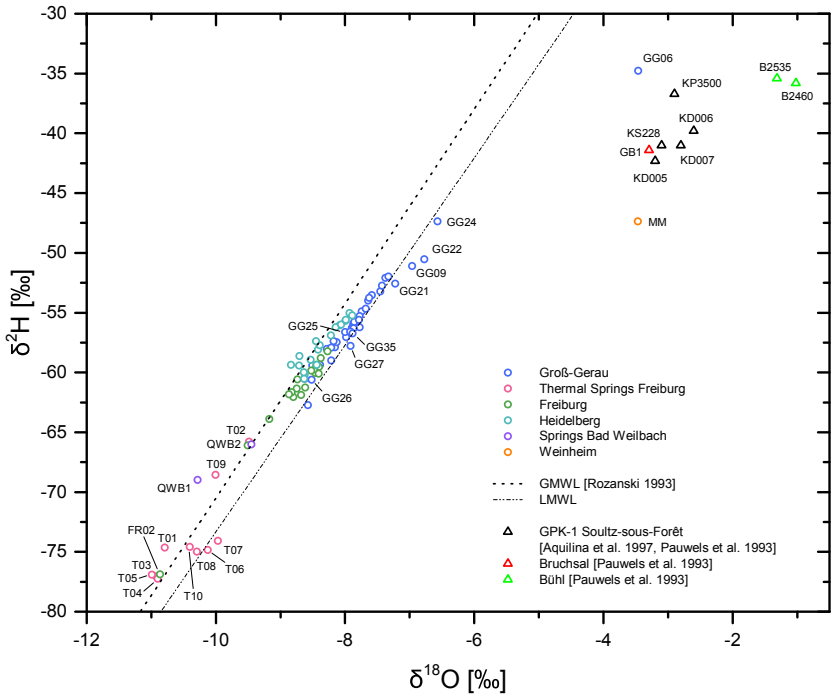

Figure 7.3: Complete stable isotope data analysed for this study. For comparison, data from different depths of the GPK-1 well at Soultz-sous-Forêt (western main fault) is included: KP3500 is from 3500 m depth at 165°C [Aquilina et al., 1997], KS228 was sampled at the wellhead, and KD005, KD006 and KD007 at 1810 m, 1845 m and 1930 m respectively [Pauwels et al., 1993]. Water from a borehole at Bühl (eastern main fault) is sampled from depths of 2460 m and 2535 m [Pauwels et al., 1993].

Analysis of the set of samples from the Groß-Gerau region showed the additional ^{3}H-^{3}He dating to be a useful tool to discern the possible nature of the ^{3}He compositions found in the groundwater. If apparent ages are of interest, however, the validity of the dating breaks down for those waters heavily affected by the mantle-derived mixing component, resulting in unreasonable apparent ages beyond the scale of the ^{3}H-^{3}He dating system. This is illustrated in Fig. 6.3, where the most affected samples from the Groß-Gerau region – if ages could be calculated at all – scatter far below the input curve. As this is mainly caused by a wrong estimation of the $^3He_{tri}$ component, once the radiogenic endmember affecting the samples' compositions is identified, a correction is possible, as is attempted in section 7.5.

7.2 Heidelberg

The groundwater samples from the Heidelberg region almost all result in reasonable apparent ^{3}H-^{3}He ages as visible from Fig. 6.3, ranging from 2 to 30 yr. The three outliers regarding the ^{3}H concentrations (HD01, HD02 and HD09, all above 40 TU) are all located in close proximity and downstream of turns of the Neckar river (see Fig. 3.6). This indicates that river infiltration is the likely source. The Neckar's average tritium activity in the sampling region is as shown in Fig. B.18, according to GNIR data, in the range of 67 TU [IAEA, 2017]. The high tritium activities of the river water are anthropogenic [LfU, 2003], likely by legal disposal of tritiated water of the nuclear power plant *Neckarwestheim*, about 95 km upstream of the sampling region.

As noted in section 6.3.1, only samples HD08, HD12, HD13, HD14 and HD18 deviate from atmospheric noble gas composition and require further discussion. Of these samples, HD12, HD13 and HD14 originate from the upper aquifer, while HD08 and HD18 source from the middle aquifer, as the unremarkable HD06 does.

The sampling site of HD13 is the only one located within the Odenwald, about 50 m of elevation higher than the other wells. This sample can be construed as a mixture of older, crustally characterised water (high amounts of accumulated radiogenic ^{4}He), with very recent recharge water accounting for the ^{3}H activity of (6.67 ± 0.97) TU. This is supported by its relatively shallow well depth of 26.4 m, its position directly within a recharge area and its extremely young ^{3}H-^{3}He age of (2.9 ± 1.2) yr. Schmidt et al. [2017b] found HD13 to have the highest ^{87}Sr/^{86}Sr ratio of the region, with $0.710\,165 \pm 0.000\,021$, and argue that it results from water-rock interaction with silicates from the granitic shallow aquifer. As apparent in this case, a crustal mixing component, free of mantle-derived ^{3}He$_{\text{ter}}$ and ^{3}H, does not disturb ^{3}H-^{3}He ages, as it dilutes both concentrations equally.

HD12 also shows an increased ^{87}Sr/^{86}Sr ratio according to Schmidt et al. [2017b], while its ^{3}He/^{4}He is well above that of HD13. Located right above the eastern main fault and at a well depth of 50.2 m, this could potentially indicate a mantle-derived water signature, however small at best, given the high ^{20}Ne/^{4}He ratio of HD12. As Fig. 6.3 reveals, sample HD12 is the only one from the region that is located below the input curve, indicating that two component mixing is affecting the ^{3}He composition of the water. It is therefore very likely, that a small fraction of the measured ^{3}He of the sample is not tritiogenic. Sample HD12 is also notable concerning its ^{222}Rn activity, which is at $(11\,288 \pm 795)$ Bq/m^{3} above the range of the other samples from the region. The well, located within the city centre of Heidelberg, right below the Gaisberg, is rather shallow. However, a well drilled close-by to the east to a depth of 998 m in 1918 found water with high radon contents [Mumm, 2000; Salomon-Calvi, 1927][3]. Given the depth difference, a direct connection along the main fault seems to be an unlikely explanation for the origin of the ^{222}Rn

[3] As the well collapsed only a short time after commissioning, it could unfortunately not be sampled for this study, nor was any data of further importance found.

in light of its short half-life combined with the likely small deep water mixing component. However, the aquifer rock might be the source of the radon in both cases, as the displacement of the main fault is very high. HD12 could already be sourcing from the outcropping of the bedrock of the graben shoulder, rather than the quaternary sediments, which is supported by the high $^{87}Sr/^{86}Sr$ ratios found by Schmidt et al. [2017b]. The other well likely sourcing from the granitic bedrock, as indicated by the $^{87}Sr/^{86}Sr$, is the previously discussed HD13, however sampling conditions did not allow for a reasonable ^{222}Rn sampling.

Sample HD14 is rather unremarkable, with a $^{20}Ne/^{4}He$ ratio of 3.190 ± 0.014 and a $^{3}He/^{4}He$ ratio of $(1.04 \pm 0.06)\,R_a$ slightly above the crustal mixing line. Which is why its $^{40}Ar/^{36}Ar$ ratio of 312.6 ± 4.2 is surprisingly high – in fact the highest ratio found in shallow groundwaters in this study, as shown in Fig 6.7. It is only surpassed by the deep thermal waters in the southern Upper Rhine Graben and one of the Weilheim springs. Given its low absolute amount of ^{3}He and the fact that the high $^{40}Ar/^{36}Ar$ stems from a low ^{36}Ar measurement rather than a high ^{40}Ar concentration relative to the other samples (compare table C.9), this is not interpreted as a signature of an old water component. An analytical error of the argon measurement could be the case, however a secondary evaluation of the B sample is not possible, as its analysis failed due to leakage.

The samples HD08 and HD18 both source in the middle aquifer, though at very different depths (compare table C.7). The water from the (at 204 m depth by about 140 m) deeper well HD08 shows a lot more radiogenic ^{4}He and a much higher $^{3}He/^{4}He$ ratio of $(1.63 \pm 0.05)\,R_a$ than HD18 at $(1.34 \pm 0.06)\,R_a$. A terrigenic ^{3}He component is likely in both cases, based on the ratios, the depth and the data from wells of the same aquifer close-by [Friedrich, 2007]. A graphical extrapolation of the possible mantle endmember, by plotting a line through both samples and the atmospheric endmember (compare Fig. 2.4), results in a terrigenic endmember larger than $2.5\,R_a$, which is unrealistic given the available data for deep thermal waters in the Upper Rhine Graben found by this study and others [Friedrich, 2007; Griesshaber et al., 1992; Hooker et al., 1985]. Additionally, both samples' ^{3}H-^{3}He ages match the input curve (see Fig. 6.3) quite well, favouring a tritiogenic origin of the high $^{3}He/^{4}He$ ratios. As both wells contain significant amounts of ^{3}H, HD08 at (11.79 ± 1.11) TU and HD18 at (9.07 ± 1.07) TU, and the high $^{20}Ne/^{4}He$ ratio suggest very little mixture of pre-bomb water, a possible mantle-derived helium signal could be masked by the strong tritiogenic signal.

The third sample from the middle aquifer, HD06 from a depth of 153 m, is the only ^{3}H-dead sample of the region and shows absolutely no influence of tritiogenic ^{3}He nor any kind of unusual terrigenic signature in its $^{3}He/^{4}He$. It is also the sample farthest to the west, at the greatest distance to the eastern main fault.

7.3 Freiburg

In the search for mantle-derived signatures, most of the data analysed from the Freiburg region is easily discarded: the measured $^3He/^4He$ ratios, in combination with the $^{20}Ne/^4He$ ratios as seen in the three-isotope plot in Fig. 6.5 identify almost all samples as meteoric waters, without any trace of admixture of neither old crustal nor old mantle-derived components. This is also apparent from the ^3H-^3He dating, as all but one sample result in consistent apparent ages, indicating no influence on the ^3He budget of the shallow aquifer other than ^3H decay. However, two samples have to be discussed further.

The first, sample FR02, sourcing from a depth of 170 m, shows by far the highest $^3He/^4He$ ratio found in this study with $(4.73 \pm 0.17)\,R_a$. A mixing component of mantle-derived helium would also include high amounts of ^4He, which is not the case for FR02 at a $^{20}Ne/^4He$ ratio of 3.34 ± 0.04. The origin of the high ratio is therefore likely to be tritiogenic. This is also indicated by the higher than usual ^3H concentration of the sample, of (16.09 ± 1.10) TU. The geographical location of the well – only 2 km downstream of the nuclear power station at *Fessenheim* – might suggest the notion that the nuclear power plant might be the cause of the high $^3He/^4He$ ratio, by infiltrating highly tritiated water into the ground. According to a government report, a ^3H activity of about 60 TU was found in 2011 in a monitoring well on the power station's grounds [Landtag BW, 2011]. No information on the depth of said well is available, nor on other releases of tritiated water by the plant into the groundwater. The sample also shows a very high salinity, with an $EC_{\kappa 25}$ of 19.9 mS/cm. Al Najem [2016] identifies the source of the salinity, based on the rare earth composition, as the Fessenheim sedimentation basin (compare Fig. 3.5), not the Weinstetter Diapir located below the sampling site. While this demonstrates that groundwater transport from the Fessenheim site towards FR02 is occurring, Fig. 6.3 illustrates that the calculated ^3H-^3He age and the sum of ^3H and $^3He_{tri}$ is very much consistent with the ^3H input function. Therefore, the origin of the high $^3He/^4He$ ratio can reasonably assumed to be entirely attributed to bomb-peak input, by tritiogenic production from water of an apparent recharge age of about 40 yr, in a confined aquifer, unrelated to any kind of releases of ^3H by the Fessenheim power plant.

The stable isotope composition of FR02, sourcing from the second aquifer, the Breisgau Formation (compare Fig. 3.4) is, while scattering close to the GMWL, very much depleted compared to the groundwaters from the shallow aquifer and resembles the composition of the thermal wells of the region. The second sample accessing the Breisgau Formation, FR14, is unremarkable however, indicating that the deviation in isotopic composition is not necessarily typical for the deeper aquifer. Also somewhat lighter in isotopic composition is FR01, a well from the upper aquifer, which is affected by river infiltration [Al Najem, 2016]. The cause of the light isotopic signature of FR02 therefore remains unclear, as a connection to the thermal waters can be eliminated based on the helium composition. Overall, the samples from the Freiburg region are slightly on the isotopically more depleted side compared to the GNIP precipitation data from the close-by Weil am Rhein (about 30 km), indicating an autumn/winter recharge.

A second sample exhibiting a higher than usual ^{3}H concentration is FR16, at (18.03 ± 1.06) TU, but is, in contrast to FR02, unremarkable in its ^{3}He/^{4}He signature. This well shares similarities with the previously discussed high-^{3}H wells at Heidelberg: it is located at a distance of less than 500 m of the Rhine river, and is calculated to have a ^{3}H-^{3}He age of only (0.5 ± 0.5) yr, failing the consistency check given by Fig. 6.3. The combination of atmospheric ^{3}He and ^{3}H above present day precipitation indicates that river infiltration might affect the sampling site FR16 (compare Fig. B.19 for ^{3}H activities of the Rhine river, measured close-by). River water, while containing relatively high amounts of ^{3}H, is an open system for helium, losing the tritiogenic ^{3}He to the atmosphere. This is supported by the data of Al Najem [2016], who finds FR01 and FR16 to be affected by Rhine river water infiltration. It is also apparent in Fig. 6.3, where FR16 plots well above the input curve, indicating a ^{3}H source beyond that of natural precipitation.

Sample FR05 shows a deviation in the ^{20}Ne/^{22}Ne ratio, however none of the other noble gases nor the ^{40}Ar/^{36}Ar show any indication for the sample to deviate from atmospheric composition. The observed deviation is therefore taken to be a measurement inaccuracy.

The observed wide ranging ^{222}Rn activities of the region show a geographical dependency, as seen in Fig. B.10. Samples close to the northeast of the region show the highest activities, while samples closer to the Rhine show the lowest. Most likely, this may represent an influence of the local geology affecting the direct input of ^{222}Rn from the aquifer matrix. The samples with the highest ^{222}Rn activities (FR06, FR08, FR10, FR13, FR14 and FR18) also show an overlap with those samples identified by Al Najem [2016] to show imprints of the crystalline (FR6, FR7, FR10, FR13 und FR18).

7.4 Thermal Wells and Springs

7.4.1 Bad Weilbach Springs

At ^{3}He/^{4}He ratios of $(1.772 \pm 0.028)\,R_a$ and $(1.828 \pm 0.028)\,R_a$, respectively, the Bad Weilbach springs QWB1 and QWB2 clearly are composed of a mixture of old and meteoric water, but are differentiated by distinct mixing ratios. While their ^{3}He/^{4}He ratios do not differ much, the ^{20}Ne/^{4}He ratios suggest that the amount of old, ^{4}He enriched water is greater in QWB1. This is supported by several indicators: the apparent ^{14}C age is beyond the dating range for QWB1 while just at the upper limit for QWB2. QWB1 also shows the largest deviation of the ^{20}Ne/^{22}Ne as well as a large deviation from the atmospheric value of the ^{40}Ar/^{36}Ar (see Fig. 6.7), both indicators of highly aged waters [Lippmann et al., 2003] or MORB signatures [Aeschbach-Hertig et al., 1996; Moreira and Kurz, 2013]. The latter is hardly the case though, as apparent from Fig. B.3, where the ^{40}Ar/^{36}Ar and ^{20}Ne/^{22}Ne data is plotted including an atmospheric-MORB mixing line. In the sample from QWB2, those ratios are perfectly within the atmospheric range.

QWB1 is the only sample in the study where a high radon activity of $(11\,145 \pm 741)\,\mathrm{Bq/m^3}$ conclusively coincides with a high mantle-derived ^{3}He concentration, while the second, QWB2 shows little deviation from the eastern groundwater wells, even though it features a higher $^3\mathrm{He}/^4\mathrm{He}$ than QWB1 and also quite high absolute ^{3}He concentrations. This suggest that the occurrence of high ^{222}Rn and mantle helium in QWB1 may be coincidental. In regard to ^{3}H concentration, QWB1 shows a higher value of $(14.10 \pm 1.09)\,\mathrm{TU}$ than QWB2 at $(9.27 \pm 0.98)\,\mathrm{TU}$, both are dated to unreasonable $^3\mathrm{H}$-$^3\mathrm{He}$ ages beyond 100 yr, unsurprisingly, given their high amount of terrigenic ^{3}He. Based on this data, it is likely that the Bad Weilbach springs feed from the same mantle-influenced reservoir, while their mixing ratios with meteoric surface water differ. This conclusion is also supported by the rare earth element analysis of Al Najem [2016].

7.4.2 Weinheim Thermal Well

Neither tritium measurements nor a ^{14}C analysis for the deep thermal well MM at Weinheim exist. However, due to the low $^{20}\mathrm{Ne}/^4\mathrm{He}$ ratio found, it is unlikely that tritiogenic ^{3}He has had much influence on the $^3\mathrm{He}/^4\mathrm{He}$ composition of the water. The measured ratio is therefore assumed to be the endmember ratio of the mantle-derived fluid produced from the well.

The sample MM from the Weinheim well shows an extremely light δ^{18}O value relative to the LMWL (see Fig. 7.3). Geothermal alteration of the stable isotope compositions is a likely candidate for this deviation of the deep water from the LMWL, supported by the similar composition of samples from geothermal wells located in the Upper Rhine Graben [Aquilina et al., 1997; Pauwels et al., 1993]. Since the production temperature of 60.5℃ at 1050 m depth is not sufficient to cause geothermal alteration, as temperatures above 100℃ are required [Clark and Fritz, 1997; Kato, 2000], an upward flow of water from even greater depth and temperature is indicated by the data.

7.4.3 Thermal Wells of the Freiburg Region

The composition of the thermal well samples is well constrained by their source aquifers, as already indicated in the previous chapter, though even more so by the sampling sites themselves. Samples from each well group scatter closely, not surprisingly given the relatively similar filtration depths of the well groups To3, To4 and To5 (Bad Krozingen) and To6, To7 and To8 (Bad Bellingen), as listed in table C.5).

The high $^{40}\mathrm{Ar}/^{36}\mathrm{Ar}$ ratios of the wells with high ^{3}He concentrations can be explained by the accumulation of radiogenic ^{40}Ar [Lippmann et al., 2003], indicating that the samples affected by this are far beyond the range of the ^{14}C dating, or at least have a mixing component of much higher age. This is not an unreasonable assumption, as He et al. [1999] found the Hauptrogenstein waters to contain a fossil seawater

component, which Al Najem [2016] confirmed. As the marine connections of the Upper Rhine Graben were cut off during Chattian times [Schumacher, 2002], this allows to date the seawater component to at least 23 Myr. For the waters from the upper Muschelkalk, with even higher $^{40}Ar/^{36}Ar$ ratios, Al Najem [2016] rules out a marine component and characterises them as chemically not as evolved as the Hauptrogenstein waters. However, for the terrigenic noble gas components, the Muschelkalk aquifer's geological setting at greater depth than the Hauptrogenstein aquifer allows for an estimation of even higher ages, based on the amount of radiogenic ^{40}Ar. While the observed $^{40}Ar/^{36}Ar$ ratios deviate from the atmospheric ratio, relative to MORB ratios of approximately 30 000 as given by Moreira and Kurz [2013], the deviation is small. No relation to the mixing line between atmosphere and MORB ratio can be discerned, as is visible in Fig. B.3, where the $^{40}Ar/^{36}Ar$ ratio is plotted over the $^{20}Ne/^{22}Ne$ ratio, another possible tracer system for geothermal imprints. The deviation of the thermal well waters from the atmospheric $^{20}Ne/^{22}Ne$ ratio is minimal however, as seen in Fig. 6.7.

Two samples (T02 and T09) behave very different from the other thermal wells. Both are characterised by higher $^{20}Ne/^{4}He$ ratios, an indication of admixture of younger water and both have lower production temperatures than the other thermal wells. They both share a more depleted $\delta^{13}C$ isotopic composition, compared to the massively enriched thermal wells (see table C.15), and their stable isotope composition is closer to that of the analysed groundwater samples than to the isotopic composition of the other thermal wells. The ^{3}H analysis of T09 shows with (6.36 ± 0.84) TU an amount that would be in accordance with recent precipitation, while the ^{14}C dating results in an apparent age of approximately 14 000 yr BP. This leads to the conclusion that T09 (Badenweiler) has an influx of young meteoric water[4]. A similar argument based on the stable isotope composition and $^{20}Ne/^{4}He$ ratio, which is supported by the chemical composition of the water [Al Najem, 2016], can be made for sample T02 (Mooswald TB3), which according to He et al. [1999] accesses the Hauptrogenstein aquifer. However, no ^{3}H analysis was done so far, and the ^{14}C date is beyond the reasonable range.

The thermal spring waters all scatter at lighter isotopic composition, which might be a result of higher infiltration altitudes of the feeding aquifers and/or colder temperatures at the time of recharge. No indication of geothermal alteration, as would be indicative of a water component from greater depth and high temperature [Kato, 2000], is found. However, the likelihood of colder recharge temperatures is supported by the resulting NGTs, which, for all thermal wells unaffected by meteoric water mixing, deviate far from the present day MAAT [DWD, 2017] (compare table C.12). The average CE NGT of the thermal wells, excluding T02 and T09, is 5.1 ± 0.7°C, which is in good agreement with the data for pre-Holocene water from central Europe [Stute and Deák, 1989].

[4]Additionally, the sampling conditions were far from ideal for dissolved gas sampling as described in section 4.1.3, however, this conclusion is mainly based on tracers likely to be unaffected by this.

7.5 Recalculation of the ^{3}H-^{3}He Dating

The deviation of calculated apparent ^{3}H-^{3}He ages from the ^{3}H input curve allows to improve the identification of terrigenic ^{3}He imprints as shown in the sections above. However, in order to acquire valid ^{3}H-^{3}He ages the different terrigenic source ratios need to be identified. As shown in section 2.4.1, the component separation of helium uses equation 2.37 to estimate the amount of radiogenic ^{3}He affecting the sample's helium composition:

$$^3\mathrm{He}_{\mathrm{tri}} = {}^3\mathrm{He}_{\mathrm{sample}} - {}^3\mathrm{He}_{\mathrm{eq}} - {}^3\mathrm{He}_{\mathrm{exc}} - \left({}^4\mathrm{He}_{\mathrm{ter}} \cdot \mathrm{R}_{\mathrm{ter}}\right) \tag{7.2}$$

For systems without mantle-derived helium components, a good estimation of the radiogenic component is achieved by using the ^{3}He/^{4}He ratio of the crustal endmember $\mathrm{R}_{\mathrm{rad}} = \mathrm{R}_{\mathrm{c}} = 0.02\,\mathrm{R}_{\mathrm{a}}$. As seen in Fig. 6.3, many of the samples from this study are heavily affected by mantle-derived helium, which would lead to an overestimation of ^{3}H-^{3}He ages. Using graphical extrapolation (compare Fig. 2.4) or directly measured ratios for samples with very small ^{20}Ne/^{4}He ratios, a determination of each mixing system's terrigenic endmember ratio is therefore attempted, to correct the resulting ages.

For the Groß-Gerau region, the endmember ratio estimation has been discussed in section 7.1. All samples of the groups GG$^\beta$, GG$^\epsilon$ and GG$^\delta$ are recalculated using $\mathrm{R}_{\mathrm{ter}}^{\mathrm{GG}} = (0.41 \pm 0.02)\,\mathrm{R}_{\mathrm{a}}$. As the origin of the ^{3}He/^{4}He signal in the Sirona springs GG16 and GG17 remains unclear, they are re-evaluated separately with a ratio acquired from a graphical extrapolation of the two samples in the three-isotope plot, resulting in $\mathrm{R}_{\mathrm{ter}}^{\mathrm{Sir}} = (0.38 \pm 0.03)\,\mathrm{R}_{\mathrm{a}}$. The terrigenic endmember of the mixing system of the Bad Weilbach springs' reservoir was estimated to be about $(1.77 \pm 0.03)\,\mathrm{R}_{\mathrm{a}}$, using the ^{3}He/^{4}He ratio of QWB1, as it is less affected by the meteoric mixing component. That endmember differentiates the reservoir feeding the springs from the reservoir accounting for the mantle-derived helium in the Groß-Gerau region. This could indicate that the fault's permeability might be much higher at Bad Weilbach, allowing for greater transport rates of helium causing the fluid that forms the crustal mixing component to carry a stronger mantle imprint.

Friedrich [2007] calculates the terrigenic endmember $\mathrm{R}_{\mathrm{ter}}$ for a sample from 153 m depth, found about 40 km north of the Heidelberg region, by ignoring the tritiogenic component as the sample in question is ^{3}H-dead, to a value of $\mathrm{R}_{\mathrm{ter}} = (0.346 \pm 0.033)\,\mathrm{R}_{\mathrm{a}}$. A more reasonable assumption of an endmember ratio $\mathrm{R}_{\mathrm{ter}}$ for the Heidelberg area is chosen to be sample MM, the 1050 m deep thermal well at Weinheim. At only 15 km distance from the sampling area, it is more likely than the sample found by Friedrich [2007] to represent the deep water mixing component assumed to affect the Heidelberg groundwater. Given its very low ^{20}Ne/^{4}He ratio of 5.8×10^{-5}, the measured ^{3}He/^{4}He ratio of $(0.43 \pm 0.01)\,\mathrm{R}_{\mathrm{a}}$ is used directly for $\mathrm{R}_{\mathrm{ter}}^{\mathrm{HD}}$. As discussed in section 7.2, only sample HD12 from the Heidelberg area shows a probable terrigenic mixing component. For comparison, samples HD08 and HD18, more likely dominated by tritiogenic than terrigenic ^{3}He, are also treated with the ratio.

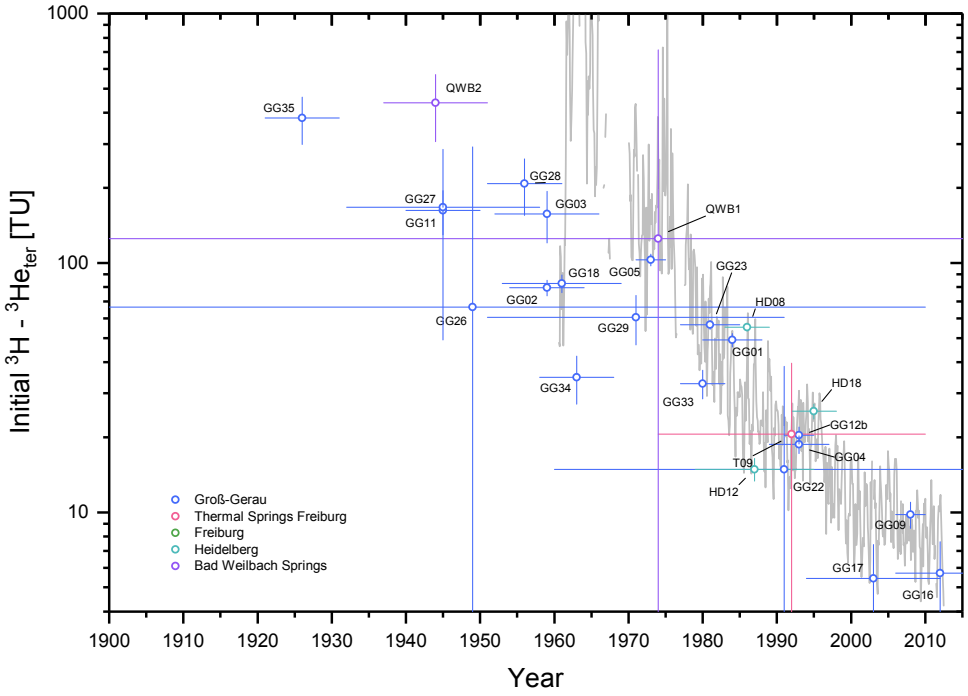

Figure 7.4: The sum of ^{3}H and ^{3}He$_{tri}$ minus the estimated terrigenic component, plotted logarithmically over the ^{3}H-^{3}He dates corrected with the respective R_{rad} ratios selected for the samples. Note that samples younger than 1960 exceed the reasonable dating range of ^{3}H-^{3}He dating. GNIP input function from Stuttgart from IAEA/WMO [2017].

Based on the observed ^{3}He/^{4}He ratios and overall noble gas composition of the shallow groundwaters of the Freiburg region, a recalculation of the ^{3}H-^{3}He dating is not required, (compare also Fig. 6.3). For the thermal well sample T09, a ratio of $R_{ter}^{T09} = (0.35 \pm 0.02)\, R_a$ is chosen.

The resulting recalculated ^{3}H-^{3}He ages are listed in table C.14 and plotted against the ^{3}H input curve from Stuttgart [IAEA/WMO, 2017] in Fig. 7.4. Overall, the re-evaluation leads to a much improved overlap of some of the less affected samples with the input curve, though at the cost of increased uncertainty. The stronger the mantle-derived water component, the larger is the uncertainty. This is most apparent for the samples GG26 and QWB1. They now scatter within the range of the plot, but show entirely unusable uncertainties. For samples characterised by a large mantle-derived mixing component, reliable ^{3}H-^{3}He dating (of the younger, meteoric component) can not be achieved, as it is essentially meaningless, even using the correction for the terrigenic ^{3}He. However, for samples with smaller mantle-derived components, the correction appears to deliver reasonable apparent ages, e. g. GG01, GG04 and GG05 – which, with the correction applied, produce apparent ^{3}H-^{3}He ages consistent with the input curve, to be interpreted

as the apparent age of the young mixing component. The failure of the correction at high amounts of terrigenic ^{3}He is also apparent in Fig. B.9, where the conservative and the corrected ^{3}H-^{3}He ages are plotted against the absolute ^{3}He concentration. The correction works reasonably well for the thermal water sample T09, giving its young mixing component an age of (20.9 ± 15.8) yr, which is a definite improvement over the previously calculated and unrealistic (98.5 ± 2.3) yr.

The Sirona springs, GG16 and GG17, result in ages of (1.1 ± 2.8) yr and (9.8 ± 4.1) yr, respectively, indicating an extremely recent mixing component or an over-correction, even with the slightly lower R_{rad} chosen for the samples. Similarly inconclusive remain samples HD08 and HD18, which are suspected to be of purely tritiogenic composition. The applied correction factor for the Heidelberg region does not distance them significantly from the input curve, making a conclusion whether the correction is unjustified or not impossible. For sample HD12, though, the correction does improve the consistency of the dating, allowing to support the conclusion that HD12 very likely shows a small but discernible amount of mantle-derived helium.

7.6 Mantle Fraction Estimation

Even though the graphical determination of the radiogenic endmembers R_{rad} for the regions already give a good estimate of the mantle helium fraction found in the most affected samples (e. g. about 5 % at Groß-Gerau), the calculation presented in section 2.3.1 is executed. Both the equation from Mamyrin and Tolstikhin [1984] as well as equation 2.24 from Kaudse [2014] are used. The second approach is adapted for the tritiogenic component estimation, using the selected radiogenic endmembers. The results are shown in table C.13. Unsurprisingly, the approach by Mamyrin and Tolstikhin [1984], neglecting the possibility of tritiogenic ^{3}He, grossly overestimated the mantle fractions for the shallow groundwaters, while the estimations agree well for the old, crustally dominated waters.

Samples from the Groß-Gerau region show, calculated with the correction for tritiogenic ^{3}He, mantle helium fractions of up to (5.3 ± 0.2) %, while those at the Freiburg region are calculated to have no relative mantle fraction in their helium budget. The calculation estimates all three of the wells from Heidelberg discussed above, HD08, HD12 and HD18, to have a small amount of mantle-derived helium, with (1.6 ± 0.8) %, (0.9 ± 0.8) % and (0.3 ± 0.9) %, respectively. However, based on the discussion of the data of these wells in the sections above and the high relative uncertainty of the calculated fractions, the existence of a mantle-derived component at the Heidelberg area remains inconclusive. Based on the combination of noble gas and tritium data, HD12 remains as the most likely sample to contain at least a small fraction of terrigenic helium.

Chapter 8

Conclusion

The successful application of helium as a tracer for mantle-derived fluids in shallow groundwater could be shown, even in areas that are not actively volcanic, as the data from the Groß-Gerau region proves. There, the easily accessible, unconfined aquifer is affected by a deep sourcing, mantle-derived fluid in several locations, as illustrated in Fig. 7.2. Some locations, where the groundwater draws up to 5 % of its ^{4}He concentration and 99 % of its ^{3}He concentration from the mantle reservoir, were identified.

The separation of terrigenic helium from tritiogenic helium is possible even for samples containing very little of the admixed mantle-influenced water by determining the original ^{3}He/^{4}He ratio of the mantle-derived mixing component. In turn, validating the consistency of the ^{3}H-^{3}He dating can be used as a way to verify the assumed endmember ratio of the local, mantle-influenced reservoir, which was applied in the correction for terrigenic ^{3}He, required for such groundwater mixtures.

In the Groß-Gerau region, applying the presented helium isotope analysis allows to discard the previously assumed Miocene sediments as the source of origin of the upwelling saline water [Schmitt, 1992; Holting, 1969]. Combining the noble gas data with the hydrogeochemical analysis by Al Najem [2016] and the ^{87}Sr/^{86}Sr isotopic composition analysed by Schmidt et al. [2017c], the uprising fluid is concluded to have a connection to deep mantle-derived fluids. Based on the data of this study, the prospection risk for geothermal energy production at the Groß-Gerau area is assumed to be low, as the data indicates the existence of fluid migration along permeable pathways at great depth. The intended goal of the TRACE project – the establishment of a small scale tracer suite able to reduce areas of geothermal exploration interest is therefore achieved.

The failure of the geothermal drilling project at the Groß-Gerau region in 2016, for lack of acceptable amounts of fluid [ÜWG, 2016], is a setback. However, the placement of the borehole was independent of the data from this study. The drilling site is situated more than 4 km outside the area of the high

mantle-derived helium amounts that this study identified in the shallow groundwater. Therefore, the developed method to identify possible permeable fault zones remains valid. However, the pathways might be spatially narrow, as is also indicated by the relatively small areas of mantle-derived imprint in the shallow aquifer, as apparent in Fig. 7.2.

The tracers applied in this study are shown to be of different importance – while the key tracer system is obviously the helium isotopic composition, the application of ^{3}H-^{3}He dating is a valuable tool to differentiate the helium data. The remaining tracers, ^{14}C, δ^{13}C, ^{222}Rn and stable isotopes play a lesser role in identifying mantle imprints. They are, however, very helpful to understand certain scenarios and allow for a much more detailed analysis when the noble gas data requires further differentiation.

The applied set of tracers is able to identify fault permeability by the detection of mantle-signatures in shallow waters, provided the sedimentary aquitards are locally permeable, allowing for signal migration upwards to the unconfined aquifer. This was not the case in the Freiburg region, where no mantle-derived fluid component could be found in the upper aquifer. Even though aquifers at great depth, feeding the thermal wells of the region, show high mantle-derived helium fractions of up to 26.9 %, the aquitards of the Quaternary sediments are likely to be impermeable, preventing any signal from reaching the surface.

The situation in the Heidelberg region is likely similar: only a single sample of the uppermost aquifer, HD12, could be shown to possibly have an imprint of mantle-derived helium, however small. Two samples, both from the middle aquifer, remain inconclusive regarding their helium composition.

The analysis of ^{3}He/^{4}He ratios in shallow aquifers, combined with the other tracers presented in this study and in Al Najem [2016], is shown to be a valid tool for locating permeable fault zones located at great depth. Given the aquitards of the shallow groundwater system are locally permeable, allowing for vertical migration of the signal, access to readily available shallow groundwater monitoring wells is sufficient for a successful application of the method.

Appendix A

Figures

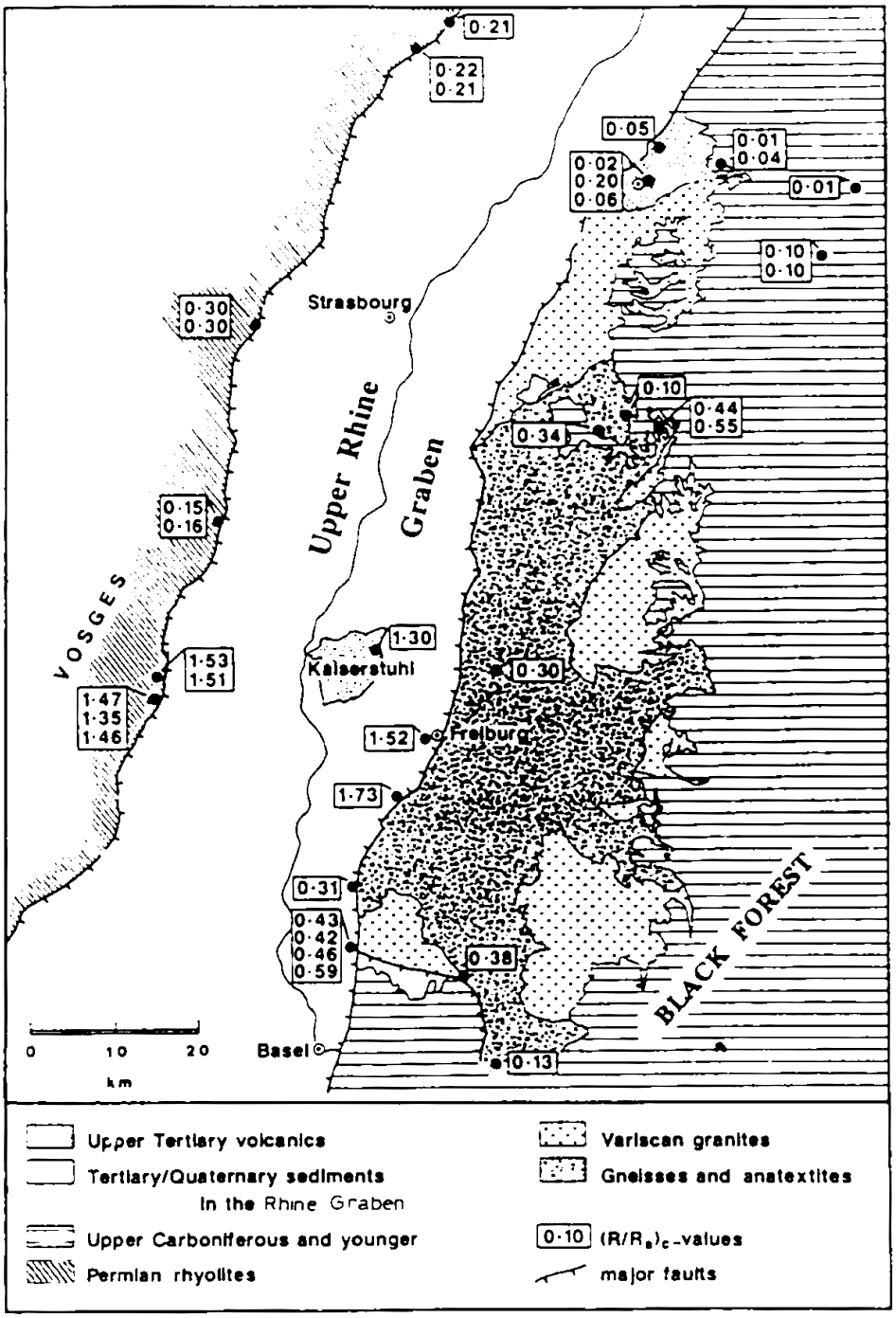

Figure A.1: Data of deep aquifer $^3He/^4He$ ratios given in R_a in the Upper Rhine Graben from Griesshaber et al. [1992], note that the ratios are likely calculated with $R_a = 1.4 \times 10^{-6}$.

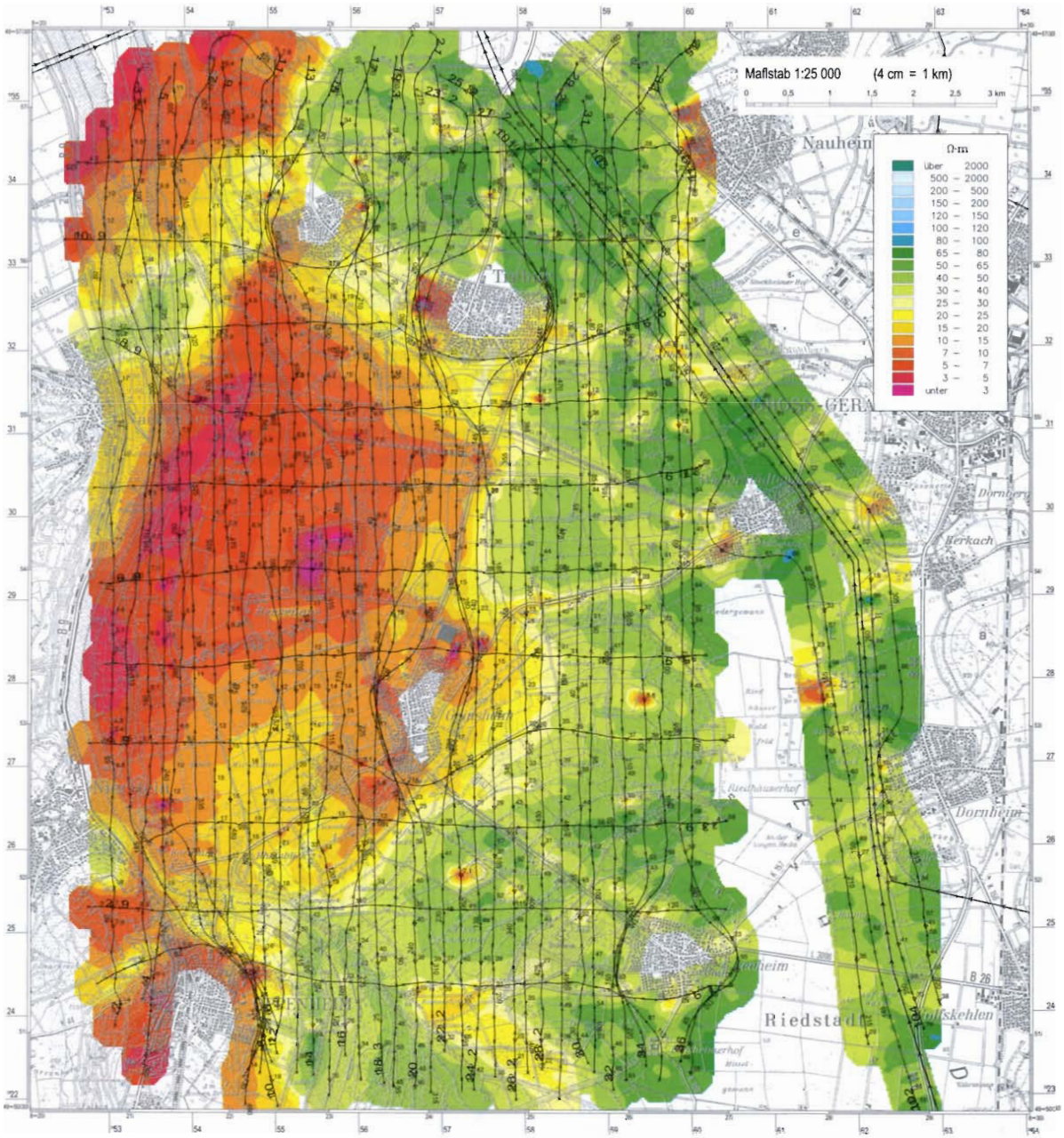

Figure A.2: The results of Siemon et al. [2001] airborne electrical conductivity study, showing the apparent resistivity of the upper, unconfined aquifer, indicating an upwelling of saline water.

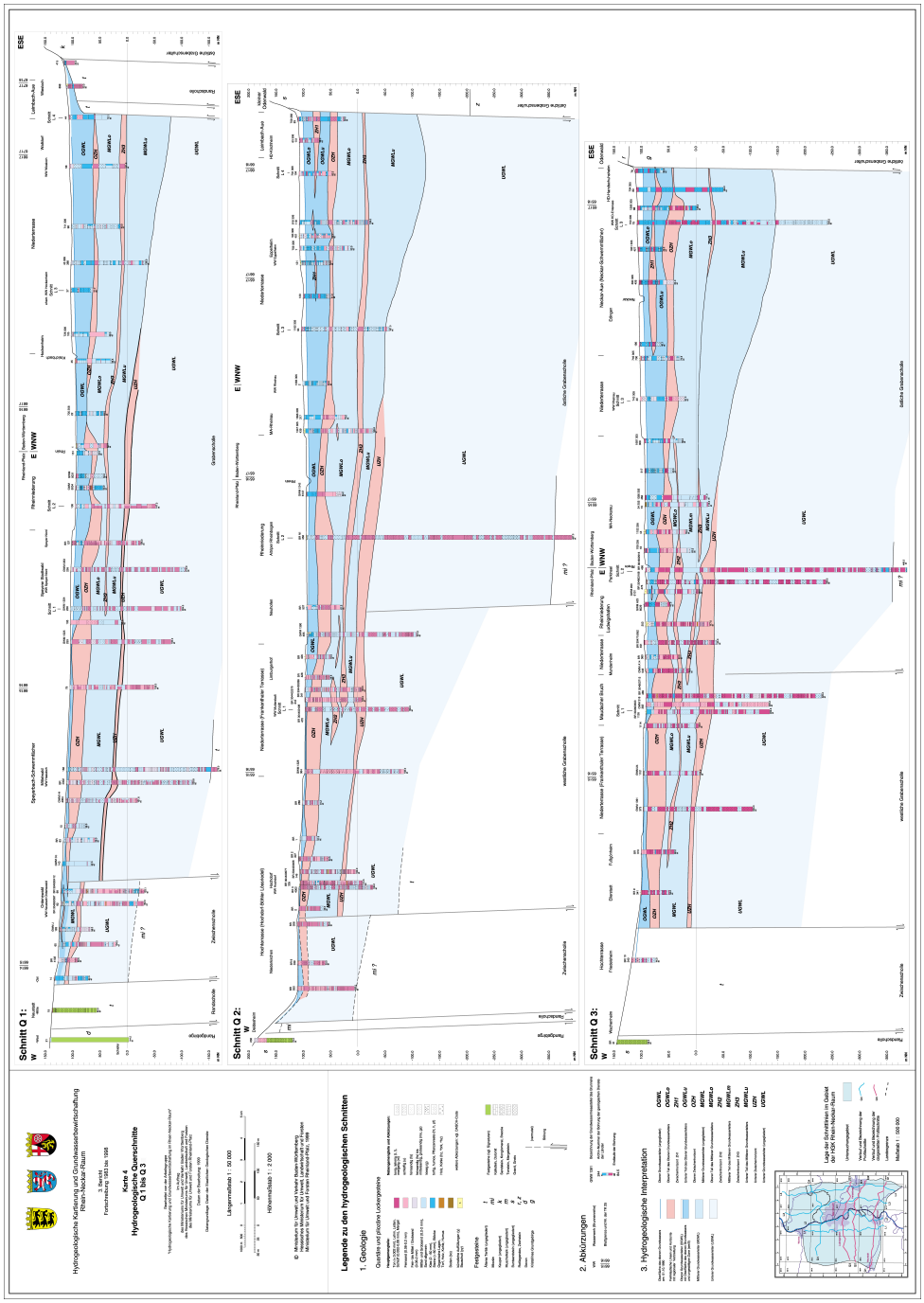

Figure A.3: Geological cross-sections of the Upper Rhine Graben in the Heidelberg area [LUBW, 1999].

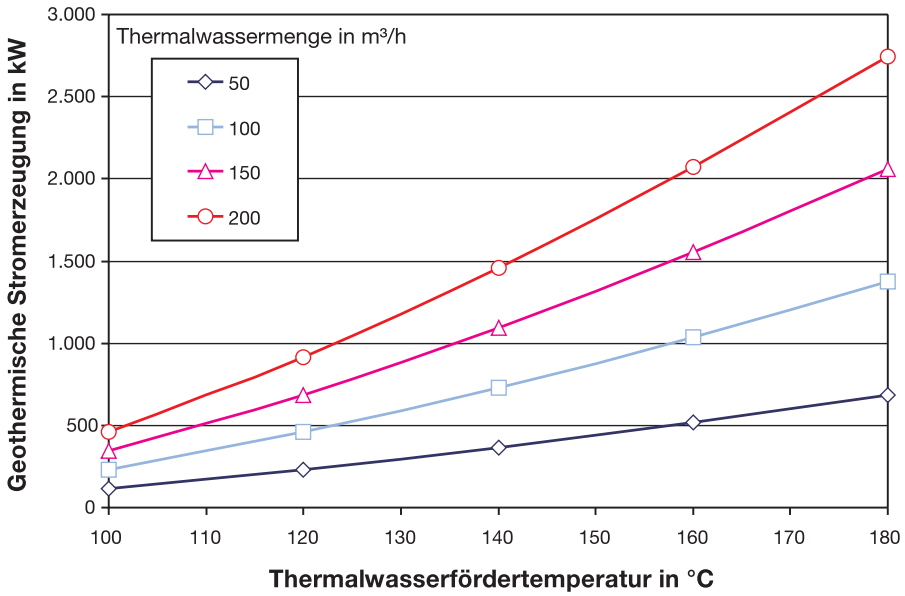

Figure A.4: The relationship of production well temperature and power plant output, for different pump rates, calculated for an *Organic Rankine Cycle* system, from [STMWIVT, 2004].

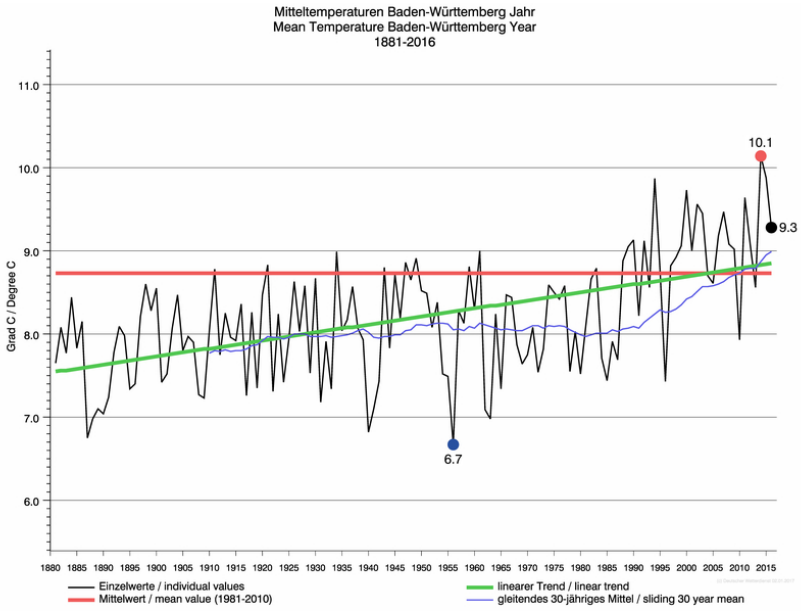

Figure A.5: Mean annual air temperature (MAAT) for Baden-Württemberg, provided by DWD [2017].

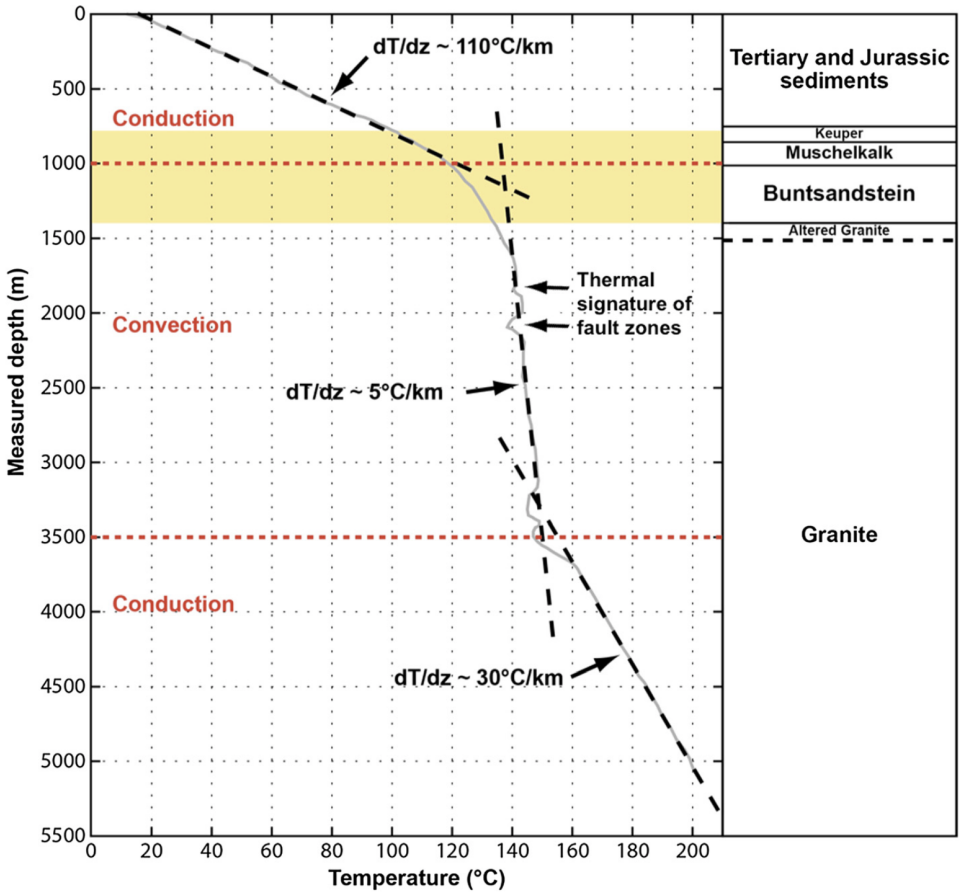

Figure A.6: Temperature profile and gradients at the borehole GPK-2 at Soultz-sous-Forets [Vidal et al., 2015].

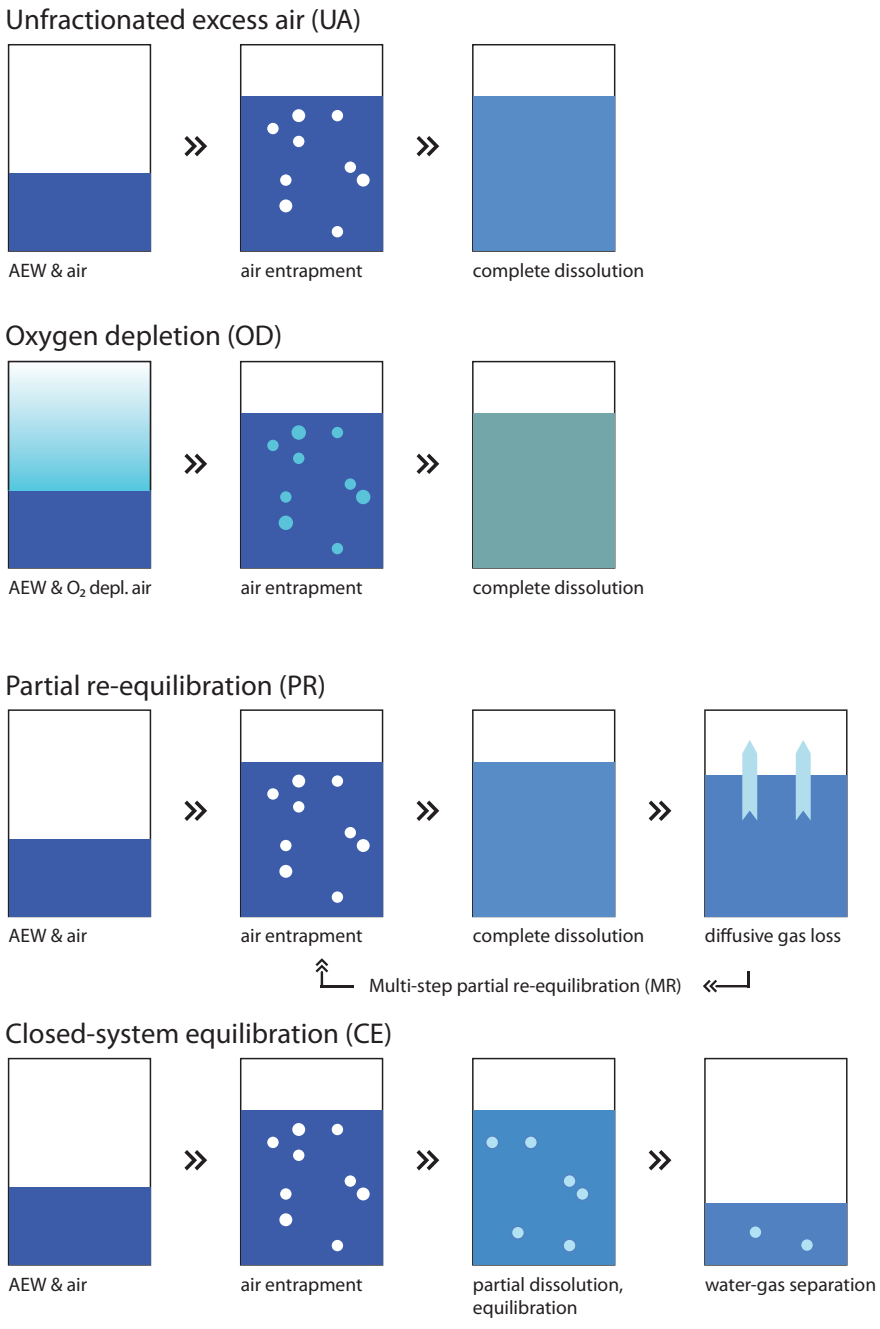

Figure A.7: Visualisation of the components of dissolved noble gases in groundwater, normalised to equilibrium concentrations, adapted from Wieser [2011].

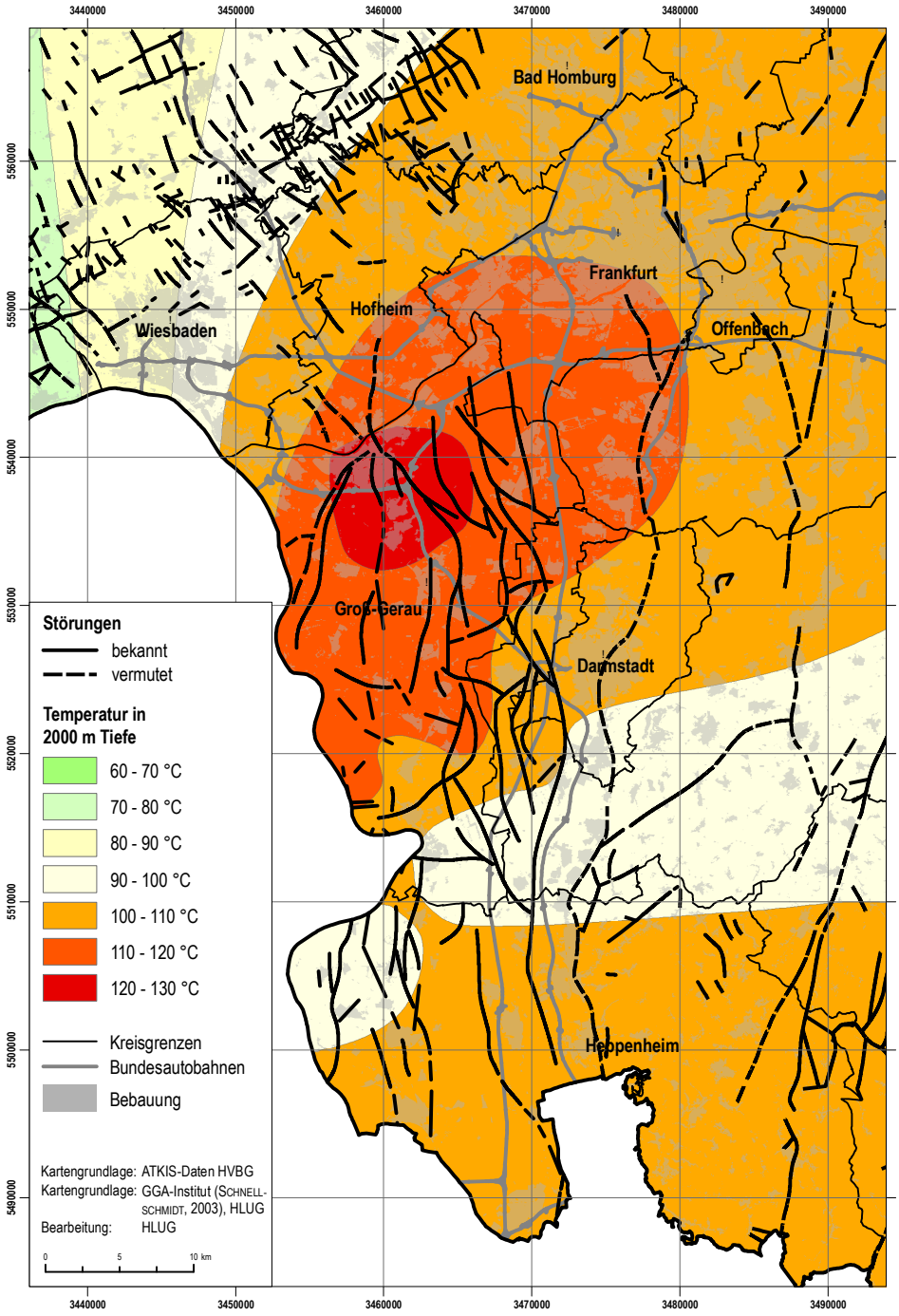

Figure A.8: Heat anomaly in the Groß-Gerau area, at 2 km depth, showing 110 to 130°C below most of the groundwater wells sampled in this region for this study [HLNUG, 2017].

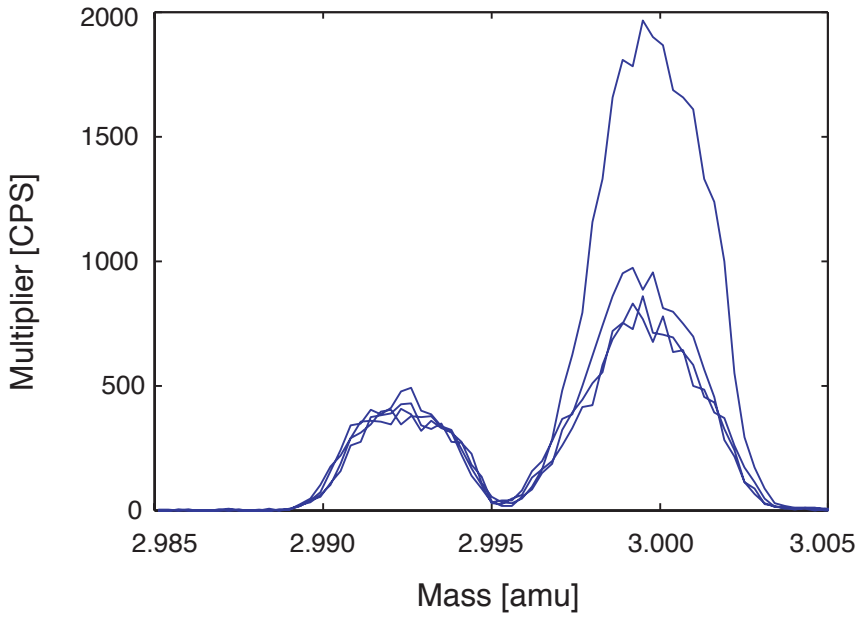

Figure A.9: Peak shapes of ^{3}He and HD as measured by Friedrich [2007] on the *GV5400* at the *IUP*.

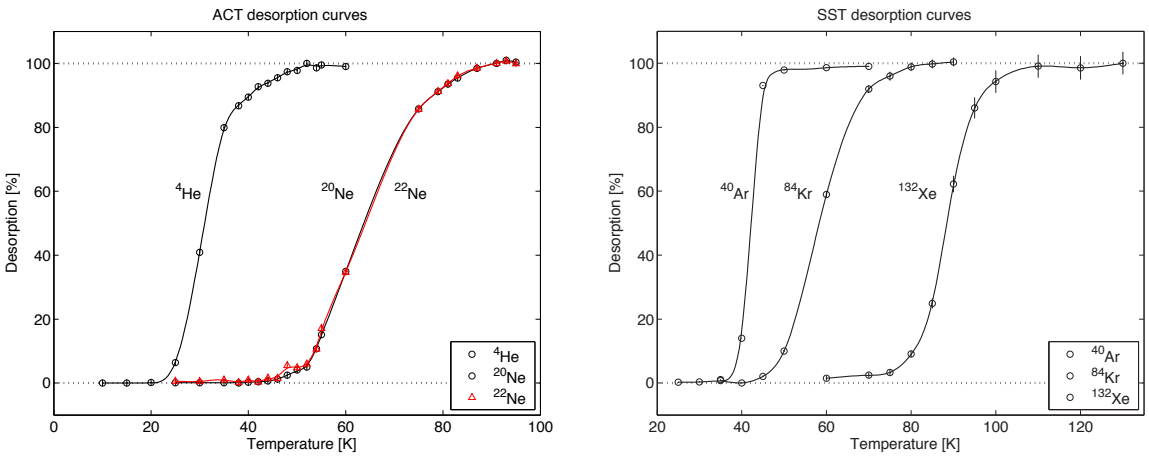

(a) **(b)**

Figure A.10: Desorption curves for the noble gases on the charcoal and stainless steel trap of the *GV5400* as measured by Friedrich [2007] and Träumner [2005].

(a)

(b)

(c)

(d)

(e)

(f)

Figure A.11: Impressions from the sampling campaigns: (a) cold winter conditions during the sampling of GG04b (b) C. Scholz, A. Schiller and S. Al Najem during hydrochemical analysis in the field at GG25 (c) G. Schmidt collecting Sr samples at QWB2 (d) J. Hartmann during field measurements of CO_2 isotopic composition (e) G. Schmidt, F. Neuwirth and J. Hartmann during the sampling of FR02 (f) Noble gas sampling at night (Photo by J. Hartmann).

Appendix B

Data Plots

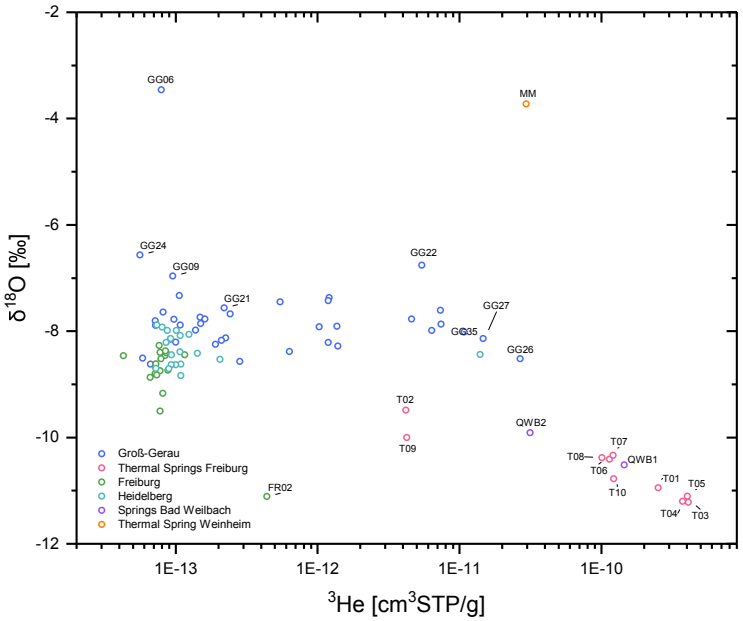

Figure B.1: δ^{18}O values of all samples plotted over the absolute ^{3}He concentrations.

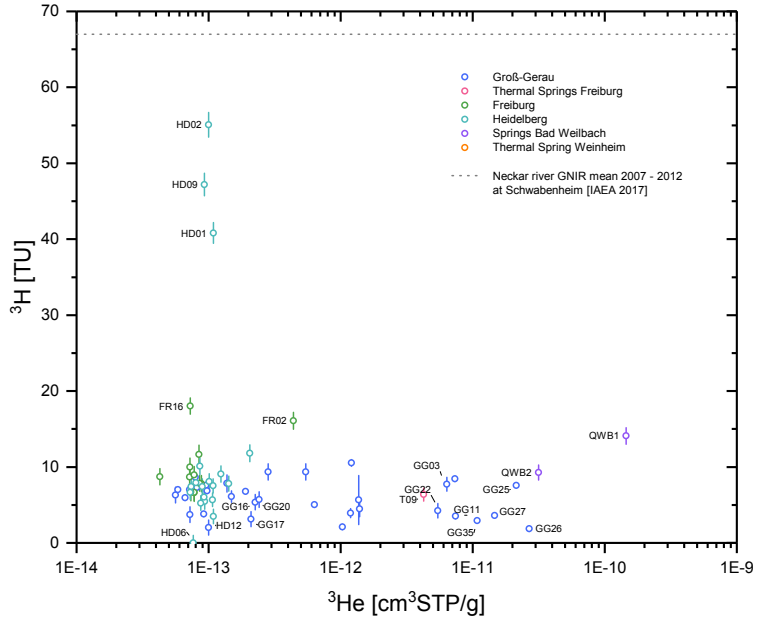

Figure B.2: Tritium activity data for all ^{3}H-analysed wells from all study regions plotted against the ^{3}He concentrations.

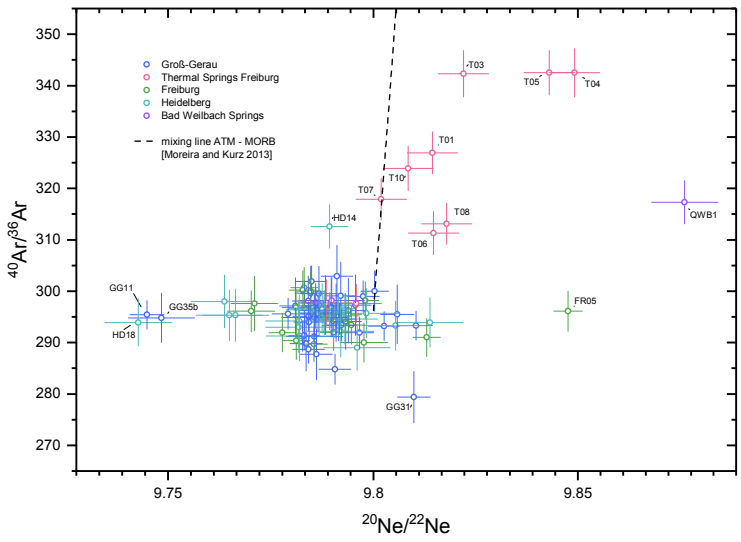

Figure B.3: The $^{40}Ar/^{36}Ar$ ratio plotted over the $^{20}Ne/^{4}He$ ratio, with a mixing line between the atmospheric and MORB signature [Moreira and Kurz, 2013].

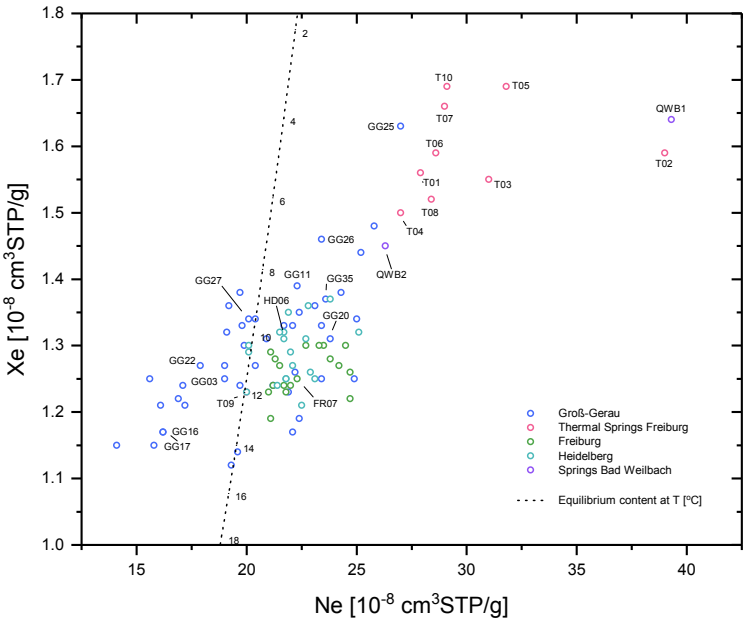

Figure B.4: Xenon-Neon plot of all samples. The dotted line represents the equilibrium concentrations at the indicated temperatures, calculated based on data from Clever [1979a] and Clever [1979b]. Data right of the equilibrium line indicate an excess air component, while data left on the line indicates gas loss due to degassing.

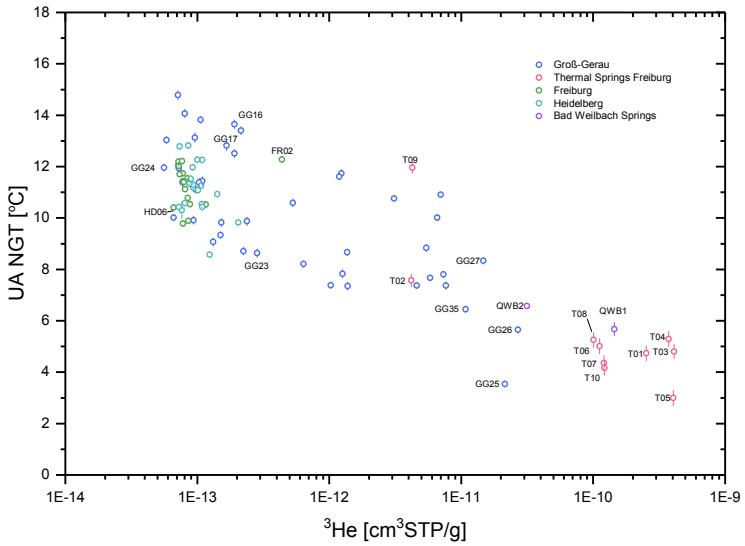

Figure B.5: Noble gas temperatures calculated using the UA model, plotted over the ^{3}He concentration.

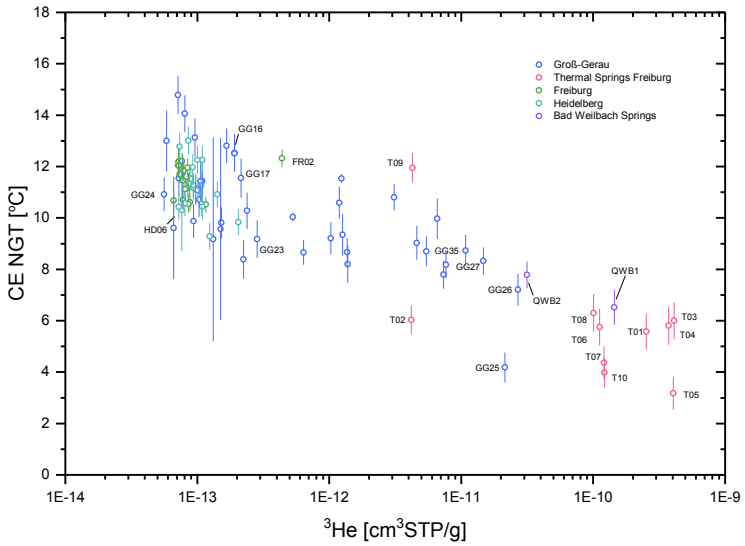

Figure B.6: Noble gas temperatures calculated using the CE model, plotted over the ^{3}He concentration.

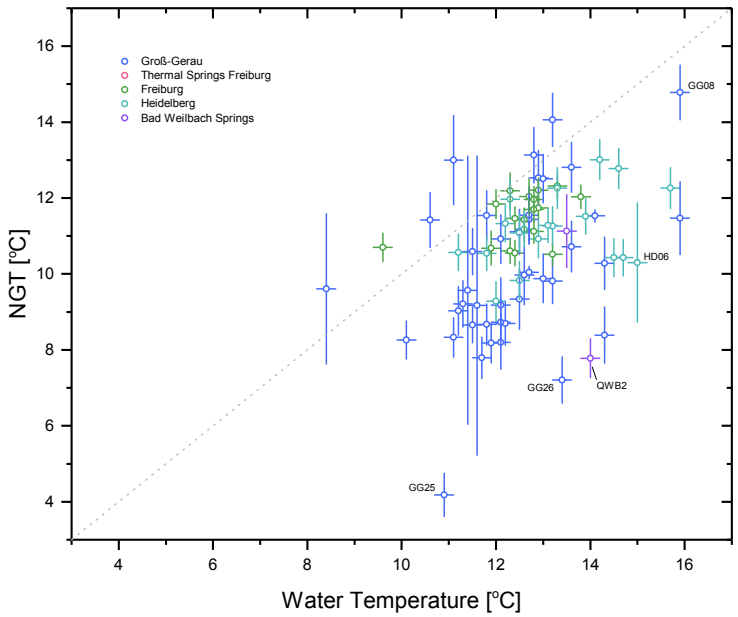

Figure B.7: Noble gas temperatures calculated using the CE model, plotted over the water temperature measured during sampling. The dotted line indicates where NGT = T.

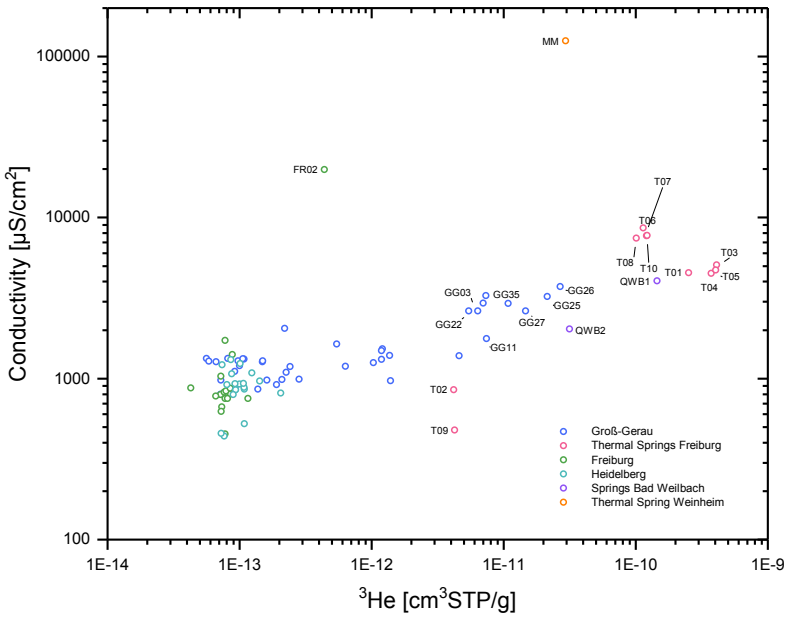

Figure B.8: Measured conductivity in µS/cm² of all samples plotted versus their absolute ^{3}He concentrations.

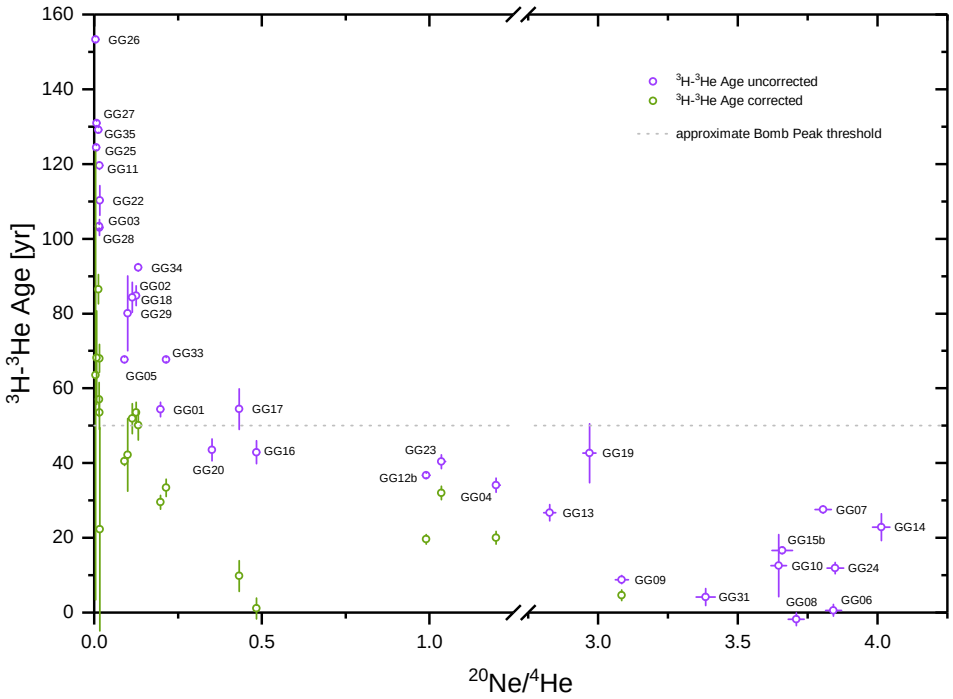

Figure B.9: The apparent ^{3}H-^{3}He ages, as calculated without and with a correction for terrigenic ^{3}He. The assumed radiogenic endmember R_{rad} for each sample can be found in table C.14.

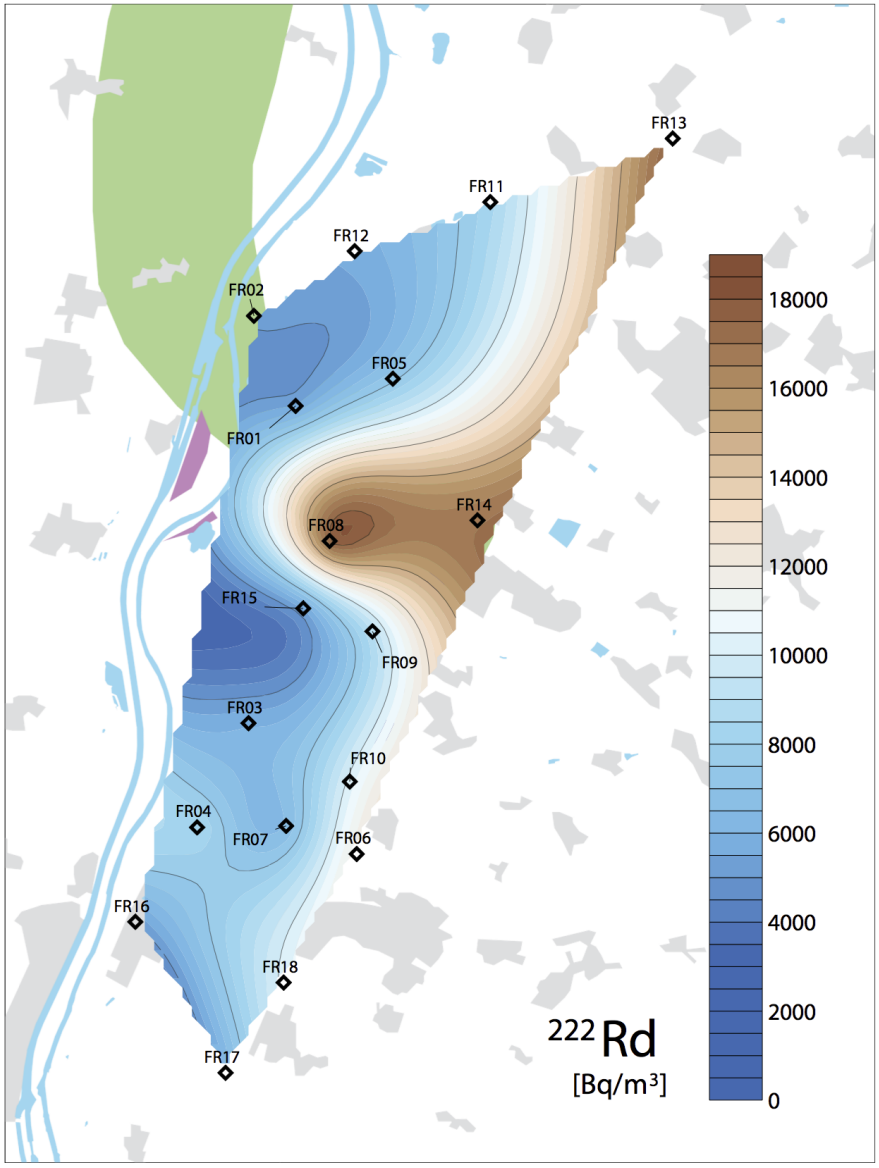

Figure B.10: Activities of ^{222}Rn measured at the Freiburg region, interpolated using a minimum curvature algorithmn.

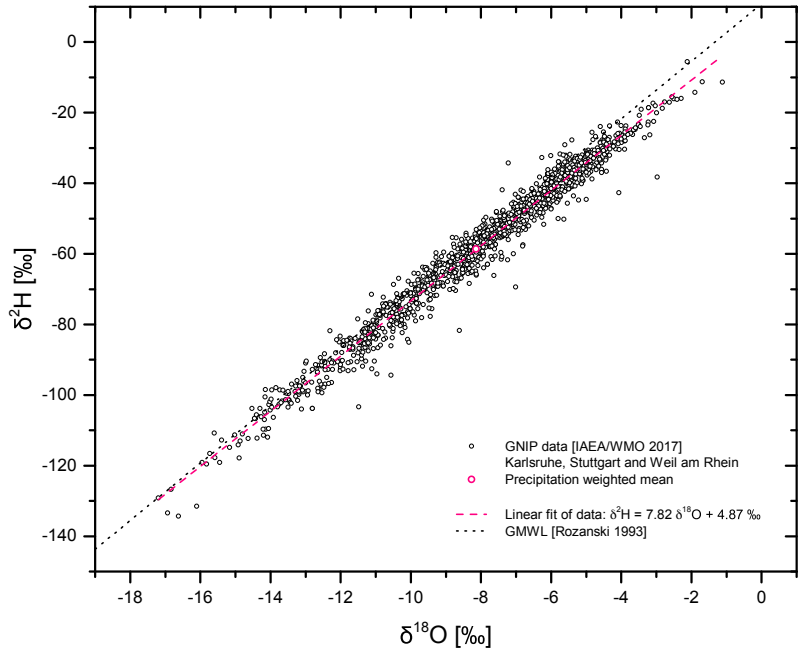

Figure B.11: LMWL fit of GNIP data from Karlsruhe, Stuttgart and Weil am Rhein [IAEA/WMO, 2017].

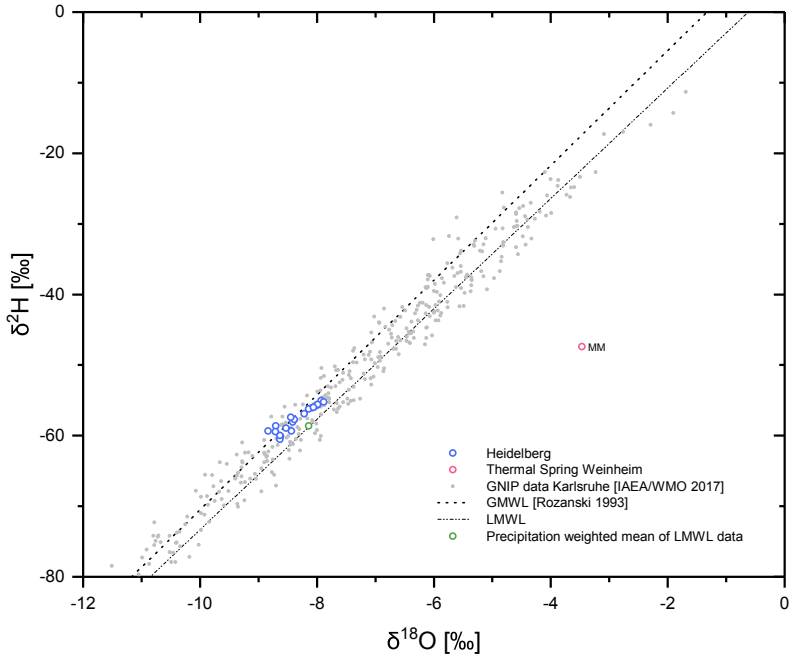

Figure B.12: Stable isotope data of the Heidelberg region and the thermal spring at Weinheim.

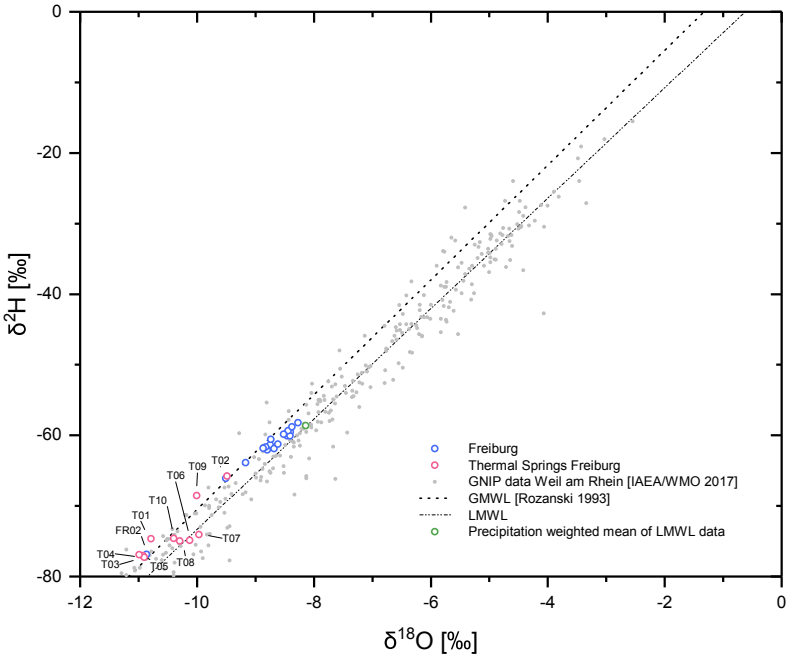

Figure B.13: Stable isotope data of the Freiburg region and the thermal springs of the surrounding area.

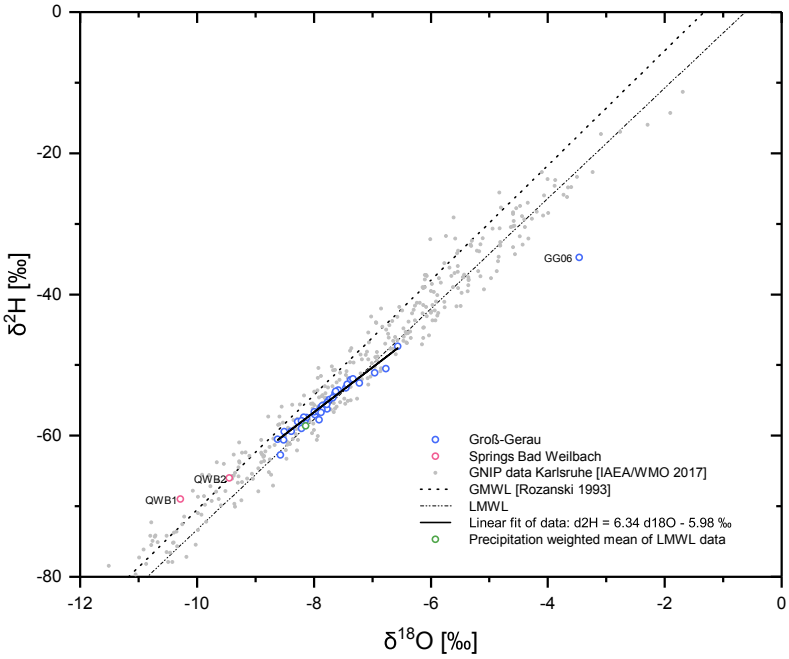

Figure B.14: Stable isotope data of the Groß-Gerau region and the springs at Bad Weilbach.

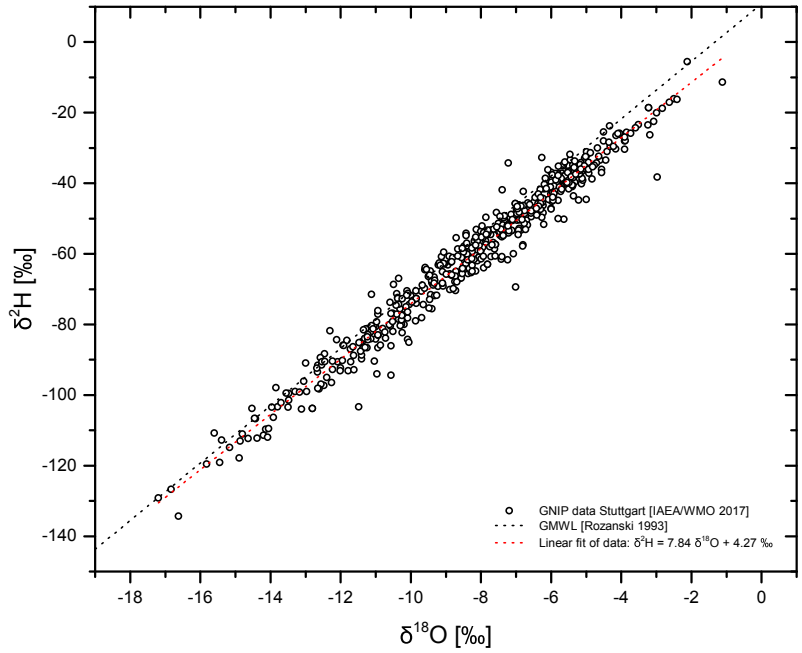

Figure B.15: Stable isotope data in precipitation at Stuttgart [IAEA/WMO, 2017], with GMWL and a linear fit of the LMWL.

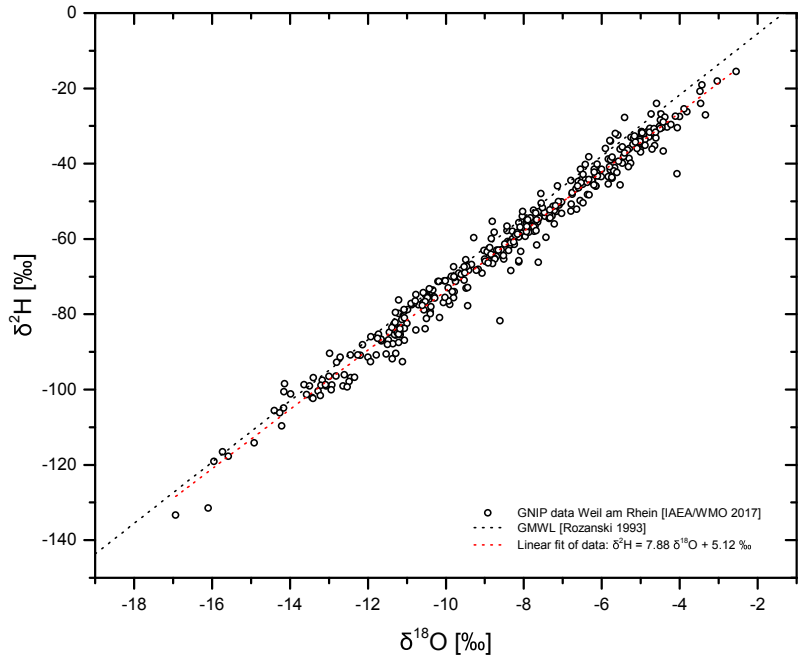

Figure B.16: Stable isotope data in precipitation at Weil am Rhein [IAEA/WMO, 2017], with GMWL and a linear fit of the LMWL.

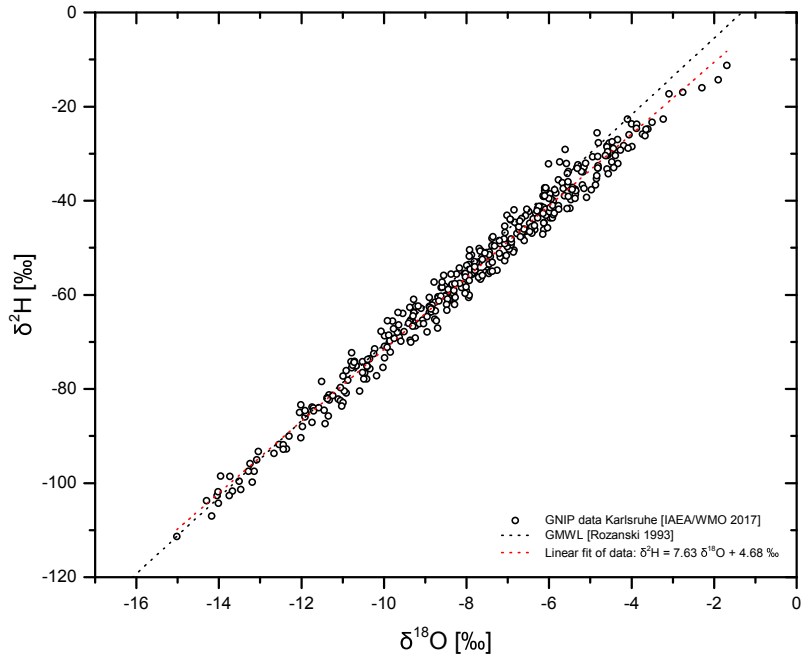

Figure B.17: Stable isotope data in precipitation at Karlsruhe [IAEA/WMO, 2017], with GMWL and a linear fit of the LMWL.

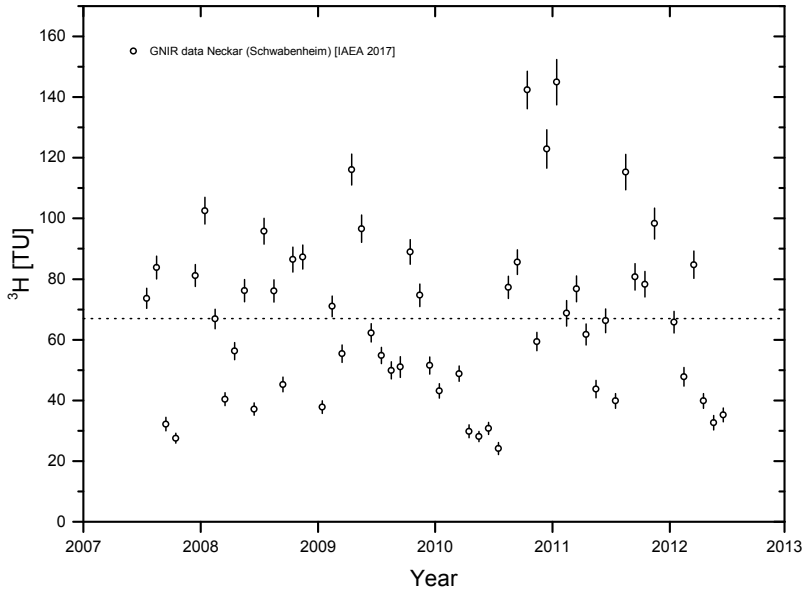

Figure B.18: Tritium activity of the Neckar river water at Schwabenheim, close to Heidelberg [IAEA, 2017]. The dotted line indicates the mean of the data.

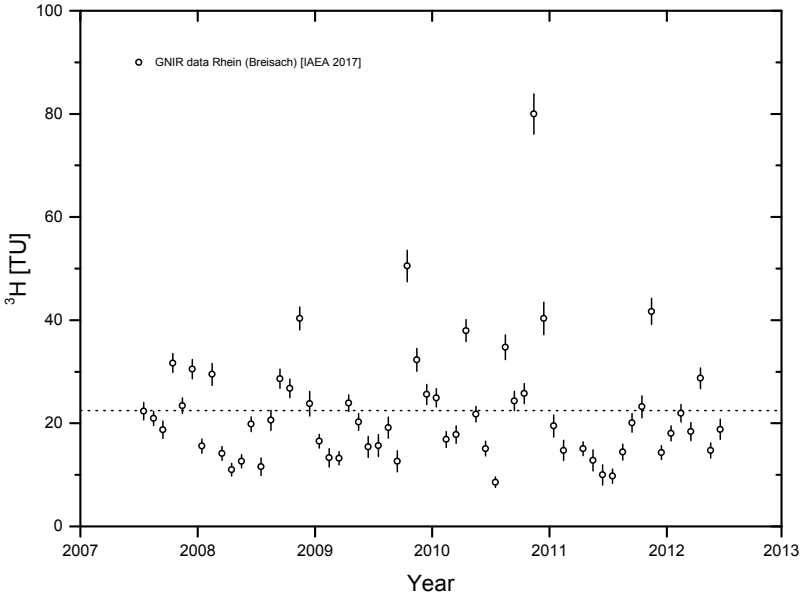

Figure B.19: Tritium activity of the Rhine river water at Breisach, close to Freiburg [IAEA, 2017]. The dotted line indicates the mean of the data

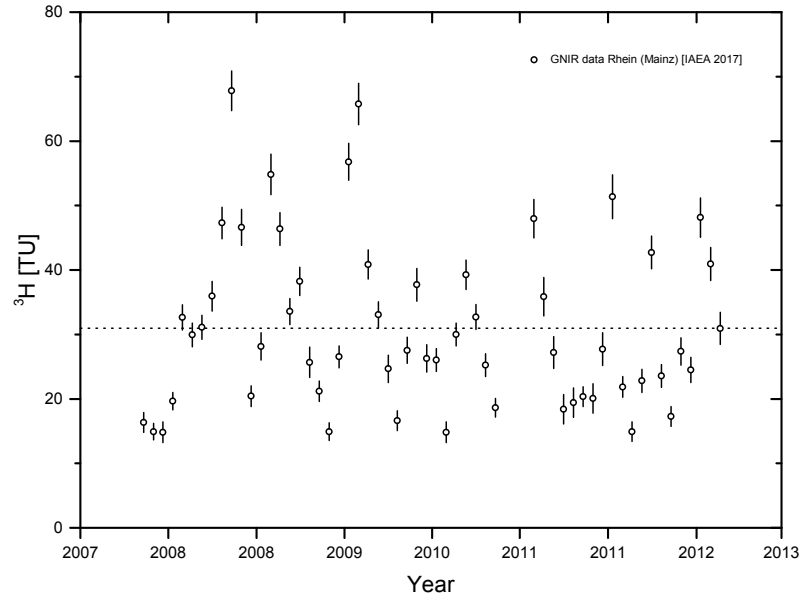

Figure B.20: Tritium activity of the Rhine river water at Mainz, close to Groß-Gerau [IAEA, 2017]. The dotted line indicates the mean of the data

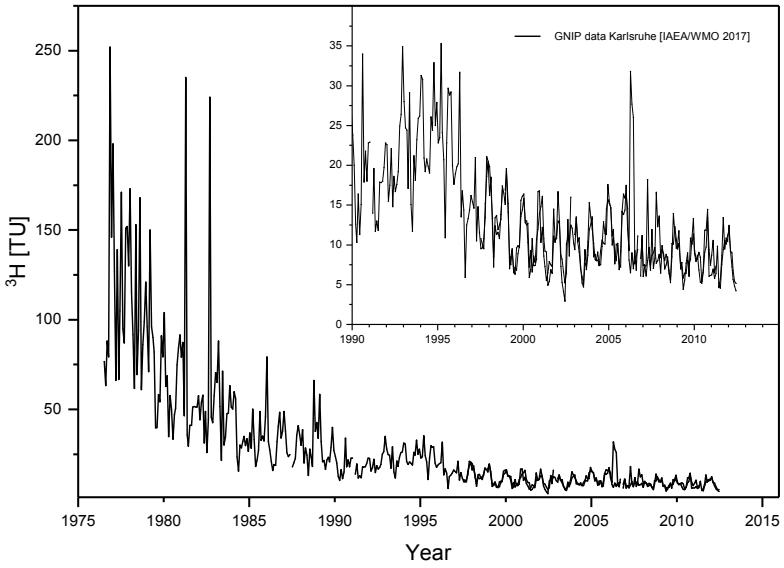

Figure B.21: Tritium input curve at Karlsruhe [IAEA/WMO, 2017].

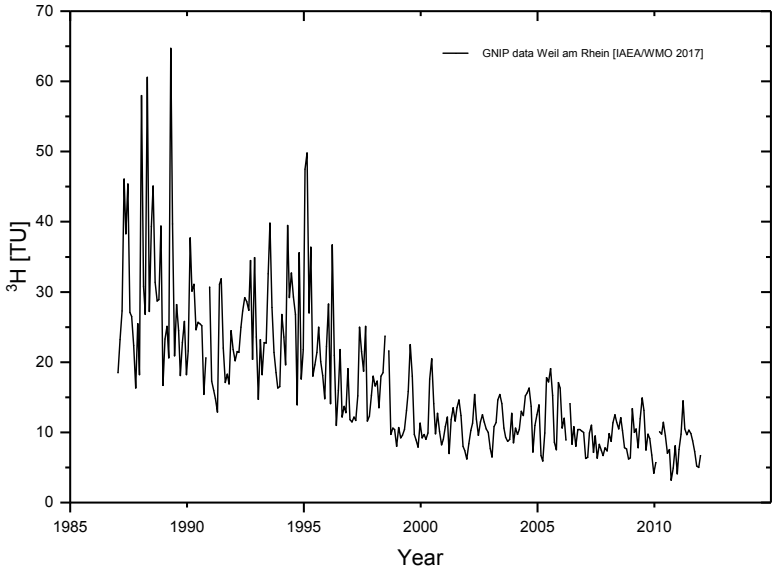

Figure B.22: Tritium input curve at Weil am Rhein [IAEA/WMO, 2017].

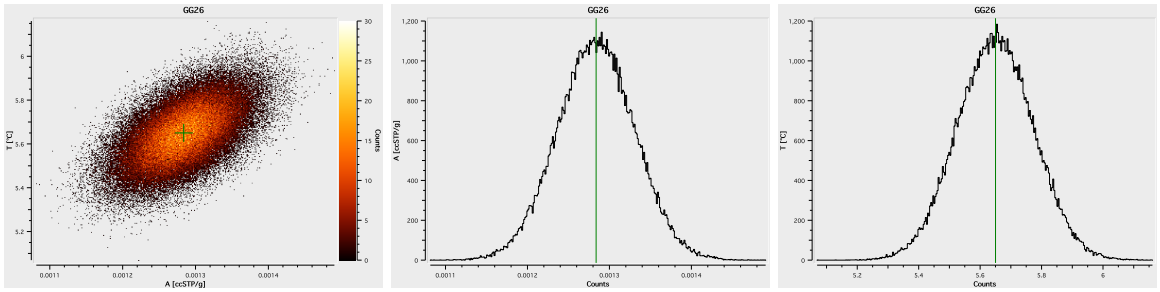

(a)

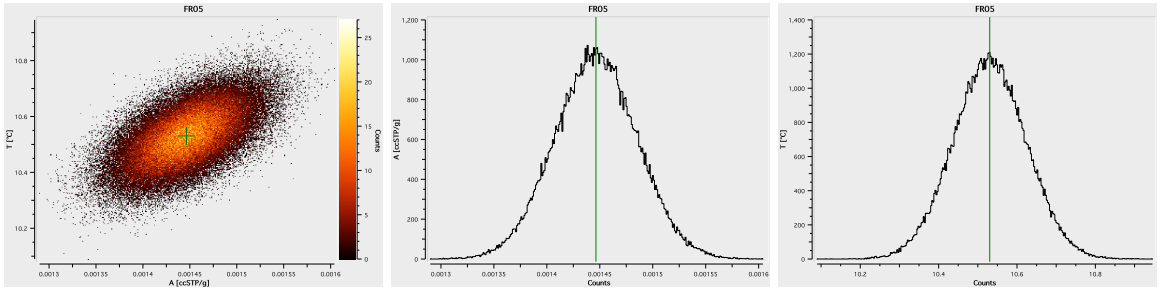

(b)

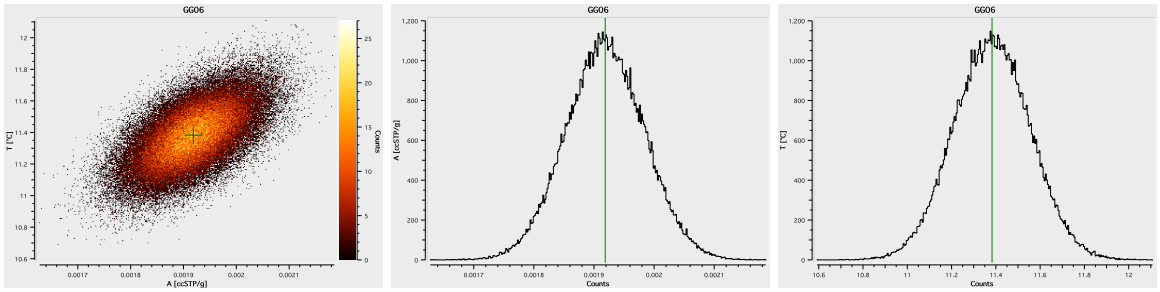

(c)

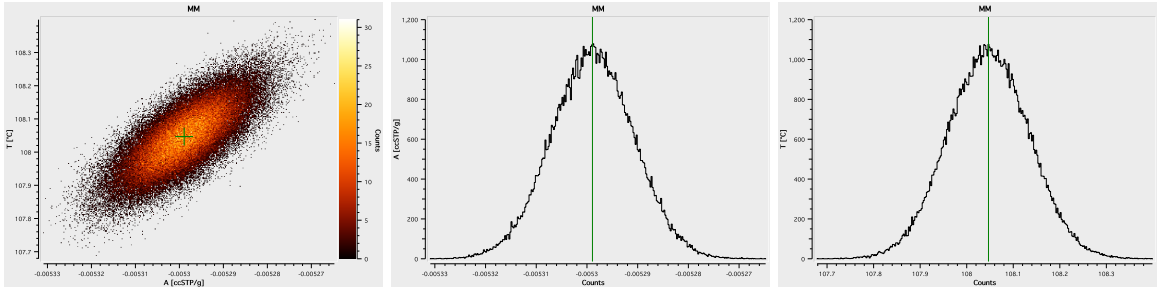

(d)

Figure B.23: Exemplary results of the Monte Carlo simulations for the UA-model fit using *PANGA*, for (a) GG26 ($\chi^2 = 10.2$, Prob = 0.6 %), (b) FR05 ($\chi^2 = 0.1$, Prob = 93.9 %), (c) GG06 ($\chi^2 = 0.2$, Prob = 89.6 %) and (d) MM ($\chi^2 = 71688.5$, Prob = 0.0 %). The histograms' axis labels are swapped, likely due to a software bug (*PANGA for OSX*).

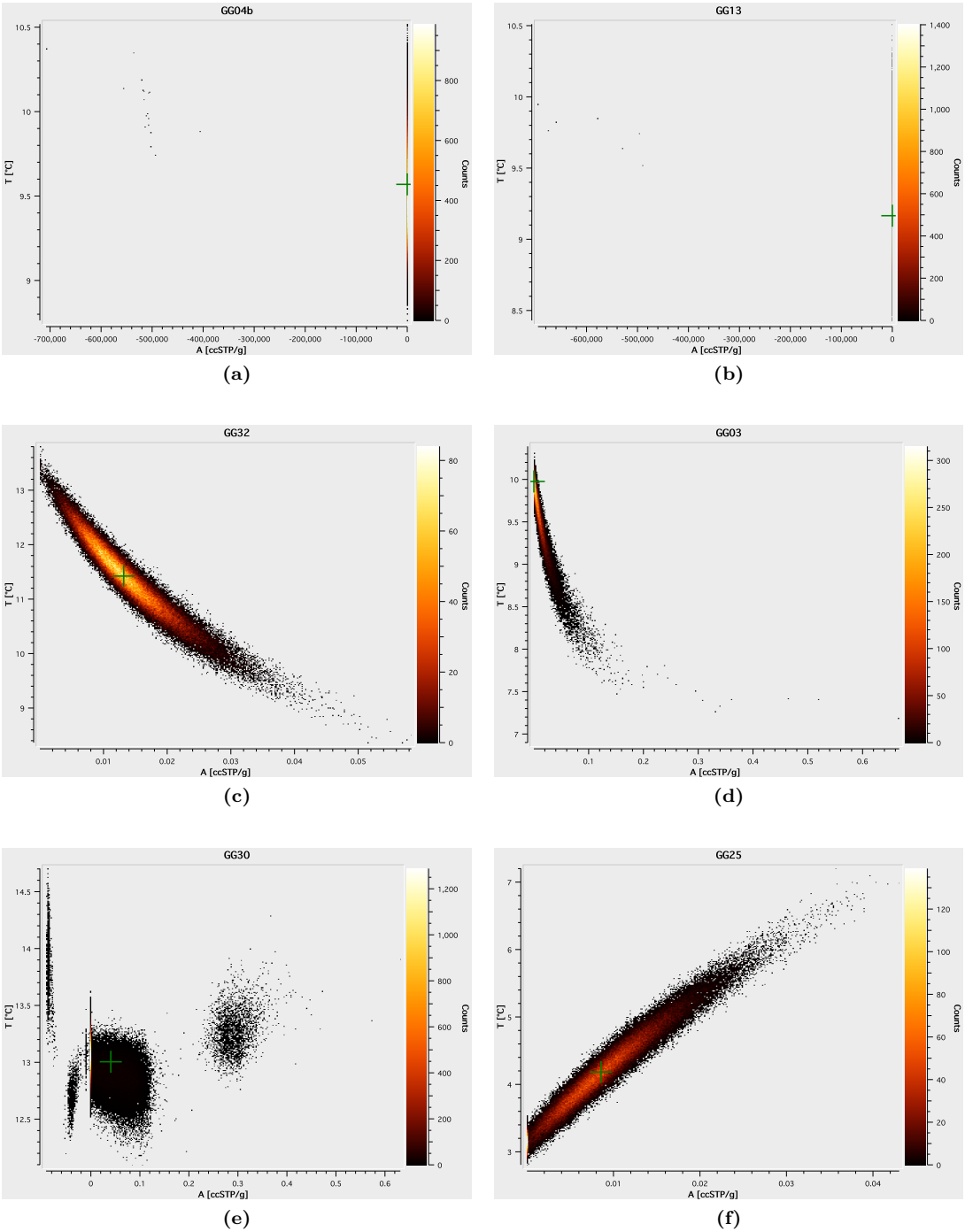

Figure B.24: Various cases of Monte Carlo simulation results: (a) and (b): unrealistic A_{CE} values with reasonable temperatures, leading to high ΔT (c) typical degassing (d) UA limit case (e) unexplained multiple maxima (f) extremely low temperature at inconspicuous Monte Carlo results

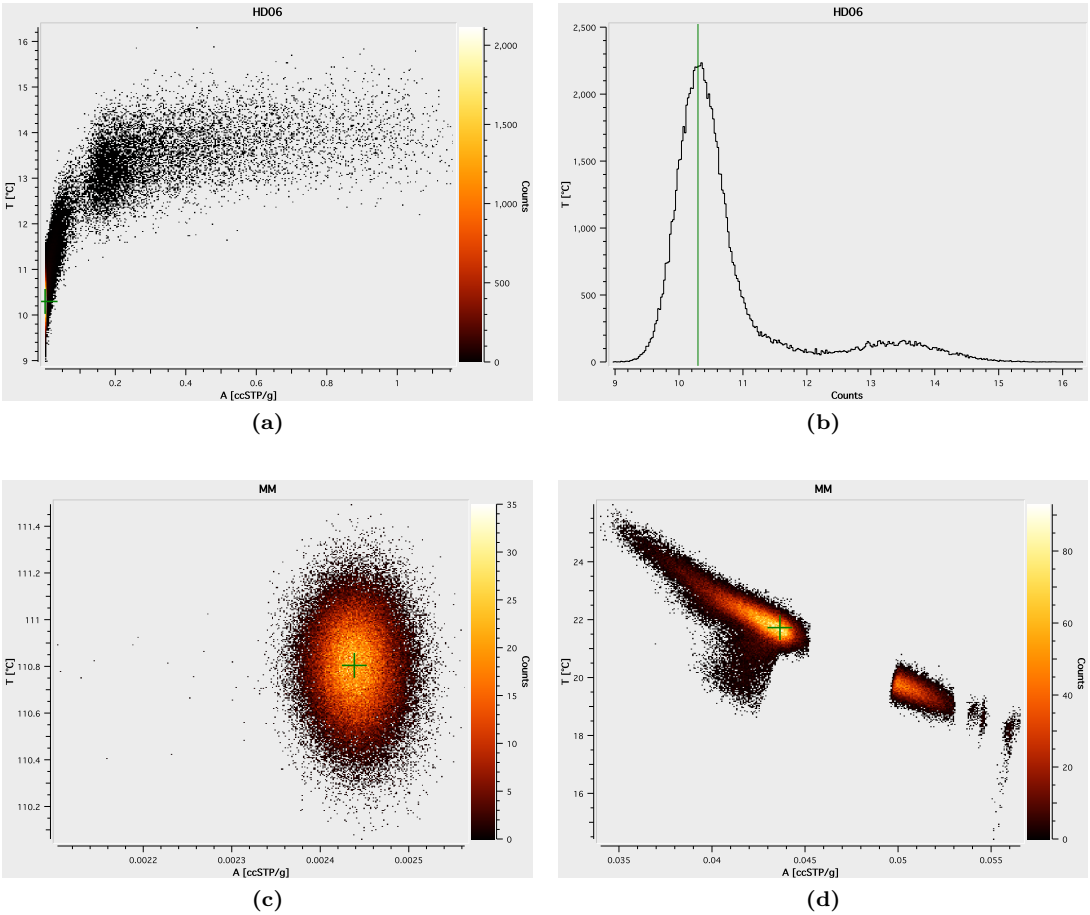

Figure B.25: Various cases of Monte Carlo simulation results: (a) and (b): Sample HD06, showing an indication of multiple maxima (c) Monte Carlo results for sample MM, using T = 10°C as an initial start parameter and (d) using T = 100°C, leading to extremely different results.

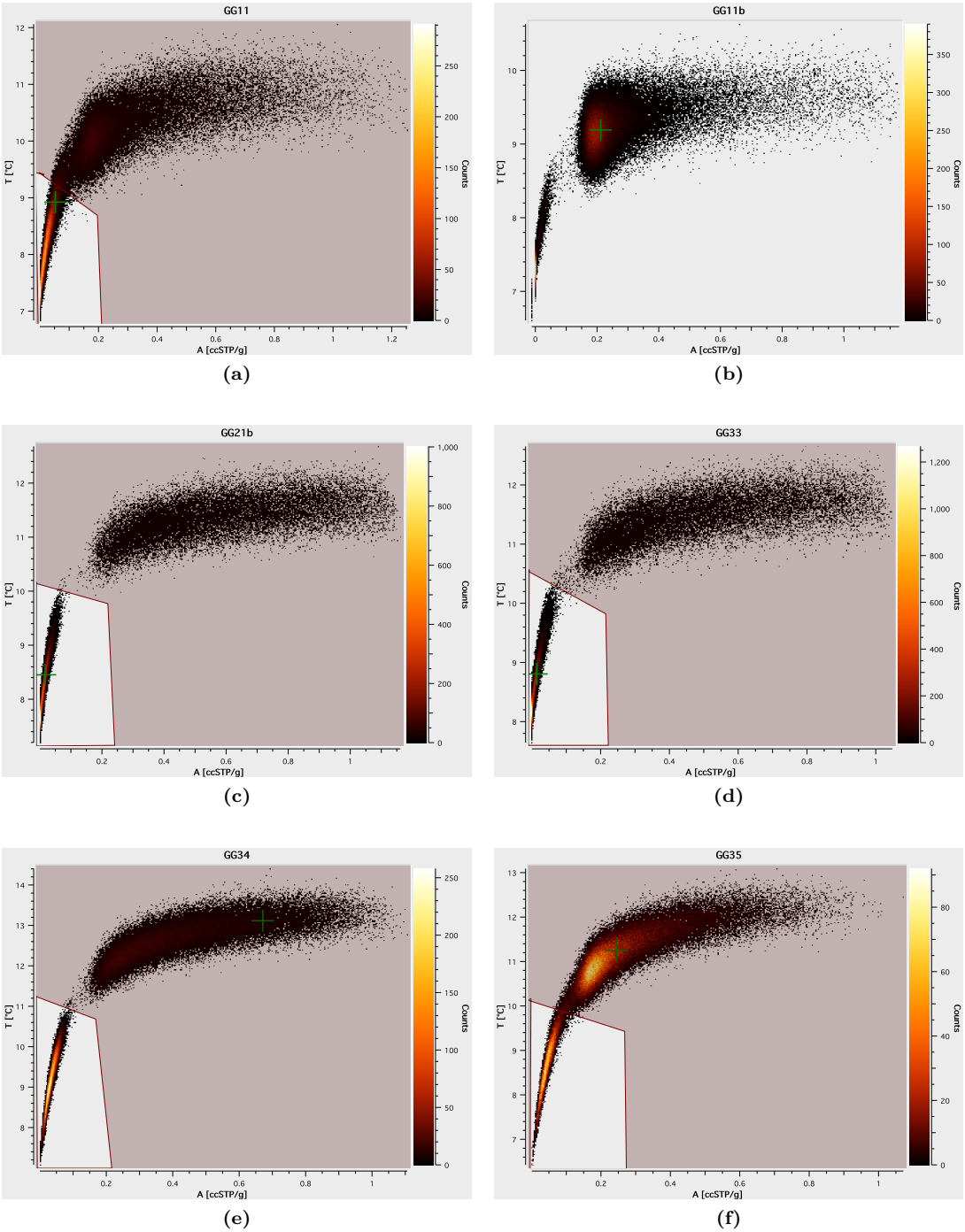

(a) (b) (c) (d) (e) (f)

Figure B.26: The chosen Monte Carlo data masks for samples with multiple temperature maxima at Groß-Gerau: (a) GG11 (b) GG11b (c) GG21b (d) GG33 (e) GG34 (f) GG35.

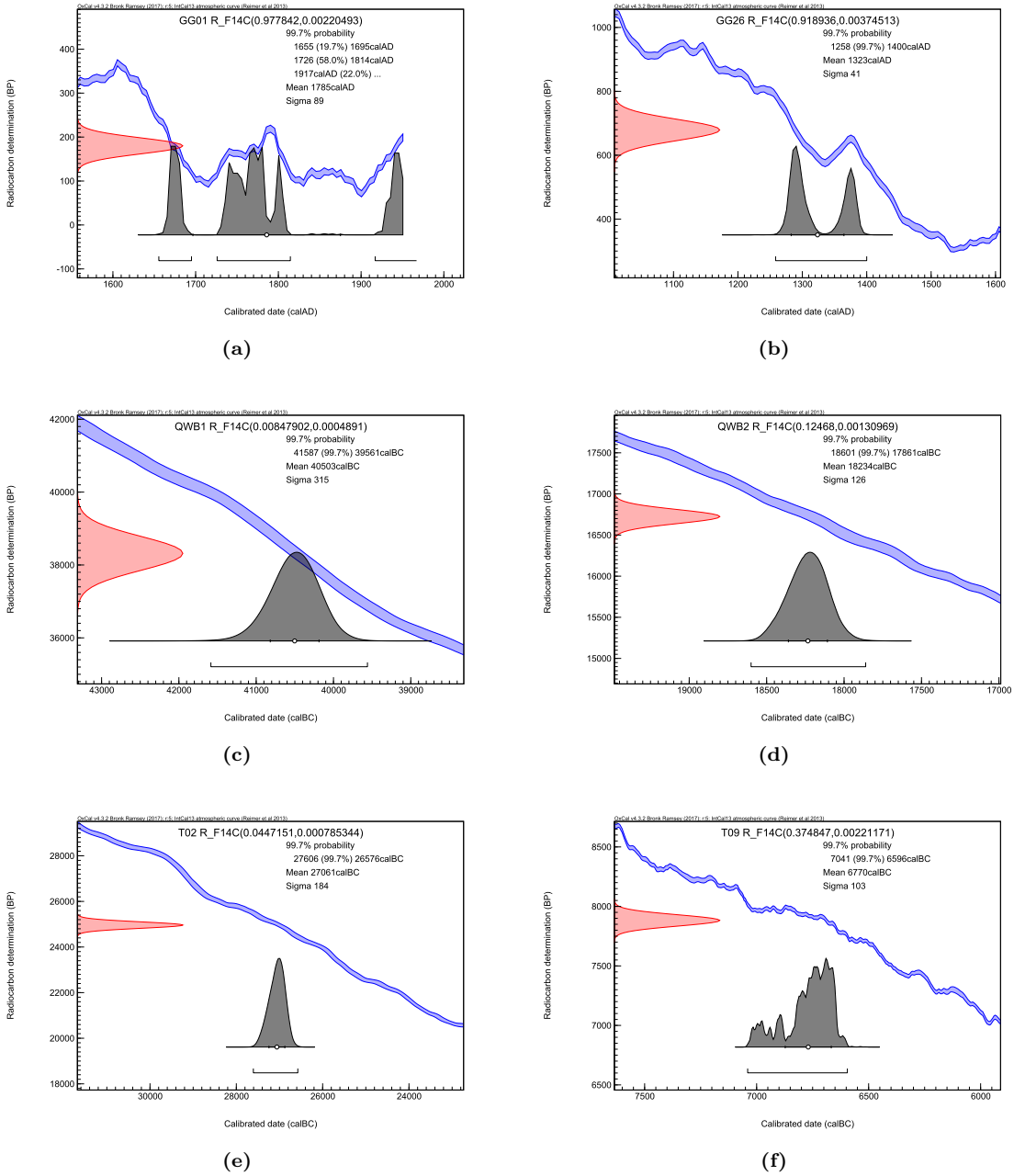

Figure B.27: Selected results of the ^{14}C dating done with *OxCal* [Bronk Ramsey, 2009] using the *IntCal13* calibration curve [Reimer et al., 2013] and Fontes and Garnier [1979] corrected input data (b – f) while (a) is based on raw data.

Appendix C

Tables and Calculations

Error of ^{3}He correction for tritium ingrowth

The error of the tritium correction

$$\left(\frac{^3\mathrm{He}}{^4\mathrm{He}}\right)_{\mathrm{corr}} = \left(\frac{^3\mathrm{He}}{^4\mathrm{He}}\right)_{\mathrm{meas}} - \left(\frac{^3\mathrm{H}}{^4\mathrm{He}}\right)_{\mathrm{meas}} \cdot \left(1 - e^{-\lambda t}\right) \tag{C.1}$$

is calculated from

$$\begin{aligned}\Delta\left(\frac{^3\mathrm{He}}{^4\mathrm{He}}\right)_{\mathrm{corr}} = \Bigg[&\left(\Delta\left(\frac{^3\mathrm{He}}{^4\mathrm{He}}\right)_{\mathrm{meas}}\right)^2 + \left(\frac{1+e^{-\lambda t}}{^4\mathrm{He}_{\mathrm{meas}}} \cdot \Delta^3\mathrm{He}_{\mathrm{meas}}\right)^2 \\ &+ \left(\frac{\mathrm{He}_{\mathrm{meas}}(1+e^{-\lambda t})}{^3\mathrm{H}^2{}_{\mathrm{meas}}} \cdot \Delta^4\mathrm{He}_{\mathrm{meas}}\right)^2 \\ &+ \left(\lambda\left(\frac{^3\mathrm{H}}{^4\mathrm{He}}\right)_{\mathrm{meas}} \cdot \left(1-e^{-\lambda t}\right) \cdot \Delta t\right)^2\Bigg]^{\frac{1}{2}}\end{aligned} \tag{C.2}$$

Table C.1: Parameters of fitting noble gas solubilities from Benson [1976].

noble gas	a_0	a_1 [K]	a_2 [K^2]
He	-5.0746	-4127.8	627250
Ne	-4.2988	-4871.1	793580
Ar	-4.2123	-5239.6	995240
Kr	-3.6326	-5664.0	1122400
Xe	-2.0917	-6693.5	1341700

Table C.2: ^{3}He/^{4}He ratios and Ne/He ratios compiled by Griesshaber et al. [1992] compared with data from this study for some of the thermal wells of the Freiburg area. The ^{3}He/^{4}He ratios of Griesshaber et al. [1992] were recalculated from $R_a = 1.4 \times 10^{-6}$ to $R_a = 1.384 \times 10^{-6}$ as used in this study [Clarke et al., 1976], however it is not entirely clear which R_a value Griesshaber et al. [1992] actually used, as the publication's text contradicts the data table's annotations.

		This Study			Griesshaber et al. [1992]	
Thermal Well	**ID**	**^{3}He/^{4}He** [R/R$_a$]	**Δ**	**Ne/He**	**^{3}He/^{4}He** [R/R$_a$]	**Ne/He**
Mooswald TB1	T01	1.52	0.07	0.0023	1.54	0.0130
Bad Krozingen TB4	T03	1.93	0.09	0.0020	1.75	0.0020
Bad Bellingen TB3	T06	0.49	0.02	0.0017	0.47	0.0072
Bad Bellingen TB2	T08	0.48	0.02	0.0019	0.60	0.0323
Badenweiler	T09	0.36	0.02	0.0232	0.31	0.0667

Table C.3: Noble gas volume mixing ratios and isotope composition in dry atmospheric air, compiled by Porcelli et al. [2002]. Note that this study uses an atmospheric $^3He/^4He$ ratio of 1.384×10^{-6} by Clarke et al. [1976] instead of the 1.4×10^{-6} given here.

Noble gas	Volume fraction in atmospheric air	Isotope	Relative isotopic abundance
He	$(5.24 \pm 0.05) \times 10^{-6}$	^{3}He	0.000140
		^{4}He	100
Ne	$(1.82 \pm 0.04) \times 10^{-5}$	^{20}Ne	90.5
		^{21}Ne	0.268
		^{22}Ne	9.23
Ar	$(9.34 \pm 0.01) \times 10^{-3}$	^{36}Ar	0.3364
		^{38}Ar	0.0632
		^{40}Ar	99.60
Kr	$(1.14 \pm 0.01) \times 10^{-6}$	^{78}Kr	0.3469
		^{80}Kr	2.2571
		^{82}Kr	11.523
		^{83}Kr	11.477
		^{84}Kr	57.00
		^{86}Kr	17.398
Xe	$(8.7 \pm 0.1) \times 10^{-8}$	^{124}Xe	0.0951
		^{126}Xe	0.0887
		^{128}Xe	1.919
		^{129}Xe	26.44
		^{130}Xe	4.070
		^{131}Xe	21.22
		^{132}Xe	26.89
		^{134}Xe	10.430
		^{136}Xe	8.857

Table C.4: Deviation of A and B samples, in percent relative to the mean of both measurements. Empty cells denote cases where the measurement of a single isotope failed for one of the samples.

ID	^{3}He	^{4}He	^{20}Ne	^{22}Ne	^{36}Ar	^{40}Ar	^{84}Kr	^{132}Xe
GG01	2.5	0.6	0.4	0.5	0.9	0.1	0.6	0.0
GG02	4.9	0.6	1.0	1.0	1.0	0.1	0.0	0.5
GG03	3.0	3.0	0.8	0.8	1.0	0.2	0.9	1.5
GG04	1.4	0.1	0.0	0.0	0.5	0.2	0.2	1.6
GG05	2.6	1.3	0.3	0.3	0.3	0.0	1.2	0.2
GG06	2.5	2.2	1.0	0.9	0.6	0.3	0.1	0.2
GG07	2.1	0.7	0.5	0.4	0.3	0.3	0.7	0.3
GG08	0.4	0.0	0.5	0.4	0.8	0.2	1.3	1.4
GG09	0.5	1.5	1.5	1.5	1.1	0.6	0.2	1.2
GG10	1.3	0.4	0.3	0.4	2.1	0.0	0.7	1.3
GG11	3.1	1.1	0.2	0.1	0.2	0.1	0.5	0.3
GG12	3.6	1.3	1.5	1.6	1.3	0.8	0.4	0.8
GG13	4.3	1.6	1.6	1.5	0.2	0.4	0.3	0.6
GG14	0.5	0.9	0.7	0.7	1.1	0.8	0.9	1.6
GG15	0.8	0.1	0.4	0.4	0.8	0.1	0.8	0.6
GG16	17.0	15.8	10.1	10.1	3.0	2.7	1.5	1.7
GG17	2.2	1.2	0.8	0.7	0.5	0.3	1.1	0.4
GG18	0.2	0.5	0.6	0.6	0.1	0.0	0.3	0.7
GG19	2.5	0.5	0.7	0.4	0.6	0.1	0.5	0.1
GG20	1.6	1.0	0.0	0.1	1.2	0.0	0.5	0.6
GG21	1.8	0.5	0.3	0.5	0.3	0.1	0.1	2.8
GG23	0.3	0.3	1.2	1.1	0.4	0.4	0.2	2.1
GG26	0.6	0.7	0.2	0.3				
GG33	0.6	0.6	0.0	0.1	0.0	0.1	0.0	0.3
To6	2.1	0.5	0.8	0.9	0.3	0.3	0.0	1.4
To8	0.6	1.3	0.4	0.4	0.4	0.9	0.8	3.3
FR07		0.3	0.2	0.0	1.4	0.3	0.3	0.3
MM	97.5	45.3	15.6	16.7		37.4	21.9	15.1

Table C.5: The sampled thermal wells of the Freiburg region, with the associated aquifers, well depth and filter depth [He et al., 1999], as well as production temperature during sampling.

ID	Well	Aquifer	Depth [m]	filtered at [m]	Temp [°C]
T01	Mooswald TB1	upper Muschelkalk	858	858 – 722	44.7
T02	Mooswald TB3	Hauptrogenstein	488	483 – 418	29.1
T03	Bad Krozingen TB4	upper Muschelkalk	579	579 – 524	37.0
T04	Bad Krozingen TB3	upper Muschelkalk	610	610 – 555	39.3
T05	Bad Krozingen TB2	upper Muschelkalk	597	597 – 554	39.0
T06	Bad Bellingen TB3	Hauptrogenstein	648	558 – 527	39.1
T07	Bad Bellingen TB4	Hauptrogenstein	650	660 – 522	37.3
T08	Bad Bellingen TB2	Hauptrogenstein	650	650 – 558	36.6
T09	Badenweiler	crystaline bedrock	364	364 – 119	25.6
T10	Steinenstadt	Hauptrogenstein	487	487 – 390	32.1

Table C.6: Elemental concentrations in cm^3STP/g of sample GG16, compared to theoretical equilibrium concentrations calculated for 10 °C [Clever, 1979a,b, 1980].

Sample	He	Ne	Ar	Kr	Xe
10 °C	4.73×10^{-8}	2.10×10^{-7}	4.14×10^{-4}	9.94×10^{-8}	1.47×10^{-8}
GG16 A	3.03×10^{-7}	1.62×10^{-7}	3.38×10^{-4}	8.17×10^{-8}	1.17×10^{-8}
GG17 B	4.00×10^{-7}	1.95×10^{-7}	3.56×10^{-4}	8.42×10^{-8}	1.21×10^{-8}

Table C.7: Sampling parameters for all sampling sites of the study.

ID	Date	Rechtswert	Hochwert	Height	Air Pressure	Water Table	Depth	Pump Depth	Pump Rate	Purge	Water Temp	EC (K_{25})	O_2	pH
		GK3		[m]	[mbar]	[m ROK]	[m ROK]	[m ROK]	[l/s]	[min]	[°C]	[µS/cm]	[mg/l]	
FR01	16/09/2013	3395016	5308673	189	985	8.88	> 30	15.0	0.33	75	9.6	452	7.71	7.44
FR02	16/09/2013	3394152	5310539	235	981	9.85	170.0	15.0		150	13.3	19860	4.75	7.58
FR03	17/09/2013	3394040	5302105	221	986	18.83	26.3	22.0	0.30	50	12.4	753	8.84	6.96
FR04	17/09/2013	3392977	5299946	220	986	8.99	24.8	12.0	0.26	60	12.7	794	8.95	7.00
FR05	17/09/2013	3397027	5309238	207	985	14.20	55.0	18.0	0.42	60	12.3	1409	6.95	6.92
FR06	18/09/2013	3396278	5299395	233	978	19.39	27.4	21.0	0.43	65	12.8	839	9.31	6.93
FR07	18/09/2013	3394818	5299976	228	977	19.95	25.4	21.7	0.34	30	12.6	875	8.12	7.00
FR08	18/09/2013	3395719	5305877	223		15.47	37.4		1.67	260	12.3	1032	9.04	6.97
FR09	19/09/2013	3396606	5304006	224	990	16.12	22.6	19.0	0.45	60	12.9	1727	8.91	6.98
FR10	19/09/2013	3396135	5300894	233	990	20.52	23.1	21.5	0.25	35	12.4	803	9.57	6.92
FR11	19/09/2013	3399042	5312896	203	991	10.52	15.0	13.0	0.27	40	12.8	666	7.36	7.09
FR12	20/09/2013	3396237	5311879	268	995	7.94	18.2	10.0	0.47	40	11.9	777	8.16	7.09
FR13	20/09/2013	3402816	5314212	221	995	2.51	15.5	7.0	0.37	30	12.9	822	6.19	6.81
FR14	23/09/2013	3398777	5306305	206	997	13.37	36.0	17.0	0.47	30	13.2	751	7.22	6.91
FR15	24/09/2013	3395172	5304481	215	993	17.27	64.0	21.0	0.47	45	12.0	838	8.95	7.02
FR16	24/09/2013	3391699	5297990	235	990	10.72	39.5	15.0	0.47	45	13.8	625	7.33	7.22
FR17	24/09/2013	3393566	5294864	228	987	21.29	25.7	23.9	0.27	45	12.6	872	9.66	6.99
FR18	25/09/2013	3394767	5296733	231	986	21.24	26.6	23.5	0.33	60	12.8	753	5.74	7.20
GG01	17/09/2012	3454757	5528064	75	1005	2.19	10.3		0.33	60	12.7	1640	0.00	7.17
GG02	17/09/2012	3454267	5527859	84	1004	2.41	12.6	5.0	0.33	55	12.5	1317	0.00	6.90
GG03	17/09/2012	3454774	5531856	88	1004	2.86	17.6		0.30	45	12.6	2630	0.00	7.08
GG04	18/09/2012	3455483	5533818	96	1004	2.92	7.4	5.0	0.36	60	13.2	1270	0.08	6.99
GG04b	12/03/2013	3455483	5533818	96		2.45		5.0		70	11.4	1290	0.26	6.96
GG05	18/09/2012	3454500	5534813	94	1002	3.50	6.8		0.33		14.1	1529	0.05	6.94
GG05b	14/03/2013	3454494	5534804	98	1002	3.05	6.8	5.5	0.33	65	11.5	1488	0.25	6.86
GG06	18/09/2012	3456753	5537086	92	1000	1.30	5.8	3.3	0.33		15.9	800	0.00	7.20
GG07	19/09/2012	3457073	5534429	91	1008	5.40	9.2	7.5	0.30	45	13.0	1108	0.51	7.20
GG08	19/09/2012	3455863	5536166	84	1009	5.22	6.1		0.11		15.9	800	0.00	7.20
GG09	20/09/2012	3457225	5538244	96	1015	7.61	10.5	9.5		60	12.8	915	5.99	7.06
GG10	20/09/2012	3456977	5532019	75	1015	2.54	11.5	5.0	0.33		13.2	1331	0.00	7.16
GG11	20/09/2012	3456474	5529976	79	1014	1.43	33.0	4.0	0.42		11.9	1770	0.00	7.17
GG11b	14/03/2013	3456471	5529973	89	1002	0.89		3.5	0.42	120	11.2	1386	0.00	7.45
GG12	20/09/2012	3456652	5528010	80	1012	4.20	9.1	6.5	0.33		13.6	976	4.81	7.17
GG12b	15/03/2013	3456660	5528007	98	1008	3.78	9.4	6.5	0.30	30	13.0	916	4.69	7.00
GG13	21/09/2012	3460219	5527840	85	1010	3.39	25.5		0.33	60	11.6	858	0.00	7.28
GG14	21/09/2012	3462731	5528456	81	1009	3.14	10.3	5.0	0.33	45	11.8	978	0.00	6.93
GG15	21/09/2012	3457541	5532279	107	1007	3.50	11.8	6.0	0.35		12.7	1320	0.98	7.05
GG15b	14/03/2013	3457544	5532268	80	1000	3.03	11.8	5.5	0.33	45	12.5	1289	1.23	7.13
GG16	25/09/2012	3453537	5525476							artesian	12.9	1093	3.82	7.41
GG17	25/09/2012	3453537	5525476							artesian	12.7	984	3.25	7.37
GG18	26/09/2012	3459033	5527983	85	992	2.27	8.5	5.0	0.30	60	12.1	970	0.00	7.14
GG19	26/09/2012	3461353	5531754	78	993	2.20	9.4	4.5	0.33		13.6	1200	0.00	6.92
GG20	27/09/2012	3452384	5532240	88	999	2.39	9.7	6.0	0.33	60	14.3	1187	0.49	7.17
GG21	27/09/2012	3452276	5533226	81	999	2.75	6.4	5.0	0.33	60	14.3	2050	0.00	7.03
GG21b	18/03/2013	3452272	5533229	72	984	1.55	6.5	4.0	0.32	30	10.1	2020	0.00	6.98
GG22	03/10/2012	3454957	5529170	77	1006	1.77	11.1	4.0	0.33	60	12.2	2630	0.00	6.90
GG23	03/10/2012	3455027	5525879	82	1005	2.04	11.4	4.5	0.33	45	12.1	992	0.00	7.08
GG24	03/10/2012	3460028	5531566	86	1004	2.91	8.4	5.0	0.33	45	12.1	1330	0.00	7.01
GG25	15/03/2013	3454552	5531908	70	1008	2.98	>35	5.5	0.30	65	10.9	3230	0.80	7.29
GG26	15/03/2013	3456038	5529285	77	1007	1.68	12.4		0.32	45	13.4	3720	0.02	6.95
GG27	15/03/2013	3455482	5528802	80	1007	0.90	12.0	3.5	0.32	50	11.1	2630	0.00	6.84
GG28	15/03/2013	3455613	5530027	79	1007	0.99		3.5	0.32	40	11.7	3270	0.01	6.91
GG29	18/03/2013	3454050	5528216	72	985	1.20	9.1	3.5	0.32	67	11.8	1390	0.00	6.89
GG30	18/03/2013	3452543	5529098	105	981					artesian	11.1	1280	10.20	7.57
GG31	18/03/2013	3452690	5529338	101	983					artesian	8.4	1270	10.28	7.50
GG32	18/03/2013	3454785	5533699	78	986	2.82	5.4	4.8	0.25	30	10.6	1326	1.29	6.92
GG33	19/03/2013	3454748	5526727	75	989	1.15	10.0	3.5	0.33	30	11.5	1190	0.00	7.02
GG34	19/03/2013	3454647	5527192	82	990	0.68	13.3	3.5	0.33	40	11.3	1254	0.00	7.13
GG35	19/03/2013	3454080	5529609	79	991	0.96	11.7	3.5	0.27	30	12.1	2930	0.00	7.35
GG35b	30/10/2013	3454080	5529609	79		1.23		7.0	0.30	75	12.1	2940	0.00	6.82
HD01	04/06/2014	3472253	5475384	110	997		20.0	16.0		30	13.3	858	5.70	7.25
HD02	04/06/2014	3476421	5475903	110	995	15.12	23.0	17.5	0.37	30	15.7	925	2.69	7.17
HD03	04/06/2014	3470592	5484785	102	995		9.0	7.8		70	11.2	916	6.62	7.16
HD04	05/06/2014	3472877	5481987	94	1003		35.0		58.82		11.8	881	6.41	7.11
HD05	05/06/2014	3473221	5472768	127	1003		12.0				14.6	1218	6.36	6.93
HD06	10/06/2014	3469496	5473911	104			153.0			25	15.0	440	4.31	7.41
HD07	10/06/2014	3472401	5471786	106		10.09	15.7	13.0	0.22	30	12.5	1237	1.75	6.94
HD08	11/06/2014	3472824	5481793	107			204.0		64.10	active	12.5	813	2.86	7.21
HD09	11/06/2014	3474054	5479050	106			44.0			active	12.6	851	3.24	7.20
HD10	11/06/2014	3474436	5483887	104			40.0	36.0	41.67	active	12.9	965	3.98	7.07
HD11	11/06/2014	3473671	5483017	107			22.0			active	13.2	932	6.23	7.11
HD12	12/06/2014	3478619	5474895	117		6.86	50.2		0.50	195	14.7	523	7.21	6.96
HD13	17/06/2014	3477328	5482171	159			26.4			active	14.5	457	8.24	6.78
HD14	17/06/2014	3475551	5480498	106		13.35	17.7	16.5		30	13.1	850	7.18	7.11
HD15	17/06/2014	3476273	5469229	109		8.73	18.8	11.0	0.33	40	12.2	1068	0.00	6.97
HD16	17/06/2014	3477611	5471842	109		13.95	25.3	16.0	0.50	70	13.9	796	7.85	7.08
HD17	18/06/2014	3476266	5464821	108		5.31	15.9	7.5	0.50	30	12.3	929	0.14	7.00
HD18	18/06/2014	3476266	5464821	108		5.81	65.0	8.0	0.58	20	12.0	1082	0.78	6.90
HD19	18/06/2014	3476952	5477414	113		13.37	29.2	16.0	0.58	100	14.2	1309	5.44	6.83
MM	03/02/2015	3474212	5488437				1050.0			active	60.5	1.25E+05	0.00	5.45
QWB1	25/07/2014	3459324	5544670	117			29.1		0.01	artesian	13.5	4040	0.05	6.85
QWB2	25/07/2014	3459116	5544291	116			5.6			artesian	14.0	2030	0.00	6.97
T01	17/06/2013	3408013	5316900				858.00			active	44.7	4540	0.00	5.96
T02	19/06/2013	3407925	5316837	232	985		579.00		31.14	active	29.1	852	0.00	7.06
T03	17/06/2013	3402113	5309672				610.00			active	37.0	5080	0.00	5.94
T04	17/06/2013	3402350	5309827	244	984		597.00		123.48	active	39.3	4510	0.00	5.95
T05	18/06/2013	3402330	5309778	262	989		648.00			active	39.0	4710	0.00	6.04
T06	18/06/2013	3391332	5288367	242	987		650.00		2.87	active	39.1	8630	0.00	6.22
T07	18/06/2013	3391384	5288895	223	986		650.00		2.98	active	37.3	7700	0.00	6.26
T08	18/06/2013	3391400	5288658	196	985		488.00		2.15	active	36.6	7460	0.00	6.28
T09	19/06/2013	3400683	5296795	431	963		364.00			artesian	25.6	478	5.41	7.46
T10	19/06/2013	3392141	5292233	225	984		487.00			active	32.1	7750	0.00	6.07

Table C.8: Complete dataset for ^{3}H, stable isotopes and ^{222}Rn.

ID	^{3}H	Δ	δ^{18}O	Δ	δ^{2}H	Δ	^{222}Rn	Δ
	[TU]		[‰]		[‰]		[Bq/m^3]	
FR01	6.60	1.12	-9.50	0.01	-66.11	0.11	5395	485
FR02	16.09	1.10	-10.86	0.05	-76.89	0.31	5008	465
FR03	6.67	1.07	-8.75	0.02	-61.35	0.06	5941	511
FR04	8.66	1.08	-8.80	0.01	-62.06	0.05	8210	612
FR05	7.81	1.08	-8.74	0.04	-60.60	0.10	7195	569
FR06	11.66	1.22	-8.46	0.02	-60.06	0.03	11805	759
FR07	8.71	1.08	-8.46	0.02	-59.73	0.12	6563	540
FR08	9.99	1.18	-8.68	0.02	-61.89	0.17	17343	962
FR09	8.95	1.10	-8.40	0.03	-59.55	0.04	9089	651
FR10	7.84	1.04	-8.41	0.03	-60.10	0.08	10250	698
FR11	6.69	1.16	-8.82	0.02	-61.66	0.04	8337	648
FR12			-8.87	0.02	-61.83	0.04	5779	507
FR13			-8.27	0.02	-58.24	0.17	17223	1118
FR14			-8.44	0.00	-59.37	0.03	16922	947
FR15			-8.52	0.05	-59.85	0.07	5416	484
FR16	18.03	1.06	-8.61	0.03	-61.27	0.06	5017	465
FR17			-8.38	0.02	-58.82	0.06	7067	563
FR18			-9.17	0.01	-63.89	0.09	10269	699
GG01	9.34	1.06	-7.45	0.02	-53.23	0.08	1802	271
GG02	3.92	0.58	-8.21	0.02	-59.01	0.08	765	174
GG03	7.73	0.91					2471	336
GG04	6.10	0.75	-7.74	0.03	-54.91	0.07	1102	211
GG04b			-7.85	0.02	-55.77	0.10		
GG05	10.55	0.43	-7.37	0.02	-52.11	0.05	1172	219
GG05b			-7.43	0.04	-52.75	0.08		
GG06	8.62	0.37	-3.46	0.04	-34.78	0.05	2056	375
GG07	3.82	0.19	-8.15	0.03	-57.89	0.07	1889	277
GG08	7.01	0.31	-7.80	0.03	-55.66	0.05	1266	245
GG09	7.56	0.43	-6.96	0.03	-51.10	0.07	3662	396
GG10	7.30	0.32	-7.64	0.02	-54.00	0.05	2215	301
GG11	3.53	0.19	-7.87	0.02	-55.95	0.05	1820	272
GG11b			-7.77	0.03	-55.29	0.04		
GG12			-7.77	0.02	-56.22	0.09	2115	311
GG12b	6.77	0.19	-7.86	0.12	-56.33	0.49		
GG13	7.84	1.13	-7.98	0.02	-57.06	0.11	3822	403
GG14	3.72	1.02	-7.89	0.03	-56.29	0.09	1994	285
GG15			-7.88	0.02	-56.30	0.06	1956	437
GG15b	6.85	0.19	-7.78	0.05	-55.61	0.02		
GG16	5.36	1.01	-8.13	0.06	-57.46	0.14	20128	1116
GG17	3.13	1.00	-8.17	0.03	-57.40	0.06	26173	1412
GG18	4.46	1.01	-8.28	0.01	-58.03	0.04	1574	281
GG19	2.03	0.99	-8.21	0.02	-57.92	0.05	2364	366
GG20	5.71	1.02	-7.68	0.01	-54.66	0.05	7721	637
GG21			-7.22	0.04	-52.57	0.16	2520	348
GG21b	9.57	0.32	-7.62	0.13	-53.76	0.38		
GG22	4.24	0.94	-6.77	0.12	-50.54	0.28	1571	253
GG23	9.35	1.08	-8.57	0.04	-62.74	0.07	2412	316
GG24	6.30	1.02	-6.57	0.02	-47.37	0.06	737	181
GG25	7.56	0.22	-7.99	0.03	-56.62	0.44		
GG26	1.87	0.07	-8.51	0.09	-60.61	0.19		
GG27	3.61	0.11	-7.91	0.13	-57.78	0.36		
GG28	8.43	0.23	-7.58	0.09	-53.55	0.36		
GG29	5.65	3.22	-7.91	0.02	-56.62	0.05		
GG30	7.02	0.25	-8.51	0.01	-59.44	0.02		
GG31	5.96	0.17	-8.62	0.02	-60.53	0.10		
GG32			-7.33	0.03	-51.99	0.03		
GG33	5.03	0.15	-8.38	0.04	-59.38	0.09		
GG34	2.08	0.11	-7.92	0.02	-56.61	0.05		
GG35	2.93	0.09	-7.88	0.18	-56.75	0.19		
GG35b								
HD01	40.82	1.38	-8.62	0.04	-60.13	0.10	2269	306
HD02	55.05	1.62	-8.63	0.01	-60.54	0.08	3427	263
HD03	7.94	0.94	-7.93	0.01	-55.03	0.04	1293	245
HD04	7.51	0.94	-8.08	0.03	-56.07	0.05	5837	517
HD05	7.41	1.01	-7.89	0.07	-55.23	0.25	2258	469
HD06	below limit	0.00	-8.44	0.03	-59.37	0.05	3262	391
HD07	8.08	1.05	-7.99	0.03	-55.69	0.07	2160	343
HD08	11.79	1.11	-8.53	0.02	-58.94	0.05	4753	528
HD09	47.19	1.49	-8.64	0.03	-59.98	0.09	3526	455
HD10	7.80	0.99	-8.41	0.02	-58.09	0.07	5087	590
HD11	5.68	0.90	-8.39	0.02	-57.73	0.07	5245	710
HD12	3.49	0.96	-8.83	0.01	-59.37	0.06	11288	795
HD13	6.67	0.97	-8.70	0.02	-58.62	0.04		
HD14	5.45	1.03	-8.45	0.02	-57.39	0.03	4030	416
HD15	5.24	0.96	-7.99	0.03	-55.60	0.05	2996	353
HD16	7.40	1.03	-8.71	0.08	-59.44	0.06	4453	456
HD17	6.04	0.87	-8.14	0.04	-56.23	0.17	3359	375
HD18	9.07	1.07	-8.06	0.11	-56.01	0.19	3715	399
HD19	10.10	1.09	-8.22	0.08	-56.90	0.13	4733	522
MM			-3.47	0.07	-47.39	0.24	620	158
QWB1	14.10	1.09	-10.28	0.14	-68.99	0.24	11145	741
QWB2	9.27	0.98	-9.45	0.08	-66.02	0.26	3355	264
T01			-10.79	0.11	-74.65	0.41	4107	420
T02			-9.49	0.08	-65.79	0.12	734	170
T03			-10.92	0.05	-77.04	0.35	629	190
T04			-10.90	0.04	-77.26	0.31	2474	372
T05			-10.99	0.06	-76.92	0.35	1505	283
T06			-10.13	0.08	-74.86	0.25	1757	290
T07			-9.96	0.05	-74.07	0.38	735	170
T08			-10.29	0.06	-74.98	0.09		
T09	6.36	0.84	-10.00	0.05	-68.56	0.06		
T10			-10.40	0.01	-74.59	0.19	985	195

Table C.9: Noble gas isotope data of all samples analysed for this study, in cm^3STP/g.

ID	^3He	Δ	^4He	Δ	^{20}Ne	Δ	^{22}Ne	Δ	^{36}Ar	Δ	^{40}Ar	Δ	^{84}Kr	Δ	^{132}Xe	Δ
	[cm^3STP/g]		[cm^3STP/g]		[cm^3STP/g]		[cm^3STP/g]		[cm^3STP/g]		[cm^3STP/g]		[cm^3STP/g]		[cm^3STP/g]	
FR01	7.78E-14	2.13E-15	5.54E-08	5.63E-10	2.13E-07	6.40E-10	2.18E-08	6.86E-11	1.36E-06	1.65E-08	4.04E-04	7.56E-07	5.30E-08	3.05E-10	3.49E-09	4.57E-11
FR02	4.39E-13	1.45E-14	6.69E-08	6.86E-10	2.23E-07	6.70E-10	2.28E-08	7.14E-11	1.34E-06	1.68E-08	3.90E-04	7.56E-07	5.07E-08	2.97E-10	3.28E-09	4.24E-11
FR03	7.77E-14	2.10E-15	5.15E-08	5.23E-10	1.93E-07	5.81E-10	1.97E-08	6.17E-11	1.26E-06	1.61E-08	3.80E-04	7.12E-07	5.01E-08	2.73E-10	3.44E-09	4.52E-11
FR04	7.19E-14	5.10E-15	5.21E-08	3.03E-10	1.96E-07	6.53E-10	2.01E-08	7.43E-11	1.27E-06	1.69E-08	3.76E-04	9.04E-07	5.01E-08	4.54E-10	3.33E-09	5.72E-11
FR05	8.83E-14	2.29E-15	5.56E-08	5.66E-10	2.06E-07	6.22E-10	2.09E-08	6.66E-11	1.33E-06	1.75E-08	3.94E-04	7.39E-07	5.20E-08	3.19E-10	3.48E-09	4.64E-11
FR06	8.44E-14	2.32E-15	6.00E-08	6.14E-10	2.23E-07	6.71E-10	2.28E-08	7.12E-11	1.37E-06	1.59E-08	3.96E-04	7.58E-07	5.11E-08	2.77E-10	3.39E-09	4.64E-11
FR07	8.55E-14	2.36E-15	5.65E-08	5.78E-10	2.01E-07	6.04E-10	2.05E-08	6.41E-11	1.32E-06	1.65E-08	3.84E-04	7.26E-07	5.09E-08	2.75E-10	3.37E-09	4.31E-11
FR08	7.22E-14	5.23E-15	4.97E-08	2.88E-10	1.91E-07	6.31E-10	1.95E-08	7.18E-11	1.28E-06	1.67E-08	3.72E-04	9.00E-07	5.03E-08	4.94E-10	3.21E-09	5.42E-11
FR09	7.77E-14	2.16E-15	5.92E-08	7.40E-10	1.99E-07	6.00E-10	2.04E-08	6.36E-11	1.30E-06	1.60E-08	3.81E-04	7.13E-07	5.04E-08	2.45E-10	3.34E-09	4.43E-11
FR10	8.55E-14	2.31E-15	6.02E-08	6.18E-10	2.21E-07	6.65E-10	2.26E-08	7.05E-11	1.39E-06	1.58E-08	4.08E-04	7.59E-07	5.35E-08	2.83E-10	3.50E-09	4.68E-11
FR11	7.35E-14	2.03E-15	5.14E-08	5.21E-10	1.94E-07	5.87E-10	1.98E-08	6.24E-11	1.29E-06	1.62E-08	3.77E-04	7.17E-07	5.04E-08	2.60E-10	3.41E-09	4.78E-11
FR12	6.61E-14	1.41E-15	4.90E-08	7.86E-10	1.91E-07	5.94E-10	1.95E-08	6.18E-11	1.30E-06	2.28E-08	3.87E-04	1.14E-06	5.17E-08	4.82E-10	3.47E-09	4.56E-11
FR13	7.66E-14	2.04E-15	5.04E-08	5.12E-10	1.90E-07	5.73E-10	1.94E-08	6.21E-11	1.24E-06	1.56E-08	3.71E-04	7.05E-07	4.95E-08	2.75E-10	3.31E-09	4.19E-11
FR14	1.16E-13	3.29E-15	5.75E-08	5.86E-10	2.11E-07	6.33E-10	2.15E-08	6.71E-11	1.33E-06	1.59E-08	3.97E-04	7.41E-07	5.24E-08	2.74E-10	3.48E-09	4.51E-11
FR15	7.90E-14	2.15E-15	5.11E-08	5.19E-10	1.92E-07	5.78E-10	1.96E-08	6.13E-11	1.28E-06	1.56E-08	3.79E-04	7.27E-07	5.02E-08	2.89E-10	3.35E-09	4.31E-11
FR16	7.26E-14	2.02E-15	5.21E-08	5.29E-10	1.97E-07	5.92E-10	2.02E-08	6.34E-11	1.30E-06	1.66E-08	3.78E-04	6.99E-07	4.98E-08	2.63E-10	3.32E-09	4.29E-11
FR17	8.50E-14	2.38E-15	5.92E-08	6.05E-10	2.19E-07	6.56E-10	2.23E-08	7.02E-11	1.35E-06	1.64E-08	3.99E-04	7.71E-07	5.24E-08	3.12E-10	3.42E-09	4.51E-11
FR18	8.10E-14	2.13E-15	5.83E-08	5.95E-10	2.16E-07	6.47E-10	2.20E-08	6.88E-11	1.31E-06	1.62E-08	3.94E-04	7.57E-07	5.17E-08	2.79E-10	3.45E-09	4.45E-11
GG01	5.31E-13	1.82E-14	7.15E-07	4.07E-09	1.41E-07	6.86E-10	1.44E-08	7.05E-11	1.20E-06	1.23E-08	3.55E-04	1.18E-06	5.15E-08	6.88E-10	3.36E-09	7.72E-11
GG02	1.26E-12	4.41E-14	1.80E-06	1.13E-08	2.26E-07	1.09E-09	2.31E-08	1.11E-10	1.47E-06	1.40E-08	4.28E-04	1.39E-06	5.71E-08	7.32E-10	3.60E-09	9.41E-11
GG03	6.58E-12	2.02E-13	1.09E-05	8.67E-08	1.72E-07	5.71E-10	1.76E-08	5.09E-11	1.30E-06	1.66E-08	3.79E-04	6.54E-07	5.29E-08	9.00E-10	3.37E-09	9.99E-11
GG04	1.52E-13	5.26E-15	1.48E-07	9.08E-10	1.78E-07	8.48E-10	1.82E-08	8.78E-11	1.31E-06	1.19E-08	3.85E-04	1.27E-06	5.23E-08	6.77E-10	3.34E-09	7.64E-11
GG04b	1.50E-13	5.32E-15	1.36E-07	1.38E-09	1.84E-07	6.36E-10	1.88E-08	6.86E-11	1.32E-06	2.50E-08	3.91E-04	1.05E-06	5.34E-08	5.90E-10	3.41E-09	7.77E-11
GG05	1.24E-12	4.46E-14	1.73E-06	1.09E-08	1.56E-07	7.46E-10	1.59E-08	7.77E-11	1.19E-06	1.14E-08	3.56E-04	1.15E-06	4.96E-08	6.19E-10	3.25E-09	7.70E-11
GG05b	1.19E-12	3.93E-14	2.03E-06	2.27E-08	1.53E-07	5.30E-10	1.56E-08	5.76E-11	1.20E-06	2.52E-08	3.54E-04	1.00E-06	4.99E-08	5.19E-10	3.28E-09	7.39E-11
GG06	7.74E-14	2.68E-15	5.50E-08	3.13E-10	2.11E-07	1.02E-09	2.16E-08	1.03E-10	1.34E-06	1.25E-08	3.90E-04	1.25E-06	5.13E-08	8.36E-10	3.36E-09	1.43E-10
GG07	9.39E-14	3.28E-15	4.53E-08	2.62E-10	1.72E-07	8.39E-10	1.76E-08	8.39E-11	1.28E-06	1.20E-08	3.80E-04	1.24E-06	5.20E-08	7.07E-10	3.42E-09	8.27E-11
GG08	7.14E-14	2.52E-15	5.38E-08	3.11E-10	2.00E-07	9.66E-10	2.03E-08	9.74E-11	1.22E-06	1.17E-08	3.58E-04	1.15E-06	4.80E-08	6.30E-10	3.15E-09	7.49E-11
GG09	9.58E-14	3.20E-15	7.29E-08	4.14E-10	2.25E-07	1.14E-09	2.30E-08	1.14E-10	1.31E-06	1.19E-08	3.85E-04	1.24E-06	5.04E-08	7.03E-10	3.35E-09	8.15E-11
GG10	8.04E-14	2.95E-15	4.79E-08	2.81E-10	1.75E-07	8.42E-10	1.79E-08	8.49E-11	1.23E-06	1.17E-08	3.51E-04	1.13E-06	4.64E-08	6.22E-10	3.01E-09	7.61E-11
GG11	7.65E-12	2.70E-13	1.27E-05	7.85E-08	2.01E-07	1.01E-09	2.07E-08	1.03E-10	1.42E-06	1.27E-08	4.18E-04	1.35E-06	5.64E-08	7.79E-10	3.74E-09	9.01E-11
GG11b	4.60E-12	1.63E-13	7.57E-06	7.45E-08	1.97E-07	6.79E-10	2.01E-08	7.32E-11	1.39E-06	2.43E-08	4.16E-04	1.12E-06	5.65E-08	6.27E-10	3.57E-09	8.83E-11
GG12	1.67E-13	5.76E-15	1.70E-07	1.28E-09	2.03E-07	1.01E-09	2.08E-08	1.04E-10	1.27E-06	1.22E-08	3.75E-04	1.20E-06	4.99E-08	6.74E-10	3.19E-09	7.29E-11
GG12b	1.91E-13	6.52E-15	2.03E-07	2.20E-09	2.01E-07	6.96E-10	2.05E-08	7.53E-11	1.26E-06	2.44E-08	3.75E-04	1.05E-06	4.96E-08	5.82E-10	3.38E-09	8.02E-11
GG13	1.32E-13	4.47E-15	6.54E-08	3.83E-10	1.85E-07	9.12E-10	1.89E-08	8.97E-11	1.33E-06	1.23E-08	3.93E-04	1.29E-06	5.35E-08	7.22E-10	3.60E-09	8.33E-11
GG14	7.26E-14	2.60E-15	3.62E-08	2.15E-10	1.45E-07	7.20E-10	1.48E-08	7.19E-11	1.18E-06	1.40E-08	3.48E-04	1.14E-06	4.84E-08	6.44E-10	3.24E-09	7.65E-11
GG15	1.09E-13	3.81E-15	5.17E-08	3.06E-10	1.92E-07	1.17E-09	1.95E-08	1.24E-10	1.29E-06	1.20E-08	3.79E-04	1.22E-06	5.10E-08	6.63E-10	3.34E-09	8.03E-11
GG15b	9.72E-14	3.26E-15	5.42E-08	5.07E-10	1.98E-07	6.85E-10	2.03E-08	7.39E-11	1.30E-06	2.43E-08	3.84E-04	1.05E-06	5.22E-08	5.83E-10	3.30E-09	7.70E-11
GG16	1.91E-13	6.68E-15	3.03E-07	1.99E-09	1.47E-07	7.12E-10	1.50E-08	7.24E-11	1.14E-06	1.20E-08	3.36E-04	1.09E-06	4.66E-08	6.31E-10	3.16E-09	7.09E-11
GG17	2.15E-13	7.61E-15	3.39E-07	2.23E-09	1.47E-07	7.25E-10	1.49E-08	7.54E-11	1.15E-06	1.16E-08	3.38E-04	1.09E-06	4.80E-08	6.01E-10	3.14E-09	7.27E-11
GG18	1.38E-12	4.77E-14	2.01E-06	1.28E-08	2.28E-07	1.10E-09	2.33E-08	1.12E-10	1.46E-06	1.30E-08	4.33E-04	1.38E-06	5.72E-08	7.44E-10	3.86E-09	1.00E-10
GG19	1.03E-13	3.59E-15	5.20E-08	3.17E-10	1.54E-07	7.54E-10	1.58E-08	7.57E-11	1.21E-06	1.17E-08	3.58E-04	1.20E-06	4.99E-08	6.50E-10	3.33E-09	7.81E-11
GG20	2.38E-13	8.38E-15	6.13E-07	4.59E-09	2.16E-07	1.07E-09	2.20E-08	1.10E-10	1.40E-06	1.25E-08	4.04E-04	1.31E-06	5.35E-08	7.23E-10	3.51E-09	8.44E-11
GG21	2.24E-13	7.78E-15	4.06E-07	2.72E-09	1.78E-07	8.54E-10	1.82E-08	8.88E-11	1.33E-06	1.44E-08	3.93E-04	1.28E-06	5.40E-08	7.57E-10	3.70E-09	8.53E-11
GG21b					2.02E-07	7.13E-10	2.07E-08	7.63E-11	1.40E-06	2.54E-08	4.16E-04	1.15E-06	5.69E-08	6.05E-10	3.63E-09	8.34E-11
GG22	5.44E-12	1.88E-13	9.49E-06	5.69E-08	1.62E-07	7.87E-10	1.66E-08	7.97E-11	1.27E-06	1.21E-08	3.83E-04	1.22E-06	5.27E-08	6.63E-10	3.42E-09	7.82E-11
GG23	2.84E-13	1.04E-14	2.12E-07	1.34E-09	2.20E-07	1.22E-09	2.25E-08	1.22E-10	1.41E-06	1.27E-08	4.17E-04	1.35E-06	5.50E-08	7.33E-10	3.72E-09	9.92E-11
GG24	5.61E-14	2.11E-15	3.31E-08	1.94E-10	1.27E-07	6.42E-10	1.30E-08	6.31E-11	1.14E-06	1.39E-08	3.38E-04	1.09E-06	4.78E-08	6.30E-10	3.09E-09	7.53E-11
GG25	2.14E-11	8.26E-13	3.90E-05	4.56E-07	2.45E-07	8.56E-10	2.50E-08	9.28E-11	1.61E-06	2.56E-08	4.79E-04	1.30E-06	6.52E-08	7.12E-10	4.37E-09	1.08E-10
GG26	2.69E-11	1.04E-12	4.71E-05	5.67E-07	2.11E-07	7.31E-10	2.16E-08	7.94E-11	1.53E-06	2.57E-08	4.40E-04	1.21E-06	5.94E-08	6.72E-10	3.92E-09	8.63E-11
GG27	1.47E-11	5.31E-13	2.52E-05	2.92E-07	1.82E-07	6.28E-10	1.85E-08	6.85E-11	1.35E-06	2.58E-08	3.99E-04	1.11E-06	5.42E-08	5.93E-10	3.59E-09	7.97E-11
GG28	7.34E-12	2.48E-13	1.20E-05	1.26E-07	1.79E-07	6.20E-10	1.83E-08	6.70E-11	1.33E-06	2.60E-08	4.02E-04	1.10E-06	5.59E-08	6.95E-10	3.58E-09	7.70E-11
GG29	1.37E-12	4.86E-14	2.10E-06	2.36E-08	2.09E-07	7.25E-10	2.14E-08	7.82E-11	1.42E-06	2.54E-08	4.10E-04	1.11E-06	5.55E-08	6.00E-10	3.67E-09	8.06E-11
GG30	5.85E-14	2.07E-15	4.63E-08	4.31E-10	1.77E-07	6.15E-10	1.81E-08	6.67E-11	1.21E-06	2.37E-08	3.59E-04	9.79E-07	4.90E-08	5.44E-10	3.07E-09	7.24E-11
GG31	6.63E-14	2.46E-15	5.33E-08	4.99E-10	1.80E-07	6.24E-10	1.84E-08	6.74E-11	1.37E-06	2.42E-08	3.82E-04	1.03E-06	5.29E-08	5.42E-10	3.49E-09	8.52E-11
GG32	1.06E-13	3.61E-15	9.58E-08	9.25E-10	1.43E-07	5.01E-10	1.46E-08	5.38E-11	1.11E-06	2.38E-08	3.33E-04	9.10E-07	4.79E-08	5.38E-10	3.10E-09	6.95E-11
GG33	6.38E-13	2.02E-14	9.30E-07	9.15E-09	2.00E-07	7.24E-10	2.04E-08	7.80E-11	1.39E-06	2.52E-08	4.10E-04	1.10E-06	5.56E-08	5.77E-10	3.58E-09	9.70E-11
GG34	1.03E-12	3.44E-14	1.60E-06	1.73E-08	2.11E-07	7.32E-10	2.16E-08	7.93E-11	1.43E-06	2.53E-08	4.25E-04	1.15E-06	5.71E-08	6.12E-10	3.59E-09	7.82E-11
GG35	1.08E-11	3.78E-13	1.73E-05	1.94E-07	2.14E-07	7.40E-10	2.18E-08	8.27E-11	1.45E-06	2.53E-08	4.34E-04	1.18E-06	5.75E-08	6.56E-10	3.67E-09	9.00E-11
GG35b	7.00E-12	1.17E-13	1.32E-05	7.89E-08	1.73E-07	4.40E-10	1.77E-08	5.08E-11	1.26E-06	2.05E-08	3.71E-04	8.65E-07	5.06E-08	4.53E-10	3.54E-09	7.12E-11
HD01	1.09E-13	1.74E-15	5.07E-08	2.95E-10	1.93E-07	4.90E-10	1.98E-08	5.64E-11	1.27E-06	2.08E-08	3.73E-04	8.74E-07	4.95E-08	5.10E-10	3.32E-09	6.57E-11
HD02	1.00E-13	1.58E-15	5.29E-08	4.39E-10	1.98E-07	5.00E-10	2.02E-08	5.75E-11	1.29E-06	2.17E-08	3.76E-04	8.66E-07	4.96E-08	4.68E-10	3.36E-09	7.30E-11
HD03	8.04E-14	1.39E-15	4.63E-08	2.69E-10	1.82E-07	4.61E-10	1.85E-08	5.36E-11	1.29E-06	2.06E-08	3.79E-04	8.78E-07	5.13E-08	4.56E-10	3.49E-09	6.96E-11
HD04	1.08E-13	1.57E-15	5.15E-08	1.88E-10	1.97E-07	4.49E-10	2.01E-08	4.67E-11	1.31E-06	1.53E-08	3.88E-04	1.09E-06	5.21E-08	4.06E-10	3.54E-09	7.13E-11
HD05	7.36E-14	1.30E-15	4.72E-08	2.82E-10	1.81E-07	4.61E-10	1.85E-08	5.32E-11	1.23E-06	2.09E-08	3.63E-04	8.48E-07	4.82E-08	4.82E-10	3.30E-09	6.50E-11
HD06	7.64E-14	3.15E-15	5.31E-08	4.42E-10	1.96E-07	1.03E-09	2.01E-08	1.07E-10	1.32E-06	1.67E-08	3.89E-04	2.66E-06	5.41E-08	2.08E-09	3.52E-09	1.80E-10
HD07	1.01E-13	1.66E-15	4.64E-08	2.74E-10	1.82E-07	4.63E-10	1.86E-08	5.33E-11	1.28E-06	2.12E-08	3.75E-04	8.82E-07	5.06E-08	4.44E-10	3.46E-09	7.29E-11
HD08	2.05E-13	4.05E-15	9.04E-08	5.27E-10	2.06E-07	5.20E-10	2.10E-08	5.97E-11	1.35E-06	2.16E-08	3.99E-04	9.36E-07	5.28E-08	5.04E-10	3.64E-09	7.32E-11
HD09	9.31E-14	1.56E-15	5.24E-08	3.04E-10	1.99E-07	5.05E-10	2.04E-08	5.80E-11	1.29E-06	2.21E-08	3.85E-04	8.87E-07	5.12E-08	4.33E-10	3.46E-09	7.12E-11
HD10	1.42E-13	2.19E-15	6.09E-08	3.54E-10	2.27E-07	5.72E-10	2.32E-08	6.60E-11	1.39E-06	2.10E-08	4.03E-04	9.27E-07	5.25E-08	4.77E-10	3.56E-09	7.14E-11
HD11	1.07E-13	1.78E-15	5.81E-08	3.42E-10	2.07E-07	5.24E-10	2.12E-08	6.09E-11	1.31E-06	2.17E-08	3.88E-04	9.02E-07	5.19E-08	4.94E-10	3.39E-09	6.80E-11
HD12	1.09E-13	1.70E-15	6.83E-08	3.95E-10	1.98E-07	5.01E-10	2.02E-08	5.74E-11	1.32E-06	2.16E-08	3.89E-04	9.28E-07	5.22E-08	4.42E-10	3.63E-09	7.55E-11
HD13	7.25E-14	1.21E-15	6.45E-08	3.73E-10	1.94E-07	4.93E-10	1.98E-08	5.65E-11	1.30E-06	2.08E-08	3.87E-04	9.07E-07	5.25E-08	4.83E-10	3.55E-09	7.51E-11
HD14	9.33E-14	1.38E-15	6.43E-08	2.33E-10	2.05E-07	4.67E-10	2.10E-08	4.84E-11	1.24E-06	1.61E-08	3.87E-04	1.09E-06	5.15E-08	3.76E-10	3.53E-09	7.50E-11
HD15	8.72E-14	1.44E-15	5.03E-08	2.93E-10	1.97E-07	5.00E-10	2.02E-08	5.74E-11	1.30E-06	2.25E-08	3.82E-04	8.73E-07	5.10E-08	4.58E-10	3.37E-09	6.69E-11
HD16	8.95E-14	1.20E-15	5.32E-08	1.99E-10	2.00E-07	4.54E-10	2.03E-08	4.71E-11	1.29E-06	1.70E-08	3.82E-04	1.09E-06	5.06E-08	4.09E-10	3.43E-09	6.99E-11
HD17	9.23E-14	1.81E-15	5.64E-08	3.28E-10	2.09E-07	5.28E-10	2.13E-08	6.09E-11	1.32E-06	2.15E-08	3.84E-04	8.79E-07	5.03E-08	4.58E-10	3.36E-09	6.98E-11
HD18	1.24E-13	2.04E-15	6.60E-08	5.46E-10	2.15E-07	5.42E-10	2.21E-08	6.37E-11	1.41E-06	2.18E-08	4.15E-04	9.70E-07	5.49E-08	4.91E-10	3.67E-09	7.18E-11
HD19	8.58E-14	1.71E-15	5.59E-08	3.24E-10	2.04E-07	5.16E-10	2.08E-08	5.86E-11	1.28E-06	2.07E-08	3.75E-04	8.71E-07	4.87E-08	4.49E-10	3.26E-09	6.50E-11
MM	2.95E-11	7.15E-13	4.91E-05	3.05E-07	2.83E-09	1.01E-10	3.11E-10	1.07E-11			2.02E-05	1.53E-07	2.06E-09	1.34E-10	1.55E-10	6.37E-12
QWB1	1.45E-10	2.15E-12	5.93E-05	3.46E-07	3.56E-07	9.03E-10	3.60E-08	1.00E-10	1.80E-06	2.35E-08	5.72E-04	1.30E-06	6.51E-08	5.33E-10	4.41E-09	8.82E-11
QWB2	3.15E-11	4.37E-13	1.25E-05	7.49E-08	2.38E-07	5.99E-10	2.43E-08	6.79E-11	1.50E-06	2.16E-08	4.46E-04	1.04E-06	5.85E-08	4.92E-10	3.89E-09	7.98E-11
T01	2.52E-10	1.12E-11	1.20E-04	8.16E-07	2.52E-07	1.10E-09	2.57E-08	1.11E-10	1.60E-06	1.88E-08	5.24E-04	2.51E-06	6.40E-08	7.23E-10	4.19E-09	9.08E-11
T02	4.19E-12	1.83E-13	2.69E-06	1.89E-08	3.53E-07	1.53E-09	3.60E-08	1.55E-10	1.67E-06	1.92E-08	4.97E-04	2.38E-06	6.35E-08	7.28E-10	4.28E-09	9.06E-11
T03	4.11E-10	1.83E-11	1.54E-04	1.09E-06	2.81E-07	1.22E-09	2.86E-08	1.23E-10	1.66E-06	2.01E-08	5.67E-04	2.73E-06	6.52E-08	6.87E-10	4.18E-09	8.92E-11
T04	3.74E-10	1.66E-11	1.35E-04	9.40E-07	2.45E-07	1.07E-09	2.49E-08	1.07E-10	1.55E-06	1.99E-08	5.32E-04	2.56E-06	6.24E-08	6.78E-10	4.04E-09	1.09E-10
T05	4.04E-10	1.75E-11	1.58E-04	1.12E-06	2.88E-07	1.26E-09	2.93E-08	1.27E-10	1.71E-06	2.01E-08	5.86E-04	2.82E-06	6.89E-08	8.48E-10	4.55E-09	1.08E-10
T06	1.12E-10	4.68E-12	1.66E-04	1.17E-06	2.59E-07	1.13E-09	2.64E-08	1.15E-10	1.62E-06	2.01E-08	5.03E-04	2.42E-06	6.27E-08	7.23E-10	4.27E-09	9.43E-11
T07	1.21E-10	5.12E-12	1.64E-04	1.17E-06	2.62E-07	1.14E-09	2.67E-08	1.15E-10	1.59E-06	1.88E-08	5.07E-04	2.44E-06	6.47E-08	7.59E-10	4.45E-09	1.07E-10
T08	1.01E-10	4.30E-12	1.52E-04	1.07E-06	2.57E-07	1.12E-09	2.62E-08	1.13E-10	1.59E-06	1.86E-08	4.99E-04	2.41E-06	6.31E-08	7.41E-10	4.08E-09	9.07E-11
T09	4.26E-12	2.35E-13	8.65E-06	5.34E-08	1.81E-07	8.08E-10	1.85E-08	8.25E-11	1.23E-06	1.76E-08	3.68E-04	1.80E-06	4.98E-08	5.38E-10	3.30E-09	6.81E-11
T10	1.22E-10	5.08E-12	8.91E-05	5.64E-07	2.63E-07	1.15E-09	2.69E-08	1.16E-10	1.63E-06	2.03E-08	5.27E-04	2.55E-06	6.46E-08	6.65E-10	4.54E-09	1.01E-10

Table C.10: Noble gas ratio and elemental concentration data, as obtained from the *WuCem* software and calculated according to Table 5.1.

ID	$^3He/^4He$	Δ	$^{20}Ne/^4He$	Δ	$^{20}Ne/^{22}Ne$	Δ	$^{40}Ar/^{36}Ar$	Δ	He	Δ	Ne	Δ	Ar	Δ	Kr	Δ	Xe	Δ
	[R/R_a]								[cm^3STP/g]		[cm^3STP/g]		[cm^3STP/g]		[cm^3STP/g]		[cm^3STP/g]	
FR01	1.01	0.08	3.8462	0.0408	9.781	0.003	296.8	3.6	5.54E-08	5.63E-10	2.35E-07	6.45E-10	4.06E-04	7.59E-07	9.31E-08	5.34E-10	1.30E-08	1.70E-10
FR02	4.73	0.17	3.3378	0.0357	9.778	0.003	291.9	3.7	6.69E-08	6.86E-10	2.47E-07	6.75E-10	3.92E-04	7.59E-07	8.90E-08	5.22E-10	1.22E-08	1.58E-10
FR03	1.09	0.08	3.7475	0.0397	9.783	0.003	300.7	3.9	5.15E-08	5.23E-10	2.13E-07	5.86E-10	3.81E-04	7.15E-07	8.78E-08	4.79E-10	1.28E-08	1.68E-10
FR04	0.99	0.10	3.7660	0.0252	9.770	0.006	296.1	4.0	5.21E-08	3.03E-10	2.17E-07	6.59E-10	3.78E-04	9.08E-07	8.79E-08	7.96E-10	1.24E-08	2.13E-10
FR05	1.14	0.08	3.6990	0.0392	9.848	0.003	296.1	3.9	5.56E-08	5.66E-10	2.27E-07	6.27E-10	3.95E-04	7.42E-07	9.13E-08	5.60E-10	1.30E-08	1.73E-10
FR06	1.01	0.08	3.7203	0.0397	9.785	0.003	289.7	3.4	6.00E-08	6.14E-10	2.47E-07	6.77E-10	3.98E-04	7.61E-07	8.97E-08	4.87E-10	1.26E-08	1.72E-10
FR07	1.09	0.08	3.5666	0.0380	9.813	0.003	291.0	3.7	5.65E-08	5.78E-10	2.23E-07	6.09E-10	3.86E-04	7.29E-07	8.93E-08	4.83E-10	1.25E-08	1.60E-10
FR08	1.05	0.11	3.8358	0.0256	9.798	0.006	290.0	3.8	4.97E-08	2.88E-10	2.11E-07	6.37E-10	3.74E-04	9.03E-07	8.83E-08	8.66E-10	1.19E-08	2.01E-10
FR09	0.94	0.07	3.3709	0.0434	9.790	0.003	292.0	3.6	5.92E-08	7.40E-10	2.20E-07	6.05E-10	3.82E-04	7.16E-07	8.83E-08	4.29E-10	1.24E-08	1.65E-10
FR10	1.02	0.07	3.6734	0.0393	9.791	0.003	294.4	3.4	6.02E-08	6.18E-10	2.45E-07	6.70E-10	4.10E-04	7.62E-07	9.38E-08	4.96E-10	1.30E-08	1.74E-10
FR11	1.03	0.09	3.7802	0.0400	9.795	0.003	293.4	3.7	5.14E-08	5.21E-10	2.15E-07	5.92E-10	3.79E-04	7.20E-07	8.85E-08	4.56E-10	1.27E-08	1.78E-10
FR12	0.97	0.03	3.8882	0.0635	9.771	0.006	297.6	5.3	4.90E-08	7.86E-10	2.11E-07	5.99E-10	3.88E-04	1.14E-06	9.07E-08	8.46E-10	1.29E-08	1.70E-10
FR13	1.10	0.03	3.7764	0.0401	9.783	0.003	300.2	3.8	5.04E-08	5.12E-10	2.10E-07	5.78E-10	3.73E-04	7.08E-07	8.69E-08	4.82E-10	1.23E-08	1.56E-10
FR14	1.45	0.04	3.6688	0.0390	9.798	0.003	298.2	3.6	5.75E-08	5.86E-10	2.33E-07	6.38E-10	3.98E-04	7.44E-07	9.19E-08	4.81E-10	1.30E-08	1.68E-10
FR15	1.12	0.03	3.7606	0.0398	9.794	0.003	295.4	3.6	5.11E-08	5.19E-10	2.12E-07	5.83E-10	3.81E-04	7.30E-07	8.81E-08	5.07E-10	1.24E-08	1.60E-10
FR16	1.00	0.08	3.7881	0.0401	9.781	0.003	290.4	3.7	5.21E-08	5.29E-10	2.18E-07	5.97E-10	3.79E-04	7.02E-07	8.74E-08	4.62E-10	1.23E-08	1.60E-10
FR17	1.04	0.03	3.6946	0.0394	9.788	0.003	295.6	3.6	5.92E-08	6.05E-10	2.42E-07	6.62E-10	4.01E-04	7.75E-07	9.18E-08	5.47E-10	1.27E-08	1.68E-10
FR18	1.00	0.03	3.7011	0.0394	9.785	0.003	300.0	3.7	5.83E-08	5.95E-10	2.38E-07	6.53E-10	3.96E-04	7.60E-07	9.07E-08	4.89E-10	1.28E-08	1.65E-10
GG01	0.54	0.02	0.1973	0.0015	9.788	0.004	294.8	3.2	7.15E-07	4.07E-09	1.56E-07	6.92E-10	3.57E-04	1.19E-06	9.04E-08	1.21E-09	1.25E-08	2.87E-10
GG02	0.50	0.02	0.1257	0.0010	9.783	0.004	291.2	2.9	1.80E-06	1.13E-08	2.50E-07	1.10E-09	4.30E-04	1.39E-06	1.00E-07	1.28E-09	1.34E-08	3.50E-10
GG03	0.44	0.01	0.0158	0.0001	9.786	0.007	291.2	3.8	1.09E-05	8.67E-08	1.90E-07	5.75E-10	3.80E-04	6.57E-07	9.27E-08	1.58E-09	1.25E-08	3.72E-10
GG04	0.74	0.03	1.1985	0.0093	9.803	0.004	293.2	2.8	1.48E-07	9.08E-10	1.97E-07	8.55E-10	3.86E-04	1.28E-06	9.17E-08	1.19E-09	1.24E-08	2.84E-10
GG04b	0.80	0.03	1.3554	0.0145	9.788	0.004	297.3	5.7	1.36E-07	1.38E-09	2.04E-07	6.41E-10	3.93E-04	1.05E-06	9.37E-08	1.03E-09	1.27E-08	2.89E-10
GG05	0.52	0.02	0.0902	0.0007	9.798	0.004	299.0	3.0	1.73E-06	1.09E-08	1.72E-07	7.52E-10	3.57E-04	1.15E-06	8.69E-08	1.09E-09	1.21E-08	2.87E-10
GG05b	0.42	0.01	0.0753	0.0009	9.794	0.004	296.2	6.3	2.03E-06	2.27E-08	1.69E-07	5.35E-10	3.56E-04	1.01E-06	8.76E-08	9.11E-10	1.22E-08	2.75E-10
GG06	1.01	0.04	3.8425	0.0287	9.783	0.004	291.4	2.9	5.50E-08	3.13E-10	2.34E-07	1.03E-09	3.92E-04	1.25E-06	9.00E-08	1.47E-09	1.25E-08	5.30E-10
GG07	1.50	0.06	3.8058	0.0288	9.786	0.004	295.6	2.9	4.53E-08	2.62E-10	1.90E-07	8.45E-10	3.81E-04	1.24E-06	9.13E-08	1.24E-09	1.27E-08	3.08E-10
GG08	0.96	0.04	3.7089	0.0280	9.792	0.004	294.6	3.0	5.38E-08	3.11E-10	2.21E-07	9.74E-10	3.60E-04	1.16E-06	8.42E-08	1.10E-09	1.17E-08	2.78E-10
GG09	0.95	0.04	3.0852	0.0235	9.810	0.004	293.3	2.8	7.29E-08	4.14E-10	2.49E-07	1.15E-09	3.86E-04	1.24E-06	8.83E-08	1.23E-09	1.25E-08	3.03E-10
GG10	1.21	0.05	3.6464	0.0277	9.791	0.004	284.8	2.9	4.79E-08	2.81E-10	1.93E-07	8.49E-10	3.52E-04	1.13E-06	8.14E-08	1.09E-09	1.12E-08	2.83E-10
GG11	0.43	0.02	0.0158	0.0001	9.745	0.004	295.4	2.8	1.27E-05	7.85E-08	2.23E-07	1.02E-09	4.20E-04	1.36E-06	9.90E-08	1.37E-09	1.39E-08	3.35E-10
GG11b	0.44	0.02	0.0260	0.0003	9.785	0.004	299.6	5.3	7.57E-06	7.45E-08	2.17E-07	6.85E-10	4.17E-04	1.12E-06	9.91E-08	1.10E-09	1.33E-08	3.28E-10
GG12	0.71	0.03	1.1946	0.0108	9.790	0.004	294.2	3.0	1.70E-07	1.28E-09	2.24E-07	1.01E-09	3.76E-04	1.21E-06	8.76E-08	1.18E-09	1.19E-08	2.71E-10
GG12b	0.68	0.02	0.9904	0.0113	9.790	0.004	296.9	5.8	2.03E-07	2.20E-09	2.22E-07	7.02E-10	3.77E-04	1.06E-06	8.70E-08	1.02E-09	1.26E-08	2.98E-10
GG13	1.46	0.08	2.8272	0.0217	9.791	0.004	294.5	2.9	6.54E-08	3.83E-10	2.04E-07	9.18E-10	3.95E-04	1.29E-06	9.39E-08	1.27E-09	1.34E-08	3.10E-10
GG14	1.45	0.11	4.0137	0.0311	9.786	0.004	295.7	3.6	3.62E-08	2.15E-10	1.61E-07	7.26E-10	3.50E-04	1.14E-06	8.50E-08	1.13E-09	1.21E-08	2.85E-10
GG15	1.53	0.05	3.7014	0.0315	9.792	0.004	293.3	2.9	5.17E-08	3.06E-10	2.12E-07	1.18E-09	3.80E-04	1.23E-06	8.94E-08	1.16E-09	1.24E-08	2.99E-10
GG15b	1.29	0.05	3.6587	0.0364	9.791	0.004	295.8	5.6	5.42E-08	5.07E-10	2.19E-07	6.91E-10	3.86E-04	1.06E-06	9.15E-08	1.02E-09	1.23E-08	2.86E-10
GG16	0.45	0.02	0.4841	0.0040	9.786	0.004	296.2	3.3	3.03E-07	1.99E-09	1.62E-07	7.17E-10	3.38E-04	1.09E-06	8.17E-08	1.11E-09	1.17E-08	2.64E-10
GG17	0.46	0.02	0.4325	0.0036	9.792	0.004	293.4	3.1	3.39E-07	2.23E-09	1.62E-07	7.31E-10	3.39E-04	1.10E-06	8.42E-08	1.05E-09	1.17E-08	2.71E-10
GG18	0.50	0.02	0.1133	0.0009	9.787	0.004	297.1	2.8	2.01E-06	1.28E-08	2.52E-07	1.11E-09	4.35E-04	1.38E-06	1.00E-07	1.31E-09	1.44E-08	3.73E-10
GG19	1.43	0.09	2.9692	0.0232	9.779	0.004	295.6	3.0	5.20E-08	3.17E-10	1.71E-07	7.60E-10	3.59E-04	1.21E-06	8.75E-08	1.14E-09	1.24E-08	2.90E-10
GG20	0.28	0.01	0.3515	0.0032	9.784	0.004	288.7	2.7	6.13E-07	4.59E-09	2.38E-07	1.08E-09	4.06E-04	1.32E-06	9.39E-08	1.27E-09	1.31E-08	3.14E-10
GG21	0.40	0.01	0.4383	0.0036	9.784	0.004	294.0	3.3	4.06E-07	2.72E-09	1.97E-07	8.61E-10	3.94E-04	1.29E-06	9.48E-08	1.33E-09	1.38E-08	3.17E-10
GG21b					9.781	0.004	297.1	5.5			2.24E-07	7.19E-10	4.17E-04	1.16E-06	9.98E-08	1.06E-09	1.35E-08	3.10E-10
GG22	0.41	0.01	0.0171	0.0001	9.785	0.004	301.9	3.0	9.49E-06	5.69E-08	1.79E-07	7.93E-10	3.85E-04	1.23E-06	9.25E-08	1.16E-09	1.27E-08	2.91E-10
GG23	0.96	0.04	1.0357	0.0087	9.784	0.004	295.1	2.8	2.12E-07	1.34E-09	2.43E-07	1.23E-09	4.19E-04	1.35E-06	9.65E-08	1.29E-09	1.38E-08	3.69E-10
GG24	1.22	0.12	3.8490	0.0298	9.786	0.004	297.7	3.8	3.31E-08	1.94E-10	1.41E-07	6.46E-10	3.40E-04	1.09E-06	8.38E-08	1.11E-09	1.15E-08	2.80E-10
GG25	0.40	0.02	0.0063	0.0001	9.784	0.004	298.1	4.8	3.90E-05	4.56E-07	2.70E-07	8.64E-10	4.81E-04	1.30E-06	1.14E-07	1.25E-09	1.63E-08	4.02E-10
GG26	0.41	0.02	0.0045	0.0001	9.786	0.004	287.7	4.9	4.71E-05	5.67E-07	2.34E-07	7.37E-10	4.42E-04	1.22E-06	1.04E-07	1.18E-09	1.46E-08	3.21E-10
GG27	0.42	0.02	0.0072	0.0001	9.806	0.004	295.5	5.7	2.52E-05	2.92E-07	2.01E-07	6.33E-10	4.00E-04	1.12E-06	9.52E-08	1.04E-09	1.34E-08	2.96E-10
GG28	0.44	0.02	0.0149	0.0002	9.791	0.004	302.9	6.0	1.20E-05	1.26E-07	1.98E-07	6.25E-10	3.94E-04	7.72E-06	9.80E-08	1.22E-09	1.33E-08	2.86E-10
GG29	0.47	0.02	0.0995	0.0012	9.784	0.004	289.8	5.3	2.10E-06	2.36E-08	2.31E-07	7.31E-10	4.12E-04	1.11E-06	9.74E-08	1.05E-09	1.36E-08	3.00E-10
GG30	0.91	0.04	3.8300	0.0380	9.796	0.004	297.3	5.9	4.63E-08	4.31E-10	1.96E-07	6.20E-10	3.60E-04	9.83E-07	8.60E-08	9.54E-10	1.14E-08	2.69E-10
GG31	0.90	0.04	3.3848	0.0337	9.810	0.004	279.4	5.0	5.33E-08	4.99E-10	1.99E-07	6.29E-10	3.84E-04	1.03E-06	9.27E-08	9.52E-10	1.30E-08	3.17E-10
GG32	0.80	0.03	1.4911	0.0153	9.792	0.004	299.1	6.5	9.58E-08	9.25E-10	1.58E-07	5.05E-10	3.34E-04	9.13E-07	8.41E-08	9.44E-10	1.15E-08	2.58E-10
GG33	0.50	0.02	0.2148	0.0023	9.793	0.004	294.1	5.4	9.30E-07	9.15E-09	2.21E-07	7.30E-10	4.11E-04	1.10E-06	9.76E-08	1.01E-09	1.33E-08	3.61E-10
GG34	0.47	0.02	0.1319	0.0015	9.783	0.004	296.7	5.3	1.60E-06	1.73E-08	2.34E-07	7.39E-10	4.26E-04	1.15E-06	1.00E-07	1.07E-09	1.33E-08	2.91E-10
GG35	0.45	0.02	0.0123	0.0001	9.787	0.004	299.5	5.3	1.73E-05	1.94E-07	2.36E-07	7.46E-10	4.36E-04	1.18E-06	1.01E-07	1.15E-09	1.37E-08	3.35E-10
GG35b	0.38	0.01	0.0131	0.0001	9.748	0.008	294.8	4.8	1.32E-05	7.89E-08	1.91E-07	4.44E-10	3.73E-04	8.68E-07	8.88E-08	7.96E-10	1.32E-08	2.65E-10
HD01	1.50	0.10	3.8146	0.0242	9.793	0.008	294.6	4.9	5.07E-08	2.95E-10	2.14E-07	4.95E-10	3.75E-04	8.77E-07	8.69E-08	8.95E-10	1.24E-08	2.44E-10
HD02	1.29	0.11	3.7363	0.0324	9.792	0.008	292.2	5.0	5.29E-08	4.39E-10	2.18E-07	5.05E-10	3.77E-04	8.69E-07	8.70E-08	8.22E-10	1.25E-08	2.71E-10
HD03	1.24	0.08	3.9254	0.0249	9.814	0.008	293.9	4.8	4.63E-08	2.69E-10	2.01E-07	4.66E-10	3.81E-04	8.81E-07	9.00E-08	8.00E-10	1.30E-08	2.59E-10
HD04	1.51	0.07	3.8183	0.0165	9.789	0.004	296.1	3.6	5.15E-08	1.88E-10	2.17E-07	4.52E-10	3.89E-04	1.09E-06	9.14E-08	7.12E-10	1.32E-08	2.65E-10
HD05	1.12	0.08	3.8383	0.0249	9.766	0.008	295.3	5.1	4.72E-08	2.82E-10	2.00E-07	4.65E-10	3.64E-04	8.51E-07	8.46E-08	8.45E-10	1.23E-08	2.42E-10
HD06	1.04	0.04	3.6954	0.0363	9.788	0.006	295.8	4.3	5.31E-08	4.42E-10	2.17E-07	1.04E-09	3.91E-04	2.67E-06	9.49E-08	3.64E-09	1.31E-08	6.69E-10
HD07	1.56	0.08	3.9238	0.0252	9.782	0.008	293.0	4.9	4.64E-08	2.74E-10	2.01E-07	4.67E-10	3.77E-04	8.85E-07	8.88E-08	7.79E-10	1.29E-08	2.71E-10
HD08	1.63	0.05	2.2788	0.0145	9.798	0.008	295.7	4.8	9.04E-08	5.27E-10	2.28E-07	5.25E-10	4.01E-04	9.40E-07	9.27E-08	8.84E-10	1.36E-08	2.72E-10
HD09	1.22	0.10	3.8071	0.0241	9.764	0.008	298.0	5.1	5.24E-08	3.04E-10	2.20E-07	5.09E-10	3.86E-04	8.90E-07	8.98E-08	7.60E-10	1.29E-08	2.65E-10
HD10	1.68	0.06	3.7287	0.0236	9.796	0.008	289.0	4.4	6.09E-08	3.54E-10	2.51E-07	5.77E-10	4.04E-04	9.31E-07	9.20E-08	8.37E-10	1.32E-08	2.66E-10
HD11	1.32	0.06	3.5674	0.0228	9.787	0.008	296.4	5.0	5.81E-08	3.42E-10	2.29E-07	5.29E-10	3.90E-04	9.06E-07	9.10E-08	8.67E-10	1.26E-08	2.53E-10
HD12	1.15	0.05	2.8945	0.0182	9.765	0.008	295.3	4.9	6.83E-08	3.95E-10	2.19E-07	5.06E-10	3.91E-04	9.32E-07	9.17E-08	7.76E-10	1.35E-08	2.81E-10
HD13	0.80	0.05	3.0083	0.0190	9.788	0.008	296.6	4.8	6.45E-08	3.73E-10	2.15E-07	4.97E-10	3.89E-04	9.10E-07	9.20E-08	8.47E-10	1.32E-08	2.79E-10
HD14	1.04	0.06	3.1915	0.0137	9.789	0.004	312.6	4.2	6.43E-08	2.33E-10	2.27E-07	4.71E-10	3.68E-04	4.78E-06	9.04E-08	6.59E-10	1.31E-08	2.79E-10
HD15	1.25	0.07	3.9261	0.0250	9.782	0.008	294.2	5.1	5.03E-08	2.93E-10	2.18E-07	5.05E-10	3.84E-04	8.77E-07	8.95E-08	8.03E-10	1.25E-08	2.49E-10
HD16	1.21	0.07	3.7522	0.0164	9.791	0.005	295.2	4.0	5.32E-08	1.99E-10	2.21E-07	4.58E-10	3.84E-04	1.10E-06	8.88E-08	7.18E-10	1.27E-08	2.60E-10
HD17	1.18	0.06	3.7012	0.0235	9.782	0.008	291.3	4.8	5.64E-08	3.28E-10	2.31E-07	5.33E-10	3.86E-04	8.83E-07	8.83E-08	8.03E-10	1.25E-08	2.60E-10
HD18	1.34	0.06	3.2533	0.0281	9.743	0.008	293.9	4.6	6.60E-08	5.46E-10	2.38E-07	5.47E-10	4.17E-04	9.74E-07	9.63E-08	8.62E-10	1.37E-08	2.67E-10
HD19	1.10	0.07	3.6483	0.0231	9.805	0.008	293.3	4.8	5.59E-08	3.24E-10	2.25E-07	5.21E-10	3.77E-04	8.74E-07	8.55E-08	7.87E-10	1.21E-08	2.42E-10
MM	0.43	0.01	0.000058	0.000002	9.569	0.015			4.91E-05	3.05E-07	3.15E-09	1.02E-10	2.03E-05	1.53E-07	3.62E-09	2.36E-10	5.78E-10	2.37E-11
QWB1	1.77	0.03	0.00600	0.00004	9.876	0.008	317.3	4.2	5.93E-05	3.46E-07	3.93E-07	9.11E-10	5.36E-04	6.99E-06	1.14E-07	9.36E-10	1.64E-08	3.28E-10
QWB2	1.83	0.03	0.01910	0.00012	9.790	0.008	298.2	4.4	1.25E-05	7.49E-08	2.63E-07	6.04E-10	4.48E-04	1.04E-06	1.03E-07	8.63E-10	1.45E-08	2.97E-10
T01	1.52	0.07	0.0021	0.0000	9.814	0.006	326.9	4.1	1.20E-04	8.16E-07	2.79E-07	1.11E-09	4.76E-04	5.58E-06	1.12E-07	1.27E-09	1.56E-08	3.38E-10
T02	1.12	0.05	0.1309	0.0011	9.796	0.006	297.6	3.7	2.69E-06	1.89E-08	3.90E-07	1.55E-09	4.99E-04	2.39E-06	1.11E-07	1.28E-09	1.59E-08	3.37E-10
T03	1.93	0.09	0.0018	0.0000	9.822	0.006	342.3	4.5	1.54E-04	1.09E-06	3.10E-07	1.23E-09	4.93E-04	5.99E-06	1.14E-07	1.20E-09	1.55E-08	3.32E-10
T04	2.00	0.09	0.0018	0.0000	9.849	0.006	342.5	4.7	1.35E-04	9.40E-07	2.70E-07	1.08E-09	4.62E-04	5.90E-06	1.10E-07	1.19E-09	1.50E-08	4.05E-10
T05	1.85	0.08	0.0018	0.0000	9.843	0.006	342.5	4.3	1.58E-04	1.12E-06	3.18E-07	1.27E-09	5.09E-04	5.97E-06	1.21E-07	1.49E-09	1.69E-08	4.02E-10
T06	0.49	0.02	0.0016	0.0000	9.815	0.006	311.3	4.2	1.66E-04	1.17E-06	2.86E-07	1.14E-09	4.80E-04	5.99E-06	1.10E-07	1.27E-09	1.59E-08	3.51E-10
T07	0.53	0.02	0.0016	0.0000	9.802	0.006	317.9	4.0	1.64E-04	1.17E-06	2.90E-07	1.15E-09	4.74E-04	5.59E-06	1.14E-07	1.33E-09	1.66E-08	3.98E-10
T08	0.48	0.02	0.0017	0.0000	9.818	0.006	313.1	4.0	1.52E-04	1.07E-06	2.84E-07	1.13E-09	4.74E-04	5.53E-06	1.11E-07	1.30E-09	1.52E-08	3.37E-10
T09	0.36	0.02	0.0210	0.0002	9.789	0.006	297.7	4.5	8.65E-06	5.34E-08	2.00E-07	8.14E-10	3.69E-04	1.80E-06	8.74E-08	9.43E-10	1.23E-08	2.53E-10
T10	0.99	0.04	0.0030	0.0000	9.808	0.006	323.9	4.3	8.91E-05	5.64E-07	2.91E-07	1.16E-09	4.84E-04	6.02E-06	1.13E-07	1.17E-09	1.69E-08	3.76E-10

Table C.11: Results of the UA model fit using *PANGA* with 10^5 Monte Carlo simulations.

ID	χ^2	Prob	A	Δ	T	Δ
		[%]	[cm^3STP/g]		[°C]	
FR01	9.3	0.9	1.82E-03	4.00E-05	9.8	0.1
FR02	3.0	22.6	2.72E-03	4.18E-05	12.3	0.1
FR03	2.4	30.1	7.69E-04	3.65E-05	11.4	0.1
FR04	1.1	56.4	1.05E-03	4.17E-05	12.0	0.1
FR05	0.1	93.9	1.45E-03	3.90E-05	10.5	0.1
FR06	1.8	41.2	2.66E-03	4.18E-05	11.5	0.1
FR07	1.6	46.0	1.32E-03	3.78E-05	11.4	0.1
FR08	8.4	1.5	7.34E-04	4.05E-05	12.2	0.1
FR09	1.0	61.8	1.18E-03	3.74E-05	11.7	0.1
FR10	7.3	2.6	2.38E-03	4.13E-05	9.9	0.1
FR11	5.1	7.9	8.96E-04	3.68E-05	11.7	0.1
FR12	0.7	69.0	5.54E-04	3.86E-05	10.4	0.1
FR13	2.2	33.9	6.76E-04	3.60E-05	12.2	0.1
FR14	0.5	79.1	1.77E-03	3.94E-05	10.5	0.1
FR15	2.2	32.8	7.15E-04	3.63E-05	11.4	0.1
FR16	0.4	81.2	1.10E-03	3.70E-05	12.0	0.1
FR17	3.9	14.4	2.30E-03	4.11E-05	10.8	0.1
FR18	0.2	91.5	2.11E-03	4.04E-05	11.1	0.1
GG01	10.4	0.5	-2.46E-03	4.48E-05	10.6	0.1
GG02	9.4	0.9	2.43E-03	6.89E-05	7.8	0.2
GG03	5.1	7.9	-6.45E-04	3.65E-05	10.0	0.1
GG04	9.2	1.0	-2.71E-04	5.44E-05	9.8	0.2
GG04b	8.3	1.6	5.61E-05	4.13E-05	9.3	0.1
GG05	3.6	16.3	-1.46E-03	4.82E-05	11.7	0.2
GG05b	8.5	1.4	-1.64E-03	3.51E-05	11.6	0.1
GG06	0.2	89.6	1.92E-03	6.53E-05	11.4	0.2
GG07	2.6	26.7	-6.53E-04	5.38E-05	9.9	0.2
GG08	9.2	1.0	1.51E-03	6.14E-05	14.8	0.2
GG09	4.1	12.7	2.90E-03	7.19E-05	13.1	0.2
GG10	1.0	61.7	-7.27E-05	5.40E-05	14.1	0.2
GG11	4.1	12.6	8.86E-04	6.42E-05	7.4	0.2
GG11b	14.5	0.1	5.53E-04	4.40E-05	7.4	0.1
GG12	2.9	23.6	1.51E-03	6.35E-05	12.8	0.2
GG12b	2.4	30.4	1.37E-03	4.51E-05	12.5	0.1
GG13	0.6	74.8	2.46E-05	5.81E-05	9.1	0.2
GG14	1.2	55.7	-2.04E-03	4.67E-05	11.9	0.2
GG15	1.6	46.0	7.11E-04	7.34E-05	11.4	0.2
GG15b	7.0	3.0	1.06E-03	4.43E-05	11.1	0.1
GG16	3.2	20.7	-1.83E-03	4.61E-05	13.6	0.2
GG17	13.2	0.1	-1.85E-03	4.69E-05	13.4	0.2
GG18	1.7	41.9	2.48E-03	6.95E-05	7.4	0.2
GG19	2.6	27.2	-1.55E-03	4.88E-05	11.4	0.2
GG20	1.0	59.9	1.98E-03	6.77E-05	9.9	0.2
GG21	0.4	83.0	-4.04E-04	5.49E-05	8.7	0.2
GG21b	9.8	0.8	9.73E-04	4.60E-05	7.7	0.1
GG22	10.4	0.5	-1.37E-03	5.06E-05	8.8	0.1
GG23	0.7	71.0	2.13E-03	7.66E-05	8.6	0.2
GG24	5.0	8.1	-3.14E-03	4.19E-05	12.0	0.1
GG25	3.0	22.8	2.99E-03	5.47E-05	3.5	0.1
GG26	10.2	0.6	1.28E-03	4.71E-05	5.7	0.1
GG27	3.8	15.3	-2.20E-04	4.10E-05	8.3	0.1
GG28	11.7	0.3	-4.45E-04	4.05E-05	7.8	0.1
GG29	2.4	30.3	1.46E-03	4.66E-05	8.7	0.1
GG30	9.7	0.8	-1.04E-05	4.00E-05	13.0	0.1
GG31	4.4	10.8	-1.53E-04	4.05E-05	10.0	0.1
GG32	26.4	0.0	-2.03E-03	3.32E-05	13.8	0.1
GG33	5.6	6.0	8.65E-04	4.65E-05	8.2	0.1
GG34	21.0	0.0	1.49E-03	4.71E-05	7.4	0.1
GG35	22.0	0.0	1.50E-03	4.76E-05	6.4	0.1
GG35b	4.3	11.8	-4.99E-04	2.93E-05	10.9	0.1
HD01	0.6	72.7	9.05E-04	3.24E-05	12.3	0.1
HD02	0.9	64.6	1.13E-03	3.29E-05	12.3	0.1
HD03	0.5	79.6	1.85E-05	3.06E-05	10.6	0.1
HD04	2.0	36.2	8.93E-04	3.04E-05	10.5	0.1
HD05	1.8	40.7	1.86E-04	3.06E-05	12.8	0.1
HD06	1.1	59.0	8.69E-04	7.24E-05	10.3	0.3
HD07	1.0	59.8	7.06E-05	3.06E-05	11.1	0.1
HD08	0.9	64.5	1.43E-03	3.42E-05	9.8	0.1
HD09	0.9	63.8	1.13E-03	3.30E-05	11.2	0.1
HD10	0.6	73.1	2.80E-03	3.71E-05	10.9	0.1
HD11	2.8	24.4	1.63E-03	3.43E-05	11.3	0.1
HD12	3.5	17.5	9.91E-04	3.30E-05	10.4	0.1
HD13	2.6	26.6	7.72E-04	3.25E-05	10.4	0.1
HD14	4.6	9.8	1.52E-03	3.14E-05	11.3	0.1
HD15	1.2	54.7	1.03E-03	3.28E-05	11.3	0.1
HD16	0.3	86.1	1.22E-03	3.08E-05	11.5	0.1
HD17	0.1	97.2	1.81E-03	3.45E-05	12.0	0.1
HD18	2.3	31.1	1.84E-03	3.54E-05	8.6	0.1
HD19	0.2	88.5	1.57E-03	3.38E-05	12.8	0.1
MM	28942.1	0.0	-5.30E-03	1.04E-05	108.0	0.1
QWB1	5.0	8.2	1.00E-02	6.13E-05	5.7	0.3
QWB2	7.6	2.3	2.99E-03	3.88E-05	6.6	0.1
T01	5.4	6.6	3.64E-03	7.39E-05	4.7	0.3
T02	8.6	1.4	1.01E-02	9.58E-05	7.6	0.2
T03	9.6	0.8	5.36E-03	7.96E-05	4.8	0.3
T04	6.9	3.1	3.21E-03	7.29E-05	5.3	0.3
T05	4.8	9.1	5.55E-03	8.43E-05	3.0	0.3
T06	1.7	43.5	4.06E-03	7.59E-05	5.0	0.3
T07	3.3	19.0	4.18E-03	7.71E-05	4.4	0.3
T08	7.6	2.2	3.98E-03	7.52E-05	5.3	0.3
T09	2.0	37.0	1.01E-04	5.28E-05	12.0	0.2
T10	0.4	81.8	4.22E-03	7.62E-05	4.2	0.3

Table C.12: Results of the CE model fit using *PANGA* with 10^5 Monte Carlo simulations, data fitted in *constrained mode* is marked by a star.

ID		χ^2	Prob	A	Δ	F	Δ	T	Δ	ΔNe	Δ
			[%]	[cm^3STP/g]				[°C]		[%]	
FR01		1.2	27.7	1.21E-02	4.47E-03	0.72	0.05	10.7	0.4	17.3	0.7
FR02		3.0	8.6	3.02E-03	2.04E-03	0.08	0.48	12.3	0.3	25.1	0.7
FR03		2.4	12.3	1.48E-03	6.04E-03	0.45	1.97	11.5	0.3	7.1	0.6
FR04	*	1.1	28.4	1.05E-03	6.28E-03	0.00	5.44	12.0	0.5	9.6	0.8
FR05		0.1	81.1	2.41E-03	3.74E-03	0.35	0.81	10.6	0.3	13.2	0.6
FR06		0.0	95.1	5.55E-03	2.32E-03	0.41	0.16	12.0	0.3	24.7	0.7
FR07		1.6	21.3	1.40E-03	3.56E-03	0.06	2.11	11.4	0.3	12.0	0.6
FR08	*	8.4	0.4	7.34E-04	8.74E-03	0.00	11.10	12.2	0.5	6.7	0.8
FR09	*	1.0	32.6	1.18E-03	3.72E-03	0.00	2.82	11.7	0.3	10.8	0.6
FR10		2.5	11.3	7.93E-03	2.85E-03	0.57	0.09	10.5	0.3	22.1	0.7
FR11	*	5.1	2.4	8.96E-04	5.04E-03	0.00	5.17	11.7	0.3	8.2	0.6
FR12		0.3	59.9	9.66E-03	1.61E-02	0.89	0.09	10.7	0.4	5.3	0.7
FR13	*	2.2	14.1	6.76E-04	6.44E-03	0.00	8.92	12.2	0.3	6.2	0.6
FR14	*	0.5	49.4	1.77E-03	2.78E-03	0.00	1.34	10.5	0.3	16.1	0.6
FR15		0.5	49.0	1.17E-02	1.07E-02	0.87	0.05	11.8	0.4	6.9	0.6
FR16		0.4	51.9	1.18E-03	4.07E-03	0.06	2.93	12.0	0.3	10.1	0.6
FR17		2.5	11.2	5.31E-03	2.73E-03	0.46	0.18	11.2	0.3	21.3	0.7
FR18		0.2	67.4	2.13E-03	2.42E-03	0.01	0.93	11.1	0.3	19.2	0.6
GG01		7.8	0.5	2.08E-03	3.32E-03	2.90	2.50	10.0	0.2	-22.9	1.0
GG02		4.6	3.1	1.64E-02	8.23E-03	0.68	0.06	9.3	0.8	23.1	1.3
GG03	*	5.1	2.4	2.38E-05	1.53E-02	29.99	2E+04	10.0	0.8	-5.8	1.2
GG04	*	9.3	0.2	9.61E-06	3.02E-02	29.99	9E+04	9.8	0.6	-2.4	1.1
GG04b		7.6	0.6	1.94E-01	1.18E+01	0.99	0.01	9.6	3.5	0.8	3.7
GG05		3.0	8.6	2.73E-03	5.90E-03	1.80	1.35	11.5	0.2	-13.7	1.0
GG05b		5.0	2.5	6.50E-03	5.64E-03	1.50	0.26	10.6	0.6	-15.8	0.9
GG06		0.2	64.6	2.63E-03	7.63E-03	0.23	1.77	11.5	1.0	17.6	1.4
GG07	*	2.7	9.9	2.41E-05	1.29E-02	30.00	2E+04	9.9	0.6	-5.9	1.0
GG08	*	9.2	0.2	1.51E-03	6.13E-03	0.00	3.51	14.8	0.7	14.3	1.1
GG09	*	4.1	4.2	2.90E-03	3.90E-03	0.00	1.04	13.1	0.7	26.9	1.3
GG10		1.0	32.6	2.53E-06	1.10E-01	29.97	1E+06	14.1	0.7	-0.7	13.9
GG11		0.9	34.6	5.30E-02	7.36E-02	0.90	0.01	8.2	0.5	9.4	1.8
GG11b		7.2	0.7	2.12E-01	1.40E+00	0.93	0.01	9.0	0.6	6.8	3.4
GG11c		1.6	21.2	1.70E-03	1.50E-02	0.69	2.37	10.8	0.5	4.4	0.7
GG12	*	2.9	8.9	1.51E-03	6.20E-03	0.00	3.58	12.8	0.7	13.9	1.1
GG12b	*	2.4	12.3	1.37E-03	6.51E-03	0.00	4.19	12.5	0.6	12.6	0.9
GG13		0.5	47.4	2.03E-01	3.22E+01	1.00	0.01	9.2	3.9	0.3	4.3
GG14	*	0.8	38.3	8.94E-05	3.58E-03	30.00	1E+03	11.5	0.7	-19.0	1.0
GG15	*	1.6	21.3	7.11E-04	1.27E-02	0.00	16.70	11.4	0.6	6.5	1.2
GG15b	*	7.0	0.8	1.06E-03	7.94E-03	0.00	6.76	11.1	0.6	9.7	0.9
GG16		0.3	57.4	5.23E-03	5.17E-03	1.66	0.42	12.5	0.7	-17.8	1.0
GG17		5.2	2.3	1.12E-02	6.80E-03	1.45	0.12	11.6	0.8	-18.5	1.1
GG18		0.0	91.7	9.84E-03	6.48E-03	0.60	0.13	8.2	0.7	22.7	1.3
GG19		1.5	22.6	3.86E-03	6.01E-03	1.66	0.74	10.7	0.7	-14.7	1.0
GG20		0.6	42.2	5.60E-03	6.27E-03	0.54	0.33	10.3	0.7	18.3	1.2
GG21		0.1	71.9	1.35E-02	3.97E-02	1.07	0.09	8.4	0.7	-3.9	1.2
GG21b		8.4	0.4	1.71E-02	1.74E-02	0.86	0.05	8.3	0.5	9.4	1.0
GG22	*	11.8	0.1	5.45E-05	5.63E-03	30.00	3E+03	8.7	0.6	-12.3	1.0
GG23		0.0	96.0	7.16E-03	6.76E-03	0.58	0.23	9.2	0.7	19.5	1.3
GG24	*	10.2	0.1	1.60E-04	2.15E-03	30.00	4E+02	10.9	0.6	-29.4	0.9
GG25		1.5	22.3	8.56E-03	5.00E-03	0.51	0.16	4.2	0.6	26.0	1.0
GG26		1.3	26.2	5.49E-02	4.59E-02	0.86	0.01	7.2	0.6	13.5	1.5
GG27	*	3.8	5.2	7.74E-06	3.52E-02	30.00	1E+05	8.3	0.5	-1.9	1.2
GG28	*	11.8	0.1	1.60E-05	1.79E-02	30.00	3E+04	7.8	0.5	-3.9	1.1
GG29		2.4	12.2	1.58E-03	6.18E-03	0.07	3.16	8.7	0.5	13.0	0.9
GG30		9.7	0.2	4.07E-02	3.40E+00	1.00	0.02	13.0	1.2	-0.1	1.4
GG31		3.6	5.7	7.85E-02	8.81E-01	1.02	0.01	9.6	2.0	-1.8	2.2
GG32		11.2	0.1	1.32E-02	6.20E-03	1.48	0.09	8.7	0.5	-20.6	0.9
GG33		4.8	2.9	1.43E-02	1.83E-02	0.86	0.07	9.2	0.6	8.3	1.0
GG34		5.8	1.6	6.71E-01	1.15E+00	0.84	0.01	8.7	0.6	19.4	1.3
GG35		1.5	21.5	2.45E-01	5.34E-01	0.84	0.01	11.2	2.6	18.4	2.8
HD01	*	0.6	42.4	9.05E-04	7.96E-03	0.00	8.07	12.3	0.5	8.3	0.7
HD02	*	0.9	35.0	1.13E-03	6.53E-03	0.00	5.22	12.3	0.5	10.4	0.7
HD03	*	0.5	50.0	1.85E-05	3.45E-01	0.00	2E+04	10.6	0.5	0.2	0.9
HD04	*	2.0	15.4	8.93E-04	7.65E-03	0.00	7.88	10.5	0.4	8.1	0.7
HD05	*	1.8	18.0	1.86E-04	3.52E-02	0.00	2E+02	12.8	0.5	1.7	0.7
HD06	*	1.1	30.4	8.69E-04	2.61E-02	0.00	27.63	10.3	1.6	7.9	2.0
HD07	*	1.0	31.0	7.06E-05	9.14E-02	0.00	1E+03	11.1	0.5	0.6	0.7
HD08	*	0.9	34.9	1.43E-03	5.49E-03	0.00	3.38	9.8	0.5	12.8	0.7
HD09	*	0.9	34.3	1.13E-03	6.21E-03	0.00	4.97	11.2	0.5	10.3	0.7
HD10	*	0.6	42.8	2.80E-03	3.03E-03	0.00	0.85	10.9	0.5	25.5	0.8
HD11	*	2.8	9.3	1.63E-03	4.71E-03	0.00	2.49	11.3	0.5	14.9	0.7
HD12	*	3.5	6.2	9.91E-04	7.21E-03	0.00	6.63	10.4	0.5	9.0	0.7
HD13	*	2.6	10.4	7.72E-04	9.44E-03	0.00	11.38	10.4	0.5	7.0	0.7
HD14	*	4.6	3.1	1.52E-03	4.66E-03	0.00	2.67	11.3	0.5	13.9	0.7
HD15	*	1.2	27.2	1.03E-03	6.74E-03	0.00	5.92	11.3	0.5	9.4	0.7
HD16	*	0.3	58.4	1.22E-03	5.81E-03	0.00	4.26	11.5	0.5	11.1	0.7
HD17	*	0.1	81.1	1.81E-03	4.19E-03	0.00	1.96	12.0	0.5	16.6	0.7
HD18		0.1	74.9	9.36E-03	5.86E-03	0.68	0.10	9.3	0.5	17.2	0.8
HD19		0.1	74.4	3.33E-03	4.99E-03	0.46	0.61	13.0	0.5	14.7	0.7
MM	*	5921.6	0.0	2.44E-03	3.58E-04	30.00	3.30	110.8	0.3	-90.4	0.6
QWB1		2.8	9.7	1.55E-02	4.02E-03	0.19	0.09	6.5	0.7	88.1	1.3
QWB2		0.7	40.3	1.25E-02	4.30E-03	0.59	0.06	7.8	0.5	27.5	0.8
T01		3.3	6.7	1.41E-02	8.27E-03	0.56	0.11	5.6	0.7	32.2	1.3
T02		5.4	2.0	1.69E-02	6.57E-03	0.46	0.08	6.0	0.7	47.6	1.4
T03		6.3	1.2	9.98E-03	8.93E-03	0.52	0.22	5.8	0.7	28.3	1.3
T04		4.7	3.1	7.26E-03	5.00E-03	0.16	0.35	3.2	0.6	46.8	1.3
T05		0.0	98.5	1.25E-02	7.54E-03	0.49	0.14	5.8	0.7	35.8	1.3
T06		3.3	6.8	4.18E-03	5.52E-03	0.00	0.96	4.4	0.6	35.6	1.2
T07	*	4.7	3.0	1.58E-02	8.03E-03	0.55	0.09	6.3	0.7	35.6	1.3
T08		0.0	87.6	4.57E-03	1.74E-03	-0.63	0.44	6.0	0.5	85.7	1.4
T09	*	2.0	15.8	1.01E-04	7.89E-02	0.00	8E+02	12.0	0.6	0.9	0.9
T10		0.3	60.3	2.27E-03	5.27E-03	-0.62	3.14	4.0	0.6	35.5	1.2

Table C.13: $^3He/^4He$ ratios as measured, corrected for ^3H ingrowth during storage and finally corrected for the estimated tritiogenic ^3He component. Mantle helium components of ^4He and ^3He (^4X_m and ^3X_m) are calculated as described in section 2.3.1, according to Mamyrin and Tolstikhin [1984] and to Kaudse [2014] (using the $^3He_{tri}$ correction based on the assumed R_{rad}). Cases where the calculation results in unphysical negative values are set to zero.

ID	measured		^3H ingrowth corrected		corrected for R_{tri}		R_{rad}	Mamyrin [1984]		Kaudse [2014] + $^3He_{tri}$ correction			
	$^3He/^4He$	Δ	$^3He/^4He$	Δ	$^3He/^4He$	Δ	[R_a]	^4X_M	Δ	^4X_M	Δ	^3X_M	Δ
FR01	1.40E-06	4.10E-08	1.36E-06	1.05E-07	1.33E-06	1.08E-07	0.02	0.0	1.1	0.0	1.1	0	8
FR02	6.56E-06	2.26E-07	6.38E-06	2.34E-07	1.06E-06	2.59E-07	0.02	50.7	2.4	0.0	2.6	0	25
FR03	1.51E-06	4.35E-08	1.46E-06	1.09E-07	1.29E-06	1.12E-07	0.02	0.0	1.1	0.0	1.1	0	9
FR04	1.38E-06	9.81E-08	1.34E-06	1.38E-07	1.31E-06	1.40E-07	0.02	0.0	1.4	0.0	1.4	0	11
FR05	1.59E-06	4.42E-08	1.54E-06	1.03E-07	1.28E-06	1.06E-07	0.02	0.9	1.0	0.0	1.1	0	8
FR06	1.41E-06	4.12E-08	1.36E-06	1.06E-07	1.32E-06	1.08E-07	0.02	0.0	1.1	0.0	1.1	0	8
FR07	1.51E-06	4.46E-08	1.47E-06	1.02E-07	1.24E-06	1.05E-07	0.02	0.7	1.0	0.0	1.1	0	9
FR08	1.45E-06	1.06E-07	1.41E-06	1.54E-07	1.33E-06	1.56E-07	0.02	0.0	1.5	0.0	1.6	0	12
FR09	1.31E-06	4.00E-08	1.27E-06	9.78E-08	1.17E-06	1.01E-07	0.02	0.0	1.0	0.0	1.0	0	9
FR10	1.42E-06	4.09E-08	1.38E-06	9.23E-08	1.28E-06	9.51E-08	0.02	0.0	0.9	0.0	1.0	0	8
FR11	1.43E-06	4.21E-08	1.39E-06	1.16E-07	1.31E-06	1.19E-07	0.02	0.0	1.2	0.0	1.2	0	9
FR12	1.35E-06	3.60E-08	1.31E-06	3.51E-08	1.33E-06	4.83E-08	0.02	0.0	0.4	0.0	0.5	0	4
FR13	1.52E-06	4.34E-08	1.48E-06	4.23E-08	1.30E-06	5.00E-08	0.02	0.0	0.5	0.0	0.5	0	4
FR14	2.01E-06	6.07E-08	1.96E-06	5.92E-08	1.27E-06	6.77E-08	0.02	5.2	0.6	0.0	0.7	0	6
FR15	1.55E-06	4.49E-08	1.51E-06	4.37E-08	1.28E-06	5.02E-08	0.02	0.3	0.5	0.0	0.5	0	4
FR16	1.39E-06	4.12E-08	1.34E-06	1.07E-07	1.32E-06	1.10E-07	0.02	0.0	1.1	0.0	1.1	0	8
FR17	1.44E-06	4.28E-08	1.40E-06	4.17E-08	1.30E-06	4.81E-08	0.02	0.0	0.4	0.0	0.5	0	4
FR18	1.39E-06	3.91E-08	1.35E-06	3.81E-08	1.31E-06	4.53E-08	0.02	0.0	0.4	0.0	0.5	0	4
GG01	7.43E-07	2.58E-08	7.24E-07	2.61E-08	5.86E-07	2.70E-08	0.41	6.3	0.3	5.0	0.3	86	6
GG02	6.98E-07	2.49E-08	6.80E-07	2.43E-08	5.75E-07	2.53E-08	0.41	6.1	0.2	5.1	0.3	89	6
GG03	6.05E-07	1.92E-08	5.89E-07	1.87E-08	5.55E-07	2.04E-08	0.41	5.6	0.2	5.3	0.2	96	5
GG04	1.02E-06	3.60E-08	9.94E-07	4.28E-08	7.81E-07	4.48E-08	0.41	5.1	0.4	3.5	0.5	44	6
GG04b	1.10E-06	4.07E-08	1.07E-06	3.97E-08	8.13E-07	6.26E-08	0.41	5.3	0.4	3.2	0.6	40	8
GG05	7.18E-07	2.62E-08	6.99E-07	2.55E-08	5.67E-07	2.66E-08	0.41	6.5	0.3	5.2	0.3	91	6
GG05b	5.86E-07	2.05E-08	5.70E-07	1.99E-08	5.67E-07	2.29E-08	0.41	5.2	0.2	5.2	0.2	92	5
GG06	1.41E-06	4.94E-08	1.37E-06	5.80E-08	1.35E-06	6.79E-08	0.02	0.0	0.6	0.0	0.7	0	5
GG07	2.07E-06	7.36E-08	2.02E-06	7.46E-08	1.24E-06	8.25E-08	0.02	5.3	0.8	0.0	0.9	0	7
GG08	1.33E-06	4.74E-08	1.29E-06	5.41E-08	1.32E-06	6.08E-08	0.02	0.0	0.6	0.0	0.6	0	5
GG09	1.31E-06	4.45E-08	1.28E-06	5.19E-08	1.20E-06	5.79E-08	0.41	0.6	0.5	0.4	0.6	4	5
GG10	1.68E-06	6.23E-08	1.63E-06	6.90E-08	1.24E-06	3.64E-07	0.02	2.0	0.7	0.0	4.1	0	33
GG11	6.02E-07	2.15E-08	5.86E-07	2.10E-08	5.55E-07	2.19E-08	0.41	5.6	0.2	5.3	0.2	96	5
GG11b	6.08E-07	2.24E-08	5.92E-07	2.18E-08	5.57E-07	2.40E-08	0.41	5.6	0.2	5.3	0.2	95	6
GG12	9.81E-07	3.47E-08	9.56E-07	3.38E-08	7.94E-07	3.68E-08	0.41	4.7	0.3	3.4	0.4	43	5
GG12b	9.44E-07	3.38E-08	9.19E-07	3.32E-08	7.52E-07	3.74E-08	0.41	5.2	0.3	3.8	0.4	50	6
GG13	2.03E-06	6.94E-08	1.97E-06	1.08E-07	9.28E-07	1.23E-07	0.02	8.6	1.1	0.0	1.2	0	13
GG14	2.01E-06	7.27E-08	1.95E-06	1.53E-07	1.28E-06	1.57E-07	0.02	3.8	1.5	0.0	1.6	0	12
GG15	2.11E-06	7.47E-08	2.06E-06	7.27E-08	1.26E-06	8.09E-08	0.02	6.0	0.7	0.0	0.8	0	7
GG15b	1.79E-06	6.24E-08	1.74E-06	6.34E-08	1.26E-06	7.19E-08	0.02	3.0	0.7	0.0	0.8	0	6
GG16	6.30E-07	2.24E-08	6.13E-07	2.71E-08	6.10E-07	2.81E-08	0.38	4.1	0.3	4.3	0.3	70	6
GG17	6.33E-07	2.28E-08	6.17E-07	2.64E-08	6.00E-07	2.74E-08	0.38	4.3	0.3	4.3	0.3	72	6
GG18	6.88E-07	2.41E-08	6.70E-07	2.36E-08	5.73E-07	2.47E-08	0.41	6.1	0.2	5.1	0.2	90	6
GG19	1.98E-06	7.01E-08	1.93E-06	1.15E-07	9.57E-07	1.17E-07	0.02	7.6	1.2	0.0	1.2	0	12
GG20	3.88E-07	1.40E-08	3.78E-07	1.58E-08	5.93E-07	1.70E-08	0.02	2.2	0.2	4.5	0.2	76	4
GG21	5.51E-07	1.95E-08	5.37E-07	1.90E-08	6.03E-07	2.02E-08	0.02	3.5	0.2	4.3	0.2	72	4
GG21b							0.02						
GG22	5.74E-07	2.01E-08	5.59E-07	1.96E-08	5.56E-07	2.05E-08	0.41	5.3	0.2	5.3	0.2	96	5
GG23	1.34E-06	4.96E-08	1.30E-06	5.42E-08	7.47E-07	5.61E-08	0.41	8.8	0.5	3.6	0.6	48	8
GG24	1.69E-06	6.46E-08	1.65E-06	1.62E-07	1.20E-06	1.65E-07	0.02	1.4	1.6	0.0	1.7	0	14
GG25	5.48E-07	2.21E-08	5.34E-07	2.15E-08	5.54E-07	2.43E-08	0.41	5.1	0.2	5.3	0.2	96	6
GG26	5.72E-07	2.31E-08	5.57E-07	2.25E-08	5.53E-07	2.55E-08	0.41	5.4	0.2	5.3	0.3	96	6
GG27	5.85E-07	2.22E-08	5.70E-07	2.16E-08	5.54E-07	2.45E-08	0.41	5.5	0.2	5.3	0.2	96	6
GG28	6.12E-07	2.17E-08	5.96E-07	2.11E-08	5.54E-07	2.38E-08	0.41	5.7	0.2	5.3	0.2	96	6
GG29	6.53E-07	2.43E-08	6.36E-07	2.48E-08	5.71E-07	2.77E-08	0.41	5.8	0.2	5.2	0.3	91	7
GG30	1.26E-06	4.63E-08	1.23E-06	5.24E-08	1.32E-06	5.84E-08	0.02	0.0	0.5	0.0	0.6	0	5
GG31	1.24E-06	4.77E-08	1.21E-06	4.92E-08	1.22E-06	6.68E-08	0.02	0.0	0.5	0.3	0.7	3	6
GG32	1.10E-06	3.91E-08	1.08E-06	3.81E-08	8.33E-07	4.23E-08	0.41	4.8	0.4	3.0	0.4	36	5
GG33	6.85E-07	2.28E-08	6.68E-07	2.22E-08	5.93E-07	2.48E-08	0.41	5.7	0.2	5.0	0.2	84	5
GG34	6.45E-07	2.26E-08	6.29E-07	2.20E-08	5.78E-07	2.49E-08	0.41	5.6	0.2	5.1	0.2	89	6
GG35	6.24E-07	2.29E-08	6.08E-07	2.23E-08	5.54E-07	2.52E-08	0.02	5.8	0.2	5.3	0.3	96	6
GG35b	5.30E-07	9.42E-09	5.16E-07	9.18E-09			0.41						
HD01	2.15E-06	3.65E-08	2.02E-06	1.36E-07	1.31E-06	1.39E-07	0.02	5.2	1.4	0.0	1.4	0	11
HD02	1.89E-06	3.38E-08	1.74E-06	1.55E-07	1.29E-06	1.57E-07	0.02	2.7	1.6	0.0	1.6	0	12
HD03	1.74E-06	3.17E-08	1.68E-06	1.01E-07	1.32E-06	1.03E-07	0.02	1.4	1.0	0.0	1.0	0	8
HD04	2.10E-06	3.14E-08	2.04E-06	9.22E-08	1.30E-06	9.50E-08	0.02	5.4	0.9	0.0	1.0	0	7
HD05	1.56E-06	2.91E-08	1.51E-06	1.06E-07	1.31E-06	1.09E-07	0.02	0.0	1.1	0.0	1.1	0	8
HD06	1.44E-06	6.05E-08	1.40E-06	5.89E-08	1.27E-06	8.74E-08	0.02	0.0	0.6	0.0	1.0	0	8
HD07	2.18E-06	3.80E-08	2.10E-06	1.14E-07	1.31E-06	1.18E-07	0.02	5.6	1.1	0.0	1.2	0	9
HD08	2.27E-06	4.68E-08	2.19E-06	7.41E-08	9.96E-07	7.80E-08	0.43	12.9	0.7	1.6	0.8	17	8
HD09	1.78E-06	3.16E-08	1.64E-06	1.41E-07	1.31E-06	1.43E-07	0.02	1.5	1.4	0.0	1.4	0	11
HD10	2.33E-06	3.84E-08	2.26E-06	8.59E-08	1.31E-06	9.00E-08	0.02	7.9	0.9	0.0	0.9	0	7
HD11	1.84E-06	3.24E-08	1.78E-06	8.01E-08	1.24E-06	8.36E-08	0.02	3.8	0.8	0.0	0.9	0	7
HD12	1.59E-06	2.65E-08	1.55E-06	7.16E-08	1.13E-06	7.49E-08	0.43	4.1	0.7	0.9	0.8	8	7
HD13	1.12E-06	1.98E-08	1.08E-06	7.40E-08	1.04E-06	7.65E-08	0.02	0.0	0.7	0.0	0.8	0	8
HD14	1.45E-06	2.21E-08	1.41E-06	7.93E-08	1.12E-06	8.12E-08	0.02	1.5	0.8	0.0	0.8	0	7
HD15	1.73E-06	3.04E-08	1.68E-06	9.56E-08	1.35E-06	9.88E-08	0.02	1.4	1.0	0.0	1.0	0	7
HD16	1.68E-06	2.33E-08	1.63E-06	9.50E-08	1.30E-06	9.73E-08	0.02	1.5	1.0	0.0	1.0	0	8
HD17	1.64E-06	3.35E-08	1.58E-06	8.04E-08	1.30E-06	8.37E-08	0.02	1.3	0.8	0.0	0.9	0	7
HD18	1.87E-06	3.45E-08	1.81E-06	8.42E-08	1.20E-06	8.81E-08	0.43	5.3	0.9	0.3	0.9	2	7
HD19	1.53E-06	3.18E-08	1.48E-06	9.79E-08	1.28E-06	9.99E-08	0.02	0.4	1.0	0.0	1.0	0	8
MM	6.01E-07	1.50E-08	5.85E-07	1.46E-08	7.02E-07	1.48E-08	0.43	5.7	0.1	5.7	0.1	97	3
QWB1	2.45E-06	3.90E-08	2.39E-06	3.80E-08	2.38E-06	4.53E-08	1.77	23.7	0.4	23.7	0.5	99	3
QWB2	2.53E-06	3.83E-08	2.46E-06	3.73E-08	2.38E-06	4.54E-08	1.77	24.4	0.4	24.4	0.5	99	3
T01	2.10E-06	9.41E-08	2.05E-06	9.16E-08			0.02	20.3	0.9	20.3	0.9	99	6
T02	1.56E-06	6.89E-08	1.52E-06	6.71E-08			1.13	14.5	0.7	14.5	0.7	95	6
T03	2.67E-06	1.21E-07	2.60E-06	1.17E-07			0.02	25.8	1.2	25.8	1.2	99	6
T04	2.77E-06	1.24E-07	2.70E-06	1.21E-07			0.02	26.9	1.2	26.9	1.2	99	6
T05	2.56E-06	1.12E-07	2.49E-06	1.09E-07			0.02	24.8	1.1	24.8	1.1	99	6
T06	6.75E-07	2.86E-08	6.58E-07	2.79E-08			0.02	6.4	0.3	6.4	0.3	97	6
T07	7.36E-07	3.16E-08	7.16E-07	3.07E-08			0.02	7.0	0.3	7.0	0.3	97	6
T08	6.68E-07	2.87E-08	6.50E-07	2.80E-08			0.02	6.3	0.3	6.3	0.3	97	6
T09	4.93E-07	2.73E-08	4.80E-07	2.66E-08	4.76E-07	2.71E-08	0.35	4.5	0.3	4.5	0.3	94	8
T10	1.37E-06	5.76E-08	1.33E-06	5.61E-08			0.02	13.1	0.6	13.1	0.6	99	6

Table C.14: Results of the ^{3}H-^{3}He-dating as described in section 2.4.1 for all samples with existing tritium measurements, using both a fixed R_{rad} of 0.02 R_a as well as an assumed R_{rad} accounting for local variations. Values of He/Ne indicating probable mantle ^3He_m influence are marked in red.

					corrected for ^3He_M		uncorrected		corrected for ^3He_M	
ID	**He/Ne**	**^{3}H**	**Δ**	**assumed R_{rad}**	**$^3He_{trit}$**	**Δ**	**Age**	**Δ**	**Age**	**Δ**
		[TU]		[R_a]	[TU]		[yr]		[yr]	
FR01	0.24	6.60	1.12	0.02	0.82	0.51	2.1	1.3		
FR02	0.27	16.09	1.10	0.02	143.03	2.57	40.7	1.1		
FR03	0.24	6.67	1.07	0.02	3.63	0.53	7.7	1.4		
FR04	0.24	8.66	1.08	0.02	0.60	0.48	1.2	0.9		
FR05	0.24	7.81	1.08	0.02	5.85	0.60	9.9	1.3		
FR06	0.24	11.66	1.22	0.02	0.99	0.56	1.5	0.8		
FR07	0.25	8.71	1.08	0.02	5.09	0.59	8.2	1.1		
FR08	0.24	9.99	1.18	0.02	1.59	0.48	2.6	0.8		
FR09	0.27	8.95	1.10	0.02	2.35	0.63	4.1	1.1		
FR10	0.25	7.84	1.04	0.02	2.23	0.56	4.4	1.1		
FR11	0.24	6.69	1.16	0.02	1.60	0.53	3.8	1.3		
FR12				0.02						
FR13				0.02						
FR14				0.02						
FR15				0.02						
FR16	0.24	18.03	1.06	0.02	0.47	0.51	0.5	0.5		
FR17				0.02						
FR18				0.02						
GG01	4.59	9.34	1.06	0.41	39.71	2.00	54.3	1.9	29.5	1.8
GG02	7.20	3.92	0.58	0.41	75.64	5.19	84.8	2.6	53.5	2.8
GG03	57.12	7.73	0.91	0.41	149.42	35.78	103.0	2.1	53.5	4.5
GG04	0.76	6.10	0.75	0.41	12.66	0.77	34.1	1.9	20.0	1.7
GG04b				0.41						
GG05	10.03	10.55	0.43	0.41	92.33	5.12	67.6	0.7	40.5	1.1
GG05b				0.41						
GG06	0.24	8.62	0.37	0.02	0.30	0.78	0.6	1.6		
GG07	0.24	3.82	0.19	0.02	14.16	0.64	27.5	0.9		
GG08	0.24	7.01	0.31	0.02	-0.66	0.60	-1.8	1.7		
GG09	0.29	7.56	0.43	0.41	2.24	0.75	8.8	1.1	4.6	1.4
GG10	0.25	7.30	0.32	0.02	7.49	6.88	12.5	8.3		
GG11	57.09	3.53	0.19	0.41	158.76	32.26	119.6	1.0	68.0	3.7
GG11b				0.41						
GG12				0.41						
GG12b	0.91	6.77	0.19	0.41	13.64	1.40	36.7	0.6	19.6	1.3
GG13	0.32	7.84	1.13	0.02	27.42	1.54	26.7	2.1		
GG14	0.23	3.72	1.02	0.02	9.76	0.49	22.9	3.6		
GG15				0.02						
GG15b	0.25	6.85	0.19	0.02	10.62	0.73	16.6	0.8		
GG16	1.87	5.36	1.01	0.38	0.35	0.91	42.9	3.1	1.1	2.8
GG17	2.09	3.13	1.00	0.38	2.30	1.00	54.4	5.4	9.8	4.1
GG18	7.99	4.46	1.01	0.41	78.30	5.82	84.3	4.0	51.9	4.0
GG19	0.30	2.03	0.99	0.02	20.31	0.53	42.6	7.9		
GG20	2.57	5.71	1.02	0.02	-53.02	1.50	43.5	2.9		
GG21				0.02			35.9	0.6		
GG21b		9.57	0.32	0.02						
GG22	52.94	4.24	0.94	0.41	10.63	22.65	110.2	3.9	22.3	27.2
GG23	0.87	9.35	1.08	0.41	47.15	1.21	40.4	1.9	32.0	1.8
GG24	0.24	6.30	1.02	0.02	5.99	0.42	11.9	1.5		
GG25	144.46	7.56	0.22	0.41	-321.64	176.09	124.4	0.6		
GG26	201.62	1.87	0.07	0.41	64.70	224.95	153.3	0.7	63.5	60.1
GG27	125.45	3.61	0.11	0.41	163.64	117.94	130.9	0.6	68.2	12.5
GG28	60.60	8.43	0.23	0.41	199.72	52.52	103.4	0.6	57.0	4.5
GG29	9.09	5.65	3.22	0.41	54.86	10.30	80.1	10.0	42.2	9.7
GG30	0.24	7.02	0.25	0.02	-1.72	0.48				
GG31	0.27	5.96	0.17	0.02	-0.19	0.97	4.2	2.3		
GG32				0.41						
GG33	4.21	5.03	0.15	0.41	27.82	4.15	67.7	0.6	33.4	2.3
GG34	6.86	2.08	0.11	0.41	32.66	7.47	92.4	1.0	50.1	3.9
GG35	73.39	2.93	0.09	0.02	377.79	81.91	129.1	0.6	86.5	3.9
GG35b				0.41						
HD01	0.24	40.82	1.38	0.02	14.50	0.56	5.4	0.2		
HD02	0.24	55.05	1.62	0.02	9.52	0.62	2.8	0.2		
HD03	0.23	7.94	0.94	0.02	6.69	0.31	10.9	1.0		
HD04	0.24	7.51	0.94	0.02	15.32	0.47	19.8	1.5		
HD05	0.24	7.41	1.01	0.02	3.65	0.50	7.1	1.1		
HD06				0.02						
HD07	0.23	8.08	1.05	0.02	14.81	0.58	18.5	1.6		
HD08	0.40	11.79	1.11	0.43	43.50	0.85	30.0	1.4	27.5	1.3
HD09	0.24	47.19	1.49	0.02	6.99	0.51	2.5	0.2		
HD10	0.24	7.80	0.99	0.02	23.28	0.65	24.6	1.7		
HD11	0.25	5.68	0.90	0.02	12.64	0.56	20.8	2.0		
HD12	0.31	3.49	0.96	0.43	11.40	0.60	29.9	4.0	25.8	3.8
HD13	0.30	6.67	0.97	0.02	1.16	0.51	2.9	1.2		
HD14	0.28	5.45	1.03	0.02	7.52	0.45	15.4	2.0		
HD15	0.23	5.24	0.96	0.02	6.59	0.50	14.5	2.0		
HD16	0.24	7.40	1.03	0.02	6.97	0.45	11.8	1.3		
HD17	0.24	6.04	0.87	0.02	6.40	0.52	12.8	1.5		
HD18	0.28	9.07	1.07	0.43	16.34	0.68	19.9	1.5	18.3	1.4
HD19	0.25	10.10	1.09	0.02	4.58	0.44	6.6	0.8		
MM				0.43						
QWB1	150.84	14.10	1.09	1.77	111.14	589.78	147.9	1.4	38.8	83.7
QWB2	47.38	9.27	0.98	1.77	428.84	130.46	128.2	1.9	68.5	5.6
T01				0.02						
T02				1.13						
T03				0.02						
T04				0.02						
T05				0.02						
T06				0.02						
T07				0.02						
T08				0.02						
T09	43.15	6.36	0.84	0.35	14.20	18.22	98.5	2.3	20.9	15.8
T10				0.02						

Table C.15: AMS Results for ^{14}C and $\delta^{13}C$, including the hydrochemical parameters of the respective waters analysed by Al Najem [2016] and the ^{3}H concentrations, used in the reservoir effect modeling approaches.

ID	$A^{14}C$ [pmC]	Δ	$\delta^{13}C$ [‰]	^{3}H [TU]	Δ	Mg^{2+} [mg/l]	Na^{+} [mg/l]	K^{+} [mg/l]	HCO_3^- [mmol/l	Cl^- [mg/l]	SO_4^{2-} [mg/l]	F^- [mg/l]	NO_3^- [mg/l]	Ca^{2+} [mmol/l
GG01	97.78	0.22	-12.58	9.34	1.06	63.6	33.0	1.42	9.88	155	331	0.84	0.10	5.04
GG13	82.28	0.24	-10.32	7.84	1.13	23.4	15.0	2.97	6.40	46	148	0.29	0.00	2.88
GG22	80.23	0.24	-10.40	4.24	0.94	56.7	146.0	10.20	8.30	555	156	0.69	1.60	6.06
GG25	76.90	0.27	-15.12	7.56	0.22	61.9	370.0	13.30	5.50	684	151	0.13	4.00	4.06
GG26	55.30	0.23	-10.61	1.87	0.07	41.6	409.0	4.44	6.16	1048	75	0.17	0.00	5.92
T01	0.29	0.02	3.03			145.5	390.0	71.00	19.20	90	2239	3.58	1.04	16.09
T02	2.83	0.05	-2.52			40.0	51.5	5.65	7.80	29	111	0.51	0.10	1.88
T03	0.31	0.02	15.81			88.0	296.0	75.00	25.80	119	1758	2.21	0.00	18.59
T04	0.10	0.02	2.63			92.5	356.0	79.50	27.66	178	1817	2.04	0.13	18.84
T05	0.20	0.02	11.41			87.5	296.5	74.00	26.26	122	1788	2.40	0.61	18.96
T06	0.35	0.02	3.15			134.5	1035.0	37.30	15.24	2017	535	1.86	0.38	10.99
T07	0.36	0.02	2.01			118.5	1055.0	34.85	17.26	2051	284	1.21	0.00	9.59
T08	0.21	0.02	2.21			129.5	955.0	35.65	15.66	1827	553	1.53	0.00	10.89
T09	25.26	0.15	-6.10	6.36	0.84	7.1	31.5	3.05	3.36	11	70	0.82	3.57	1.26
T10	0.08	0.04	2.79			119.5	1040.0	40.95	21.76	1973	340	0.61	1.21	11.40
HD06	69.21	0.24	-8.41	> 1.00	1.00	12.8	4.5	1.36	5.12	0	13	0.53	0.00	1.35
QWB1	0.48	0.03	-2.77	14.10	1.09	17.2	911.0	22.20	25.08	664	143	0.03	0.00	0.67
QWB2	7.54	0.08	-0.80	9.27	0.98	66.2	244.0	36.20	19.94	197	57	0.01	0.00	2.48

Table C.16: Results from feeding the values from different reservoir modeling approaches to *OxCal* [Bronk Ramsey, 2009], calibrating the measured and corrected data to the *IntCal13* [Reimer et al., 2013] reference curve. The given apparent recharge ages are the mean of the fit to the calibration curve – empty cells signify cases where one of the limits of the possible age range exceeded the limits of the calibration curve, for samples either too young or too old.

	Vogel		Fontes & Garnier		Pearsons		Clark & Fritz		Mean of all Models		uncorrected data	
ID	Age [yr BP]	Δ [yr]	Age [yr BP]	Δ [yr]	Age [yr BP]	Δ [yr]	Age [yr BP]	Δ [yr]	Age [yr BP]	Δ [yr]	Age [yr BP]	Δ [yr]
GG01					200	100			200	100	150	100
GG13					1500	50			1500	50	1450	50
GG22					1750	50			1750	50	1700	50
GG25	700	0			2200	100			1450	50	2100	50
GG26	3750	50	7450	50	5550	50	650	50	4350	50	5500	50
T01	48850	650	37300	850			44450	600	43533	700		
T02	31200	100	33750	150	32800	300	29000	200	31688	188	32700	300
T03	48450	750	33750	650			43650	550	41950	650	49400	450
T04	54650	1750			56000	1750			55325	1750	56000	1750
T05			38900	1150	50250	1000	47500	1000	45550	1050	50200	1000
T06	47400	700	40650	550	48800	600	43650	500	45125	588	48750	650
T07	47150	650	39750	600	48600	650	43500	450	44750	588	48550	650
T08			44100	700	49650	850	47500	900	47083	817	49600	850
T09	11150	50	23550	100	12950	50	8700	100	14088	75	12900	50
T10	62950	8350			64300	8350			63625	8350	64250	8350
HD06	1550	50	8650	50	3200	50	0	0	3350	38	3100	50
QWB1	45050	400	37700	600	46250	500	42450	300	42863	450	46200	500
QWB2	23450	150	16200	150	25100	150	20200	150	21238	150	25050	200

List of Figures

List of Tables

Acknowledgements

First and foremost I would like to thank my thesis supervisor Werner Aeschbach for all the support he gave me over the years that I have been a member of his research group – and the chance to work on this project in the first place. Thanks also to Mario Trieloff for agreeing to be my second thesis referee, and to Margot Isenbeck-Schröter for the support during the research.

Getting through this project would not have been possible without my colleague Sami Al Najem, who made the extensive field work we did together very much enjoyable and who quickly became a good friend – which is also the case for the other (former) bachelor and master students of Margot Isenbeck-Schröter's research group: Jan, Simon, Filip, Luke and Amanda, I would not want to miss you, neither in the field nor as friends. And of course, Christian Scholz, for sharing his extensive knowledge and experience in field work – the same goes to Stefan Rheinberger, though more for his comments. Getting adopted by all of you into your research group was amazing!

Of course, I should not forget Werner's group, especially my friends Tillmann Kaudse and Martin Wieser, from whom I learned a lot in and outside the lab, as well as Simon Mayer, an always reliable source of information and help. Of course, nothing in the lab would have worked without the help of Stefan Schäfer and Karl-Friedrich Reis. And a special thank you goes to my friend Tim Schneider: for being the only constant in my 14 years at Heidelberg University, from the very first lecture day until today, more than a decade later.

The various people of different research groups at the IUP, making for such a great work atmosphere, without attempting to name them all: Johannes, Fiete, Freya, Joelle, Arne, Stefan, Jenny, Martin, ...

For analysing samples for me, I would like to thank several people: Michael Sabasch of the IUP and Paul Königer of the BGR Hannover for measuring my stable isotope samples. Ronny Friedrich and the staff of the Klaus-Tschira-Archäometrie-Zentrum for analysing my ^{14}C-samples. Jürgen Sültenfuss for analysing some of my ^{3}H Samples, as well as Tim Schneider and the students working and keeping up the tritium lab at the IUP – Tim also for tutoring me on the use to the gas chromatograph for SF_6-measurements, even though those measurements never made it into this work. Sampling the many wells in the three

regions was made a lot easier by the technical and logistical support of *GeoThermal Engineering GmbH*, especially Dr. Michael Kraml and Dr. René Grobe. I also have to thank our various contacts at the local authorities, clearing the sampling requests and providing access, as well as various local property owners who gave us permission to sample their wells.

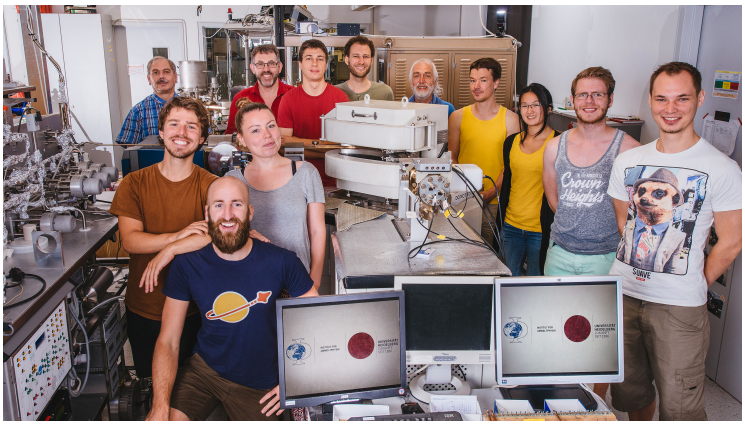

Bibliography

[Aeschbach-Hertig 1994] Aeschbach-Hertig, W.: *Helium und Tritium als Tracer für physikalische Prozesse in Seen*, ETH Zürich, Dissertation, 1994 25, 28, 30, 66, 67

[Aeschbach-Hertig 2005] Aeschbach-Hertig, W.: A comment on "Helium sources in passive margin aquifers - New evidence for a significant mantle 3He source in aquifers with unexpectedly low in situ 3He/4He production" by M. C. Castro [Earth Planet. Sci. Lett. 222 (2004) 897-913]. In: *Earth and Planetary Science Letters* 240 (2005), Nr. 3-4, p. 827–829. – ISSN 0012821X 22, 23

[Aeschbach-Hertig et al. 2002] Aeschbach-Hertig, W. ; Beyerle, U. ; Holocher, J. ; Peeters, F. ; Kipfer, R.: Excess air in groundwater as a potential indicator of past environmental changes. In: *Study of Environmental Change Using Isotope Techniques*. Bd. 13/P. Vienna : IAEA, 2002, p. 174–183 16, 17

[Aeschbach-Hertig et al. 2008] Aeschbach-Hertig, W. ; El-Gamal, H. ; Wieser, M. ; Palcsu, L.: Modeling excess air and degassing in groundwater by equilibrium partitioning with a gas phase. In: *Water Resources Research* 44 (2008), Nr. 8, p. 1–12. – ISBN 0043-1397 16, 17

[Aeschbach-Hertig et al. 1996] Aeschbach-Hertig, W. ; Kipfer, R. ; Hofer, M. ; Imboden, D.M.M. ; Wieler, R. ; Signer, P.: Quantification of gas fluxes from the subcontinental mantle: The example of Laacher See, a maar lake in Germany. In: *Geochimica et Cosmochimica Acta* 60 (1996), Nr. I, p. 31–41 46, 98

[Aeschbach-Hertig et al. 2000] Aeschbach-Hertig, W. ; Peeters, F. ; Beyerle, U. ; Kipfer, R.: Palaeotemperature reconstruction from noble gases in ground water taking into account equilibration with entrapped air. In: *Nature* 405 (2000), p. 1040–4. – ISBN 0028-0836 17, 68

[Aeschbach-Hertig and Solomon 2013] Aeschbach-Hertig, W. ; Solomon, D.K.: Noble Gas Thermometry in Groundwater Hydrology. In: *The Noble Gases as Geochemical Tracers*. 2013, p. 81–122 16, 18, 68

[Agemar et al. 2013] Agemar, T. ; Brunken, J. ; Jodocy, M. ; Schellschmidt, R. ; Schulz, R. ; Stober, I.: Untergrundtemperaturen in Baden-Württemberg. In: *Zeitschrift der Deutschen Gesellschaft für Geowissenschaften* 164 (2013), Nr. 1, p. 49–62. – ISSN 18601804 41

[Al Najem 2016] Al Najem, S.: *Hydrogeochemische Charakterisierung von Grundwässern des Oberrheingrabens zur Identifizierung störungsbedingter Tiefenwasser-Einflüsse*, Heidelberg University, Dissertation, 2016 9, 39, 43, 45, 55, 73, 89, 91, 92, 97, 98, 99, 100, 105, 106, 148

[Anderson 1993] Anderson, D.L.: Helium-3 from the mantle: primordial signal or cosmic dust? In: *Science* 261 (1993), Nr. 5118, p. 170–176. – ISBN 0036-8075 20

[Andrews and Lee 1979] Andrews, J.N. ; Lee, D.J.: Inert gases in groundwater from the Bunter Sandstone of England as indicators of age and palaeoclimatic trends. In: *Journal of Hydrology* 41 (1979), Nr. 3-4, p. 233–252. – ISBN 0022-1694 15, 25

[Aquilina et al. 1997] Aquilina, L. ; Pauwels, H. ; Genter, A. ; Fouillac, C.: Water-rock interaction processes in the Triassic sandstone and the granitic basement of the Rhine Graben: Geochemical investigation of a geothermal reservoir. In: *Geochimica et Cosmochimica Acta* 61 (1997), Nr. 20, p. 4281–4295. – ISBN 0016-7037 41, 93, 94, 99

[Baertschi 1976] Baertschi, P.: Absolute 18O content of standard mean ocean water. In: *Earth and Planetary Science Letters* 31 (1976), Nr. 3, p. 341–344. – ISBN 0012-821X 32

[Ballentine and Burnard 2002] Ballentine, C.J. ; Burnard, P.G.: Production, Release and Transport of Noble Gases in the Continental Crust. In: *Reviews in Mineralogy and Geochemistry* 47 (2002), Nr. 1, p. 481–538. – ISBN 1529-6466\r0-939950-59-6 24, 25, 26

[Baria et al. 1999] Baria, R. ; Baumgärtner, J. ; Gérard, A. ; Jung, R. ; Garnish, J.: European HDR research programme at Soultz-sous-Forets (France) 1987-1996. In: *Geothermics* 28 (1999), p. 655–669. – ISBN 0375-6505 6

[Barragán Reyes et al. 2008] Barragán Reyes, R.M. ; Arellano, V.M. ; Portugal, E. ; Segovia, N.: Effects of changes in reservoir thermodynamic conditions on 222Rn composition of discharged fluids: Study for two wells at Los Azufres geothermal field (Mexico). In: *Geofluids* 8 (2008), p. 252–262. – ISSN 14688115 31

[Battino 1984] Battino, R.: The Ostwald Coefficient of Gas Solubility. In: *Fluid Phase Equilibria* 15 (1984), p. 231–240 15

[Bauer 2014] Bauer, M. (Ed.): *Handbuch Tiefe Geothermie*. Berlin, Heidelberg : Springer Spektrum, 2014 (SpringerLink : Bücher). – Online–Ressource (XXXII, 854 S. 333 Abb., 264 Abb. in Farbe, online resource) p. – ISBN 978-364-25451-1-5 5, 6, 7, 8

[Bauer et al. 2005] Bauer, M. ; Eichinger, L. ; Elsass, P. ; Kloppmann, W. ; Wirsing, G.: Isotopic and hydrochemical studies of groundwater flow and salinity in the Southern Upper Rhine Graben. In: *International Journal of Earth Sciences* 94 (2005), Nr. 4, p. 565–579. – ISBN 0053100505005 45, 48

[Beck 2014] Beck, B.: *Lokalisierung von aktiven geologischen Störungszonen im Oberrheingraben durch Messung von 3He/4He-Verhältnissen in der Bodenluft*, Master thesis, 2014 52, 57, 93

[Becker and Kromer 1993] Becker, B. ; Kromer, B.: The continental tree-ring record - absolute chronology, 14C calibration and climatic change at 11 ka. In: *Palaeogeography, Palaeoclimatology, Palaeoecology* 103 (1993), Nr. 1-2, p. 67–71. – ISBN 0031-0182 35

[Bender 2003] Bender, K.: Grundwasserströmungsmodell für den Großraum Rhein-Neckar. In: *Grundwasser – Zeitschrift der Fachsektion Hydrogeologie* 1 (2003), p. 41–49. ISBN 0621290289 43

[Benson 1976] Benson, B.B.: Empirical laws for dilute aqueous solutions of nonpolar gases. In: *The Journal of Chemical Physics* 64 (1976), Nr. 2, p. 689. – ISSN 00219606 14, 15, 136, 155

[Benson and Krause 1980] Benson, B.B. ; Krause, D.: Isotopic fractionation of helium during solution: A probe for the liquid state. In: *Journal of Solution Chemistry* 9 (1980), Nr. 12, p. 895–909. – ISSN 00959782 21

[Beyerle et al. 2000] Beyerle, U. ; Aeschbach-Hertig, W. ; Imboden, D.M. ; Baur, H. ; Graf, Th. ; Kipfer, R.: A Mass Spectrometric System for the Analysis of Noble Gases and Tritium from Water Samples. In: *Envir. Sci.* 34 (2000), Nr. 10, p. 2042–2050. – ISSN 0013-936X 57

[BGR 2009] BGR, Bundesanstalt für Geowissenschaften und Rohstoffe: *Energierohstoffe 2009: Reserven, Ressourcen, Verfügbarkeit. Teil 3: Situation Deutschland, Verfügbarkeit der Energierohstoffe*. 2009. – URL `http://www.bgr.bund.de/DE/Themen/Energie/Produkte/energierohstoffe_2009.html?nn=1542234`. – Access date: 2017-02-28 8

[Blume et al. 2009] Blume, H.P. ; Brümmer, G.W. ; Scheffer, F. ; Horn, R. ; Kandeler, E. ; Schachtschabel, P. ; Kögel-Knabner, I. ; Welp, G. ; Kretzschmar, R. ; Thiele-Bruhn, S. et al.: *Scheffer/Schachtschabel: Lehrbuch der Bodenkunde*. Spektrum Akademischer Verlag, 2009 (Spektrum Lehrbuch). – ISBN 9783827422514 12

[Bottomley et al. 1984] Bottomley, D.J. ; Ross, J.D. ; Clarke, W.B.: Helium and neon isotope geochemistry of some ground waters from the Canadian Precambrian Shield. In: *Geochimica et Cosmochimica Acta* 48 (1984), Nr. 10, p. 1973–1985. – ISBN 0016-7037 25

[Bräuer et al. 2013] Bräuer, K. ; Kämpf, H. ; Niedermann, S. ; Strauch, G.: Indications for the existence of different magmatic reservoirs beneath the Eifel area (Germany): A multi-isotope (C, N, He, Ne, Ar) approach. In: *Chemical Geology* 356 (2013), p. 193–208. – ISBN 0009-2541 46

[Bronk Ramsey 2009] Bronk Ramsey, C.: Bayesian Analysis of Radiocarbon Dates. In: *Radiocarbon* 51 (2009), Nr. 1, p. 337–360. – ISBN 0033-8222 35, 80, 134, 149

[Burnard and Farley 2000] Burnard, P.G. ; Farley, K.A.: Calibration of pressure-dependent sensitivity and discrimination in Nier-type noble gas ion sources. In: *Geochemistry Geophysics Geosystems* 1 (2000), Nr. Figure 1. – ISSN 1525-2027 61, 62

[Castro et al. 2009] Castro, M.C. ; Ma, L. ; Hall, C.M.: A primordial, solar He-Ne signature in crustal fluids of a stable continental region. In: *Earth and Planetary Science Letters* 279 (2009), Nr. 3-4, p. 174–184. – ISBN 0012-821X 20, 47

[Clark and Fritz 1997] Clark, I.D. ; Fritz, P.: *Environmental Isotopes in Hydrogeology*. Taylor & Francis, 1997. – ISBN 9781566702492 36, 37, 38, 80, 99

[Clarke et al. 1976] Clarke, W.B. ; Jenkins, W.J. ; Top, Z.: Determination of tritium by mass spectrometric measurement of 3He. In: *The International Journal Of Applied Radiation And Isotopes* 27 (1976), Nr. 9, p. 515–522. – ISBN 0020-708X 19, 46, 68, 136, 137

[Clauser et al. 2002] Clauser, C. ; Griesshaber, E. ; Neugebauer, H.J.: Decoupled thermal and mantle helium anomalies: Implications for the transport regime in continental rift zones. In: *Journal of Geophysical Research* 107 (2002), Nr. B11, p. 2269. – ISSN 01480227 20, 24

[Clever 1979a] Clever, H. L. (Ed.): *Helium and Neon - Gas Solubilities*. Vol. *1*. Oxford, New York, Toronto, Sydney, Paris, Frankfurt : Pergamon Press, 1979 73, 119, 139

[Clever 1979b] Clever, H. L. (Ed.): *Krypton, Xenon and Radon - Gas Solubilities*. Vol. *2*. Oxford, New York, Toronto, Sydney, Paris, Frankfurt : Pergamon Press, 1979 73, 119, 139

[Clever 1980] Clever, H. L. (Ed.): *Argon - Gas Solubilities*. Vol. *4*. Oxford, New York, Toronto, Sydney, Paris, Frankfurt : Pergamon Press, 1980 73, 139

[Cook and Solomon 1997] Cook, P.G. ; Solomon, D.K.: Recent advances in dating young groundwater; chlorofluorocarbons, 3H/3He and 85Kr. In: *Journal of Hydrology* 191 (1997), Nr. 1-4, p. 245–265. – ISBN 0022-1694 29

[Coplen et al. 2000] Coplen, T.B. ; Herczeg, A.L. ; Barnes, C.: *Isotope Engineering—Using Stable Isotopes of the Water Molecule to Solve Practical Problems*. p. 79–110. In: Cook, P.G. (Ed.) ; Herczeg, A.L. (Ed.): *Environmental Tracers in Subsurface Hydrology*. Boston, MA : Springer US, 2000. – ISBN 978-1-4615-4557-6 32

[Craig 1957] Craig, H.: Isotopic standards for carbon and oxygen and correction factors for mass-spectrometric analysis of carbon dioxide. In: *Geochimica et cosmochimica acta* 12 (1957), Nr. 1, p. 133–149. – ISBN 1581152833 38

[Craig 1961] Craig, H.: Isotopic Variations in Meteoric Waters. In: *Science (New York, N.Y.)* 133 (1961), Nr. 3465, p. 1702–1703. – ISBN 00368075 33

[Crowe 1958] Crowe, C.: Carbon-14 Activity during the past 5,000 Years. In: *Nature* 182 (1958), p. 470–471 35

[Damon et al. 1989] Damon, P.E. ; Cheng, S. ; Linick, T.W.: Fine and hyperfine structure in the spectrum of secular variations of atmospheric 14C. In: *Radiocarbon* 31 (1989), Nr. 3, p. 704–718. – ISBN 0033-8222 35

[Dansgaard 1964] Dansgaard, W.: Stable isotopes in precipitation. In: *Tellus* 16 (1964), Nr. 4, p. 436–468. – ISBN 2153-3490 32, 33

[Darcy 1856] Darcy, H.: *Les fontaines publiques de la ville de Dijon: Exposition et application des principes a suivre et des formules a employer dans les questions de distribution d'eau; ouvrage terminé par un appendice relatif aux fournitures d'eau de plusieurs villes au filtrage des eaux et a la fabrication des tuyaux de fonte, de plomb, de tole et de bitume. Atlas.* Victor Dalmont, Libraire des Corps imperiaux des ponts et chaussées et des mines, 1856 13

[DiPippo 2012] DiPippo, R.: *Geothermal power plants.* 3rd ed. Oxford, UK : Butterworth-Heinemann, 2012. – Online–Ressource (1 v. p.) p. – ISBN 978-0-12-394787-1 and 0-12-394787-1 and 978-0-08-098206-9 5, 6

[DVGW 2011] DVGW: Arbeitsblatt W 112 2011-10, Grundsätze der Grundwasserprobenahme aus Grundwassermessstellen. 2011. – Research report. – 33 p 56

[DWD 2011] DWD, Deutscher Wetterdienst: *Temperatumittelwerte der Periode 1961 bis 1990.* 2011. – URL http://www.dwd.de/. – Access date: 2011-01-25 74

[DWD 2017] DWD, Deutscher Wetterdienst: *Mitteltemperaturen Baden-Württemberg Jahr.* 2017. – URL http://www.dwd.de/DE/klimaumwelt/klimaueberwachung/deutschland/deutschland_node.html. – Access date: 2017-04-19 74, 76, 100, 111

[Elliot et al. 1993] Elliot, T. ; Ballentine, C.J. ; O'Nions, R.K. ; Ricchiuto, T.: Carbon, helium, neon and argon isotopes in a Po basin (northern Italy) natural gas field. In: *Chemical Geology* 106 (1993), Nr. 3-4, p. 429–440. – ISBN 0009-2541 24

[Etiope and Martinelli 2002] Etiope, G. ; Martinelli, G.: Migration of carrier and trace gases in the geosphere: An overview. In: *Physics of the Earth and Planetary Interiors* 129 (2002), Nr. 3-4, p. 185–204. – ISBN 0031-9201 24, 25, 31

[Fairbanks et al. 2005] Fairbanks, R.G. ; Mortlock, R.A. ; Chiu, R.C. ; Cao, L. ; Kaplan, A. ; Guilderson, T.P. ; Fairbanks, T.W. ; Bloom, A.L. ; Grootes, P.M. ; Nadeau, M.J.: Radiocarbon

calibration curve spanning 0 to 50,000 years BP based on paired 230Th/234U/238U and 14C dates on pristine corals. In: *Quaternary Science Reviews* 24 (2005), Nr. 16-17, p. 1781–1796. – ISBN 0277-3791 35

[Faure and Powell 1972] Faure, G. ; Powell, J.L.: *Minerals, Rocks and Mountains*. Vol. 5: *Strontium Isotope Geology*. Berlin, Heidelberg : Springer-Verlag, 1972 ISSN 0343-2181 24

[Fleischer and Mogro-Campero 1985] Fleischer, R.L. ; Mogro-Campero, A.: Association of subsurface radon changes in Alaska and the northeastern United States with earthquakes. In: *Geochimica et Cosmochimica Acta* 49 (1985), Nr. 4, p. 1061–1071. – ISSN 00167037 31

[Fontes and Garnier 1979] Fontes, J.C. ; Garnier, J.M.: Determination of the initial 14C activity of the total dissolved carbon: A review of the existing models and a new approach. In: *Water Resources Research* 15 (1979), Nr. 2, p. 399–413 37, 80, 134

[Freundt et al. 2013] Freundt, F. ; Schneider, T. ; Aeschbach-Hertig, W.: Response of noble gas partial pressures in soil air to oxygen depletion. In: *Chemical Geology* 339 (2013), p. 283–290. – ISBN 0009-2541 11, 18, 36

[Friedrich 2007] Friedrich, R.: *Grundwassercharakterisierung mit Umwelttracern: Erkundung des Grundwassers der Odenwald-Region sowie Implementierung eines neuen Edelgas-Massenspektrometersystems*, Dissertation, 2007 34, 46, 61, 62, 63, 65, 96, 101, 115

[Gat et al. 2001] Gat, J.R. ; Mook, W.G. ; Meijer, A.J. ; Mook, W.G. (Ed.): *Volume II Atmospheric water*. Paris : UNESCO, 2001. – 1–113 p 28

[Geyh 2000] Geyh, M. ; Mook, W.G. (Ed.): *Volume IV Groundwater: Saturated and unsaturated zone*. Paris : UNESCO, 2000. – 1–291 p 38

[Godwin 1962] Godwin, H.: Half-life of Radiocarbon. In: *Nature* 195 (1962), Nr. 4845, p. 984–984. – ISSN 0028-0836 35

[Graham 2002] Graham, D.W.: Noble Gas Isotope Geochemistry of Mid-Ocean Ridge and Ocean Island Basalts: Characterization of Mantle Source Reservoirs. In: Porcelli, Donald (Ed.) ; Ballentine, C. J. (Ed.) ; Wieler, R. (Ed.): *Noble Gases in Geochemistry and Cosmochemistry* Vol. 47. Washington, DC : Mineralogical Society of America, 2002, p. 247–318. – ISBN 0-939950-59-6 19, 20, 25

[Griesshaber et al. 1992] Griesshaber, E. ; O'Nions, R.K. ; Oxburgh, E.R.: Helium and carbon isotope systematics in crustal fluids from the Eifel, the Rhine Graben and Black Forest, F.R.G. In: *Chemical Geology* 99 (1992), p. 213–235. – ISBN 0009-2541 20, 24, 39, 46, 67, 82, 96, 108, 136, 152, 155

[Griffiths et al. 2016] Griffiths, L. ; Heap, M.J. ; Wang, F. ; Daval, D. ; Gilg, H.A. ; Baud, P. ; Schmittbuhl, J. ; Genter, A.: Geothermics Geothermal implications for fracture-filling hydrothermal precipitation. In: *Geothermics* 64 (2016), p. 235–245. – ISSN 0375-6505 25

[Grothe 1992] Grothe, J.: *Datenerfassung und Datenauswertung am Heidelberger Low-Level-Tritium-Messsystem*, Heidelberg University, Diploma Thesis, 1992 68

[GtV 2017] GtV, Bundesverband Geothermie: *Nutzung der Geothermie in Deutschland*. 2017. – URL http://www.geothermie.de/wissenswelt/geothermie/in-deutschland.html. – Access date: 2017-02-26 5

[Hagedorn 2004] Hagedorn, E.-M.: *Sedimentpetrographie und Lithofazies der jungtertiären und quartären Sedimente im Oberrheingebiet*, Universität zu Köln, Dissertation, 2004 43

[Hagemann et al. 1970] Hagemann, R. ; Nief, G. ; Roth, E.: Absolute isotopic scale for deuterium analysis of natural waters. Absolute D/H ratio for SMOW1. In: *Tellus* 22 (1970), Nr. 6, p. 712–715. – ISBN 2153-3490 32

[Haimberger et al. 2005] Haimberger, R. ; Hoppe, A. ; Schäfer, A.: High-resolution seismic survey on the Rhine River in the northern Upper Rhine Graben. In: *International Journal of Earth Sciences* 94 (2005), Nr. 4, p. 657–668. – ISSN 14373254 43

[Hall et al. 2005] Hall, C.M. ; Castro, M.C. ; Lohmann, K.C. ; Ma, L.: Noble gases and stable isotopes in a shallow aquifer in southern Michigan: Implications for noble gas paleotemperature reconstructions for cool climates. In: *Geophysical Research Letters* 32 (2005), p. 1–4. – ISBN 0094-8276 18, 74

[Hartmann 2014] Hartmann, J.: *Entwicklung einer in situ-Methodik zur Bestimmung der Konzentration und $\delta^{13}C$-Isotopie von CH_4 und CO_2 in Wassern*, Heidelberg University, Master thesis, 2014 52, 53

[He et al. 1999] He, K. ; Stober, I. ; Bucher, K.: Chemical evolution of thermal waters from limestone aquifers of the Southern Upper Rhine Valley. In: *Applied Geochemistry* 14 (1999), p. 223–235. – ISSN 08832927 41, 45, 82, 84, 99, 100, 139

[Heath 1983] Heath, R.C.: *Basic Ground-Water Hydrology*. 1983. – 86 p. – ISBN 0607689730 12

[Heaton and Vogel 1981] Heaton, T.H.E. ; Vogel, J.C.: "Excess Air" in groundwater. In: *Journal of Hydrology* 50 (1981), p. 201–216 15, 17

[Henry 1803] Henry, W.: Experiments on the Quantity of Gases Absorbed by Water, at Different Temperatures, and under Different Pressures. In: *Philosophical Transactions of the Royal Society of London* 93 (1803), p. 29–274 14

[Hilton et al. 2002] Hilton, D.R. ; Fischer, T.P. ; Marty, B.: Noble Gases and Volatile Recycling at Subduction Zones. In: Porcelli, Donald (Ed.) ; Ballentine, C. J. (Ed.) ; Wieler, R. (Ed.): *Noble Gases in Geochemistry and Cosmochemistry* Vol. 47. Washington, DC : Mineralogical Society of America, 2002. – ISSN 1529-6466 20

[HLNUG 2017] HLNUG, Hessisches Landesamt für Naturschutz, Umwelt und Geologie: *Tiefe Geothermie, Perspektiven tiefer Geothermie in Hessen.* 2017. – URL www.hlnug.de/themen/geologie/erdwaerme-geothermie/tiefe-geothermie. – Access date: 2017-03-22 43, 114

[HLUG 2010] HLUG, Hessisches Landesamt für Umwelt und Geologie: Nutzung tiefer Geothermie in Hessen. Wiesbaden : Hessisches Ministerium für Umwelt, Energie, Landwirtschaft und Verbraucherschutz, 2010, p. 1–12 6

[Holocher et al. 2002] Holocher, J. ; Peeters, F. ; Aeschbach-Hertig, W. ; Hofer, M. ; Brennwald, M.S. ; Kinzelbach, W. ; Kipfer, R.: Experimental investigations on the formation of excess air in quasi-saturated porous media. In: *Geochimica et Cosmochimica Acta* 66 (2002), Nr. 23, p. 4103–4117 16

[Hölting and Coldewey 2009] Hölting, B. ; Coldewey, W.G.: *Hydrogeologie.* 7., neu bearb. und erw. Aufl. Heidelberg : Spektrum Akad. Verl., 2009. – 383 p 11, 12, 13

[Hooker et al. 1985] Hooker, P.J. ; O'Nions, R.K. ; Oxburgh, E.R.: Helium Isotopes in North Sea gas fields and the Rhine rift. In: *Nature* 318 (1985), p. 273–275. – ISBN 0028-0836 20, 21, 46, 96

[Hoyt et al. 1992] Hoyt, D.V. ; Kyle, H.L. ; Hickey, J.R. ; Maschhoff, R.H.: The Nimbus 7 solar total irradiance: A new algorithm for its derivation. In: *Journal of Geophysical Research: Space Physics* 97 (1992), Nr. A1, p. 51–63. – ISSN 2156-2202 35

[Holting 1969] Holting, B.: Die Ionenverhaltnisse in den Mineralwassern Hessens. In: *Notizblatt hessisches Landesamt fur Bodenforschung* 97 (1969), p. 333–351 43, 91, 105

[Hughen et al. 2006] Hughen, K. ; Southon, J. ; Lehman, S. ; Bertrand, C. ; Turnbull, J.: Marine-derived 14C calibration and activity record for the past 50,000 years updated from the Cariaco Basin. In: *Quaternary Science Reviews* 25 (2006), Nr. 23-24, p. 3216–3227. – ISBN 0277-3791 35

[Huttner and Schreiner 1989] Huttner, R. ; Schreiner, A.: *Geologische Ubersichtskarte von Baden-Wurttemberg. Maßstab: 1:500000.* 1989 44, 45

[IAEA 1993] IAEA: Reference and intercomparison materials for stable isotopes of light elements / International Atomic Energy Agency. Vienna, 1993 (December). – Research report. – 1–3 p. – ISBN IAEA-TECDOC-825 38

[IAEA 2004] IAEA: Management of Waste Containing Tritium and Carbon-14 / International Atomic Energy Agency. Vienna, 2004 (421). – Research report. – 109 p. – ISBN 92-0-114303-6 28

[IAEA 2017] IAEA, International Atomic Energy Agency: *Global Network of Isotopes in Rivers (GNIR)*. 2017. – URL http://www.iaea.org/water. – Access date: 2017-03-01 95, 127, 128

[IAEA/WMO 2017] IAEA/WMO, International Atomic Energy Agency: *Global Network of Isotopes in Precipitation (GNIP)*. 2017. – URL http://www.iaea.org/water. – Access date: 2017-03-01 27, 34, 78, 79, 86, 87, 91, 102, 124, 126, 127, 129

[ITG 2014] ITG, Informationsportal Tiefe Geothermie: *Dunkle Wolken über Geothermiekraftwerk Landau*. 2014. – URL http://www.tiefegeothermie.de/news/dunkle-wolken-ueber-geothermiekraftwerk-landau. – Access date: 2017-02-26 5

[Jacob and Sonntag 1991] Jacob, H. ; Sonntag, C.: *An 8-year record of the seasonal variation of 2H and 18O in atmospheric water vapour and precipitation at Heidelberg, Germany*. 1991 33

[Jähne et al. 1987] Jähne, B. ; Heinz, G. ; Dietrich, W.: Measurement of the Diffusion Coefficients of Sparingly Soluble Gases in Water. In: *J. Geophys. Res.* 92 (1987), Nr. 10, p. 767–776 29

[James and Palmer 2000] James, T.H. ; Palmer, M.R.: The lithium isotope composition of international rock standards. In: *Chemical Geology* 166 (2000), p. 319–326 20

[Jung and Aeschbach submitted] Jung, M. ; Aeschbach, W.: *A new software tool for the analysis of noble gas data sets from (ground)water*. submitted 16, 67, 68, 74

[Jung 2014] Jung, M.W.: *Noble Gas Thermometry in Groundwater Hydrology: Development of Advanced Evaluation Methods and Review of Data Sets from the Literature*, Heidelberg University, Dissertation, 2014 67

[Kato 2000] Kato, V.: Geothermal field studies using stable isotope hydrology: Casestudies in Uganda and Iceland. In: *The United Nations University* (2000), Nr. 10 33, 93, 99, 100

[Kaudse 2014] Kaudse, T.: *Noble gases in groundwater of the Azraq Oasis, Jordan, and along the central Dead Sea Transform*, Universität Heidelberg, Dissertation, 2014 22, 23, 47, 61, 62, 103, 146

[Kaudse et al. 2016] Kaudse, T. ; Bani-Khalaf, R. ; Tuffaha, R. ; Freundt, F. ; Aeschbach-Hertig, W.: Noble gases reveal the complex groundwater mixing pattern and origin of salinization in the Azraq Oasis, Jordan. In: *Applied Geochemistry* 66 (2016), p. 114–128. – ISSN 18729134 47

[Kennedy and van Soest 2006] Kennedy, B.M. ; van Soest, M.C.: A helium isotope perspective on the Dixie Valley, Nevada, hydrothermal system. In: *Geothermics* 35 (2006), p. 26–43 47

[Kennedy and van Soest 2007] Kennedy, B.M. ; van Soest, M.C.: Flow of mantle fluids through the ductile lower crust: helium isotope trends. In: *Science (New York, N.Y.)* 318 (2007), Nr. 2007, p. 1433–1436. – ISBN 0036-8075 47

[King 1978] King, C.Y.: Radon emanation on San Andreas fault. In: *Nature* 271 (1978), p. 516–519. – ISBN 0028-0836 31

[Kipfer et al. 2002] Kipfer, R. ; Aeschbach-Hertig, W. ; Peeters, F. ; Stute, M.: Noble Gases in Lakes and Ground Waters. In: Porcelli, Donald (Ed.) ; Ballentine, C. J. (Ed.) ; Wieler, R. (Ed.): *Noble Gases in Geochemistry and Cosmochemistry* Vol. 47. Washington, DC : Mineralogical Society of America, 2002, p. 615–700. – ISBN 1529-6466\r0-939950-59-6 14, 15, 17, 19, 25

[Kluge et al. 2007] Kluge, T. ; Ilmberger, J. ; von Rohden, C. ; Aeschbach-Hertig, W.: Tracing and quantifying groundwater inflow into lakes using radon-222. In: *Hydrology and Earth System Sciences Discussions* 4 (2007), Nr. 3, p. 1519–1548. – ISBN 1027-5606 31

[Klump et al. 2008] Klump, S. ; Cirpka, O.A. ; Surbeck, H. ; Kipfer, R.: Experimental and numerical studies on excess-air formation in quasi-saturated porous media. In: *Water Resources Research* 44 (2008), p. 1–15. – ISBN 0043-1397 16

[Klump et al. 2007] Klump, S. ; Tomonaga, Y. ; Kienzler, P. ; Kinzelbach, W. ; Baumann, T. ; Imboden, D.M. ; Kipfer, R.: Field experiments yield new insights into gas exchange and excess air formation in natural porous media. In: *Geochimica et Cosmochimica Acta* 71 (2007), p. 1385–1397. – ISBN 0016-7037 16

[Kockarts 1973] Kockarts, G.: Helium in the terrestrial atmosphere. In: *Space Science Reviews* 14 (1973), Nr. 6, p. 723–757. – ISBN 0038-6308 19

[König et al. 1976] König, L.A. ; Winter, M. ; Schüler, H.: Tritium in Niederschlägen, Oberflächen-, Grund- und Trinkwasser / Kernforschungszentrum Karlsruhe. 1976 (November). – Research report. – 96 p 28

[Kreuzer 2007] Kreuzer, A.M.: *Paläotemperaturstudie mit Edelgasen im Grundwasser der Nordchinesischen Tiefebene*, Dissertation, 2007 69, 70

[Kromer 2007] Kromer, B.: Radiokohlenstoffdatierung. In: Wagner, G.A. (Ed.): *Einführung in die Archäometrie*. Springer, 2007, p. 3–10. – ISBN 9783540719366 36

[Kromer et al. 2013] Kromer, B. ; Lindauer, S. ; Synal, H.A. ; Wacker, L.: MAMS - A new AMS facility at the Curt-Engelhorn-Centre for Achaeometry, Mannheim, Germany. In: *Nuclear Instruments and Methods in Physics Research, Section B: Beam Interactions with Materials and Atoms* 294 (2013), p. 11–13. – ISSN 0168583X 70

[Kurz and Jenkins 1981] Kurz, M.D. ; Jenkins, W.J.: The Distribution of Helium in Oceanic Basalt Glasses. In: *Earth and Planetary Science Letters* 53 (1981), p. 41–54 24

[Lal 1987] Lal, D.: Production of 3He in terrestrial rocks. In: *Chemical Geology: Isotope Geoscience Section* 66 (1987), Nr. 1-2, p. 89–98. – ISBN 0168-9622 28

[Landtag BW 2011] Landtag BW, Ministeriums fur Umwelt, Klima und Energiewirtschaft: *Atomkraftwerk Fessenheim – Tritium im Grundwasser, Sicherung der Kuhlwasserzufuhr, Haftung bei einem schweren Unfall (Kleine Anfrage der Abg. Barbl Mielich GRUNE).* 2011 97

[Le Guen 2009] Le Guen, B: Impact of tritium around EDF nuclear power plants. In: *Journal of radiological protection : official journal of the Society for Radiological Protection* 29 (2009), Nr. 2, p. 163–73. – ISSN 0952-4746 28

[Lee et al. 2006] Lee, J.Y. ; Marti, K. ; Severinghaus, J.P. ; Kawamura, K. ; Yoo, H.S. ; Lee, J.B. ; Kim, J.S.: A redetermination of the isotopic abundances of atmospheric Ar. In: *Geochimica et Cosmochimica Acta* 70 (2006), Nr. 17, p. 4507–4512. – ISBN 0016-7037 26, 85

[Lehmann et al. 1993] Lehmann, B.E. ; Davis, S.N. ; Fabryka-Martin, J.T.: Atmospheric and subsurface sources of stable and radioactive nuclides used for groundwater dating. In: *Water Resources Research* 29 (1993), Nr. 7, p. 2027–2040. – ISSN 1944-7973 16, 19

[Levin et al. 2010] Levin, I. ; Naegler, T. ; Kromer, B. ; Diehl, M. ; Francey, R.J. ; Gomez-Pelaez, A.J. ; Steele, L.P. ; Wagenbach, D. ; Weller, R. ; Worthy, D.E.: Observations and modelling of the global distribution and long-term trend of atmospheric 14CO2. In: *Tellus, Series B: Chemical and Physical Meteorology* 62 (2010), Nr. 1, p. 26–46. – ISBN 0280-6509 36

[Leya and Wieler 1999] Leya, I. ; Wieler, R.: Nucleogenic production of Ne isotopes in Earth's crust and upper mantle induced by alpha particles from the decay of U and Th. In: *Journal of Geophysical Research-Solid Earth* 104 (1999), Nr. B7, p. 15439–15450. – ISBN 0148-0227 26

[LfU 2003] LfU, Landesanstalt für Umweltschutz Baden-Württemberg: Radioaktivität in Baden-Württemberg, Jahresbericht 1998-2001. Karlsruhe, 2003. – Research report 95

[Libby 1946] Libby, W.F.: Atmospheric helium three and radiocarbon from cosmic radiation. In: *Physical Review* 69 (1946), Nr. 11-12, p. 671–672. – ISBN 0031-899X 27, 35

[Libby 1952] Libby, W.F.: *Radiocarbon Dating.* University of Chicago Press, 1952 (University of Chicago publications in the physical sciences series) 35

[Lippmann et al. 2003] Lippmann, J. ; Stute, M. ; Torgersen, T. ; Moser, D.P. ; Hall, J.A. ; Lin, L. ; Borcsik, M. ; Bellamy, R.E.S. ; Onstott, T.C.: Dating ultra-deep mine waters with noble gases and 36Cl, Witwatersrand Basin, South Africa. In: *Geochimica et Cosmochimica Acta* 67 (2003), Nr. 23, p. 4597–4619. – ISBN 0016-7037 26, 98, 99

[Lombardi and Voltattorni 2010] Lombardi, S. ; Voltattorni, N.: Rn, He and CO2 soil gas geochemistry for the study of active and inactive faults. In: *Applied Geochemistry* 25 (2010), Nr. 8, p. 1206–1220. – ISBN 0883-2927 31

[Lu et al. 2014] Lu, Z.T. ; Schlosser, P. ; Smethie, W.M. ; Sturchio, N.C. ; Fischer, T.P. ; Kennedy, B.M. ; Purtschert, R. ; Severinghaus, J.P. ; Solomon, D.K. ; Tanhua, T. ; Yokochi, R.: Tracer applications of noble gas radionuclides in the geosciences. In: *Earth-Science Reviews* 138 (2014), p. 196–214. – ISBN 0012-8252 18, 26

[LUBW 1999] LUBW: *Hydrogeologische Kartierung und Grundwasserbewirtschaftung Rhein-Neckar-Raum, Fortschreibung 1983-1998*. 1999 43, 110

[Lucas and Unterweger 2000] Lucas, L.L. ; Unterweger, M.P.: Comprehensive review and critical evaluation of the half-life of tritium. In: *Journal Of Research Of The National Institute Of Standards And Technology* 105 (2000), Nr. 4, p. 541–549. – ISBN 1044-677X 27

[Lupton 1983] Lupton, J.E.: Terrestrial Inert Gases: Isotope Tracer Studies and Clues to Primordial Components in the Mantle. In: *Annual Review of Earth and Planetary Sciences* 11 (1983), Nr. 1976, p. 371–414. – ISSN 0084-6597 19

[Lutz et al. 2013] Lutz, H. ; Lorenz, V. ; Engel, T. ; Häfner, F. ; Haneke, J.: Paleogene phreatomagmatic volcanism on the western main fault of the northern Upper Rhine Graben (Kisselwörth diatreme and Nierstein-Astheim Volcanic System, Germany). In: *Bulletin of Volcanology* 75 (2013), Nr. 7, p. 1–11. – ISBN 0044501307 41

[Majer et al. 2007] Majer, E.L. ; Baria, R. ; Stark, M. ; Oates, S. ; Bommer, J. ; Smith, B. ; Asanuma, H.: Induced seismicity associated with Enhanced Geothermal Systems. In: *Geothermics* 36 (2007), Nr. 3, p. 185–222. – ISBN 0375-6505 7

[Mamyrin and Tolstikhin 1984] Mamyrin, B.A. ; Tolstikhin, I.N.: *Developments in Geochemistry*. Vol. 3: *Helium Isotopes in Nature*. Amsterdam, Oxford, New York, Tokyo : Elsevier B.V., 1984. – ISBN 9781483289809 20, 21, 22, 24, 61, 62, 103, 146

[Marty et al. 1993] Marty, B. ; Torgersen, T. ; Meynier, V. ; O'Nions, R.K. ; de Marsily, G: Helium isotope fluxes and groundwater ages in the Dogger Aquifer, Paris Basin. In: *Water Resources Research* 29 (1993), Nr. 4, p. 1025–1035. – ISBN 1944-7973 25

[Mayer 2017] Mayer, S.: *Dynamics of reactive and inert gases in soil air and groundwater in the context of noble gases as environmental tracers*, Heidelberg University, PhD Thesis, 2017 11, 18, 31, 36, 68, 75, 76

[Mismanos and Vasquez 2015] Mismanos, J.W. ; Vasquez, A.A.: Scouting for Permeable Structures in Geothermal Systems Using Soil Gas Radon. In: *World Geothermal Congress 2015* (2015), Nr. April, p. 5 31

[Mook 1980] Mook, W.G.: Carbon-14 in hydrogeological studies. In: Fritz, P. (Ed.) ; Fontes, J.C. (Ed.): *Handbook of environmental isotope geochemistry*. Amsterdam : evier Sci. Publ. Co., 1980, p. 49–74 35

[Mook and DeVries 2000] Mook, W.G. ; DeVries, J.J.: Volume I Introduction: Theory Methods Review. In: Mook, W.G. (Ed.): *Environmental isotopes in the hydroloigical cycle: Principles and applications*. Paris : UNESCO, 2000, Chap. I 28, 31, 35

[Moreira and Kurz 2013] Moreira, M.A. ; Kurz, M.D.: Noble gases as tracers of mantle processes and magmatic degassing. In: Burnard, P. (Ed.): *The noble gases as geochemical tracers, Advances in isotope geochemistry*. Heidelberg, New York : Springer, 2013, Chap. 9, p. 371—-391 98, 100, 119

[Morrison and Pine 1955] Morrison, P. ; Pine, J.: Radiogenic Origin of the Helium Isotopes in Rock. In: *Annals of the New York Academy of Sciences* 62 (1955), Nr. 3, p. 71–92. – ISBN 0077-8923 19, 20

[Muller 1977] Muller, R.A.: Radioisotope Dating with a Cyclotron. In: *Science* 196 (1977), Nr. 4289, p. 489–494 70

[Mumm 2000] Mumm, H.: Die Erschließung der Thermalquelle und der Bau des Radium-Solbads, 1912 bis 1928. In: *Jahrbuch zur Geschichte der Stadt 5*. Heidelberg, 2000, p. 55–76 95

[Münnich and Vogel 1958] Münnich, K.O. ; Vogel, J.C.: Durch Atomexplosionen erzeugter Radiokohlenstoff in der Atmosphäre. In: *Naturwissenschaften* 45 (1958), p. 327–329 35

[Nicholson 1993] Nicholson, K.: *Geothermal fluids : chemistry and exploration techniques*. Berlin [u.a.] : Springer, 1993 33

[Nier 1950] Nier, A.O.: A redetermination of the relative abundances of the isotopes of carbon, nitrogen, oxygen, argon, and potassium. In: *Physical Review* 77 (1950), Nr. 6, p. 789–793. – ISBN 0031-899X\n1536-6065 26, 84, 85

[OpenStreetMap contributors 2017] OpenStreetMap contributors: *Planet dump retrieved from http://planet.osm.org* . `http://www.openstreetmap.org`. 2017 48, 49

[Oxburgh and O'Nions 1987] Oxburgh, E.R. ; O'Nions, R.K.: Helium Loss, Tectonics, and the Terrestrial Heat Budget. In: *Science* 237 (1987), Nr. 4822, p. 1584–1888. – ISSN 0036-8075 46

[Oxburgh et al. 1986] Oxburgh, E.R. ; O'Nions, R.K. ; Hill, R.I.: Helium isotopes in sedimentary basins. In: *Nature* 324 (1986), Nr. 18, p. 632–635 47

[Ozima and Podosek 1983] Ozima, M. ; Podosek, F.A.: *Noble Gas Geochemistry*. New York : Cambridge Univ. Press, 1983 30

[Paldus and Kachanov 2005] Paldus, B. ; Kachanov, A.: An historical overview of cavity-enhanced methods. In: *Canadian Journal of Physics* 83 (2005), Nr. 10, p. 975–999. – ISBN 0008-4204 71

[Pauwels et al. 1993] Pauwels, H. ; Fouillac, C. ; Fouillac, A.M.: Chemistry and isotopes of deep geothermal saline fluids in the Upper Rhine Graben: Origin of compounds and water-rock interactions. In: *Geochimica et Cosmochimica Acta* 57 (1993), Nr. 12, p. 2737–2749. – ISBN 0016-7037 41, 93, 94, 99

[Pearson Jr. 1965] Pearson Jr., F.J.: Use of C-13/C-12 ratios to correct radiocarbon ages of material initially diluted by limestone. In: *Radiocarbon and Tritium Dating, Proceedings of Sixth International Conference on Radiocarbon*. Washington : Pullman, 1965, p. 357—-366 37, 80

[Peeters et al. 2003] Peeters, Frank ; Beyerle, Urs ; Aeschbach-Hertig, Werner ; Holocher, Johannes ; Brennwald, M.S. ; Kipfer, R.: Improving noble gas based paleoclimate reconstruction and groundwater dating using 20Ne/22Ne ratios. In: *Geochimica et Cosmochimica Acta* 67 (2003), Nr. 4, p. 587–600. – ISSN 00167037 30

[Peisker 1984] Peisker, M.: Modellvorstellungen zur Kohlenstoff-Isotopendiskriminierung bei der Photosynthese yon C_3- und C_4-Pflanzen. In: *Kulturpflanze* 32 (1984), p. 35–65 38

[Porcelli et al. 2002] Porcelli, D. ; Ballentine, C. ; Wieler, R.: *Rev. Mineral. Geochem.*. Vol. 47: *An Overview of Noble Gas Geochemistry and Cosmochemistry*. Washington, DC : Mineralogical Society of America, Geochemical Society, 2002 15, 18, 19, 25, 26, 64, 67, 84, 85, 137, 155

[Pribnow and Schellschmidt 2000] Pribnow, D. ; Schellschmidt, R.: Termal Tracking of Upper Crustal Fluid Flow in the Rhine Graben. In: *Geophysical Research Letters* 27 (2000), Nr. 13, p. 1957–1960 41

[Pyle 1993] Pyle, D.M.: Graphical analysis of rare gas mixing systematics in geothermal systems. In: *Geochemical Journal* 27 (1993), p. 125–129 20, 21

[Reimer et al. 2013] Reimer, P.J. ; Bard, E. ; Bayliss, A. ; Beck, J.W. ; Blackwell, P.G. ; Bronk Ramsey, C. ; Buck, C.E. ; Cheng, H. ; Edwards, R.L. ; Friedrich, M. ; Grootes, P.M. ; Guilderson, T.P. ; Haflidason, H. ; Hajdas, I. ; Hatté, C. ; Heaton, T.J. ; Hoffmann, D.L. ; Hogg, A.G. ; Hughen, K.A. ; Kaiser, K.F. ; Kromer, B. ; Manning, S.W. ; Niu, M. ; Reimer, R.W. ; Richards, D.A. ; Scott, E.M. ; Southon, J.R. ; Staff, R.A. ; Turney, C.S.M. ; van der Plicht, J.: IntCal13 and Marine13 Radiocarbon Age Calibration Curves 0–50,000 Years cal BP. In: *Radiocarbon* 55 (2013), Nr. 4, p. 1869–1887. – ISSN 00338222 35, 36, 134, 149

[Ritterbusch et al. 2014] Ritterbusch, F. ; Ebser, S. ; Welte, J. ; Reichel, T. ; Kersting, A. ; Purtschert, R. ; Aeschbach-Hertig, W. ; Oberthaler, M.K.: Groundwater dating with Atom Trap Trace Analysis of 39Ar. In: *Geophysical Research Letters* 41 (2014), Nr. 19, p. 6758–6764. – ISSN 19448007 26

[Robertson and Cherry 1989] Robertson, W.D. ; Cherry, J.A.: Tritium as an indicator of recharge and dispersion in a groundwater system in central Ontario. In: *Water Resources Research* 25 (1989), Nr. 6, p. 1097–1109. – ISSN 1944-7973 28

[Roedel and Wagner 2011] Roedel, W. ; Wagner, T.: *Physik unserer Umwelt: Die Atmosphäre*. 4. Heidelberg : Springer Verlag, 2011. – 589 p. – ISBN 978-3-642-15728-8 31, 32, 33

[Roether 1968] Roether, W.: Estimating the tritium input to groundwater from wine samples: groundwater and direct run-off contribution to central european surface waters. In: *pp 73-91 of Isotopes in Hydrology. Vienna, International Atomic Energy Agency, 1967.* (1968), Oct 28, 78

[Rózański et al. 1993] Rózański, K. ; Araguas-Araguas, L.J. ; Gonfiantini, R.: Isotopic Patterns in Modern Global Precipitation. In: *Climate Change on Continental Isotopic Records*. Geophysical Monograph 78, 1993, p. 1–36 33, 87, 93

[RPF/LGRB 2008] RPF/LGRB: *Hydrogeologischer Bau und Aquifereigenschaften der Lockergesteine im Oberrheingraben (Baden-Wurttemberg)*. 2008 45

[Saar 2011] Saar, M.O.: Review: Geothermal heat as a tracer of large-scale groundwater flow and as a means to determine permeability fields. In: *Hydrogeology Journal* 19 (2011), p. 31–52. – ISBN 1004001006572 24

[Saar et al. 2005] Saar, M.O. ; Castro, M.C. ; Hall, C.M. ; Manga, M. ; Rose, T.P.: Quantifying magmatic, crustal, and atmospheric helium contributions to volcanic aquifers using all stable noble gases: Implications for magmatism and groundwater flow. In: *Geochemistry, Geophysics, Geosystems* 6 (2005), Nr. December 2004. – ISBN 1525-2027 47

[Salomon-Calvi 1927] Salomon-Calvi, W.: *Die Erbohrung der Heidelberger Radium-Sol-Therme und ihre geologischen Verhältnisse*. Berlin ; Leipzig : de Gruyter, 1927 (Abhandlungen der Heidelberger Akademie der Wissenschaften, Mathematisch-Naturwissenschaftliche Klasse ARRAY(0x34fofc8)). – 105 S. p 95

[Santschi et al. 1987] Santschi, P.H. ; Hoehn, E. ; Lueck, A. ; Farrenkothen, K.: Tritium as a tracer for the movement of surface water and groundwater in the Glatt Valley, Switzerland. In: *Environmental Science & Technology* 21 (1987), Nr. 9, p. 909–916. – ISBN 0013-936X 28

[Sarda et al. 1988] Sarda, P. ; Staudacher, T. ; Allègre, C.J.: Neon isotopes in submarine basalts. In: *Earth and Planetary Science Letters* 91 (1988), Nr. 1-2, p. 73–88. – ISBN 0012-821X 25

[Schlosser et al. 1988] Schlosser, P. ; Stute, M. ; Dörr, H. ; Sonntag, C. ; Münnich, K.O.: Tritium/3He dating of shallow groundwater. In: *Earth and Planetary Science Letters* 89 (1988), Nr. 3-4, p. 353–362. – ISBN 0012-821X 29

[Schmidt et al. 2017a] Schmidt, G. ; Al Najem, S. ; Isenbeck-Schröter, M. ; Freundt, F. ; Kraml, M. ; Aeschbach, W.: 87Sr/86Sr Ratios in Shallow and Deep Aquifers from the Southern Upper Rhine Graben, Germany. In: *15th Water-Rock Interaction International Symposium, WRI-15* Vol. 17, Procedia Earth and Planetary Science, Elsevier, 2017, p. 626–629. – ISSN 18785220 9, 73

[Schmidt et al. 2017b] Schmidt, G. ; Al Najem, S. ; Isenbeck-Schröter, M. ; Freundt, F. ; Kraml, M. ; Eichstädter, R. ; Aeschbach, W.: 87Sr/86Sr ratios in shallow and deep aquifers and thermal water from the Eastern Boundary Fault of the northern Upper Rhine Graben at the Heidelberg Basin, Germany. In: *15th Water-Rock Interaction International Symposium, WRI-15* Vol. 17, Procedia Earth and Planetary Science, Elsevier, 2017, p. 3–6 9, 73, 95, 96

[Schmidt et al. 2017c] Schmidt, G. ; Al Najem, S. ; Isenbeck-Schröter, M. ; Freundt, F. ; Kraml, M. ; Eichstädter, R. ; Aeschbach, W.: Ascending Deep Fluids into Shallow Aquifer at Hydraulically Active Segments of the Western Boundary Fault of the Rhine Graben, Germany: Constraints from 87Sr/86Sr ratios. In: *15th Water-Rock Interaction International Symposium, WRI-15* Vol. 17, Procedia Earth and Planetary Science, Elsevier, 2017, p. 81–84. – ISSN 18785220 9, 52, 73, 90, 105

[Schmitt 1992] Schmitt, M.: *Ursache und Ablauf der Versalzung der oberen Grundwasserleiter im nördlichen Oberrheingraben*, Technische Hochschule Darmstadt, Dissertation, 1992. – 220 p 41, 43, 91, 105

[Schmitt and Steuer 1974a] Schmitt, O. ; Steuer, A.: *Erlauterungen zur Geologischen Karte von Hessen, 1:25000, Blatt Nr. 6016 Groß-Gerau.* 1974 42, 43

[Schmitt and Steuer 1974b] Schmitt, O. ; Steuer, A.: *Geologische Karte von Hessen. Blatt 6016: Groß-Gerau. Maßstab 1:25000.* 1974 42, 92

[Schneider 2014] Schneider, T.: *Eine Paläoklimastudie an einem Grundwasseraquifersystem in der Nordchinesischen Ebene*, Heidelberg University, Doctoral Thesis, 2014 68

[Schumacher 2002] Schumacher, M.E.: Upper Rhine Graben: Role of preexisting structures during rift evolution. In: *Tectonics* 21 (2002), Nr. 1. – ISBN 1944-9194 39, 100

[Siemon et al. 2001] Siemon, B. ; Blum, R. ; Pöschel, W. ; Voss, W.: Aeroelektromagnetische und gleichstromgeoelektrische Erkundung eines Salzwasservorkommens im Hessischen Ried. In: *Geol. Jb. Hessen* 128 (2001), p. 115–125 43, 52, 89, 92, 109, 152

[Solomon 2000] Solomon, D.K.: 4He in Groundwater. In: Cook, Peter G. (Ed.) ; Herczeg, Andrew L. (Ed.): *Environmental Tracers in Subsurface Hydrology.* New York : Springer US, 2000, Chap. 14, p. 425–439. – ISBN 0792377079 25

[Stadt Heidelberg 2009] Stadt Heidelberg: *stadtblatt - Anzeiger der Stadt Heidelberg.* 2009. – URL http://ww2.heidelberg.de/stadtblatt-online/index.php?artikel_id=5402&bf=. – Access date: 2017-04-21 43

[Stanley et al. 2009] Stanley, R.H.R. ; Baschek, B. ; Lott, D.E. ; Jenkins, W.J.: A new automated method for measuring noble gases and their isotopic ratios in water samples. In: *Geochemistry, Geophysics, Geosystems* 10 (2009), Nr. 5. – ISSN 15252027 62

[Steiger and Jäger 1977] Steiger, R.H. ; Jäger, E.: Subcommission on geochronology: Convention on the use of decay constants in geo- and cosmochronology. In: *Earth and Planetary Science Letters* 36 (1977), Nr. 3, p. 359–362. – ISBN 0012-821X 26, 84, 85

[Steuer 1908] Steuer, A.: *Geologische Karte des Großherzogtums Hessen. Blatt 6116: Oppenheim. Maßstab 1:25000.* 1908 42

[STMWIVT 2004] STMWIVT, Bayrisches Staatsministerium für Wirtschaft, Infrastruktur, Verkehr und Technologie: Hydrothermale Energiegewinnung. In: Fritzer, Thomas (Ed.) ; Settles, Erik (Ed.) ; Dorsch, Klaus (Ed.): *Bayrischer Geothermieatlas.* München, 2004, p. 104 7, 111

[Stober and Jodocy 2009] Stober, I. ; Jodocy, M.: Eigenschaften geothermischer Nutzhorizonte im baden-württembergischen und französischen Teil des Oberrheingrabens. In: *Grundwasser* 14 (2009), p. 127–137. – ISSN 1430483X 41, 45

[Stuiver and Quay 1980] Stuiver, M. ; Quay, P.D.: Changes in Atmospheric Carbon-14 Attributed to a Variable Sun. In: *Science (New York, N.Y.)* 207 (1980), Nr. 4426, p. 11–19 35

[Sturchio et al. 2004] Sturchio, N.C. ; Du, X. ; Purtschert, R. ; Lehmann, B.E. ; Sultan, M. ; Patterson, L.J. ; Lu, Z.-T. ; Müller, P. ; Bigler, T. ; Bailey, K. ; O'Connor, T.P. ; Young, L. ; Lorenzo, R. ; Becker, R. ; El Alfy, Z. ; El Kaliouby, B. ; Dawood, Y. ; Abdallah, A.M.A.: One million year old groundwater in the Sahara revealed by krypton-81 and chlorine-36. In: *Geophysical Research Letters* 31 (2004), Nr. 5, p. 2–5. – ISBN 0094-8276 12

[Stute et al. 1995a] Stute, M. ; Clark, J.F. ; Schlosser, P. ; Broecker, W.S. ; Bonani, G.: A 30000 yr continental paleotemperature record derived from noble gases dissolved in groundwater from the San Juan Basin, New Mexico. In: *Quaternary Research* 43 (1995), p. 209–220 17

[Stute and Deák 1989] Stute, M. ; Deák, J.: Environmental Isotope Study (14C, 13C, 18O, D , Noble Gases) on Deep Groundwater Circulation Systems in Hungary with Reference to Paleoclimate. In: *Radiocarbon* 31 (1989), Nr. 3, p. 902–918 100

[Stute et al. 1995b] Stute, M. ; Forster, M. ; Frischkorn, H. ; Serejo, A. ; Clark, J.F. ; Schlosser, P. ; Broecker, W. S. ; Bonani, G.: Cooling of Tropical Brazil (5C) During the Last Glacial Maximum. In: *Science (New York, N.Y.)* 269 (1995), Nr. 5222, p. 379–383. – ISSN 0036-8075 17

[Stute et al. 1992] Stute, M. ; Sonntag, C. ; Deák, J. ; Schlosser, P.: Helium in deep circulating groundwater in the Great Hungarian Plain: Flow dynamics and crustal and mantle helium fluxes. In: *Geochimica et Cosmochimica Acta* 56 (1992), Nr. 5, p. 2051–2067. – ISSN 00167037 24, 25

[Suckow et al. 2013] Suckow, A. (Ed.) ; Aggarwal, P.K. (Ed.) ; Araguas-Araguas, L.J. (Ed.): *Isotope Methods for Dating Old Groundwater*. Vienna : IAEA, 2013 18

[Suess 1955] Suess, H.E.: Radiocarbon Concentration in Modern Wood. In: *Science* 122 (1955), Nr. 3166, p. 415–417 36

[Sültenfuß and Massmann 2004] Sültenfuss, J. ; Massmann, G.: Datierung mit der 3He-Tritium-Methode am Beispiel der Uferfiltration im Oderbruch. In: *Grundwasser* 9 (2004), Nr. 4, p. 221–234. – ISBN 0076700400556 29, 31, 69

[Sültenfuß et al. 2009] Sültenfuss, J. ; Roether, W. ; Rhein, M.: The Bremen mass spectrometric facility for the measurement of helium isotopes, neon, and tritium in water. In: *Isotopes in Environmental and Health Studies* 45 (2009), Nr. 2, p. 83–95. – PMID: 20183223 69

[Thews 1970] Thews, J.-W.: Die Mineralquellen von Bad Weilbach. In: *Horst Falke Festschrift*. Wiesbaden : Hess. Landesamt f. Bodenforschung, 1970, p. 193–213 54

[Tolstikhin and Kamenskij 1969] Tolstikhin, I.N. ; Kamenskij, I.L.: Determination of groundwater ages by the T-3He method. In: *Geochem. Int. 6* (1969), p. 810—-811 29

[Torgersen 1989] Torgersen, T.: Terrestrial helium degassing fluxes and the atmospheric helium budget: Implications with respect to the degassing processes of continental crust. In: *Chemical Geology: Isotope Geoscience Section* 79 (1989), Nr. 1, p. 1–14. – ISBN 0009-2541 19

[Torgersen and Clarke 1985] Torgersen, T. ; Clarke, W.B.: Helium accumulation in groundwater, I: An evaluation of sources and the continental flux of crustal 4He in the Great Artesian Basin, Australia. In: *Geochimica et Cosmochimica Acta* 49 (1985), Nr. 5, p. 1211–1218. – ISBN 0016-7037 24

[Träumner 2005] Träumner, K.: *Inbetriebnahme, Tests und erste Anwendung einer neuen Anlage zur massenspektrometrischen Messung von Edelgasen aus Grundwasser- und Stalagmitproben*, Heidelberg University, Diplomarbeit, 2005. – 113 p 115

[Umeda et al. 2007] Umeda, K. ; Sakagawa, Y. ; Ninomiya, A. ; Asamori, K.: Relationship between helium isotopes and heat flux from hot springs in a non-volcanic region, Kii Peninsula, southwest Japan. In: *Geophysical Research Letters* 34 (2007), p. 1–5. – ISSN 00948276 47

[Unkel 2006] Unkel, I.: *AMS- 14 C-Analysen zur Rekonstruktion der Landschafts- und Kulturgeschichte in der Region Palpa (S-Peru)*, Heidelberg University, Dissertation, 2006. – 148 p 69, 70

[Vidal et al. 2015] Vidal, J. ; Genter, A. ; Schmittbuhl, J.: How do permeable fractures in the Triassic sediments of Northern Alsace characterize the top of hydrothermal convective cells? Evidence from Soultz geothermal boreholes (France). In: *Geothermal Energy* 3 (2015), Nr. 1, p. 8. – ISSN 2195-9706 41, 112

[Vogel 1967] Vogel, J.C: Investigation of groundwater flow with radiocarbon. In: *Isotopes in hydrology.* Vienna : IAEA, 1967, p. 355–369 37, 80

[Vogel 1970] Vogel, J.C: Carbon-14 dating of groundwater. In: *Isotopes hydrology.* Vienna : IAEA, 1970, p. 355–369 37, 80

[Voltattorni and Lombardi 2010] Voltattorni, N. ; Lombardi, S.: Soil-Gas Geochemistry: Significance and Application in Geological Prospectings. In: *Natural Gas.* INTECH, 2010, Chap. 9, p. 183–204. – ISBN 9789533070865 31

[Walia et al. 2010] Walia, V. ; Lin, S.J. ; Fu, C.C. ; Yang, T.F. ; Hong, W.L. ; Wen, K.L. ; Chen, C.H.: Soil-gas monitoring: A tool for fault delineation studies along Hsinhua Fault (Tainan), Southern Taiwan. In: *Applied Geochemistry* 25 (2010), Nr. 4, p. 602–607. – ISBN 0883-2927 31

[Walter 2007] Walter, R.: *Geologie von Mitteleuropa.* 7. Auflage. Stuttgart : E. Schweizbart'sche Verlagsbuchhandlung (Nagele u. Obermiller), 2007 40

[Wetherill 1954] Wetherill, G.W.: Variations in the isotopic abundances of neon and argon extracted from radioactive minerals. In: *Physical Review* 96 (1954), Nr. 3, p. 679–683. – ISBN 0031-899X 25

[Wieser 2011] Wieser, M.: *Imprints of climatic and environmental change in a regional aquifer system in an arid part of India using noble gases and other environmental tracers*, Dissertation, 2011 16, 34, 37, 61, 64, 65, 113

[Yamaguchi et al. 1977] Yamaguchi, M. ; Flocker, W.J. ; Howard, F.D.: Soil Atmosphere as Influenced by Temperature and Moisture. In: *Soil Science Society of America* 31 (1977), Nr. 2, p. 164–167 37

[Yatsevich and Honda 1997] Yatsevich, I. ; Honda, M.: Production of nucleogenic neon in the Earth from natural radioactive decay. In: *Journal of Geophysical Research* 102 (1997), Nr. B5, p. 10291–10298. – ISBN 0148-0227 19, 25, 26

[Yurtsever and Gat 1981] Yurtsever, Y. ; Gat, J.R.: Atmospheric Waters. In: *Stable isotope hydrology, Deuterium and Oxygen-18 in the Water Cycle.* Vienna : IAEA Technical Report Series, 1981, p. 356. – ISBN 9201452810 33

[Zhu and Kipfer 2010] Zhu, C. ; Kipfer, R.: Noble gas signatures of high recharge pulses and migrating jet stream in the late Pleistocene over Black Mesa, Arizona, United States. In: *Geology* 38 (2010), Nr. 1, p. 83–86. – ISSN 00917613 16

[ÜWG 2007] ÜWG, Überlandwerk Groß-Gerau GmbH: *Geothermie Trebur: Bohrung nicht fündig. Überlandwerk Groß-Gerau GmbH stoppt Arbeiten für Geothermiekraftwerk.* 2007. – URL http://www.geothermie-trebur.de/projekt/zielsetzung/. – Access date: 2017-04-21 43

[ÜWG 2016] ÜWG, Überlandwerk Groß-Gerau GmbH: *Geothermie Trebur: Bohrung nicht fündig. Überlandwerk Groß-Gerau GmbH stoppt Arbeiten für Geothermiekraftwerk.* 2016. – URL http://www.uewg.de/privatkunden/aktuelles/aktuelle-meldungen/privatkunden-news-details/artikel/geothermie-trebur-bohrung-nicht-fuendig.html. – Access date: 2017-02-28 5, 43, 105